Universidad de Salamanca

Instituto de Biología Molecular y Celular del Cáncer (IBMCC)

Programa de doctorado:

Biociencias: Biología y Clínica del Cáncer y Medicina Traslacional

The role of VRK1 in chromatin remodeling: regulation of histone post-translational modifications and epigenetic enzymes

Tesis doctoral

Eva Monte Serrano

Director:

Dr. Pedro A. Lazo-Zbikowski Taracena

Salamanca, 2023

Prof. Dr. Pedro A. Lazo
Instituto de Biología Molecular y Celular del Cancer
Universidad de Salamanca – CSIC
Campus Miguel de Unamuno
37007 Salamanca
España

Email: pedro.lazo@csic.es; plazozbi@usal.es
Tel.: 923 29 48 04
https://www.cicancer.org/grupo?id=46

Dr. Pedro Alfonso Lazo-Zbikowski Taracena, Profesor de Investigación del Consejo Superior de Investigaciones Científicas (CSIC),

CERTIFICA:

Que la memoria de tesis doctoral titulada "**The role of VRK1 in chromatin remodeling: regulation of histone post-translational modifications and epigenetic enzymes**", presentada por la graduada en Biotecnología **Eva Monte Serrano**, ha sido realizada najo su dirección en el Instituto de Biología Molecular y Celular del Cáncer (IBMCC) y reúne, a su juicio, originalidad y contenidos suficientes para ser presentada ante el tribunal correspondiente y optar al grado de Doctor por la Universidad de Salamanca.

Y para que así conste a efectos legales, expide el presente certificado en Salamanca, a 18 de mayo de 2023.

Firmado por LAZO-ZBIKOWSKI TARACENA PEDRO ALFONSO VICTOR - ***5264** el día 18/05/2023 con un certificado emitido por AC FNMT Usuarios

Pedro A. Lazo-Zbikowski

Esta memoria ha sido realizada por **EVA MONTE SERRANO**, como autora de la misma, siendo beneficiaria de una beca predoctoral para financiar la contratación de personal investigador otorgada por la Junta de Castilla y León y cofinanciada por el Fondo Social Europeo para la realización de la tesis doctoral (2018-2023).

Asi mismo, la investigación en el laboratorio ha sido financiada por los siguientes proyectos:

FUNCIONES DE LA QUINASA VRK1 HUMANA EN LA PATOGÉNESIS DEL CÁNCER Y ENFERMEDADES NEURODEGENERATIVAS.

Investigador principal: Pedro A. Lazo-Zbikowski
Financiación: Agencia Estatal de Investigación, Ministerio de Economía y Competitividad
Referencia del proyecto: SAF2016-75774R

REGULACIÓN POR VRK1 DE LA REMODELACIÓN DE LA CROMATINA EN PATOGÉNESIS DEL CÁNCER Y NEURODEGENERACIÓN.

Investigador principal: Pedro A. Lazo-Zbikowski
Financiación: Agencia Estatal de Investigación, Ministerio de Ciencia e Innovación
Referencia del proyecto: PID2019-105610RB-I00

MANIPULACIÓN DE LA ESTABILIDAD GENÓMICA COMO ESTRATEGIA DE LETALIDAD SINTÉTICA EN ONCOLOGÍA.

Investigador principal: Pedro A. Lazo-Zbikowski
Financiación: Consejería de Educación, Junta de Castilla y León
Referencia del proyecto: CSI264P20

Summary

SUMMARY

DNA organization is essential for proper chromatin packaging and necessary to facilitate different processes that require dynamic chromatin remodeling. Modulation of chromatin structure is critical for the regulation of gene expression, since it determines which genes are accessible for transcription and the sequential recruitment of regulatory factors to the underlying DNA. Thus, to deal with inaccessible chromatin, eukaryotic cells have developed mechanisms that facilitate the opening of chromatin.

Epigenetic alterations are defined as mechanisms that control DNA accessibility for the regulation of gene expression patterns and normal development. The epigenetic transcriptional control can occur through DNA methylation, histone post-translational modifications (PTMs), the reading of these modifications by epigenetic enzymes, histone-variants exchange, and noncoding RNA. Errors in the epigenetic regulation can alter the control of chromatin-based processes, ultimately leading to abnormal gene expression. Pathological conditions such as cancers, metabolic disorders, and inflammatory and neurodegenerative diseases have been found to be related to epigenetic errors.

Post-translational modifications (PTMs) of the N-terminal tail of histones regulate DNA access. Importantly, histone PTMs are reversible, and their coordination requires a tight regulation of multiple epigenetic enzymes, known as writers (enzymes that add a mark) and erasers (enzymes that remove a mark)[111]. Among the different PTMs, acetylation and methylation are especially important. They have been extensively investigated in a context of cancer and therapy responses. The balance between de- and acetylation is controlled by deacetylases (HDACs) and acetyltransferases (HATs), while de- and methylation are regulated by demethylases (KDMs) and methyltransferases (KMTs).

An abnormal activity of the epigenetic enzymes and, subsequently, a disturbed histone PTM landscape can alter different cellular processes such as proliferation, DNA repair, gene transcription, and DNA replication, together with the expression of tumor-suppressor or cancer-associated genes. Thus, it is crucial to unveil the molecular mechanisms that modulate these changes and the histone-modifying enzymes involved in such regulation.

VRK1 (Vaccinia-related kinase 1) is a nuclear kinase implicated in different cellular processes, such as modulation of transcription factors (TFs) or proteins implicated in the DNA damage response (DDR). The location of VRK1 as a nucleus-resident kinase makes it a suitable candidate to participate in chromatin remodeling and, thus, a potential therapeutic target.

Therefore, this thesis aims to broaden the knowledge of the role of the human kinase VRK1 in chromatin remodeling, deciphering the regulation of histone PTMs patterns and characterizing new possible epigenetic enzymes substrates of VRK1. Another goal of this work is characterizing a novel VRK1 inhibitor, VRK-IN-1, to understand its mechanism of action and propose VRK1 inhibition as a potential cancer therapy.

In this work, we demonstrate that the absence of VRK1 alters the histone PTM landscape, mimicking the effect of some epigenetic enzyme inhibitors. VRK1 depletion causes a decrease of H3K4me3, H3K9ac, H3K27ac, H3K79me2 and H4K16ac levels, and an increase of H3K9me3 and H3K27me3 levels in lung adenocarcinoma and osteosarcoma cellular models. Furthermore, VRK1 can form a stable protein complex with HDAC1, SIRT1, SIRT2, SETDB1, LSD1, JMJD1A and JMJD2A, suggesting that VRK1 controls the activity of these epigenetic enzymes. In addition, we observed that the inhibition of VRK1 kinase activity by using VRK-IN-1 resembles the VRK1 depletion, thus blocking cell proliferation, impairing histone PTM patterns and altering the DDR upon DNA damage induction.

Altogether, these findings reveal VRK1 as an orchestrator of chromatin remodeling, capable of interacting with different epigenetic enzymes and maintaining histone PTMs associated with relaxed chromatin. Moreover, the present data provides a resource for investigating novel VRK1 inhibitors, as well as exploring new target therapies through the biochemical mechanisms here uncovered.

RESUMEN

La organización del ADN es esencial para el correcto empaquetamiento de la cromatina y necesaria para facilitar distintos procesos celulares que requieren una remodelación dinámica de la cromatina. La modulación de su estructura es esencial para la regulación de la expresión génica, ya que determina qué genes son accesibles y qué factores reguladores son reclutados al ADN. Por ello, las células eucariotas han desarrollado mecanismos que permiten la modulación y apertura de la cromatina cuando esta es inaccesible.

Las alteraciones epigenéticas son un mecanismo para controlar la accesibilidad del ADN y regular los patrones de expresión génica y el desarrollo normal. El control epigenético puede producirse a través de la metilación del ADN, las modificaciones postraduccionales (PTM) de las histonas, la interpretación de estas modificaciones por las enzimas epigenéticas, el intercambio de variantes de las histonas y el ARN no codificante. Los errores en estos mecanismos pueden desregular el control de los procesos basados en la accesibilidad de la cromatina, lo que conduce a una expresión anormal de distintos genes. Se ha descubierto que condiciones patológicas como el cáncer, los trastornos metabólicos y las enfermedades inflamatorias y neurodegenerativas están relacionadas con errores epigenéticos.

Las modificaciones postraduccionales (PTM) de las colas N-terminales de las histonas regulan el acceso al ADN. Es importante destacar que las PTM de las histonas son reversibles y su coordinación requiere la regulación estricta de múltiples enzimas epigenéticas, conocidas como *writers* (enzimas que añaden una modificación) y *erasers* (enzimas que eliminan una modificación). Cabe destacar la acetilación y la metilación entre las diversas PTMs, ya que ha sido ampliamente estudiada su relación

con el cáncer y su respuesta a tratamientos. El equilibrio entre la de- y la acetilación está controlado por las deacetilasas (HDAC) y las acetiltransferasas (HAT), mientras que la de- y la metilación están reguladas por las demetilasas (KDM) y las metiltransferasas (KMT).

Una actividad anómala de las enzimas epigenéticas y, por consiguiente, una alteración del patrón de PTM de histonas pueden alterar distintos procesos celulares como la proliferación, la reparación del ADN, la transcripción génica y la replicación del ADN, así como la expresión de genes supresores de tumores o asociados al cáncer. Por ello, es crucial desvelar los mecanismos moleculares que controlan estos cambios y las enzimas epigenéticas implicadas en dicha regulación.

VRK1 (Vaccinia-related kinase 1) es una quinasa nuclear implicada en diferentes procesos celulares, como la modulación de factores de transcripción o proteínas implicadas en la respuesta al daño del ADN. La localización de VRK1 en el núcleo la convierte en una posible candidata para participar en la remodelación de la cromatina y, por tanto, en una potencial diana terapéutica. Sin embargo, el diseño de inhibidores específicos para quinasas, especialmente para VRK1 debido a su estructura, sigue siendo un reto importante.

Por ello, esta tesis pretende ampliar el conocimiento del papel de la quinasa humana VRK1 en la remodelación de la cromatina, descifrando la regulación del patrón de PTMs de histonas y caracterizando nuevos posibles sustratos como las enzimas epigenéticas. Otro objetivo de este trabajo es caracterizar un nuevo inhibidor de VRK1, VRK-IN-1, para comprender su mecanismo de acción y proponer así la inhibición de VRK1 como posible tratamiento del cáncer.

En este trabajo, se ha demostrado que la ausencia de VRK1 altera completamente el patrón de PTM de histonas, siendo capaz de imitar el efecto de algunos inhibidores de enzimas epigenéticas. La depleción de VRK1 causa una disminución de los niveles de H3K4me3, H3K9ac, H3K27ac, H3K79me2 y H4K16ac, y un aumento de H3K9me3 y H3K27me3 en células de adenocarcinoma de pulmón y osteosarcoma. Además, VRK1 puede formar un complejo proteico estable con HDAC1, SIRT1, SIRT2, SETDB1, LSD1, JMJD1A y JMJD2A, lo que sugiere que VRK1 podría estar controlando la actividad de estas enzimas epigenéticas. Además, se observó que la inhibición de la actividad quinasa de VRK1 mediante el tratamiento con VRK-IN-1 muestra resultados similares a la disminución de la expresión de VRK1, bloqueando la proliferación celular, alterando el patrón PTM de histonas y la respuesta génica tras daño en el ADN.

En conjunto, estos hallazgos proponen a VRK1 como un regulador de la cromatina, capaz de interactuar con diferentes enzimas epigenéticas y mantener los PTMs de histonas asociados un estado relajado. Además, los datos presentados, no sólo proporcionan un nuevo recurso para investigar inhibidores más específicos de VRK1, sino que también abren una puerta a nuevas oportunidades para la inhibición de VRK1.

Table of contents

Table of contents

ABBREVIATIONS

Histone Residue Modification

H3K9me3

Trimethylation of histone H3 at lysine 9

ac: Acetylation
me: Monomethylation
me2: Dimethylation
me3: Trimethylation
Ph: Phosphorylation
Ub: Ubiquitination

A

AP-1: Activator protein 1

Arg, R: Arginine

ATAC-seq: Transposase-accessible chromatin using sequencing

ATM: Ataxia telangiectasia mutated

ATP: γ-phosphate of adenosine triphosphate

B

BANF1: Barrier to-autointegration factor

C

CB: Cajal body

CBP: CREB-binding protein-associated factor

CCND1: Cyclin D1

Chaet: Chaetocin

ChIP-seq: Chromatin immunoprecipitation sequencing

CHK-2: Checkpoint kinase 2

CK1: Casein kinase 1

CoREST: Corepressor of RE1 silencing transcription factor

D

DAR: Differentially accessible region

DDR: DNA damage response

DMSO: Dimethyl sulfoxide

DNA: Deoxyribonucleic acid

DNA-PK: DNA-depentednt protein kinase

DOT1L: Disruptor of telomeric silencing 1-like

DSB: DNA double-strand breaks

E

ECL: Enhanced chemiluminescence

EED: Embryonic ectoderm development

EGR1: Early growth response protein 1

Ent: Entinostat

EPZ: EPZ004777

EZH1: Enhancer of zeste

EZH2: Enhancer of zeste 2

F

FBS: Fetal bovine serum

FDA: The food and drug administration

FDR: False discovery rate

FOXO3: Forkhead box protein O3

FRIP: Fraction of reads in peaks

G

GNAT: Gcn5-related N-acetyltransferases

H

H1: Histone H1

H2A.X: Histone H2A.X

H2A: Histone H2A

H2B: Histone H2B

H3: Histone H3

H4: Histone H4

HAT: Histone acetyltransferase

HATi: HAT inhibitor(s)

HDAC: Histone deacetylase

HDACi: HDAC inhibitor(s)

HP1: Heterochromatin protein 1

I

IF: Immunofluorescence

IP: Immunoprecipitation

IPTG: Isopropyl-β-D-thiogalactoside

J

JmJC: Jumonji C

JMJD2i: JMJD2 inhibitor

K

KAT: Histone lysine acetyltransferase

KDM: Histone lysine demethylase

KDMCi: KDM inhibitor(s)

KMT: Histone lysine methyltransferase

KMTi: KMT inhibitor(s)

L

LSD: Lysine-specific histone demethylases

Lys, K: Lysine

M

Mdm2: Murine double minute 2

MLK1: Mixed lineage kinase 1

MRN: Mre11-Rad50-NBD1

N

NAD: Nicotinamide adenine dinucleotide

NBS1: Nijmegen breakage syndrome 1

NFR: Nucleosome free region

NF-κB: Nuclear factor kappa B

NR4A1: Nuclear receptor subfamily 4 group A member 1

NSCLC: Non-small cell lung cancer

Nur77: Nuclear hormone receptor NUR/77

O

OD_{600}: Optical density 600 nm

ORY: ORY-1001

P

Pan: Panobinostat

PCAF: p300/CBP-associated factor

PCNA: Proliferating cell nuclear antigen

PCR2: Polycomb repressor complex 2

PD-L1: Programmed death-ligand 1

pDNA: Plasmidic DNA

PEI: Polyethylenimine

PFA: Paraformaldehyde

Ph-RB: Phosphorylated retinoblastoma

PTM: Histone post-translational modification

PUMA: p53 up-regulated modulator of apoptosis

Q

QC: Quality control

R

RCOR1: Repressor element-1 silencing transcription corepressor

RNA: Ribonucleic acid

RT: Room temperature

S

SAGA: Spt-Ada-Gcn5-acetyltransferase

SAM: S-adenosylmethionine

SDS-PAGE: SDS-polyacrilamide gel electrophoresis

Sel: Selisistat

Ser, S: Serine

SET: Su(var)3–9, Enhancer-of-zeste and Trithorax

shrunkenLFC: Shrunken log2 fold change

siC: siControl non-targeting siRNA

SIRT: Sirtuin

siV-02: siVRK1-02

siV-03: siVRK1-03

SUZ12: Suppressor of zeste 12

T

Taz: Tazemetostat

TBS-T: Tris buffer saline-Tween 20

TCA: Trichloroacetic acid

TF: Transcription factor

Thr, T: Threonine

TM: Thiomyristoyl

TSS: Transcription start sites

TUNEL: TdT-mediated dUTP Nick-End Labeling

Tyr, Y: Tyrosine

V

VRK1: Vaccinia-related kinase 1

vvB1: Vaccinia virus B1

W

WB: Western blot

Γ

γH2A.X: Histone H2A.X phosphorylated at Ser139

53BP1: p53 binding protein 1

LIST OF FIGURES

LIST OF TABLES

Introduction

1 Introduction

1.1 DNA organization

In the nucleus of eukaryotic cells, the DNA is compacted in a macromolecular and dynamic compacted complex called chromatin, which, along with histone proteins, provides the support to pack the entire genome and contains the heritable material of eukaryotic cells. Chromatin organization displays hierarchical levels ranging from the basic repeated unit, the nucleosome, to higher-level structures, the chromosomes (**Figure 1**). The nucleosome is the basic functional unit of chromatin, it contains 147 base pairs of DNA, coiled around a central octamer of core histones, composed of two histones H2A, H2B, H3, and H4[2]. Moreover, the four core histones can diversify into variants with different properties and functions, such as H3.3, H2A.X, or macroH2A, among others[3]. Nucleosomes are connected to the adjacent through a small segment of linker DNA, which is often associated with the linker histone protein H1. Then, nucleosomes achieve a higher-order compaction: the 30 nm chromatin fiber. Finally, eukaryotic chromatin is further compacted by being folded into a series of complex structures, ultimately resulting in a chromosome[2].

Chromatin is commonly divided into two distinct functional forms: euchromatin and heterochromatin. Euchromatin corresponds with relatively open genome regions and possesses most of the actively transcribed genes. By contrast, heterochromatin refers to higher condensed regions, and is associated with transcriptional inactive genes. Additionally, heterochromatin is also divided into facultative chromatin, which are DNA regions subject to transcriptional silencing, for instance silenced genes during cell differentiation, and constitutive chromatin, which include gene-poor and repetitive sequences such as centromeric and pericentromeric repeats[4]. Therefore, while euchromatin domains are accessible to nuclear proteins, heterochromatin regions remain unreachable.

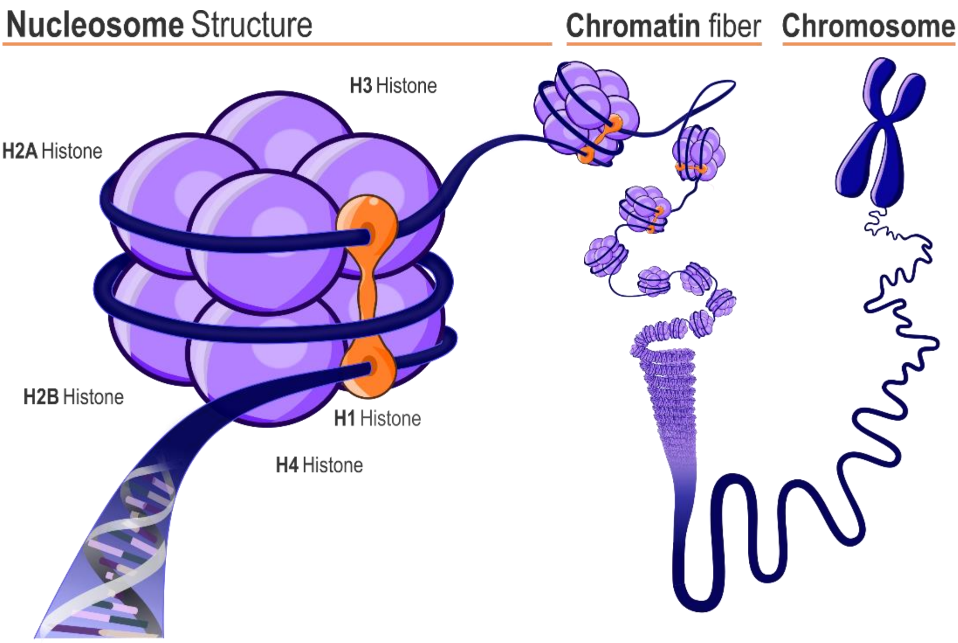

Figure 1. Schematic representation of DNA organization. DNA is coiled around histone octamer, composed of two H3-H4 and H2A-H2B histone dimers. H1, the linker protein, is bound to DNA between nucleosomes. Then, nucleosomes are compacted into the 30 nm chromatin fiber and, finally, they form the chromosome.

1.1.1 Chromatin remodeling

The modulation of the chromatin structure is critical for the regulation of gene expression, because it determines which genes are accessible and the sequential recruitment of regulatory factors to the underlying DNA. Thus, for dealing with inaccessible chromatin, eukaryotic cells have evolved mechanisms that facilitate the opening of chromatin. Despite decades of research, it has been demonstrated that all its components are subject of covalent modifications, which fundamentally alter the organization and function of chromatin[4].

Thus, the term *epigenetics* arose from Conrad Waddington in the early 1940s. It is originally described as "heritable changes in a cellular phenotype that were independent of alterations in the DNA sequence". However, this term is mostly used to describe chromatin-based events that regulate DNA-templated processes[5,6]. Thereby, epigenetic modifications alter DNA accessibility and chromatin structure, regulating patterns of gene expression and normal development. The epigenetic transcriptional control can occur through DNA methylation, histone post-translational modifications (PTMs), the reading of these modifications by epigenetic enzymes, histone-variants exchange, and noncoding RNA[7].

Errors in the epigenetic process, such as modifications on a wrong region or failures to add a chemical group to a particular histone, are believed to deregulate the control of chromatin-based processes, ultimately leading to abnormal gene expression. Pathological conditions like cancers, metabolic disorders, and inflammatory and neurodegenerative diseases have been related to epigenetic errors[6,8].

1.1.2 Histone post-translational modifications (PTMs)

Histone proteins possess a basic amino N-terminal tail which is flexible and accessible to enzymes; hence, they are susceptible to be modified by the addition or removal of chemical groups. Therefore, histone PTMs are covalent modifications carried out mainly in the N-terminal region of histones by a series of enzymes that are termed epigenetic enzymes[9,10]. It is well noted that histone PTMs mediate a variety of critical biological processes, generally via the remodeling of chromatin structure, which leads to the expression or repression of target genes[10]. Consistent with this notion, the correct reading and interpretation of histone modifications is crucial for gene expression, cell fate, and genomic stability. Consequently, aberrant patterns have been associated with many different types of human malignancies[1,11].

The main function of PTMs is disrupting the interaction between histones and DNA or the contact with other histones in adjacent nucleosomes that modify chromatin structure. Moreover, PTMs also act as marks to recruit non-histone proteins that carry out different enzymatic activities[10].

There are distinct types of histone PTMs, among which it is worth highlighting methylation, acetylation, phosphorylation and ubiquitination (**Figure 2**)[6,12]. In this project, we focus on the study of (de)acetylation, (de)methylation and phosphorylation modifications of different residues, so these PTMs will be further introduced.

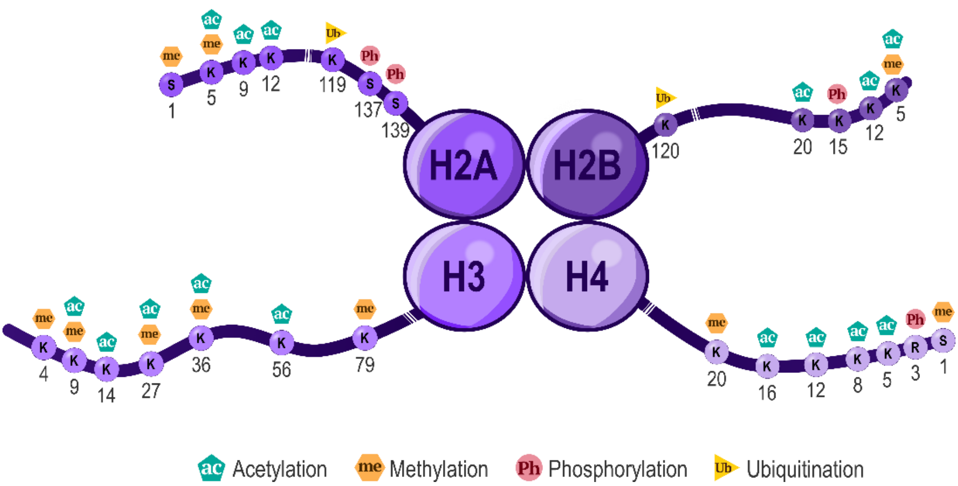

Figure 2. Schematic representation of histone post-translational modifications. Different amino acids (with position numbers underneath) constituting histone H2A, H2B, H3 and H4 tails are represented along with the different covalent modification specific of each residue. The most common PTMs are methylation (me), acetylation (ac), phosphorylation (Ph), and ubiquitination (Ub). Amino acids the histone tails are indicated by their symbol inside the circle: Lysine (K), arginine (R), serine (S), and threonine (T). Adapted from Millán-Zambrano *et al.,* 2022.

1.1.2.1 Histone acetylation

Histone acetylation is a reaction based on the addition of an acetyl group from an acetyl-CoA donor to a lysine (Lys, K) residue in the histone tail. Lys residues are positively charged and have a natural affinity for the DNA, which strengthens histone-DNA interactions and leads to close chromatin conformations. The addition of an acetyl group neutralizes this positive charge, consequently weakening its affinity for chromatin and leaving the underlying DNA more exposed. For this reason, histone acetylation is often associated with more open chromatin conformations and active transcription[12]. Indeed, acetylation marks are particularly localized at enhancers, promoters and gene bodies[1].

The most extensively studied histone acetylation sites include histone H3 Lys 9 (H3K9), histone H3 Lys 27 (H3K27) and histone H4 Lys 16 (H4K16). H3K9ac localizes around transcription start sites (TSS) of active genes, and H3K27ac is at distal regulatory regions like enhancers. H4K12ac and H4K16ac are placed at both TSS and along the gene body[12].

1.1.2.2 Histone methylation

Histone methylation is a reaction based on the addition of a methyl group from S-adenosylmethionine (SAM) to a Lys or arginine (Arg, R) residues of the histone tail. Lys can be mono-, di-, or tri-methylated, while Arg residues can be monomethylated and symmetrically or asymmetrically dimethylated. Unlike acetylation, it does not alter the overall charge of the molecule, but it alters the volume, the hydrophobic character and the stability of the nucleosome[13].

The best studied histone methylations sites are histone H3 Lys 4 (H3K4), H3K9, H3K27, histone H3 Lys 36 (H3K36), histone H3 Lys 79 (H3K79), and histone H4 Lys 20 (H4K20). Classically, methylation of

H3K4, H3K36, and H3K79 are associated with active genes in euchromatin, whereas others such as H3K9, H3K27 and H4K20 are considered to depict a silent or compressed chromatin, which is required in many developmental and physiological contexts[11,14].

1.1.2.3 Histone phosphorylation

Histone phosphorylation is a reaction based on the addition of a phosphate group from ATP to a serine (Ser, S), threonine (Thr, T) or tyrosine (Tyr, Y) residues of the histone tail. This mark adds a negative charge to the histone tail, hence opening the chromatin structure and exposing the DNA, which facilitates the interaction between transcription factors (TFs) and the chromatin[14].

Different cellular processes are regulated by phosphorylation of histones. Several residues of histones H1, H2A, H2B, H3, and H4 have been identified as susceptible to phosphorylation[14]. In the case of histone H3, phosphorylation of residues T3, S10, T11, S28, and T45 are well-characterized. The phosphorylation of histones H3 at T3, S10 and S28 is known to be involved in mitotic chromatin condensation and transcriptional activation during mitosis[15]. Moreover, phosphorylation of histone H2A.X, a histone H2A variant, is induced by a DNA damage signaling pathway[16].

1.1.3 Histone code

The abundance of histone PTMs makes necessary a crosstalk between them for the adaptation to specific functions. Indeed, the impact that one or a combination of histone marks have on the deposition, interpretation, or erasure of others is the object of numerous studies. For that reason, significant current reports have called “histone code” or "histone crosstalk" to the presence of site-specific PTM combinations and their interdependence[1,11,14].

Firstly, some of the Lys residues that are methylated in histones H3 and H4 are also found to be substrates for acetylation, such as H3K9 or H3K27. Therefore, there is a direct competition between these modifications. For example, if a Lys residue is acetylated, then it cannot be methylated, resulting in opposing transcriptional readouts[14]. This results in an antagonism between some histone PTMs. Secondly, the regulation of epigenetic enzymes (their binding to the corresponding PTM and their catalytic activity) can be altered by another modification[1].

One of the most interesting examples of histone modification crosstalk is that H3S10 phosphorylation facilitates H3K14 acetylation, H3K4 methylation. This subsequently inhibits H3K9 methylation, resulting in open chromatin conformation[17–20]. Another example is provided by mass spectrometric analysis of H3K9, H3K14 and H3K79. The loss of lysine methyltransferase KMT1 activity produces a decrease of H3K9 methylation and an increase in H3K14 acetylation, suggesting a relationship between these two modifications. H3K79me2 levels increase, also responding to this lack of activity[21]. Moreover, the association between H3K79 and H4K16 in yeast has been demonstrated and provided new insights. H4K16ac coordinates, with H2B123Ub, the stimulation of DOT1 catalytic activity, responsible for H3K79me2[22,23]. Other results showed that H3K4 and H3K9 methylation are mutually exclusive, hence inactive promoters show high levels of H3K9me and low levels of H3K4me[24]. Consequently, the role of histone modifications and their crosstalk result in different biological outcomes.

However, the numerous mechanisms that participate in histone PTM patterns add a layer of complexity in the recruitment of epigenetic modifiers and, subsequently, in the regulation of cellular processes. Although the latest achievements in the field, there is still a need for research efforts to unveil the functioning of these intricate mechanisms controlling gene expression.

1.2 Epigenetic enzymes

Histone modifications are controlled by histone-modifying enzymes or epigenetic enzymes. Epigenetic modifiers are broadly classified into three groups depending on their function: writers, readers and erasers (**Figure 3**).

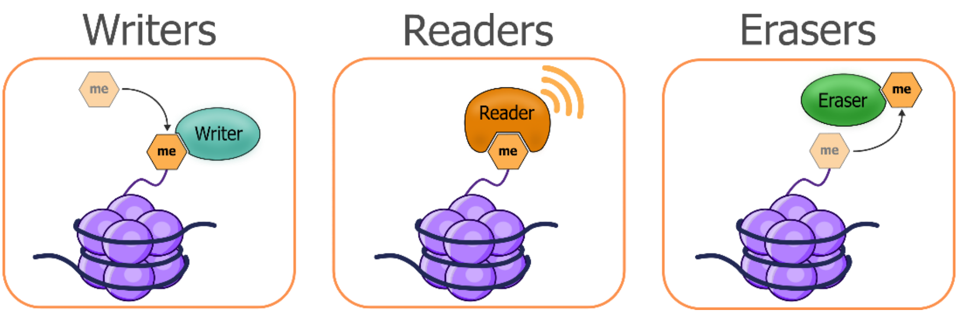

Figure 3. Schematic representation of epigenetic enzymes and their functions. Epigenetic enzymes are classified as writers, erasers or readers. Writers add the specific modifications to the histone residues. Readers can recognize a specific modification and trigger a cellular response. Finally, erasers remove the modification from the histone residues.

Epigenetic writers are responsible for placing covalent modifications to histones or DNA. Epigenetic readers recognize and interpret the chemical marks added by writers and can assist in the recruitment of transcriptional activators or repressors[25]. Finally, epigenetic erasers remove the chemical tags added by the writers, making histone marks reversible tags. Therefore, chromatin accessibility and cellular functions are regulated by the type of histone mark and its location in the genome[14]. Moreover, over the last decade a large number of studies has demonstrated that these enzymes form multiprotein complexes, guaranteeing locus and chromosomal-domain targeting as well as substrate-specificity[14].

Both acetylation and methylation are highly dynamic processes regulated by the activities of four enzymatic families: regarding acetylation, the most important families are histone acetyltransferases (HATs) and histone deacetylases (HDACs), and, concerning methylation, the main families are histone lysine methyltransferases (KMTs) and histone lysine demethylases (KDMs) (**Figure 4**)[25]. The combined activity of all epigenetic enzymes is required for the proper regulation of gene expression. Nevertheless, the major mechanisms for their coordination are still unknown. One hypothesis is that epigenetic enzymes are coordinated by members of other families, such as kinases, which can activate or inactivate them by phosphorylation or interactions.

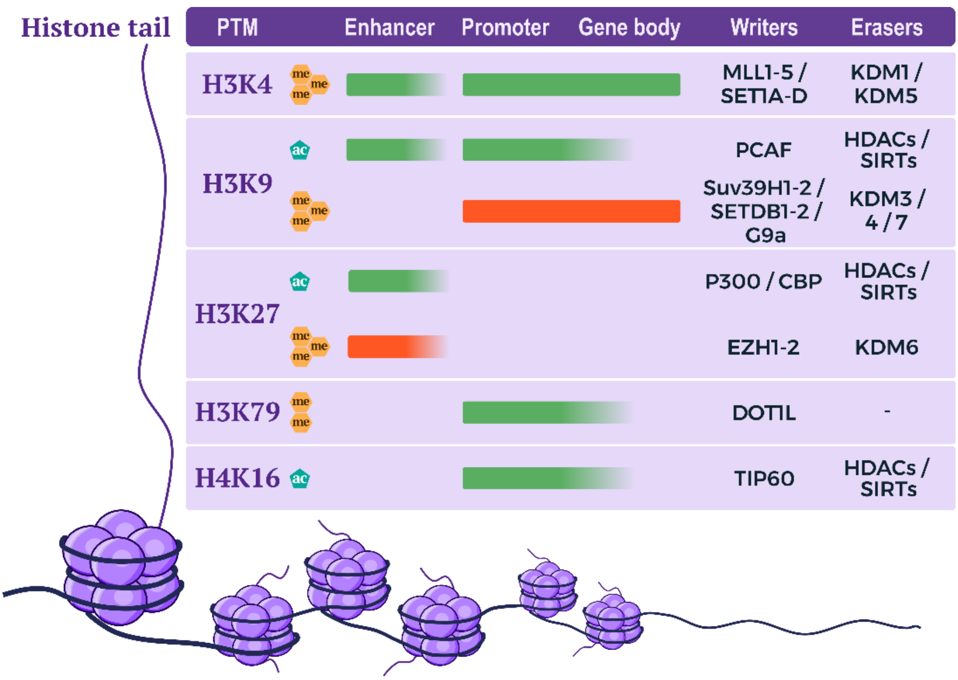

Figure 4. Histone writers and readers of histone PTMs. Histone H3 and H4 tail lysine residues, commonly subject to post-translational modifications, are listed along the left side. The usual distribution of these PTMs is also specified along the length of gene loci as shaded blocks. Green shading indicates histone marks associated with active genes, whereas red is

indicative of silent genes. Some examples of writers, erasers, and readers that may be related to these marks are indicated on the right side of the figure. Adapted from Audia and Campbell, 2016.

1.2.1 Histone acetyltransferase (HAT)

Histone acetyltransferases (HATs), also called lysine acetyltransferases (KATs), catalyze the addition of acetyl groups to histone Lys residues. In humans, there are three major classes of HATs according to the structure and function of their catalytic domains: (1) GNAT (Gcn5-related N-acetyltransferases) family, (2) MYST family, and (3) P300/CBP (CREB-binding protein-associated factor) family. They can also be grouped according to their subcellular location in type A, which are in the nucleus, and type B, mostly found in the cytoplasm[14,26]. Functionally, GNAT and P300/CBP families are involved in the activation of many TFs, while MYST family is implicated in the regulation of proliferation, apoptosis, and differentiation processes[26].

p300/CBP-associated factor (PCAF), an epigenetic enzyme of the GNAT family, owes its name to its interaction with p300 and CBP. It has notable similarities with GCN5 acetyltransferase. PCAF is necessary in the transcription process as coactivator though H3K9 acetylation at TSS[27]. Other works have focused on its acetylating action of various non-histone transcription-related proteins, such as p53[28].

TIP60 (or KAT5) is the first member discovered of MYST family. It is able to acetylate different histone residues and produces chromatin relaxation[29]. TIP60 also acetylates the Lys 7 of the histone variant H2AZ, which leads to transcriptional activation and cell proliferation[30]. Therefore, TIP60 acts as a transcription regulator due to the acetylation of promoters and non-histone proteins, such as p53[31]. Histone acetylation also plays an important role in DNA damage response (DDR). Several studies provided evidence that the acetyltransferase TIP60 is essential for the recruitment and binding of repair proteins to the DNA breakpoints. TIP60 directly acetylates H4K16 after DNA damage, a marker of chromatin relaxation and the initial signal to DDR pathways[32].

1.2.2 Histone deacetylase (HDAC)

Histone deacetylases perform opposite functions to HATs, removing acetyl groups from histone Lys residues. There are four major families, termed class I, II, III, and IV. Classes I, II, and IV are Zn^{2+}-dependent, whereas class III are nicotinamide adenine dinucleotide (NAD)-dependent[26]. Class I includes HDAC1, 2, 3 and 8; class II can be subdivided into IIa, comprised by HDAC4, 5, 7 and 9, and IIb, formed by HDAC6 and 10; class III is also known as the sirtuin family, comprised by SIRT1-7; and finally, class IV includes HDAC11[26].

HDACs are relatively low substrate specific, each individual enzyme is able to deacetylate different histone residues. HDAC1 has been the first deacetylase discovered being described as inhibitor of histone acetylation and inductor of cell-cycle arrest. HDAC1 can also prevent cell growth and induce p53 deacetylation, which consequently inhibits apoptosis[33].

SIRT1 and SIRT2, two members of the sirtuin family, have become firmly established as key regulators of cellular response upon variety of stress. Both can be in nucleus and cytoplasm and are linked to chromatin regulation through histone and other chromatin-associated machinery deacetylation[34]. When SIRT1 is recruited to euchromatin regions, there is a reduction in H4K16ac, H3K9ac, and H1K26ac marks, promoting a closed chromatin structure[35]. Likewise, SIRT2 activity participates in genome stability and cell-cycle progression. Reduction of SIRT2 levels produces an increase in H4K16ac levels, which is necessary to enter S-phase[36].

1.2.3 Histone lysine methyltransferase (KMT)

Histone lysine methyltransferases are the epigenetic enzymes that catalyze the methylation on Lys residues. There have been identified two families of KMTs: (1) Su(var)3–9, Enhancer-of-zeste and Trithorax (SET)-domain containing proteins and (2) DOT1-like proteins[26].

These enzymes have a substrate specificity towards histones. Mammals possess six different KMTs for H3K4 mono-, di- and trimethylation: SET1A-B and MLL1-4[37]. These three states of H3K4 have been shown to mark actively transcribing genes at different chromatin regions. H3K4me1 is highly enriched at enhancers, H3K4me2 is higher towards the 5′ end of transcribing genes, and H3K4me3 is a hallmark of the promoters of actively transcribing genes[38].

Another example is the KMTs responsible for H3K9 methylation. KMT1A (or SUV39H1) and KMT1B (or SUV39H2) modify monomethyl H3K9 to trimethyl H3K9 and preferentially localize to pericentric heterochromatin and other regions that contain repetitive DNA elements such as telomeres[39]. KMT1C (or G9a) converts H3K9 to mono- or dimethylated H3K9, repressing gene expression[40]. SETDB1 has also been described as responsible for H3K9 di- and trimethylation and leads repression of euchromatic genes; whereas SETDB2 affects the H3K9 trimethylation at pericentric heterochromatin[41]. Moreover, other proteins such as TFs and corepressors can interact with KMTs to offer target specificity.

Conversely, enhancer of zeste 1 (EHZ1 or KMT6A) and 2 (EZH2 or KMT6B) are KMTs that catalyze mono-, di- or trimethylation of H3K27 and form part of the polycomb repressor complex 2 (PRC2). For example, H3K27me is linked with constitutive heterochromatin, while H3K27me3 is associated with suppression of gene expression and facultative heterochromatin[42].

Otherwise, disruptor of telomeric silencing 1-like (DOT1L or KMT4A) is the only KMT that targets the H3K79 residue for mono-, di-, and trimethylation. Various reports have suggested that this modification initiates an active transcriptional state[38,23].

1.2.4 Histone lysine demethylases (KDM)

Histone lysine demethylases remove the methyl group added by KMTs. There have been identified two major families: (1) lysine-specific histone demethylases (LSD) family and (2) jumonji C (JmjC)-domain containing family[13].

Histone methylation was thought to be a stable and static modification until 2004, when LSD1 (or KDM1A) was identified as the enzyme that specifically catalyzes the demethylation of mono- and dimethylated H3K4[43]. This demethylation reaction requires a protonated nitrogen, and it is therefore only compatible with mono- and dimethylated Lys substrates. Moreover, this enzyme needs to be part of the Co-REST repressor complex, which confers nucleosomal recognition and specifies which Lys is to be demethylated by LSD1[9,43].

JmjC-domain can demethylate trimethylated Lys residues, using Fe^{+2} and α-ketoglutarate as co-factors[9]. As with the KMTs, KDMs have a high level of target Lys specificity. For example, JARID1 (or KDM5B) proteins specifically target H3K4me2 and -me3[44,45], KDM3 (or JMJD1), KDM4 (or JMJD2) and KDM7 have demethylation activity against H3K9 and KDM6 are able to demethylate H3K27[38].

1.2.5 Chromatin remodeling complexes

Over the last decade, there have been identify a number of histone modifying complexes, which can be defined as discrete and stable structures composed of various enzymes associated noncovalently that catalyze two or more sequential steps of a pathway[46]. Some subunits function like scaffolds, tethering them into complexes. Others have specific domains that allow the recruitment of histone-modifying enzymes to the proper location in the genome.

The Spt–Ada–Gcn5–acetyltransferase (SAGA) complex was the first multisubunit nuclear HAT complex described. It is composed of Gcn5 as HAT and 19 other known subunits and catalyzes histone H3K9 acetylation. These associations permit them to perform specific functions, which the enzyme by itself would not be capable of[47]. Moreover, SAGA complex is able to bind to H3K4me2 and me3 through Sgf29 subunit and thereby promoting histone H3 acetylation and mediating the crosstalk between histone PTMs[48].

Another of the best characterized complexes is PRC2, which is composed by 3 subunits: EZH1 or 2, responsible to methylate H3K27 (writer), embryonic ectoderm development (EED), which recognizes H3K27me3 (reader), and suppressor of zeste 12 (SUZ12) that acts as a scaffold for interacting with other accessory proteins. Likewise, there are many reports that describe other interaction partners, such as JARID2 or some RNAs, which can guide PRC2 recruitment or regulate its activity[38,49].

Corepressor of RE1 silencing transcription factor (CoREST) is one of the histone-modifying complexes that contains the two members of the HDAC family I HDAC1 and HDAC2 and the demethylase LSD1. This complex is formed thanks to the scaffold protein repressor element-1 silencing transcription corepressor (RCOR1). The CoREST complex can deacetylates and demethylates histone marks, preferably H3K4me and me2 and H3K9ac, resulting in transcriptional repression[50].

1.3 Cancer epigenetics

Epigenetic alterations have been considered one of the main causes of cancer progression. This is because abnormal histone PTMs patterns alter chromatin structure and gene expression, promoting the development and progression of several tumors[8,51]. Imbalance in the finely orchestrated system of chromatin-modifying enzymes and histone PTM landscape can alter the expression of tumor-suppressor or cancer-associated genes and, subsequently, different cellular processes such as proliferation, DNA repair, gene transcription, or DNA replication[14].

Hence, histone PTMs are good biomarkers for early diagnosis of cancer[26,10]. For example, in pancreatic tumor cells, H3K4me3 levels are enriched, activating the transcription of programmed death-ligand 1 (PD-L1), a membrane protein that is considered as an inhibitory factor of the immune response[52]. In breast cancer, the reduction of H3K9me3 levels[53], and the increased of H3K4me3 and H3K9ac levels are related with poor prognosis[54]. For instance, low levels of H3K27me3 is correlated with shorter overall survival rate in breast, ovarian and pancreatic cancer[55,56]. An increase in H3K79me2 levels contributes to leukemia and pancreatic cancer progression, so a reduction of this modification produces genomic instability and promotes apoptosis[57,58].

Overexpression, downexpression or mutations in epigenetic enzymes are other frequent causes of cancer progression. In most cases, abnormal levels of these enzymes are associated with poor outcomes[14,1,26]. Nevertheless, the mechanisms by which individual epigenetic enzymes regulate tumorigenesis are relatively diverse and they can operate both as tumor-suppressor genes or oncogenes. For example, HDAC1 is linked to poor survival in gastric, ovarian cancers and multiple myeloma[59–61]. SIRT1 is overexpressed in leukemia, prostate, melanoma, and colorectal[62]; on the contrary, SIRT1 downregulation has also been observed in other cancers, such as breast cancer[63]. High levels of SIRT2 have been detected in different tumor types (neuroblastoma, uveal melanoma or renal cell carcinoma), but its expression levels are lower in others (non-small cell lung cancer (NSCLC), colon cancer or breast cancer)[64]. The downregulation of the acetyltransferase PCAF is associated with hepatocellular carcinoma and BRCA1/2-deficient tumors[65,66]. Its overexpression induces autophagy of hepatocellular carcinoma cells by inhibiting Akt/mTOR signaling pathway and tumor growth[65]. On the other hand, mutations in TIP60 that inhibit its acetyltransferase activity may impair DNA damage repair mechanisms resulting in genomic instability and leading to carcinogenesis[67]. LSD1 overexpression has been identified in various sarcomas, functioning as oncogenic driver[68]. Furthermore, SUV39H-deficient mice have lower levels of H3K9me3, impairing genomic stability and showing an increased risk of developing cancer[69]. Overexpression of EZH2 enhances cell proliferation in numerous cancer types such as NSCLC, gastric cancer or meningioma[70–72]. EZH2 mutations in its catalytic domain that cause a gain of activity have been found in numerous lymphoma patients. Interestingly, there is a connection between the repression of certain genes triggered by elevated levels of H3K27me3, and blockage of B cell development[73].

Furthermore, multiomic techniques such as assay for transposase-accessible chromatin using sequencing (ATAC-seq) and chromatin immunoprecipitation sequencing (ChIP-seq) have allowed profiling the chromatin accessibility landscape of human cancers and identifying considerable driver mutations in genes encoding epigenetic enzymes and alterations in histone PTM landscape[10,74]. Specifically, ATAC-seq has rapidly emerged as one of the most powerful approaches for chromatin accessibility profiling. It reveals novel enhancers, promoters, and other regulatory regions associated to different cell context[75]. This strategy makes possible to detect nucleosome free regions (NFR), also called peaks, for different human tumor samples and TF sequences or motifs that are important for different cancer types, such as the androgen receptor in prostate cancer[76].

In conclusion, the landscape of histone PTMs that disturb chromatin-based processes and promote cancer continues to expand and highlights a potential interplay between epigenetic pathways and cancer genetics.

1.3.1 Epigenetic treatments or epidrugs

The relationship between alteration in chromatin remodeling and cancer pathogenesis makes epigenetic enzymes potential targets for therapeutic intervention. A number of inhibitors have been developed over the years against histone-modifiers, known as epigenetic treatments or epidrugs. Some of the HAT, HDAC, KMT and KDM inhibitors (HATi, HDACi, KMTi and KDMi, respectively) that are potential candidates for cancer treatment are shown in **Table 1**[77].

Table 1. Epigenetic drugs: targets and tumor type.

Epidrug	Target	Tumor types
	HATi	
C646	P300/CBP	Prostate cancer[78] Pancreatic cancer[79] Gastric cancer[80] Glioblastoma[81]
MG149	TIP60	NSCLC[32] Hepatocellular carcinoma[82]
	HDACi	
Vorinostat (SAHA)	HDAC classes I, II and IV	NSCLC[83] Breast cancer[84] Renal cancer[85]
Entinostat	HDAC class I	NSCLC[86] Breast cancer[87] Renal cancer[88] Prostate cancer[89]
Panobinostat	HDAC classes I, II and IV	NSCLC[90] Multiple myeloma[91] Ovarian cancer[92,93] Glioblastoma
Selisistat (EX-527)	SIRT1	Lung cancer[94]
AGK2	SIRT2	NSCLC[95] Colorectal cancer[96]
	KMTi	
Chaetocin	SUV39H1	Sarcoma[97] Colorectal[98] Ovarian cancer[99] Gastric cancer[100] Glioblastoma[101]
Tazemetostat (EPZ-6438)	EZH2	Lymphoma[102,103] Sarcoma[102,104]
EPZ004777	DOT1L	Leukemia[105] Ovarian Cancer[106]

EPZ004777		Breast cancer[107]
KDMi		
5-carboxy-8-Hydroxygenquinoline (5-c-8HQ, JMJD2i)	JMJD2	Liver cancer[108] Colon cancer[109]
Iadademstat (ORY-1001)	LSD1	NSCLC[110] Acute myeloid leukemia[111] Merkel cell carcinoma[112] Breast cancer[113]

In this context, treating tumor cells with these inhibitors can disrupt different biological processes including gene transcription, replication and DDR. Most of them show enzymatic inhibition occupying the site of the substrate in their binding pockets[114]. For example, tazemetostat inhibits wild-type and mutant EZH2 activity and has mainly been used in different lymphoma and sarcoma studies[102,103]. Moreover, tazemetostat shows an improved life expectancy and better outcomes in epithelioid sarcoma patients[102]. Panobinostat, a non-selective HDACi, has shown preclinical activity in all four classes of HDACs. It inhibits cell proliferation and induces apoptosis in multiple myeloma cells[115]. In 2015, the US Food and Drug Administration (FDA) approved its combination with bortezomib and dexamethasone, for the treatment of multiple myeloma. This combination has shown potential to resensitize refractory-multiple myeloma cells[116,117]

In conclusion, the manipulation of chromatin by epidrugs, in combination with other conventional treatments such as chemotherapy, radiation, immunotherapy or other inhibitors, can play a major role by increasing the tumor cell sensitivity. This potentially successful approach is known as synthetic lethality, which is based on the combination of two treatments targeting different pathways that promote tumor cell death[114].

1.4 The protein kinases

Kinases are members of one of the largest superfamilies of homologous proteins and, currently, the human kinome comprises around 538 kinases[118]. Kinases are characterized by the presence of a conserved catalytic domain spanning across 250-300 amino acid residues that catalyzes the transfer of the γ-phosphate of adenosine triphosphate (ATP) to a hydroxyl residue (Ser, Thr or Tyr) of a protein substrate. Phosphorylation is a covalent modification that leads to new activity statuses, changes in subcellular localization or interactions for the target proteins. For this reason, these protein kinases are involved in major cellular functions including differentiation, proliferation, and cell death. Their dysfunction contributes to many human diseases, most notably cancer, making them one of the most important targets for therapies[119]. Among all the Ser/Thr kinases, in this work we focus our interest in vaccinia-related kinase 1 or VRK1, a member of the VRK family.

1.5 The human kinase VRK1

Vaccinia-related kinase 1 (VRK1), together with VRK2 and VRK3, forms the VRK family and belongs to the casein kinase 1 (CK1). This family was first identified in 1997 and has notably sequence homology with the vaccinia virus B1 (vvB1) kinase, hence the family name[120,121]. VRK1 may perform similar functions to vvB1 kinase, for instance, it is involved in the early control of viral genome replication, probably due to overlapping specificity for cellular and/or viral substrates[122]. It is mostly located in the nucleus, mainly interacting with chromatin. However, in some cell types, VRK1 is also present in the cytosol, and a minor cytoplasmic subpopulation is located in the Golgi apparatus[123]. VRK1 is implicated in different cellular processes such as cell cycle regulation and cell proliferation, chromatin remodeling and DDR[120,124–126].

1.5.1 VRK1 structure

The human *VRK1* gene is located in chromosomal region 14q32.2, contains 12 coding exons and its size is ~80 kb. This gene encodes a protein of 396 amino acids (45 kDa)[121]. The N-terminal region of VRK1 contains the kinase domain with an ATP-binding site (residues 43-71) and a well-conserved catalytic site (residues 173-185), surrounded by noncatalytic regions. VRK1 has a flexible C-terminal tail comprised between residues 285 and 396 and can be subdivided in a nuclear export sequence domain (residues 285-310), a nuclear localization sequence domain (residues 356-360), and a basic-acid-basic domain (residues 360-369) (**Figure 5 A**). The C-terminal tail of VRK1 is oriented towards the catalytic domain, stablishing numerous interactions with different motifs. This conformation makes the kinase constitutively active. Moreover, the folded structure of VRK1 allows its interaction with other proteins. For that reason, the C-terminal tail is defined as a regulatory region that confers structural stability (**Figure 5 B**)[120,126].

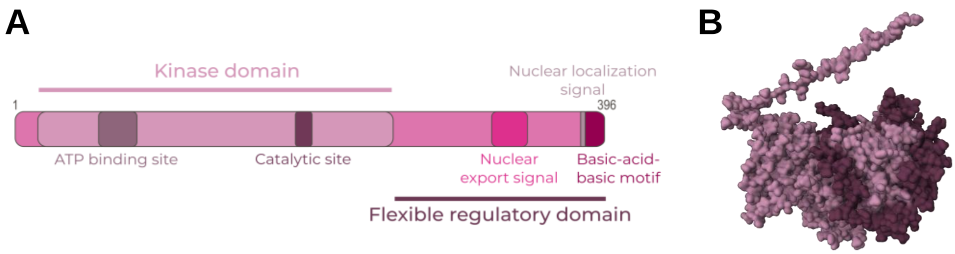

Figure 5. Schematic representations of VRK1. A. Human VRK1 is composed of 369 amino acids. VRK1 presents a kinase domain in its N-terminal region with an ATP binding site domain and a catalytic site domain within it. In the C-terminal region, there is a flexible regulatory domain with a nuclear export signal domain, a nuclear localization signal domain and a basic-acid-basic motif. Adapted from Campillo *et al.*, 2021. **B.** 3D structure of VRK1. Image made with Pymol, PDB code: 2LAV.

1.5.2 VRK1 regulation

VRK1 gene expression in cells is controlled by the presence of growth factors of the serum added to the cell culture. As a consequence of serum starvation, cells in culture suffer a drop in VRK1 protein levels, that last for several days[124]. Moreover, TFs such as E2F1, Sox2 and Myc activate *VRK1* gene expression after binding to its promoter[127–129].

VRK1 has a very active autophosphorylation potential. VRK1 is autophosphotylated at Thr355 in the absence of any other protein as substrate[130,131]. Endogenous VRK1 also shows high basal catalytic activity, which is enhanced in response to specific stimuli, such as proliferation signals, UV exposure, ionizing radiation or doxorubicin[132]. Regarding VRK1 enzymatic activity, it is negatively regulated by its interaction with Ran-GDP[133].

1.5.3 VRK1 functions

Since VRK1 identification, different studies have associated this kinase with several functions linked to its downstream phosphorylation targets, such as cellular homeostasis maintenance and cell survival. Some of these targets are histones, chromatin modifiers, TFs, DDR-related proteins and other nuclear proteins (**Figure 6**). Therefore, VRK1 deregulation is involved in some human pathologies such as cancer and neurodegenerative[126].

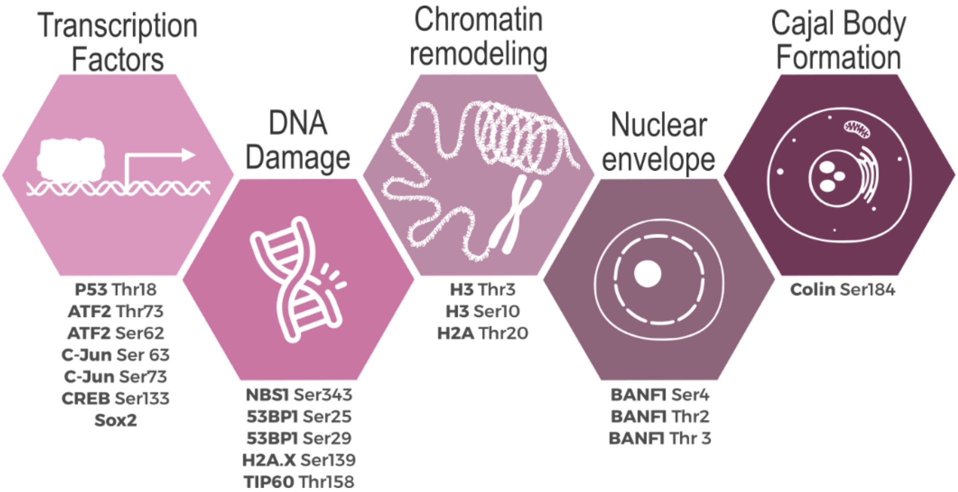

Figure 6. VRK1 functions and targets. Representation of the main VRK1 functions and its targets with their phosphorylation sites. Adapted from Campillo *et al.*, 2021.

1.5.3.1 Cell cycle and proliferation

The regulation of the cell cycle is a complex process that requires the coordination of several proteins and intracellular and extracellular factors. Over the years, studies have suggested several possible mechanisms by which VRK1 controls cell cycle progression.

Under experimental conditions, when cell cycle is blocked by serum starvation, VRK1 protein levels decrease together with the proliferating cell nuclear antigen (PCNA) and the phosphorylated form of retinoblastoma (Ph-RB), two markers of cell cycle progression. On the contrary, the levels of p27, a marker of cell cycle inhibition, increase. Moreover, VRK1 depletion leads to a specific decrease in cyclin D1 (CCND1) levels, a protein implicated in the checkpoint of G1 to S phase transition, indicating that cells do not pass this restriction point in absence of the kinase[124]. This relation between VRK1 and CCND1 occurs through Myc regulation. Myc enhances VRK1 expression, which subsequently phosphorylates CREB at Ser133, which is required for the transcriptional activation of specific genes. This allows CREB binding to CCND1 promoter, inducing its transcriptional activation[128,134].

Furthermore, VRK1 is essential for the nuclear membrane disassembly through the phosphorylation of the barrier to-autointegration factor (BANF1). VRK1 phosphorylates BANF1 at Thr2, Thr3, and Ser4, which is crucial for proper chromatin restructuring and for the formation of the nuclear envelope[135].

In addition, VRK1 is expressed in all types of human cells, particularly at high levels in proliferative tissues, suggesting an association with cell proliferation. Its overexpression is linked to proliferative phenotypes in tumor cell lines and its depletion by siRNA results in a reduced proliferation rate[125,129]. In tumor cells, VRK1 overexpression also correlates positively with high levels of proliferative markers such as Ki67, p63, survivin, cyclins A and B1 and CDK1 and 2[127,129].

1.5.3.2 **Chromatin remodeling**

VRK1 is a nuclear kinase that binds to chromatin[32,123], participating in its remodeling through interactions and phosphorylations of histones. It phosphorylates histone H3, H2A, H2B, and H4; although it has not still been demonstrated that VRK1 phosphorylates histone H1. VRK1 interacts and phosphorylates histone H3 at Thr3 and Ser10 residues, together with aurora B, which is required for chromosome compaction before mitosis[15,136].

Additionally, dynamic chromatin remodeling involves several epigenetic enzymes that modulate histone PTMs. Kinases such as VRK1 are likely candidates to regulate the balance of histone PTMs by the regulation of the enzymes responsible for them. In recent years, it has been described that VRK1 directly interacts with epigenetic enzymes such as TIP60[32].

1.5.3.3 DNA damage response

DNA damage is defined as any abnormal alteration of DNA that affects cellular biological processes, including base modifications, nicks, gaps, single-strand breaks, and double-strand breaks (DSB). Cells have various mechanisms to protect DNA from endogenous or exogenous genetic damage. In DSB, there are two major DDR mechanisms: homologous recombination (HR), which uses the other chromatid as template for the repair, and non-homologous end-joining (NHEJ), characteristic of non-dividing cells. Deregulated or defective DDR can compromise genomic stability and, therefore, promote cancer pathogenesis[137].

VRK1 plays a critical role in chromatin distortion in response to DNA damage (**Figure 7**)[138]. Firstly, VRK1 and the tumor suppressor p53 form a stable complex after DNA damage and then, p53 is immediately phosphorylated at Thr18, disrupting its interaction with p53-Murine double minute 2 (Mdm2). Mdm2 is the ubiquitin ligase responsible for p53 ubiquitination and this modification is necessary for its degradation in the proteasome. Thus, the interaction of VRK1-p53 promotes p53 accumulation and prevents cell cycle progression, triggering cell death and avoiding the transmission of mutations to the progenity[130,139]. Secondly, VRK1 directly interacts with and activates TIP60, responsible for H4K16 acetylation, which facilitates the next steps to DNA repair[32]. VRK1 directly interacts and phosphorylates histone H2A.X at Ser139 (termed γH2A.X), which serves as a signal of DNA damage site and to recruit other DNA damage signaling factors[16]. Upon DNA damage, VRK1 interacts with and phosphorylates NBS1 at Ser343, a member of the MRN complex, independently of ATM[140]. After that, VRK1 binds and phosphorylates 53BP1 at Ser25, functioning as an intermediary effector of DDR, again in an ATM-independent fashion. Moreover, VRK1 regulates other major components of DDR. Its depletion prevents the activating phosphorylation of ATM at Ser1981, Chk2 at Thr68, and DNA-PK at Ser2056, suggesting that VRK1 is an upstream regulator[132].

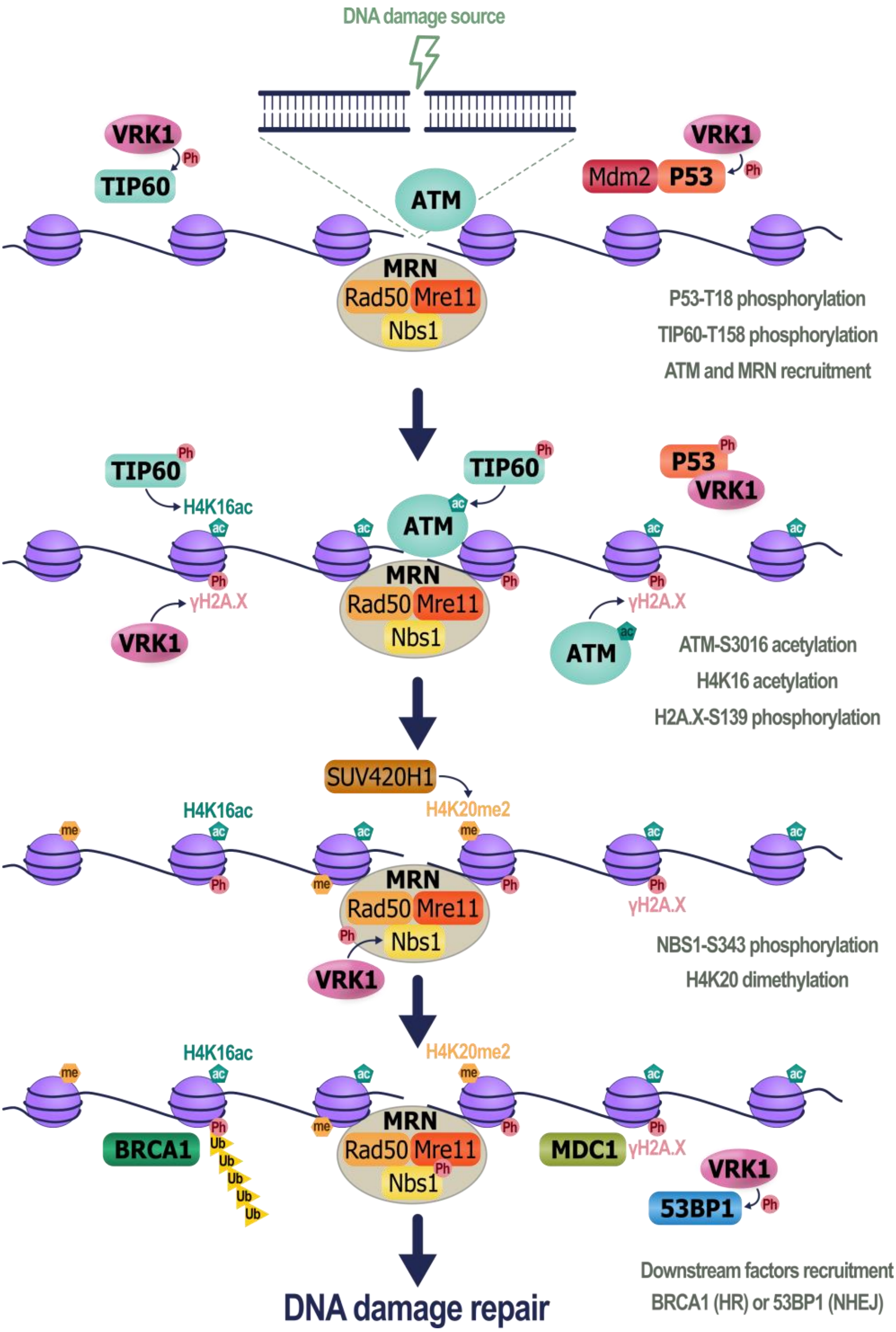

Figure 7. DNA damage response network. Double-strand DNA break signal through the sensors, transducers and mediators proteins, leading to DNA repair.

1.5.4 VRK1 implications in cancer

Considering the vast importance of VRK1 in cellular processes such as proliferation and DNA damage, its aberrant activity has an impact on human pathologies like cancer. Although VRK1 is rarely mutated in human cancer, in less than 1.5% of the cases (COSMICdatabase, https://cancer.sanger.ac.uk/cosmic/gene/analysis?ln=VRK1), the kinase is highly expressed in proliferative tissues, including embryonic tissue, adult testis, and thymus, as well as in several cancer cell lines, implying a functional role in cell cycle regulation and tumorigenicity (https://www.proteinatlas.org/ENSG00000100749-VRK1/tissue). Overexpression of VRK1, detected using microarray transcriptomic platforms, is associated with poor prognosis of cancer such as breast[141], lung[142,143], head and neck squamous cell carcinomas[127], colon[144], liver[145], gliomas[146,147], multiple myeloma[148], esophageal carcinomas[149], and oral cancer[150]. For example, VRK1 expression positively correlates with glioma pathological grade and its depletion in glioblastoma cells alters DDR and promotes tumor cells death[146,151]. This suggests that its inhibition can be combined with current treatments to reduce drug toxicity. Moreover, targeting proteins implicated in the DDR like VRK1 can sensitize tumor cells to DNA damage induced by ionizing radiation[152]. These results suggest that VKR1 inhibition may improve cancer treatments based on synthetic lethality.

1.5.5 VRK1 inhibition

Most human cell lines express 350–400 protein kinases that are integrated into different cellular pathways to regulate essential biological activities. In cancer, kinases are frequently mutated or overexpressed making them excellent targets to inhibit cell growth and/or induce tumor cell death[153]. To date, 72 drugs that target kinases have been approved by the FDA[154]. However, designing specific inhibitors remains to be the major challenge in kinase research. Considering the above-mentioned points, VRK1 is a promising candidate to target in cancer treatments. In 2018, Ngow *et al*. described the molecular insights on the VRK1 interaction with AMP-PNP, a non-hydrolyzable ATP-analog, which could be used to develop a pharmacophore model[155]. On the other hand, three aptamers (ssDNA or RNA that binds with high affinity to a specific target molecule) recognizing VRK1 (apVRKF8, apVRKF28, and apVRKF33) showed high affinity to VRK1 and, consequently, reduced viability, blocked G1 to S phase transition, and led to apoptosis in MCF7 cells[156]. Following these discoveries, a novel selective and potent ($IC_{50} \approx 150$ nM) pyridine-based inhibitor against VRK1 has been developed by Serafim *et al.* (VRK-IN-1)[157]. It consists of a small ligand resulting from a fusion between an aminopyridine core with the difluorophenol group. Upon interaction with VRK1, the kinase adopts a conformation in which the phosphate-binding loop is collapsed into the ATP binding site, inhibiting VRK1 activity. These results open a door towards identifying effective VRK1-specific inhibitors and targeting this kinase for future cancer treatments.

1.5.6 VRK1 implications in neurodegenerative disease

Since VRK1 discovery in 1997, 25 mutant variants of the kinase have been identified and associated with patients that suffer from neuromotor syndromes, including muscular spinal atrophy, ataxia, Charcot Marie Tooth, microcephaly and pontocerebellar hypoplasia. These neurological phenotypes were detected in patients having either homozygous or compound heterozygous variants of the kinase. VRK1 variant proteins are either unstable or have an altered kinase activity[158]. One of the main altered functions is organization of the Cajal bodies (CBs) by alteration of the regulation of coilin by VRK1 dysfunction. Migration and cell cycle progression are also defective and, as a consequence, there is a reduction of brain mass and motor impairment. In addition, VRK1 pathologic variants present a defective DDR and nuclear envelope assembly in cells[158,159]. However, the exact role that VRK1 variants play, and the underlying molecular mechanisms affected in these pathogeneses need to be further investigated.

Aims

2 Aims

Based on the fact that VRK1 is described as a nuclear chromatin kinase involved in cellular processes such as transcription, DNA damage and chromatin remodeling, we hypothesize that VRK1 kinase activity regulates chromatin organization via histone PTMs modulation. We speculate that VRK1 is able to interact with and control certain epigenetic enzymes as it does with TIP60. Recently, a novel specific inhibitor against VRK1 has been developed, opening new opportunities to target this kinase in clinical trials.

The objective of this thesis is to define the effect of the human kinase VRK1 on the regulation of histone PTMs patterns and to characterize new possible substrates to decipher novel molecular targets implicated in human pathologies. Also, we aim at characterizing the aforementioned VRK1 inhibitor, VRK-IN-1, to broaden the understanding of its mechanism of action and propose VRK1 inhibition as a potential cancer treatment. To achieve this goal, the following specific objectives were addressed:

1. To define the potential role of VRK1 in chromatin remodeling comparing the impact of VRK1 depletion with different epigenetic enzymes inhibitors on the following histone post-translational marks: H3K4me3, H3K9ac, H3K9me3, H3K27ac, H3K27me3, H3K79me2 and H4K16ac.
2. To identify novel interactions between VRK1 and the epigenetic enzymes that carry out these modifications (HDAC1, SIRT1, SIRT2, PCAF, SETDB1, EZH2, LSD1, JMJD1A, and JMJD2A), unveiling different multiprotein complex implicated in the regulation of the histone code.

3. To characterize the novel inhibitor of VRK1 (VRK-IN-1) studying its effect in different cellular processes such as proliferation, chromatin remodeling, and DNA damage response.

Materials and methods

3 Materials and methods

3.1 Experimental procedures

3.1.1 Reagents and inhibitors

For the experiments, cells were treated with different reagents. These reagents and inhibitors, indicated in **Table 2**, were resuspended in dimethyl sulfoxide (DMSO) and used as specified in each section of the results.

3.1.2 Bacteria transformation

Transformation is a process by which cells incorporate foreign DNA and are able to produce multiple copies. The ability to take up free, extracellular genetic material is the prerequisite for competent bacterial to undergo transformation. In this project, *E. coli* DH5α and BL21 strains were used. The different plasmids used are listed in **Table 3**. After thawing the cells for 5 minutes in ice, 50-100 ng of purified plasmid DNA were directly added to cells and mixed by gentle tapping. Cells were incubated for 30 minutes on ice and incubated exactly 42 seconds at 42 °C. Bacteria were recovered 2 minutes on ice and 1 mL of super optimal broth with catabolite repression (SOC) medium (**Table 4**) was added to each tube. Cells were incubated for 1 h at 37 ºC on agitation, and 100 µL of each transformed cell suspension were spread onto LB agar plates with plasmid's specific selection antibiotic. Plates were incubated overnight at 37 ºC, and the following day, bacteria colonies were selected and cultured as needed. To check that transformations were correct, and plasmids were incorporated by bacteria, Sanger DNA sequencing was performed by PCR with specific oligonucleotides for each vector and sequences were analyzed using Chromas software.

3.1.3 Purification of mammalian expression vectors

Mammalian expression vectors were used to promote a constitutive expression of cloned DNA inserts in mammalian cells. *E. coli* DH5α cells previously transformed with the corresponding plasmid (**Table 3**; **Section 3.1.2**) were grown in Luria-Bertani (LB) broth medium (**Table 4**) at 37 ºC. Bacteria were grown up to an optical density 600 nm (OD_{600}) of 2-3 and harvested by centrifugation (5,000 x *g*, 10 min, 4 ºC). Plasmidic DNA (pDNA) was extracted using GeneJET Plasmid Maxiprep kit (Thermo Fisher Scientific), according to the manufacturer's instructions. Briefly, pelleted cells were resuspended in Resuspension Solution by pipetting and vortexing until no visible cell clumps remained. Lysis Solution was added and mixed gently by inverting the tube 4-6 times until the solution became viscous and slightly clear. After 3 minutes of incubation at room temperature (RT), neutralization solution and endotoxin binding reagent were added sequentially and mixed immediately by inverting the tube. Mix was incubated for 5 minutes at RT and centrifuged (48,000 x *g*, 20 min). The supernatant was mixed with ethanol 96% (ratio 1:1) and transferred to the purification columns, which were centrifuged (2,000 x *g*, 3 min). After discarding the flow-through, column was washed with wash solutions I and II. Lastly, DNA was eluted incubating the column for 2 min with elution buffer and centrifuging (3,000 x *g*, 2 min). Eluted pDNA was measured using NanoDrop (NanoDrop Technologies).

3.1.4 Agarose gel electrophoresis

Agarose gel electrophoresis was carried out to separate DNA fragments by their size and confirm pDNA purification. 1% m/v agarose gel was prepared in TAE buffer (**Table 4**) which was added 0.5 µg/mL ethidium bromide for subsequent DNA visualization. Ethidium bromide signal corresponding to DNA amount was captured with Gel Doc™ 2000 (Bio-Rad). GeneRuler 1 kb Plus DNA Ladder (Thermo Fisher Scientific) was used for DNA approximate sizing. Agarose gel electrophoresis was performed under a constant voltage of 60 V for 1 h.

3.1.5 Purification of His-tagged proteins

VRK1-His and SIRT2-His proteins were purified through their His-tag. For this purpose, *E. coli* BL21 cells previously transformed with the corresponding vector were grown in their selection antibiotic overnight at 37 ºC in agitation. The next day, this pre-inoculum was centrifuged (1800 x *g*, 15 min, 25 ºC) and the pellets were resuspended in LB medium until the inoculum achieved the mid-exponential phase, at an OD_{600} = 0.6-0.8. Right after, the protein expression was induced by adding 0.1 mM isopropyl-β-D-thiogalactoside (IPTG). The inoculum was incubated 2-3 h at 37 ºC in agitation and centrifuged (5,000 x *g*, 20 min, 4 ºC). Pellets were collected for bacteria lysis. Bacteria were lysed in BC-500 buffer (**Table 4**) and bacterial lysates were sonicated (5 cycles, 50 s bursts with 10s breaks, 4ºC, output 21%). After 30 min, the lysates were centrifuged (48,000 x g, 20 min, 4 ºC) and the proteins were purified by affinity chromatography, incubating the supernatants with Ni-NTA Agarose beads (Qiagen) overnight at 4 ºC in rotation. After several washes in lysis buffer, VRK1-His and SIRT2-His proteins eluted in 50 mM Imidazole in BC-500, which was added for 10-15 min.

Then, samples were centrifuged (0.5 x *g*, 2 min, 4 ºC). This elution process was repeated until the total protein was eluted and protein supernatants were stored at -80 ºC.

3.1.6 Purification of GST-tagged proteins

GST-VRK1, GST-VRK1[K176E], GST-PCAF[1-X], GST-53BP1[1-1039], and GST-P53[1-85] proteins were purified through its GST-tag. For this purpose, BL21 competent *E. coli* cells, previously transformed with the corresponding vector, were grown with the selection antibiotic overnight in agitation at 37 ºC. The next day, these pre-inoculums were centrifuged (1800 x *g*, 15 min, 25 ºC) and pellets were resuspended in LB until the inoculums reached the optimal density (OD_{600} = 0.6-0.8). Protein expression was induced by adding 0.1 mM IPTG and inoculums were incubated 2-3 h at 37 ºC in agitation. Samples were centrifuged (5,000 x *g*, 20 min, 4 ºC) and pellets were collected for bacteria lysis. Bacteria were lysed with bacterial lysis buffer (**Table 4**) and bacteria lysates were sonicated as described earlier. After 30 min, extractions were centrifuged (48,000 x *g*, 20 min, 4 ºC) and the resulting GST-fusion proteins were purified by affinity chromatography, incubating the supernatant with Glutathion Sepharose 4B beads (GE Healthcare) overnight at 4 ºC in rotation. The following day, samples were washed with lysis buffer, and GST-tagged proteins were obtained by elution with 20 mM glutathione. For this purpose, glutathione was added for 10-15 min and then, samples were centrifuged (0.5 x *g*, 2 min, 4 ºC). Protein supernatants were stored at -80 ºC. This process was repeated until the total proteins were eluted.

3.1.7 Pull-down assay

Binding assay was performed to study the interaction between VRK1 and several proteins *in vitro*. Purified GST-VRK1, His-VRK1, GST-PCAF, and His-SIRT2 in the indicated amounts in each experiment were used. GST protein expressed from an empty vector was used as negative control in these experiments. Proteins were incubated in kinase buffer (**Table 4**) in a volume of 25 µL for 45 min at 37 ºC and gentle agitation. 40 µL of Glutathion Sepharose 4B beads (GE Healthcare) or Ni-NTA Agarose beads (Qiagen), previously equilibrated with the aforementioned buffer, were added and the mix was incubated overnight at 4 ºC. The pull-down was performed by centrifugation (500 x *g*, 2 min, 4 ºC) and beads were washed in kinase buffer three times. Electrophoresis in acrylamide gel was performed following the mentioned instructions of SDS-PAGE electrophoresis (section 3.1.15). Finally, agarose-immune complexes were stained with Coomassie Blue staining solution (**Table 4**) and washed with Coomassie Blue destaining solution (**Table 4**) to visualize them.

3.1.8 *In vitro* kinase activity assay

A kinase activity assay works by measuring the activity of the kinase. Reactions were performed in kinase buffer containing 1 µg of GST-VRK1 or GST-VRK1[K179E], varying amounts of His-SIRT2, GST-P53[1-85], human histone H3, or human histone H2A.X (H2A.X) and 10 µM ATP.

In the cases that there was not an available commercial phospho-specific antibody, and additional 7.5 µCi of γ-^{32}P was added to the mix. Reactions were performed for 45 min at 37 °C and stopped by addition of sample loading buffer (**Table 4**). Electrophoresis in acrylamide gel was performed following the mentioned instructions of SDS-PAGE electrophoresis (**section 3.1.15**). The radioactive signal was detected using Fuji Medical X-ray films. To detect control proteins, membranes were blocked in 5% w/v nonfat milk in TBS-T for 1 h at RT and incubated with the corresponding primary antibody (**Table 5**) diluted in TBS-T buffer (**Table 4**) for 2-4 h. Subsequently, membranes were washed 3 times in TBS-T and incubated with secondary enhanced chemiluminescence (ECL) antibodies (**Table 6**) for 1 h. Right after 3 more washes, blots were developed with ECL detection system (**Table 4**) after 5 min incubation, using Fuji Medical X-ray films.

In the cases where there are available commercial phospho-specific antibodies, reactions were carried out following by SDS-PAGE electrophoresis (**section 3.1.15**) and western blot (**section 3.1.16**). To detect the phospho-specific signals, membranes were incubated with the corresponding primary antibody (**Table 5**) diluted in TBS-T buffer (**Table 4**) overnight and, next day, in darkness with their corresponding DyLight secondary antibodies (**Table 6**) in TBS-T for 1 h. Finally, fluorescence signals were detected using the LI-COR Odyssey Infrared Imaging System (LI-COR Biosciences).

3.1.9 Cell lines

The cell lines used in this project were HEK 293T (CRL-3216), A549 (CCL-185) and U2OS (HTB-96) (**Table 7**), from the American Type Culture Collection (ATCC). All cells were maintained in an incubator with fixed conditions: 5% CO_2 (v/v), 85-95% humidity and 37 °C temperature. Cells were cultured in DMEM (Gibco-Life Technologies) supplemented with 10% fetal bovine serum (FBS; Gibco-Life Technologies), 5 mM glutamine (L-glutamine; Gibco-Life

Technologies), and 100 U/ml penicillin and 100 μg/ml streptomycin (Pen/Strep; Gibco-Life Technologies). Cells were washed with PBS and detached using TrypLE-Express (Gibco-Life Technologies-Invitrogen). For experimenting, cells were seeded and grown to 80% confluence. Serum starvation (DMEM supplemented with 0.5% FBS, 1% Pen/Strep, and 2 mM L-glutamine) was performed for 48 h when experiments indicated it[160].

3.1.10 JetPEI transfection

Plasmid transfections were performed to transient overexpress human proteins. Polyethylenimine (PEI; Polysciences) was used according to the manufacturer's guidelines. Briefly, 4-6 μg DNA was diluted in 150 mM NaCl, and 1 mg/mL of PEI reagent was diluted in 150 mM NaCl. Both mixes were combined and, after 30 min, added to the cells by gently pipetting dropwise to the cells. Assays were run 48 h after transfection.

3.1.11 VRK1 depletion by siRNA

SiRNAs were used for the specific depletion of VRK1. All RNAs used were purchased from Dharmacon RNA Technologies and are detailed in **Table 8**. ON-TARGET plus siControl non-targeting siRNA (siC) was used as a negative control. Briefly, lipotransfectin (Solmeglas) was diluted in Opti-MEM (GIBCO-Life Technologies) according to the manufacturer's guidelines. SiRNA was diluted in Opti-MEM at 200 nM and added to the lipotransfectin-Opti-MEM mix. The lipotransfectin-Opti-MEM-siRNA mix was incubated for 30 min and added to the cells by gently pipetting dropwise to the cells. Cells were maintained with antibiotic-free media and processed after 72 h of VRK1 depletion.

3.1.12 Whole protein extraction

All steps of protein extraction were carried out on ice. Cell lysates were prepared by resuspending cells in lysis buffer (**Table 4**) supplemented with phosphatases inhibitors (1 mM sodium fluoride and 1 mM sodium orthovanadate) and proteases inhibitors (1 mM PMSF, 10 mg/mL aprotinin, and 10 mg/mL leupeptin) right before use. The suspension was incubated for 15 minutes at 4 ºC followed by centrifugation (16,000 x *g*, 15 min, 4 ºC).

Protein concentration was determined using the BCA protein assay kit (Thermo Fisher Scientific) according to manufacturer's instructions. 20-40 µg of protein extracts were used for immunoblots.

3.1.13 Histone extraction

Histones were isolated by acidic extraction as previously described by Shechter *et al.*, 2007[161]. Shortly, cells were harvested and pelleted by centrifugation (300 x *g*, 5 min), followed by resuspension in 1 mL of hypotonic lysis buffer (**Table 4**) supplemented with phosphatases and proteases inhibitors. After transferring the extracts to a 1.5 mL microcentrifuge tube, samples were incubated for 10 min on ice and centrifuged (10,000 x *g*, 10 min, 4 ºC). Supernatant was discarded and the pellet, which contains the cell nuclei, was resuspended in 400 µl 0.4 N sulfuric acid. Nuclear extracts were incubated 30 min at 4 ºC in rotation. Then, to remove nuclear debris, the extracts were centrifuged (16,000 x *g*, 10 min, 4 ºC) and supernatants, which hold histones, were transferred to a new tube.

Histones were precipitated adding gently 33% trichloroacetic acid (TCA). The mix was incubated for 30 min on ice, followed by centrifugation (16,000 x *g*, 10 min, 4 ºC). Pellets, which contain the histones, were washed with cold acetone 3 times without resuspending the pellet and collected again by centrifugation (16,000 x *g*, 5 min, 4 ºC). Supernatant was discarded and samples were left out in the air for acetone to dry before being resuspended in 60-80 µL of MilliQ® H_2O.

Protein concentration was determined using the BCA protein assay kit (Thermo Fisher Scientific) according to manufacturer's instructions. 5-10 µg of histones extracts were used for immunoblots.

3.1.14 Immunoprecipitation (IP)

Immunoprecipitation assays were used to observe the interaction between different endogenous and/or overexpressed tag- proteins in the cell lines mentioned above. 0.5-1 mg of protein from whole-cell lysates were used for IP. Protein extracts were incubated with the corresponding antibody (**Table 5**) for each experiment for 6-8 h at 4 ºC in rotation. Subsequently, 40 µL of Protein G–Agarose Resin 4 Rapid Run (4RRPG, Agarose Bead Technologies) was added to the protein-antibody immune complexes and the mix was incubated overnight at 4º C in a rotating wheel. The immunoprecipitated was collected by centrifugation (500 x *g*, 2 min, 4 ºC) and washed three times in lysis buffer.

3.1.15 SDS-PAGE electrophoresis

Proteins are typically separated by electrophoresis based on their molecular weight. Firstly, gel preparation was performed. Depending on the target protein size to analyze, running gel had different acrylamide-bisacrylamide percentages: 12.5%-0.33% gels were used for proteins smaller than 30 kDa, 10%-0.27% gels for proteins between 30-100 kDa and 7.5%-0.2% gels for proteins larger than 100 kDa. Tetramethylethylenediamine (TEMED, Sigma Aldrich) and ammonium persulfate (APS, **Table 4**) were added to catalyze the polymerization of the gels. Before loading samples into the gel wells, lysates and immunoprecipitates were boiled at 95 ºC for 5 min in sample loading buffer to denaturalize proteins. Electrophoresis was performed under denaturing conditions in electrophoresis buffer (**Table 4**). Precision Plus Protein™ Standards Dual Color (Bio-Rad) was used as a molecular weight protein reference. Sodium dodecyl sulfate polyacrylamide gel electrophoresis (SDS-PAGE) was performed under a constant voltage: 90 V for 15 min and 120 V for 80 min.

3.1.16 Western blot (WB) analyses

Immunoblotting techniques are used to detect specific proteins in a sample of tissue homogenate or protein extract, usually separated by size and transferred to a solid support. Then, antibodies are used to identify target proteins through antigen-antibody (or protein-ligand) specific reactions. After separating samples on SDS-PAGE gels, proteins were transferred to PVDF Immobilon-FL membranes (Merck Millipore). Depending on the size of the target protein, membranes had a pore size of 0.22 µm for small proteins (< 15 kDa), or 0.45 µm, for the rest of the proteins. Membranes were activated in methanol (Sigma Aldrich) for 2 minutes. After preparing the cassette according to standardized protocols, the transfer was performed at 90 V for 30-90 min (depending on protein size) at 4 ºC. Afterwards, membranes were blocked for 1 h at RT with 5% nonfat milk in TBS-T buffer or, alternatively, with 5% w/v of BSA in TBS-T buffer when the phosphorylated state of proteins was evaluated. Next, membranes were washed 3 times for 10 min each time in TBS-T and incubated with the primary antibody (**Table 5**) in TBS-T overnight at 4 ºC. Next day, after three washes of 10 min in TBS-T buffer, membranes were incubated in darkness with their corresponding DyLight secondary antibodies (**Table 6**) in TBS-T for 1 h. Membranes were washed three more times in TBS-T buffer for 10 min. Finally, fluorescence signals were detected using the LI-COR Odyssey Infrared Imaging System (LI-COR Biosciences). All western blots were performed in triplicate and corresponds to the accompanying immunofluorescence figure. Densitometric analysis of western blots was performed using ImageJ software.

3.1.17 Immunofluorescence (IF) and confocal microscopy

Immunofluorescence assays were used to observe endogenous and/or exogenous proteins in the cell lines mentioned above. Cells were cultured as previously described (**3.1.9 section**) with glass coverslips (Thermo Scientific) in the culture dishes. After the corresponding treatments, cells were fixed with 3% paraformaldehyde (PFA) in PBS for 15 min and treated with 200 mM glycine solution to eliminate the PFA. Cells were permeabilized in 0.2% Triton X-100 for 20 min and blocked in 1% BSA in PBS with 0.1% sodium azide for 1 h at RT, or overnight at 4 ºC. Coverslips were consecutively incubated with two primary antibodies (**Table 5**) in PBS-1% BSA for concurrent protein detection. The first primary antibody was incubated 5-6 h at RT and the second primary antibody was consecutively incubated overnight at 4 ºC. Afterwards, cells were washed with PBS for 3 times and incubated with the secondary antibodies (**Table 6**) in PBS-1% BSA for 1 h at RT in the dark. All next steps were carried out in darkness. After 3 more washes with PBS, nuclei were stained with DAPI (4', 6-diamidino-2-phenylindole) at 1:1,000 dilution for 5 min, followed by three washes in PBS. Coverslips were mounted with a drop of mounting medium (MOWIOL) in microscope slides. Cell Images were captured with a LEICA SP5 DMI-6000B confocal microscope (Leica), with the following lasers: argon (488 nm), DPSS (561 nm), helio-neon (633 nm) and UV Diode (405 nm). These images were acquired with a 63.0x lens zoomed in 1.5x with a 1,024 x 1,024 frame and 600 Hz scanning speed. Images were analyzed using ImageJ software.

3.1.18 TUNEL assay

TdT-mediated dUTP Nick-End Labeling (TUNEL) assay (Roche) was used to label fragmented DNA in cells. Fluorescein-12-dUTP binds to the 3'-OH of the DNA strands and is detected by a fluorescence microscope. Cells were cultured in glass coverslips and fixed as was described in **section 3.1.17**. Coverslips were incubated with 50 µl of TUNEL reaction mixture prepared according to the manufacturer was added for 1 h at 37 ºC in darkness, followed by three washes for 10 minutes in PBS after each one. Nuclei were stained with DAPI and coverslips were mounted with MOWIOL on microscope slides. Samples were visualized using a Leica SP5 DMI-6000B confocal microscope (Leica).

3.1.19 Wound healing assay

Wound healing assay is used to study how cells migrate under different conditions. After creating a gap between cells, the change of the cell-covered area is recorded over time. For this purpose, cells were seeded in 24-well plate with a culture-insert 2 well with a defined cell-free gap (500 µm) for 42 h until a cell monolayer was achieved. After the corresponding times and treatments, the culture-inserts were taken back and the process of cell migration into the gap was monitored by taking photos at different time points, using a Nikon Eclipse TE 2000 microscope. Then, wounding area coverage was analyzed using ImageJ software.

3.1.20 ATAC-seq

ATAC-seq assay is based on transposase-mediated insertion of sequencing primers into open chromatin regions. This assay provides genome-wide profiles of open and accessible regions of chromatin that are indicative of active regulatory regions (**Figure 8**). Samples for ATAC-seq analysis were control, VRK1 depletion and VRK-IN-1 treatment condition. For that, A549 cells were cultured with 0.5% FBS for 48 h. VRK1 was knocked down using a siRNA (siV-02) for 72 h; the corresponding cells were treated cells with 600 nM VRK-IN-1 for 24 h. In total, 1×10^5 cells were flash-frozen and sent to Active Motif for subsequent ATAC-seq protocol (**Figure 9 A**). The data analysis was performed by Active motif bioinformatic services and then the results were interpreted for open regions of chromatin identification (**Figure 9 B**).

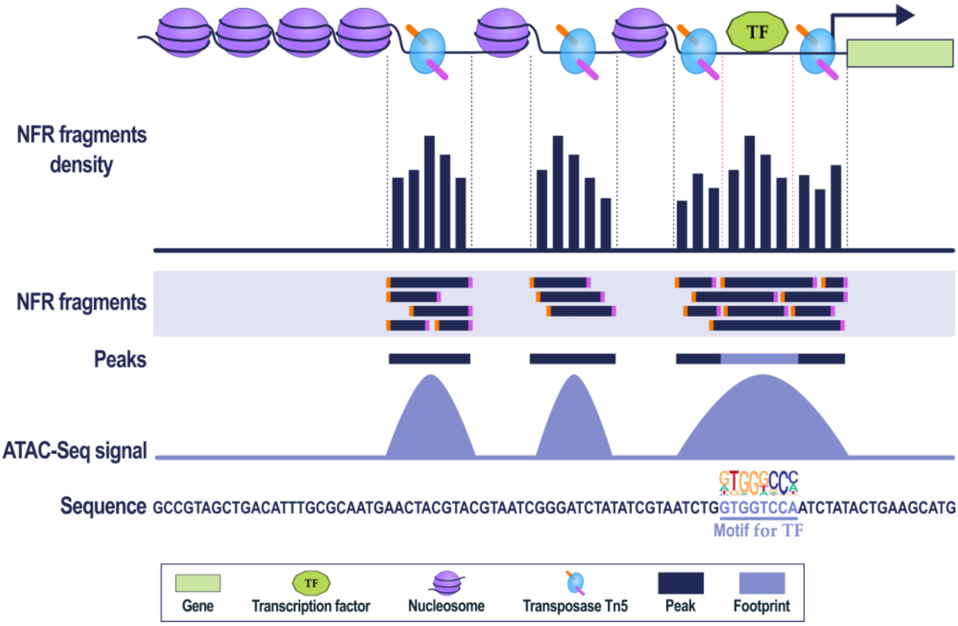

Figure 8. ATAC-seq scheme. In an ATAC-seq experiment, transposase Tn5 binds and cuts open chromatin and simultaneously ligates adapters. Fragments are sequenced to identify open chromatin regions (dark blue) and footprints (light blue). NFR and peaks fragments represent the open chromatin. ATAC-seq signal represents how data might look like, which can also help reveal the TF binding motif associated with such differential peaks, here depicted as “GTGGTCCA”. Adapted from Yan *et al.*, 2022.

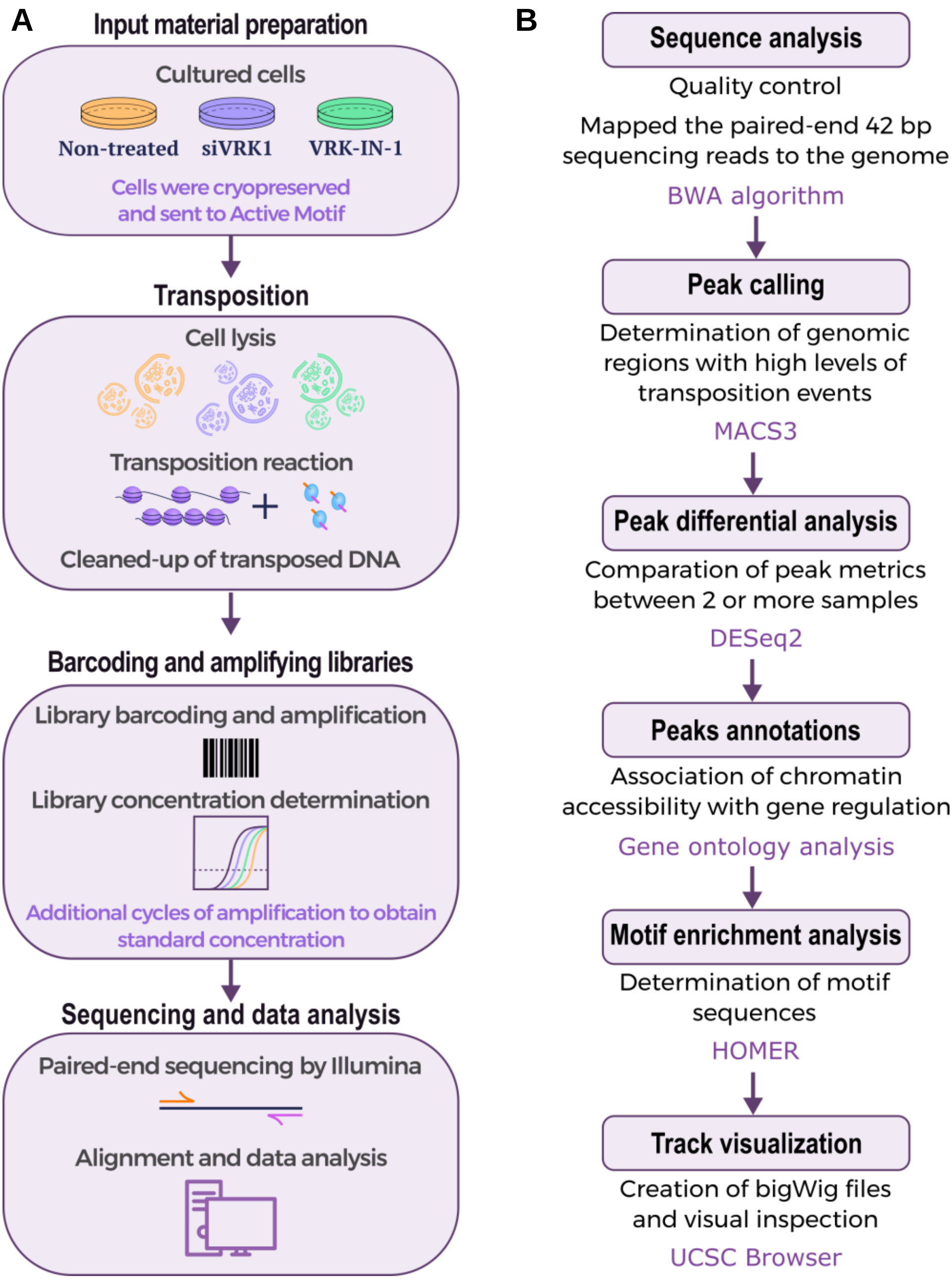

Figure 9. ATAC-seq workflow protocol and data analysis. A. The main protocol steps are shown in sequence. B. Schematic overview of ATAC-seq data analysis workflow. Broadly, ATAC-seq analysis is composed of three major steps: (i) data processing that cleans and aligns the raw reads, (ii) peak calling, merging, and insertion counting that determines the locations of Tn5 accessible chromatin and the relative signal within each accessible region, and (iii) the downstream analysis that can help assign putative functions and pathways to the called peaks.

3.1.21 Statistical analysis

Graphs and statistical differences were computed using GraphPad Prism 8. Results are presented as dot plots with the median, first and third quartiles and whiskers. After confirming samples did not adjust to a normal distribution (non-parametric distributions) according to two-tailed Kolmogorov test, Kruskal-Wallis test was used for two-group comparisons in all experiments. Values of $p < 0.05$ were considered significant. Values of $p < 0.05$ were ranked as *: $p < 0.05$, **: $p < 0.01$, and ***: $p < 0.001$. Non-significant differences were indicated as n.s.

3.2 Tables

Table 2. Treatments

Reagent	Target/Effect	Working conditions	Supplier
AGK2	SIRT2	5 µM 24 h	SelleckChem
AK7	SIRT2	8 µM 24 h	SelleckChem
Chaetocin	SUV39H1	100 nM 24 h	Sigma-Aldrich
C646	P300	5 µM 24 h	SelleckChem
Doxorubicin	Top2 inhibitor DSB induction	3 µM 2 h	Sigma-Aldrich
Entinostat (MS-275)	HDAC1 and HDAC3	5 µM 24 h	SelleckChem
EPZ004777	KMT4 (DOT1L)	80 nM 24 h	SelleckChem

L-Glutathione reduced	GST-Protein elution	20 mM 12 h	Sigma-Aldrich
Iadademsat (ORY-1001)	KDM1A (LSD1)	50 nM 24 h	SelleckChem
Imidazole	His-Protein elution	100 mM 12 h	Sigma-Aldrich
IPTG	Protein expression induction	0.1 mM 0.2 2-4 h	Sigma-Aldrich
JMJD2i (5-c-8HQ)	KDM4A (JMJD2A)	100 µM 24 h	Millipore
MG149	KAT5 (TIP60)	1 µM 24 h	Axon Medchem
Panobinostat (LBH589)	Non-selective HDAC	50 nM 24 h	SelleckChem
Selisistat (EX 527)	SIRT1	50 nM 24 h	SelleckChem
Tazemetostat (EPZ-6438)	EZH2	50 nM 24 h	SelleckChem
Thiomyristoyl	SIRT2	5 µM 24 h	SelleckChem
Vorinostat (SAHA)	Non-selective HDAC	5 µM 24 h	Axon Medchem
VRK1-IN-1	VRK1	600 nM 24 h	MedChemExpress

Table 3. Plasmids

Name	Plasmid	Tag Protein	Vector Type
EZH2	pCMV6	Myc-DDK	Mammalian Expression

Flag-Ø	pCELF	FLAG	Mammalian Expression
GST-Ø	pGEX-2TK	GST	Bacterial Expression
HA-Ø	pCELF	HA	Mammalian Expression
HDAC1	pcDNA3.1+	FLAG	Mammalian Expression
KDM1A (LSD1)	pCMV6	Myc-DDK	Mammalian Expression
KDM3A (JMJD1A)	pLenti	V5, Myc	Mammalian Expression
KDM4A (JMJD2A)	pCMV	HA	Mammalian Expression
P300	PGEX	GST	Bacterial Expression
P53	pGEXT2	GST	Bacterial Expression
PCAF	PGEX	GST	Bacterial Expression
PCAF	pCl	FLAG	Mammalian Expression
SETDB1	pIRES2-EGFP	FLAG	Mammalian Expression
SIRT1	PCMV4	FLAG	Mammalian Expression
SIRT2	pET30a	His	Bacterial Expression
SIRT2	PCMV4	FLAG	Mammalian Expression
SIRT2	PCDNA4T0	HA	Mammalian Expression
SIRT2[S368A]	PCDNA4T0	HA	Mammalian Expression

SIRT2[S368E]	PCDNA4T0	HA	Mammalian Expression
VRK1	PGEX4T1	GST	Bacterial Expression
VRK1	pET23a	His	Bacterial Expression
VRK1	pCEFL	HA	Mammalian Expression
VRK1	pcDNA3.1	Myc	Mammalian Expression
VRK1-COOH	PGEX4T1	GST	Bacterial Expression
VRK1[K179E]	PGEX4T1	GST	Bacterial Expression
VRK1-NH	PGEX4T1	GST	Bacterial Expression
VRK1[R358X]	PGEX4T1	GST	Bacterial Expression

Table 4. Reagents and buffers compositions

Name	Composition
APS	10% ammonium persulfate in H_2O
Bacterial Lysis Buffer	20mM Tris HCl pH 8.0, 500 mM NaCl, 1% Triton X-100, 0.025% NaN3, 0.2ug/mL lysozyme, and 5 mM DTT
BC-500 Bacterial Lysis Buffer	20 mM Tris HCl pH 8.0, 100 mM NaCl, 10 mM EDTA pH 8.0, 0.1% NP40, and 2% sarkosyl
Chemiluminescent solution A	0.1 M Tris HCl pH 8.5, 0.2 mM coumaric acid, and 1.25 mM Luminol
Chemiluminescent solution B	3% H_2O_2

Coomassie Blue solution	3 g/L Coomassie Brilliant Blue R250, 45% Methanol, 10% Glacial acetic acid
Coomassie Blue destaining solution	40% methanol, 10% Glacial acetic acid
Electrophoresis buffer	25 mM Tris HCl pH 8.0, 200 mM glycine and 1.7 mM SDS
Hypotonic lysis buffer	10 mM Tris HCl pH 8.0, 1 mM KCl, 1.5 mM $MgCl_2$, and 1 mM DTT
Kinase buffer 5X	100 mM Tris HCl pH 7.5, 25 mM $MgCl_2$, 2,5 mM DTT, and 750 mM KCl
LB medium	10 g/L SELECT Peptone 140, 5 g/L SELECT Yeast Extract, 5 g/L Sodium Chloride
Lysis buffer	50 mM Tris HCl pH 8.0, 150 mM NaCl, 1% Triton X-100, and 1 mM EDTA
RIPA buffer	150 mM NaCl, 1.5 mM MgCl2, 10 mM NaF, 4 mM EDTA, 50 mM Hepes, 1% Triton X-100, 0.1% SDS, and 10% glycerol
Sample loading buffer	62.5 mM Tris HCl pH 6.8, 10% glycerol, 2.3% SDS, 0.1% bromophenol blue, and 5% β-mercaptoethanol
SOC medium	2% tryptone, 0,5 % yeast extract, 10 mM NaCl, 2,5 mM KCl, 10 mM MgCl2, 10 mM MgSO4, and 20 mM glucose.
TAE buffer	40 mM Tris-Acetate and 1 mM EDTA
TBS-T	25 mM Tris HCl pH 8.0, 50 mM NaCl, 2.5 mM KCl and 0.1% Tween-20
Transfer buffer	25 mM Tris HCl pH 8.0, 19.2 mM glycine and 10-20% methanol

Table 5. Primary antibodies

Antibody	Type	Dilution (WB/IF)	Supplier
53BP1	Rabbit polyclonal	- 1:1,000	Novus Biologicals
β-actin	Mouse monoclonal	1:2,000 -	Sigma-Aldrich
Caspase-3	Mouse monoclonal	1:1,000 -	Santa Cruz Biotechnology
Flag Tag	Mouse monoclonal	1:1,000 -	Sigma-Aldrich
Flag Tag	Rabbit polyclonal	1:1,000 -	Sigma-Aldrich/ Abcam
GST Tag	Mouse monoclonal	1:1,000 -	Santa Cruz Biotechnology
γH2A.X	Mouse monoclonal	- 1:500	Millipore
H3K4me3	Rabbit polyclonal	1:800 1:1,000	Cell Signaling Technologies
H3K9ac	Rabbit polyclonal	1:2,000 1:1,000	Millipore
H3K9me3	Rabbit polyclonal	1:800 1:800	Millipore
H3K27ac	Rabbit polyclonal	1:1,000 1:1,000	Millipore
H3K27me3	Rabbit polyclonal	1:800 1:800	Millipore
H3K79me2	Rabbit polyclonal	1:800 1:800	Abcam
H3-T3ph	Rabbit polyclonal	1:1,000 -	Millipore
Histone H3	Rabbit polyclonal	1:1,000 -	Cell Signaling Technologies

H4K16ac	Rabbit monoclonal	1:500 1:1,000	Abcam
H4K20me2	Rabbit polyclonal	1:800 1:800	Cell Signaling Technologies
HA.11 Tag	Mouse monoclonal	1:1,000 -	BioLegend
HA Tag	Rabbit polyclonal	1:1,000 -	Sigma-Aldrich
His Tag	Mouse monoclonal	1:1,000 -	Sigma-Aldrich
Myc Tag	Mouse monoclonal	1:1,000 -	Millipore
Myc Tag	Rabbit polyclonal	1:1,000 -	Millipore
P53-T18ph	Rabbit polyclonal	1:1,000 -	Cell Signaling Technologies
P53	Mouse monoclonal	1:1,000 -	Santa Cruz Biotechnology
PARP-1	Mouse monoclonal	1:1,000 -	Santa Cruz Biotechnology
Phosphoserine	Mouse monoclonal	1:200 -	Millipore
V5 Tag	Mouse monoclonal	1:1,000 -	Sigma-Aldrich
V5 Tag	Rabbit polyclonal	1:1,000 -	Sigma-Aldrich
VRK1	Mouse monoclonal	1:1000 -	In-house production
VRK1	Rabbit polyclonal	1:1000 -	In-house production

Table 6. Secondary antibodies

Antibody	Fluorophore	Use dilution	Supplier
Cy™2-Goat Anti-Rabbit	Cy2 (Green)	IF 1:1,000	Jackson ImmunoResearch
Cy™3-Goat Anti-Mouse	Cy3 (Red)	IF 1:1,000	Jackson ImmunoResearch
Cy™5-Goat Anti-Mouse	Cy5 (Far Red)	IF 1:1,000	Jackson ImmunoResearch
Goat anti-Mouse IgG	DyLight 680 (Red)	WB 1:10,000	Thermo Fisher Scientific
Goat anti-Rabbit IgG	DyLight 800 (Green)	WB 1:10,000	Thermo Fisher Scientific
Goat ECL Anti-Rabbit IgG, Peroxidase Conjugated	Goat ECL Anti-Rabbit IgG, Peroxidase Conjugated	WB 1:10,000	Sigma-Aldrich
Sheep ECL Anti-Mouse IgG, Peroxidase Conjugated	Sheep ECL Anti-Mouse IgG, Peroxidase Conjugated	WB 1:10,000	Amersham Biosciences

Table 7. Cell lines

Cell Line	Specie	Culture properties	Cell type
A549	Human	Adherent	Lung adenocarcinoma
HEK-293T	Human	Adherent	Embryonic kidney
U2OS	Human	Adherent	Bone osteosarcoma

Table 8. SiRNAs

RNA	Sequence 5'→ 3'	Use
siC (ON-TARGET plus SiControl Non-targeting SiRNA)	UGGUUUACAUGUCGACUAA	RNA interference without target
siV-02	CAAGGAACCUGGUGUUGAA	RNA interference against VRK1
siV-03	GGAAUGGAAAGUAGGAUUA	RNA interference against VRK1

Results

4 Results

4.1 Implication of human kinase VRK1 in histone PTMs regulation

As previously described, histone PTMs are critical for chromatin remodeling. To further investigate the role of VRK1 in the histone PTM balance, several histone epigenetic modifications were analyzed in presence or absence of VRK1.

We used two different human tumor cell lines with high levels of VRK1 expression (checked in the Gene Expression Atlas): lung adenocarcinoma (A549) and osteosarcoma (U2OS). To study the effect of VRK1 absence, we depleted VRK1 during 72 h by using two different siRNAs (siV-02 and siV-03). We examined VRK1 absence effect by IF and WB of acidic protein extracts. Maintaining consistent cell growth conditions is often very difficult in FBS-containing media and can lead to inconsistent results during bioassays[162]. Thus, serum is often eliminated from the media to remove growth factors and reduce possible interferences, thus providing more reproducible experimental conditions. However, VRK1 activity is considerably reduced when mitogenic signals from media are removed[124]. For this reason, to reduce experimental variations and determine if mitogenic signals have some effect on the VRK1 catalytic activity on these periods of time, cells were cultured with 10% (serum-completed) or 0.5% (serum-reduced) media for 48 h.

Furthermore, we tested the effect of several epigenetic inhibitors to determine whether VRK1 depletion had the same outcome on histone

PTMs and consequently, to unveil which epigenetic enzymes may be affected by VRK1.

4.1.1 VRK1 promotes an open chromatin state, boosting H4K16ac

4.1.1.1 VRK1 depletion prevents H4K16ac

As previously stated, the initial response to DNA damage implicates a local chromatin relaxation that is associated with histone H4 acetylation in K16. TIP60 is the HAT responsible for this histone PTM and VRK1 directly interacts and activates TIP60 through its phosphorylation after DNA damage induction, so VRK1 is one of the main proteins responsible for chromatin relaxation[32].

For this reason, we first studied the effect of VRK1 on H4K16ac. We assessed the impact of VRK1 depletion on A549 and U2OS cells by using two siRNA (siV-02 and siV-03). The reduction of VRK1 expression caused a loss of acetylated H4K16 levels as compared with siC samples (**Figure 10** and **Figure 11**). To ensure this result, we measured H4K16ac levels by two different methods, IF and WB. In conclusion, all the results indicate that VRK1 knock-down causes a decrease of H4K16ac levels.

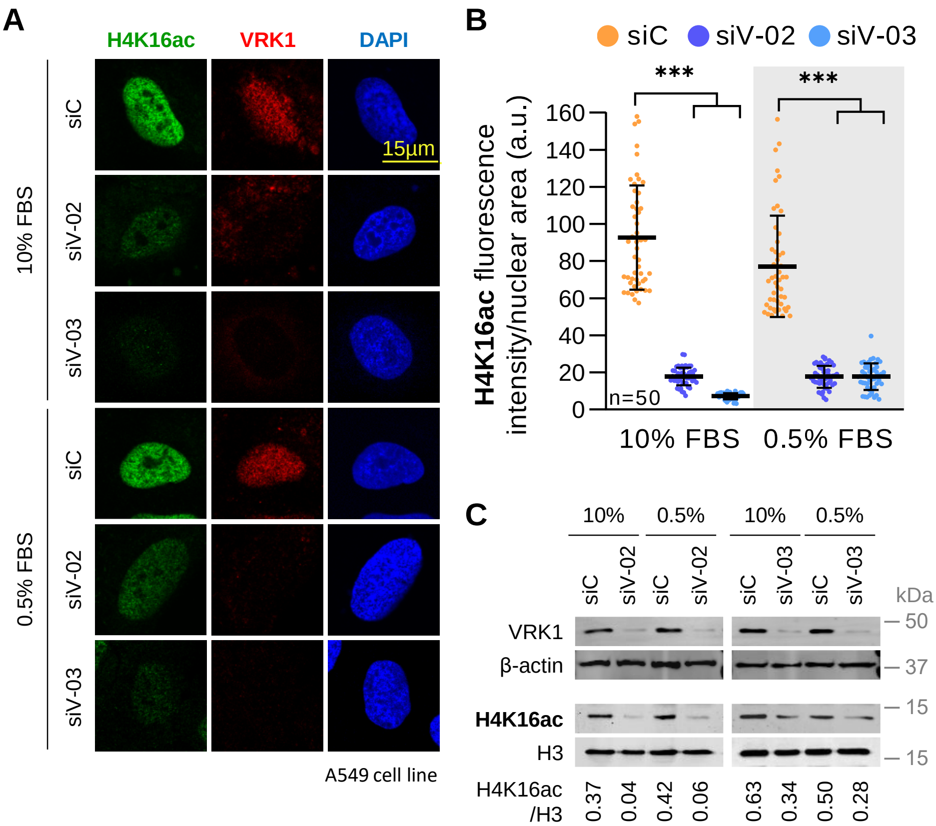

Figure 10. VRK1 depletion causes a reduction of H4K16 acetylation in A549 cells. VRK1 was depleted using two siRNAs (siV-02 and siV-03) for 72 h. siC was used as off-target siRNA. Cells were cultured with 10% or 0.5% of FBS for 48 h. **A.** Panels show IF images of H4K16ac levels detected using confocal microscopy. DAPI was used to stain the nuclei and VRK1 as knock-down control. **B.** Quantification of H4K16ac fluorescence intensity per nuclear area (a.u.) of 50 cells (per condition). **C.** WB shows H4K16ac levels of histone acidic extracts. VRK1, β-actin and histone H3 were used as knock-down and loading control, respectively. H4K16ac/H3 ratio is shown. Scale bar = 15 µm. ***: $p < 0.001$. a.u.: arbitrary units.

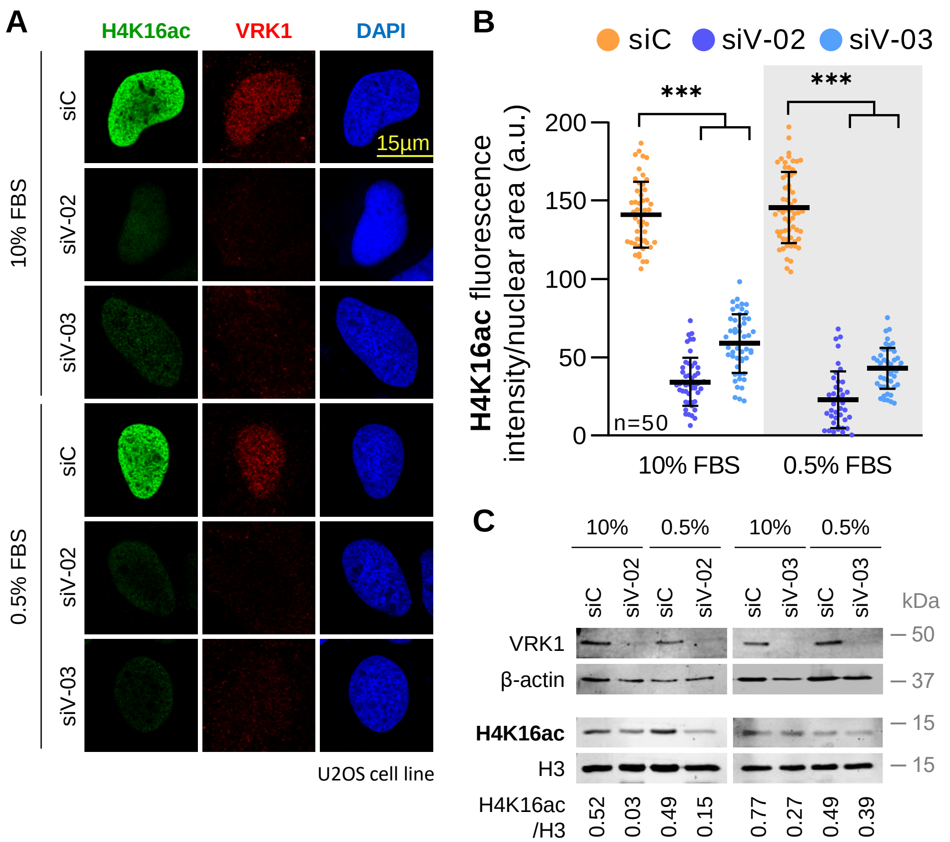

Figure 11. VRK1 knock-down prevents the H4K16 acetylation in U2OS cells. VRK1 was knocked down using two siRNA (siV-02 and siV-03) for 72 h. siC was used as off-target siRNA. Completed-serum (10% FBS) and reduced-serum (0.5% FBS) conditions were performed for 48 h. **A.** Panels show IF images of H4K16ac levels detected using confocal microscopy. DAPI was used to stain the nuclei and VRK1 as knock-down control. **B.** Quantification of H4K16ac fluorescence intensity per nuclear area (a.u.) of 50 cells (per condition). **C.** WB shows H4K16ac levels of histone acidic extracts. VRK1, β-actin and histone H3 were used as knock-down and loading control, respectively. H4K16ac/H3 ratio is shown. Scale bar = 15 µm. ***: $p < 0.001$. a.u.: arbitrary units.

4.1.1.2 **The HAT inhibitor MG149 impairs H4K16ac**

After we confirmed that VRK1 alters H4K16 acetylation, our aim was to explore the role of different treatments that target the enzymes that control this PTM. H4K16ac is regulated by the balance of HATs and HDACs. However, the way by which these two types of histone-modifying enzymes and their coordination are regulated is unknown. One potential mechanism is that TIP60 and SIRT1/2 control H4K16 acetylation and are coordinated by members of other enzyme families, such as kinases (**Figure 12**). Our laboratory previously demonstrated that VRK1 activates TIP60 after DNA damage induction[32]. For this reason, our next step was to check if the TIP60 inhibitor MG149 changes the basal pattern of H4K16 acetylation.

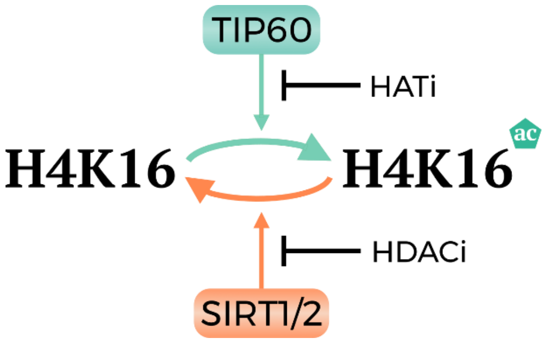

Figure 12. Regulation of H4K16 acetylation. Scheme of the main regulation of the acetylation of the histone H4 residue 16 by TIP60 and SIRT1 or 2. Blue and orange arrows promote an acetylated and a deacetylated state, respectively. Black lines indicate the steps that HATi and HDACi block. Blue pentagon (ac): acetylation.

We analyzed H4K16 acetylation after treating cells with 1 µM MG149 for 24 h. We measured the levels of this modification by IF and WB in both above mentioned cell lines, A549 and U2OS. The treatment with MG149 caused a decrease in H4K16ac levels compared with the non-treated cells, both in A549 (**Figure 13**) and in U2OS (**Figure 14**) cells detected by IF. However, this decrease was only detectable by WB in A549 cells. MG149 treatment inactivated TIP60, confirming this histone-modifying enzyme to be responsible for H4K16 acetylation. Furthermore, H4K16ac levels measurement reveal that the absence of VRK1 mimics the effect of TIP60 inhibition through MG149 treatment in A549 and U2OS cells, suggesting that VRK1 may be involved in TIP60 activity.

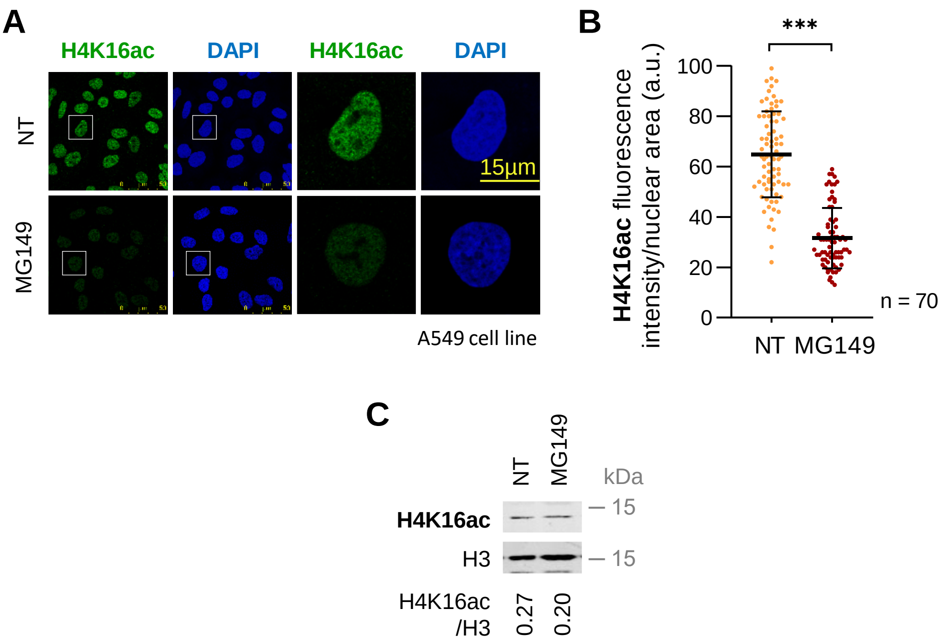

Figure 13. MG149 impairs H4K16 acetylation in A549 cells. Serum-deprived (0.5% FBS for 48 h) cells were treated with 1 μM MG149 for 24 h. **A.** Image panels show H4K16ac levels stained by IF and detected using confocal microscopy. DAPI was used to stain the nuclei. **B.** Dot plot represents quantification of H4K16ac fluorescence intensity per nuclear area (a.u.) of 70 cells (per condition). **C.** WB shows H4K16ac levels of histone acidic extracts. Histone H3 was used as loading control. H4K16ac/H3 ratio is shown. NT: Non-treated. Scale bar = 15 μm. ***: $p < 0.001$. a.u.: arbitrary units.

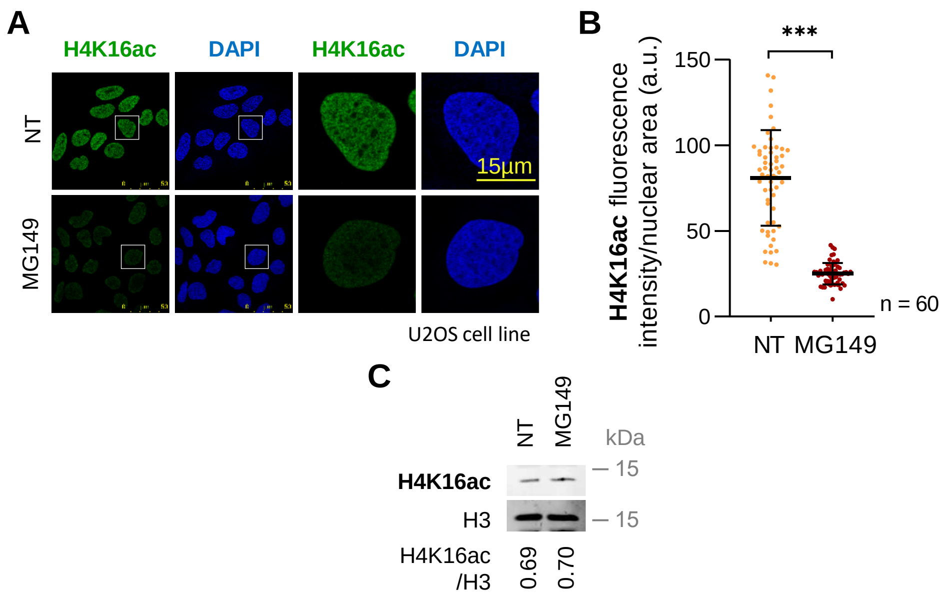

Figure 14. MG149 prevents H4K16 acetylation in U2OS cells. Serum-deprived (0.5% FBS for 48 h) cells were treated with 1 μM MG149 for 24 h. **A.** Panels show IF images of the levels of H4K16ac detected using confocal microscopy. DAPI was used to stain the nuclei and VRK1

as knock-down control. **B.** Quantification of H4K16ac fluorescence intensity per nuclear area (a.u.) of 50 cells (per condition). **C.** WB shows H4K16ac levels of histone acidic extracts. Histone H3 was used as loading control. H4K16ac/H3 ratio is shown. NT: Non-treated. Scale bar = 15 µm. ***: $p < 0.001$. a.u.: arbitrary units.

4.1.1.3 The HDAC inhibitors thiomyristoyl, AGK2, AK7, and selisistat boost H4K16ac levels

H4K16 deacetylation is carried out by some members of HDAC family, and SIRT1 and SIRT2 have been described as two suitable enzymes for this role (**Figure 12**)[34]. Thereby, we studied the effect of SIRT1 (selisistat) and SIRT2 (thiomyristoyl or TM, AGK2, AK7) inhibitors on H4K16 acetylation levels[163].

We evaluated H4K16 acetylation after treating cells with 50 nM selisistat, 5 µM TM, 5 µM AGK2 and 8 µM AK7 for 24 h. This histone mark was detected by IF and WB in both cell lines. A549 cells responded with an increase of H4K16 acetylation levels when cells were treated with SIRT1 (**Figure 15**) and SIRT2 (**Figure 16**) inhibitors as compared with non-treated cells. Likewise, U2OS cells displayed a strong increase of H4K16ac when they were treated with the SIRT2 inhibitors (**Figure 17**) detected by IF.

Altogether, these data indicate that VRK1 absence alters H4K16ac landscape similar to TIP60 inhibition and opposite to SIRT1 and SIRT2 inhibition, possibly modulating the activity of these epigenetic enzymes.

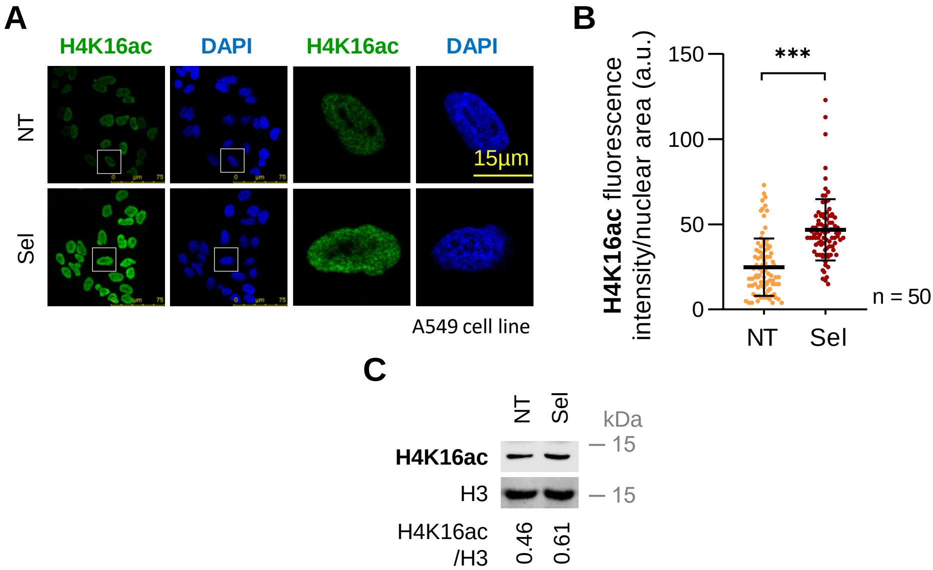

Figure 15. Selisistat enhances H4K16 acetylation in A549 cells. Cells were cultured with 0.5% FBS for 48 h and treated with 50 nM selisistat (Sel) for 24 h. NT: Non-treated. **A.** Image panels show acetylation of H4K16 levels stained by IF and detected using confocal microscopy. DAPI was used to stain the nuclei. **B.** H4K16ac fluorescence intensity per nuclear area (a.u.) quantification of 50 cells (per condition) is represented in a dot plot. **C.** WB represents the levels of H4K16ac of histone acidic extracts. Histone H3 was used as loading control. H4K16ac/H3 ratio is shown. Scale bar = 15 µm. ***: $p < 0.001$. a.u.: arbitrary units.

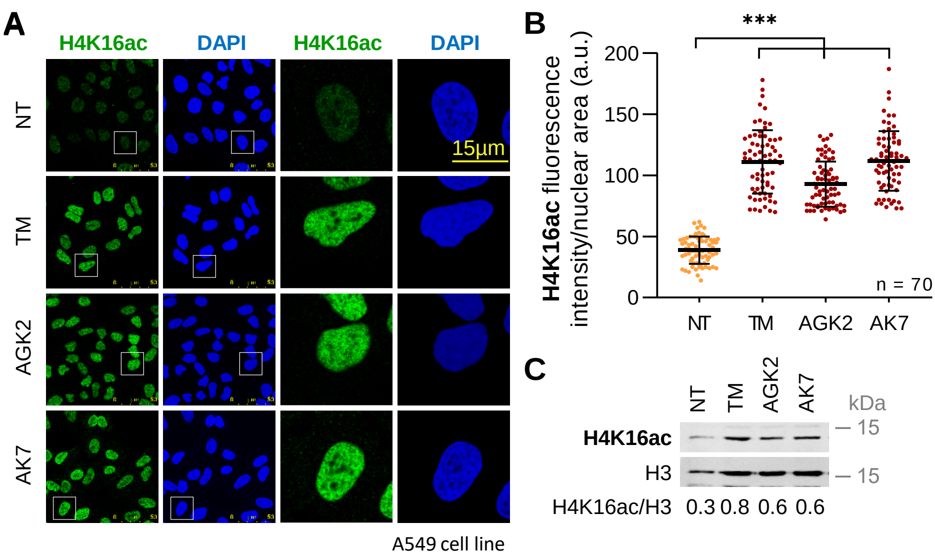

Figure 16. SIRT2 inhibitors enhance H4K16 acetylation in A549 cells. Cells were cultured with 0.5% FBS for 48 h and treated with 5 µM thiomyristoyl (TM), 5 µM AGK2 and 8 µM AK7 for 24 h. **A.** Image panels show acetylation of H4K16 levels stained by IF and detected using confocal microscopy. DAPI was used to stain the nuclei. **B.** H4K16ac fluorescence intensity per nuclear area (a.u.) quantification of 70 cells (per condition) is represented in a dot plot. **C.** WB shows H4K16ac levels of histone acidic extracts. Histone H3 was used as loading control.

H4K16ac/H3 ratio is shown. NT: Non-treated; TM: Thiomyristoyl. Scale bar = 15 μm. ***: p < 0.001. a.u.: arbitrary units.

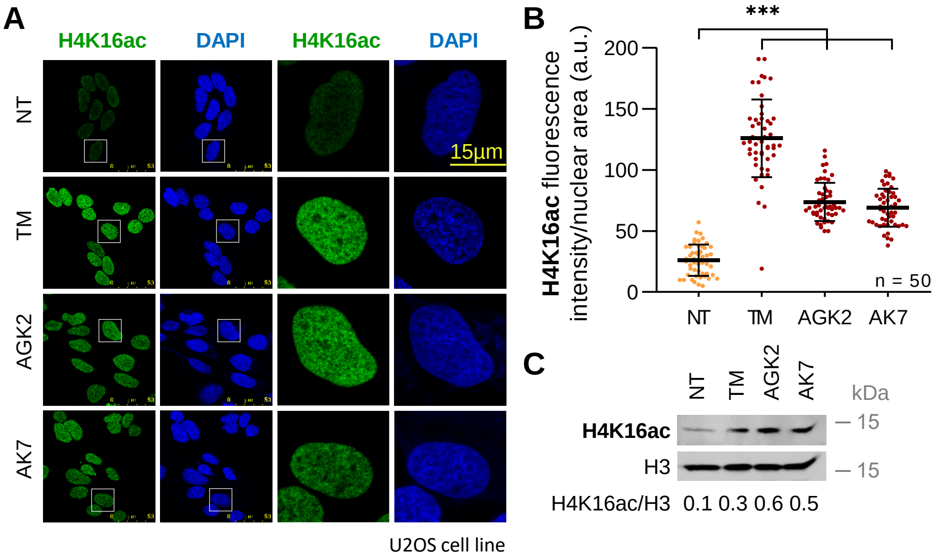

Figure 17. SIRT2 inhibitors promote H4K16 acetylation in U2OS cells. Cells were cultured with 0.5% FBS for 48 h and treated with 5 μM thiomyristoyl, 5 μM AGK2 and 8 μM AK7 for 24 h. **A.** Image panels show acetylation of H4K16 levels stained by IF and detected using confocal microscopy. DAPI was used to stain the nuclei. **B.** H4K16ac fluorescence intensity per nuclear area (a.u.) quantification of 70 cells (per condition) is represented in a dot plot. **C.** WB represents the levels of H4K16ac of histone acidic extracts. Histone H3 was used as loading control. H4K16ac/H3 ratio is shown. NT: Non-treated; TM: Thiomyristoyl. Scale bar = 15 μm. ***: p < 0.001. a.u.: arbitrary units.

4.1.1.4 **SIRT2 inhibition combined with doxorubicin facilitates H4K16ac**

It was previously reported that VRK1 is one of the responsible proteins for chromatin relaxation after DNA damage induction by doxorubicin, an DNA-intercalating agent[32]. Therefore, we aimed at determining the combinatory effect of doxorubicin and SIRT2 inhibitors, TM, AGK2 and AK7. Firstly, we corroborated that doxorubicin treatment caused an increase on H4K16ac (**Figure 18**). Then, when doxorubicin was combined with any of the three SIRT2 inhibitors, it resulted in a higher accumulation of this histone mark because of the inhibition of SIRT2 deacetylase activity (**Figure 18**), which persisted even when VRK1 was depleted (**Figure 19**). The increase in H4K16ac in response to doxorubicin treatment was impaired by either the inhibition of TIP60 by MG149 or by VRK1 depletion, which prevents TIP60 activation (**Figure 19**). Thus, the three SIRT2 inhibitors (TM, AGK2, AK7) cause a strong increase in H4K16ac, which are even higher than those of doxorubicin treatment by itself.

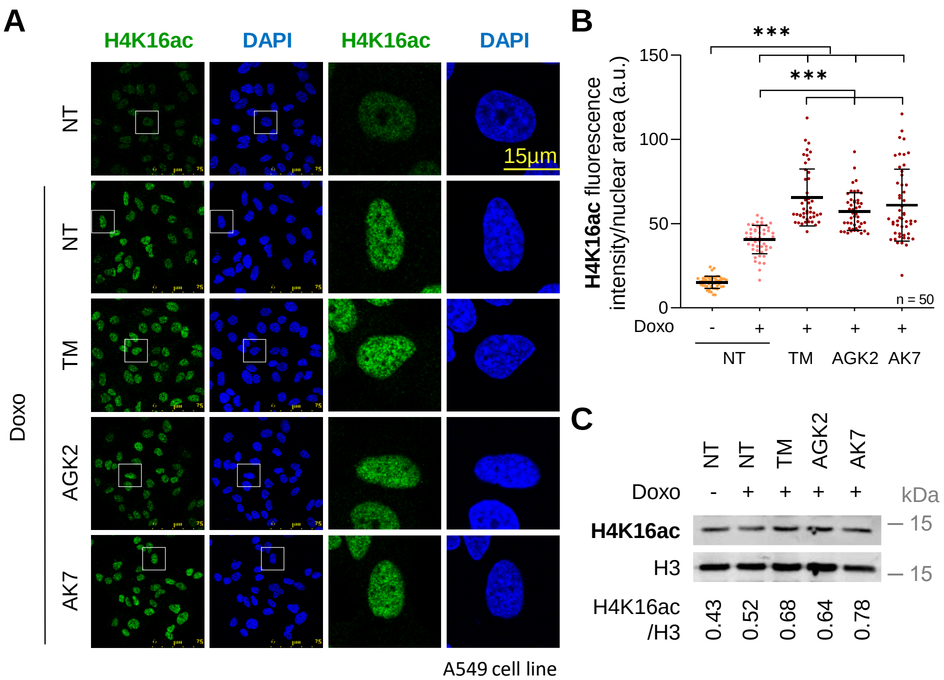

Figure 18. SIRT2 inhibitors promote H4K16ac after DNA damage induction with doxorubicin. A549 cells were cultured with 0.5% FBS for 48 h and treated with 5 µM thiomyristoyl (TM), 5 µM AGK2 and 8 µM AK7 for 24 h. Then, DNA damage was induced with 3 µM doxorubicin for 2 h. **A.** Image panels show acetylation of H4K16 levels stained by IF and detected using confocal microscopy. DAPI was used to stain the nuclei. **B.** H4K16ac fluorescence intensity per nuclear area (a.u.) quantification of 50 cells (per condition) is represented in a dot plot. **C.** WB shows H4K16ac levels of histone acidic extracts. Histone H3 was used as loading control. H4K16ac/H3 ratio is shown. NT: Non-treated, Doxo: Doxorubicin. Scale bar = 15 µm. ***: $p < 0.001$. a.u.: arbitrary units.

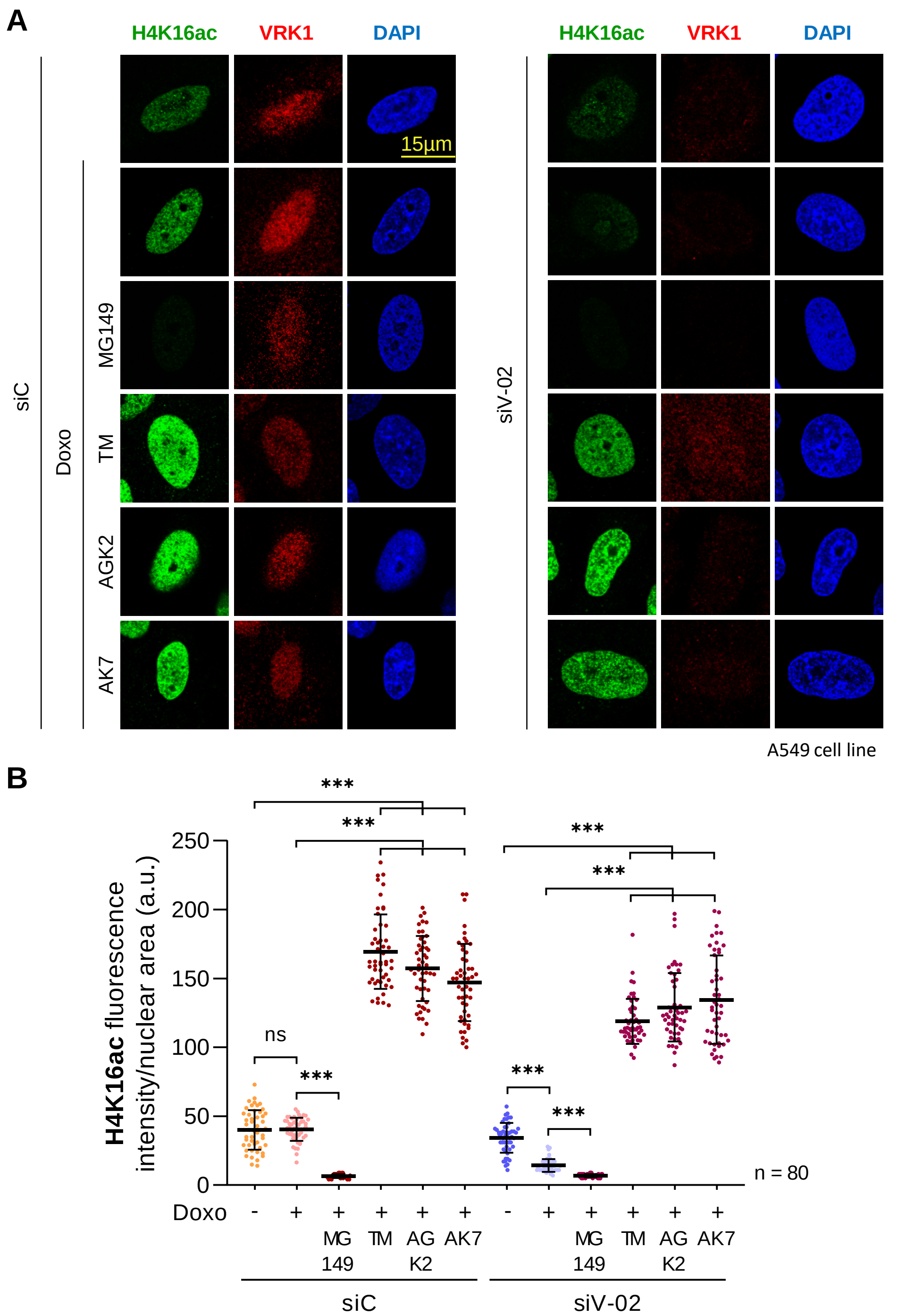

Figure 19. SIRT2 inhibitors promote H4K16ac after DNA damage induction with doxorubicin, while MG149 impairs this acetylation. A549 cells were cultured with 0.5% FBS for 48 h and treated with 1 µM MG149, 5 µM thiomyristoyl (TM), 5 µM AGK2 and 8 µM AK7 for 24 h. Then, DNA damage was induced with 3 µM doxorubicin for 2 h. **A.** Image panels show acetylation of H4K16 levels stained by IF and detected using confocal microscopy. DAPI was used to stain the nuclei. **B.** H4K16ac fluorescence intensity per nuclear area (a.u.)

quantification of 80 cells (per condition) is represented in a dot plot. NT: Non-treated, Doxo: Doxorubicin. Scale bar = 15 μm. *** = $p < 0.001$; n.s = non-significant. a.u.: arbitrary units.

4.1.2 VRK1 facilitates an open chromatin state, promoting H3K4me3

4.1.2.1 VRK1 depletion impairs H3K4me3

To evaluate VRK1 effect on histone H3 PTMs pattern, we first evaluated H3K4 trimethylation. This histone PTM is associated with chromatin relaxation and is mostly located at promoters[38]. For this reason, we studied how the presence or absence of VRK1 could alter this mark.

To test H3K4me3 levels, endogenous human VRK1 was depleted using two different siRNA (siV-02 and siV-03) in A549 and U2OS cell lines. Then, cells were cultured with or without serum to confirm the impact of mitogenic signal on VRK1 activity. Finally, H3K4me3 levels were detected by WB of isolated histones from histone acidic extracts and IF. A549 cells showed a significant decrease on H3K4me3 when VRK1 was knocked-down in both completed- and reduced-serum conditions compared with siC by IF, but we were not able to detect these differences by WB (**Figure 20**). The effect of VRK1 depletion on the loss of H3K4me3 level was also confirmed in the U2OS cell line (**Figure 21**). Briefly, VRK1 depletion produces a drastic reduction of this histone mark related to open chromatin and promoters.

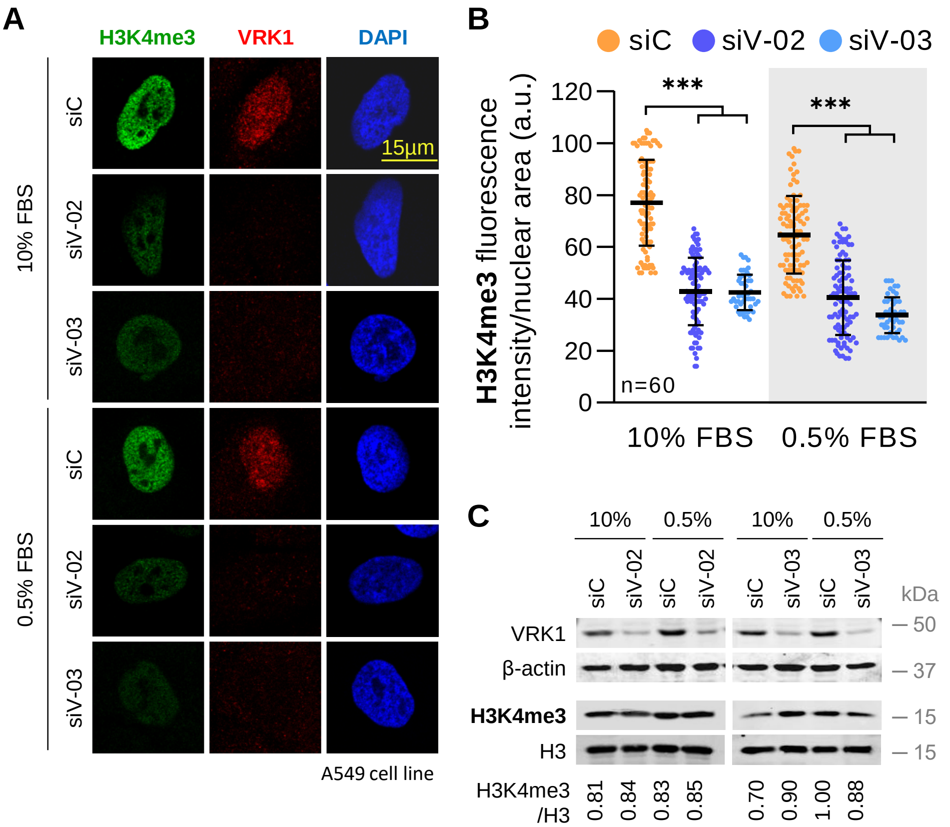

Figure 20. VRK1 knock-down impairs the trimethylation of H3K4 in A549 cells. VRK1 was depleted using two siRNAs (siV-02 and siV-03) for 72 h. siC was used as off-target siRNA. Cells were cultured with 10% or 0.5% of FBS for 48 h. **A.** Image panels show trimethylation of H3K4 and VRK1 levels stained by IF and detected using confocal microscopy. DAPI was used to stain the nuclei. **B.** Quantification of H3K4me3 fluorescence intensity per nuclear area (a.u.) of 60 cells (per condition). **C.** WB represents H3K4me3 levels of histone acidic extracts. VRK1, β-actin and histone H3 were used as knock-down and loading control, respectively. H3K4me3/H3 ratio is shown. Scale bar = 15 µm. ***: $p < 0.001$. a.u.: arbitrary units.

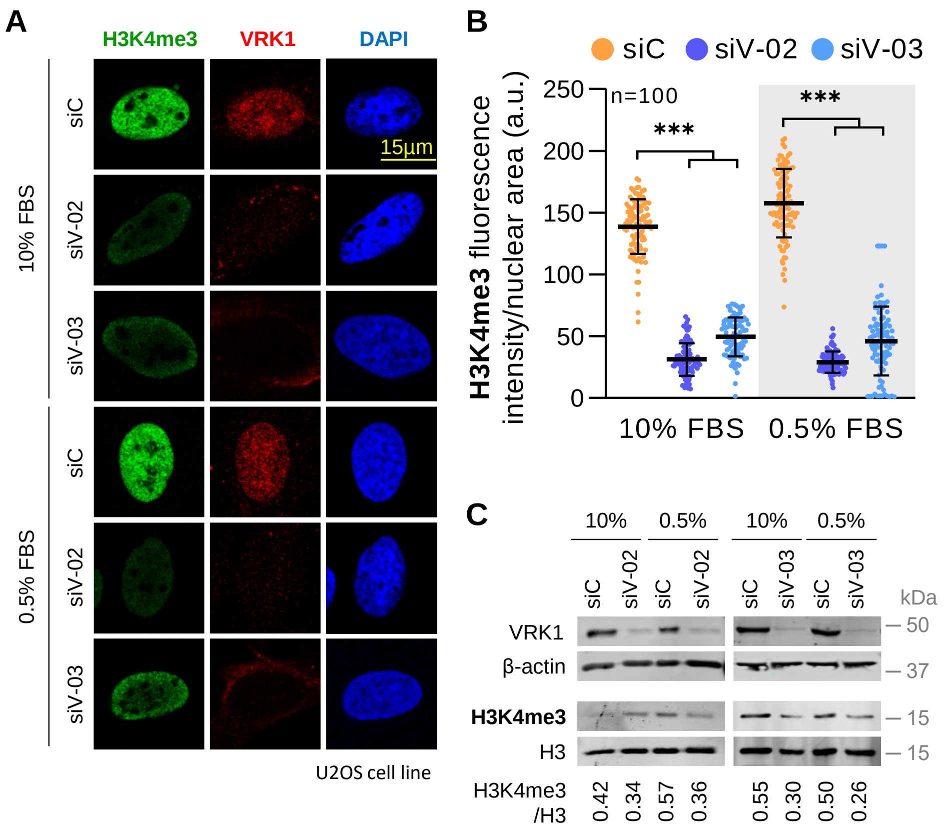

Figure 21. VRK1 depletion causes a reduction of H3K4 trimethylation in U2OS cells. VRK1 was knocked down using two siRNA (siV-02 and siV-03) for 72 h. siC was used as off-target siRNA. Completed-serum (10% FBS) and reduced-serum (0.5% FBS) conditions were performed for 48 h. **A.** Panels show IF images of the levels of H3K4me3 detected using confocal microscopy. DAPI was used to stain the nuclei and VRK1 as knock-down control. **B.** H3K4me3 fluorescence intensity per nuclear area (a.u.) quantification of 100 cells (per condition) is represented in a dot plot. **C.** WB shows H3K4me3 levels of histone acidic extracts. VRK1, β-actin and histone H3 were used as knock-down and loading control, respectively. H3K4me3/H3 ratio is shown. Scale bar = 15 µm. ***: $p < 0.001$. a.u.: arbitrary units.

4.1.2.2 The KMT inhibitor tazemetostat impairs H3K4me3

H3K4me3 is regulated by the balance of KMTs and KDMs (**Figure 22**). However, the coordination of these two enzymes is unknown. Therefore, to further characterize H3K4 trimethylation, we evaluated this modification after treating the cells with a KMT inhibitor. In this case, tazemetostat, a drug that blocks the activity of the methyltransferase EZH2, was used[102].

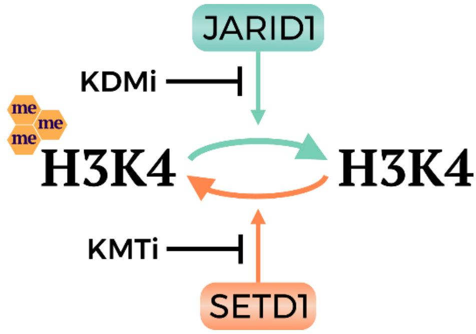

Figure 22. Regulation of H3K4 methylation. Scheme of the possible regulation of the trimethylation of the histone H3 residue 4 by SETD1 and JARID1. Blue and orange arrows promote a demethylated and a trimethylated state respectively. Black lines indicate the steps that KMTi and KDMi block. Yellow hexagon (me): methylation.

After incubating A549 cells with 50 nM of tazemetostat for 24 h, we observed by WB and IF a significant drop of H3K4me3 levels compared with non-treated cells (**Figure 23**), which mimics the absence of VRK1. In the same way, we confirmed this reduction in H3K4me3 levels in the U2OS cell line (**Figure 24**).

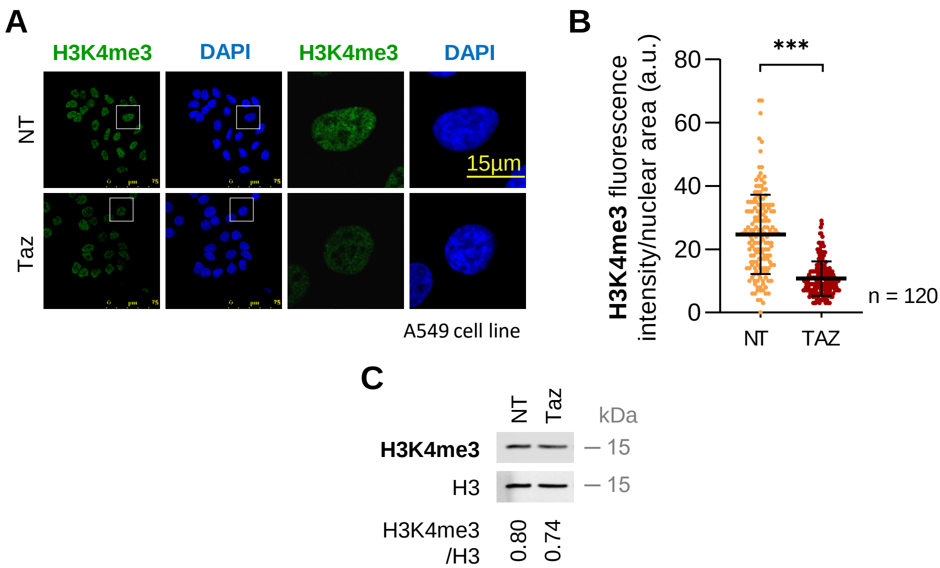

Figure 23. Tazemetostat produces a drop of H3K4me3 levels in A549 cells. Serum-reduced (0.5% FBS for 48 h) cells were treated with 50 nM tazemetostat for 24 h. **A.** Image panels show trimethylated H3K4 levels detected by immunofluorescence. DAPI was used to stain the nuclei. **B.** Dot plot represents the quantification of H3K4me3 fluorescence per nuclear area (a.u.) of 120 cells (per condition). **C.** H3K4me3 acidic extracts detected by immunoblot. Histone H3 was used as loading control. H3K4me3/H3 ratio is shown. NT: Non-treated; Taz: Tazemetostat. Scale bar = 15 µm. ***: $p < 0.001$. a.u.: arbitrary units.

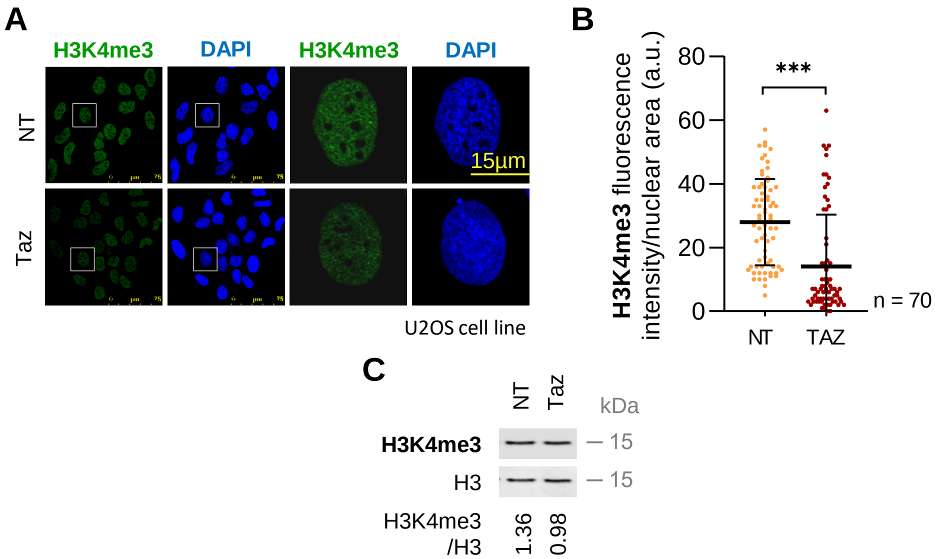

Figure 24. Tazemetostat reduces trimethylated levels of H3K4 in U2OS cells. Cells were cultured with 0.5% FBS for 48 h and treated with 50 nM tazemetostat for 24 h. **A.** Panels show IF images of H3K4me3 levels detected using confocal microscopy. DAPI was used to stain the nuclei. **B.** H3K4me3 fluorescence intensity per nuclear area (a.u.) quantification of 70 cells (per condition) is represented in a dot plot. **C.** H3K4me3 acidic extracts detected by immunoblot. Histone H3 was used as loading control. H3K4me3/H3 ratio is shown. NT: Non-treated; Taz: Tazemetostat. Scale bar = 15 µm. ***: $p < 0.001$. a.u.: arbitrary units.

4.1.2.3 The KDM inhibitor ORY-1001 promotes H3K4me3

On the other hand, we analyzed the H3K4me3 levels after the treatment with the KDM inhibitor iadademstat or ORY-1001, which inhibits LSD1 (**Figure 22**)[164]. Some references describe this enzyme as the regulator of H3K4me demethylation[44].

As we expected due to the inhibition of a KDM, the trimethylation levels of H3K4 increased after treating A549 cells with 50 nM ORY-1001 for 24 h. This ascent was perceived by WB and IF (**Figure 25**). To confirm these results, we measured H3K4me3 in U2OS cells, finding a similar effect (**Figure 26**).

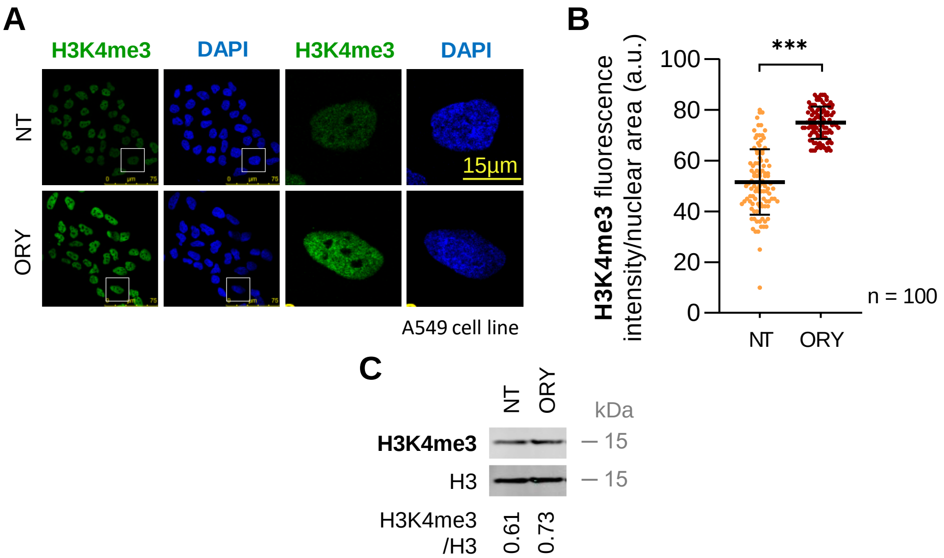

Figure 25. ORY-1001 enhances H3K4 trimethylation in A549 cells. Cells were serum-starved for 48 h and treated with 50 nM ORY-1001 for 24 h. **A.** Image panels show H3K4me3 levels detected by immunofluorescence. DAPI was used to stain the nuclei. **B.** Quantification of H3K4me3 fluorescence per nuclear area (a.u.) of 100 cells (per condition). **C.** WB shows H3K4me3 levels of histone acidic extracts. Histone H3 was used as loading control. H3K4me3/H3 ratio is shown. NT: Non-treated; ORY: ORY-1001. Scale bar = 15 µm. ***: $p < 0.001$. a.u.: arbitrary units.

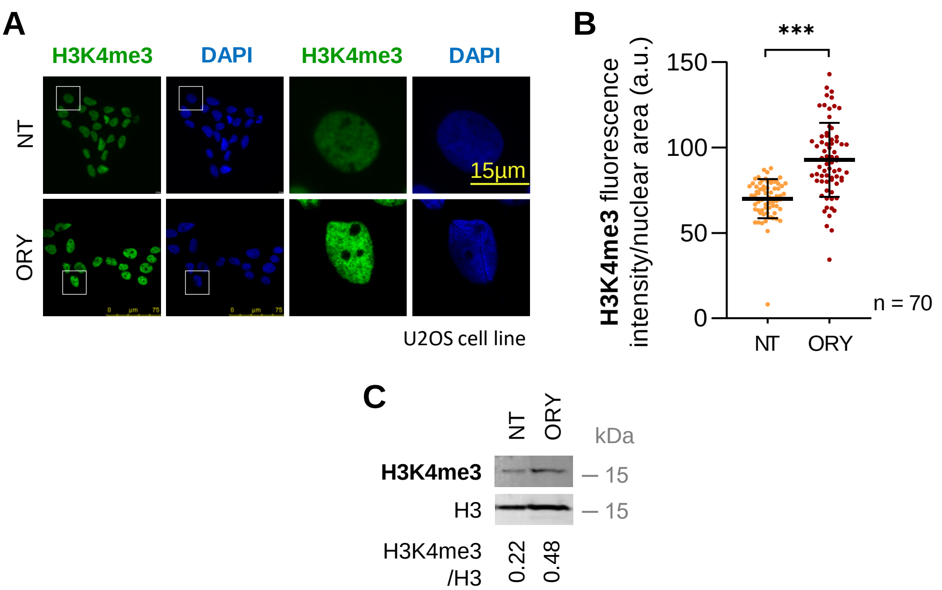

Figure 26. ORY-1001 enhances H3K4 trimethylation in U2OS cells. Serum-reduced (0.5% FBS for 48 h) cells were treated with 50 nM ORY-1001 for 24 h. **A.** Image panels show H3K4me3 levels detected by immunofluorescence. DAPI was used to stain the nuclei. **B.** H3K4me3 fluorescence intensity per nuclear area (a.u.) quantification of 70 cells (per condition) is represented in a dot plot. **C.** WB shows H3K4me3 levels of histone acidic extracts. Histone H3 was used as loading control. H3K4me3/H3 ratio is shown. NT: Non-treated; ORY: ORY-1001. Scale bar = 15 µm. ***: $p < 0.001$. a.u.: arbitrary units.

4.1.3 VRK1 enhances an open chromatin state, facilitating H3K9ac and impairing H3K9me3

4.1.3.1 VRK1 depletion impairs H3K9ac and enhances H3K9me3

Continuing with the study of chromatin remodeling, we evaluated H3K9 acetylation and trimethylation, two mutually exclusive histone PTMs, which favor relaxed and open or repressive and closed chromatin, respectively[12,14].

For this aim, we depleted endogenous human VRK1 in A549 and U2OS cells using two different siRNAs (siV-02 and siV-03) to analyze its impact and removed the serum from the media to evaluate its possible consequences on VRK1 activity. Then, H3K9 acetylation and trimethylation were detected by WB and IF. We observed a drop on the acetylation levels of H3K9 when VRK1 expression was silenced, both in serum-completed and serum-reduced media conditions in both A549 (**Figure 27**) and U2OS cell lines (**Figure 28**). On the contrary, H3K9 trimethylation, the opposite mark of this residue, suffered a significant increase when VRK1 was depleted in A549 (**Figure 29**) and U2OS (**Figure 30**) cells independently of the serum levels. In conclusion, VRK1 down expression causes a decrease in the acetylation and an increment on the trimethylation of H3K9 levels.

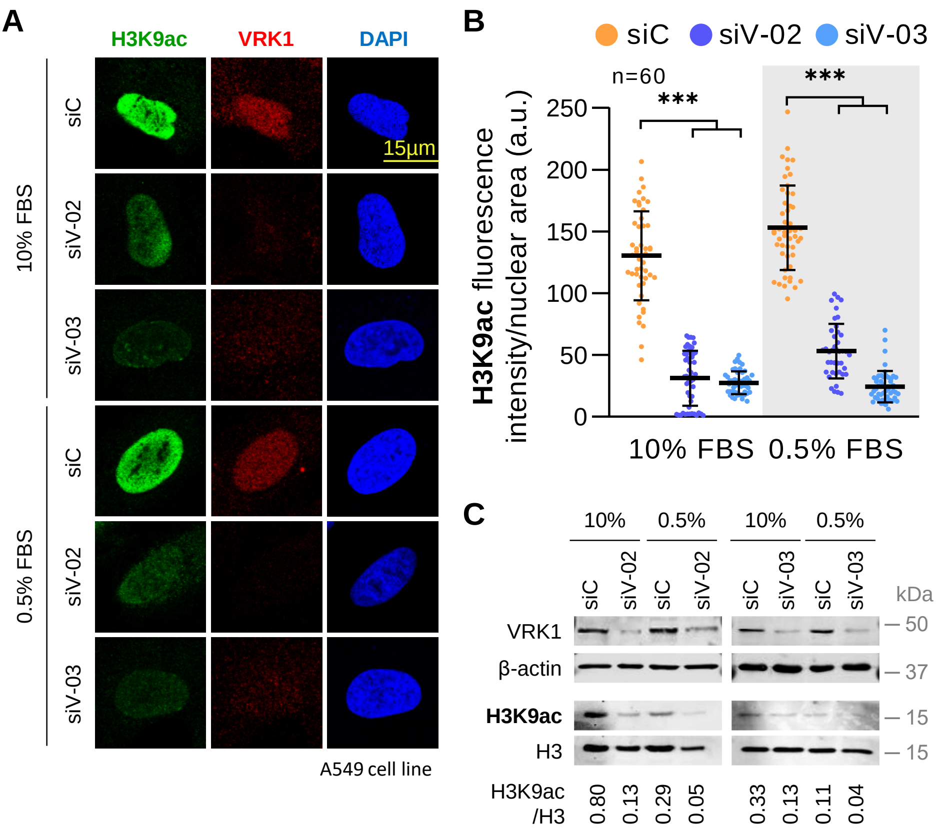

Figure 27. VRK1 depletion impairs H3K9 acetylation in A549 cells. VRK1 was depleted using two siRNAs (siV-02 and siV-03) for 72 h. siC was used as off-target siRNA. Cells were cultured with 10% or 0.5% of FBS for 48 h. A. Panels show IF images of the levels of H3K9ac detected using confocal microscopy. DAPI was used to stain the nuclei and VRK1 as knock-down control. B. Quantification of H3K9ac fluorescence intensity per nuclear area (a.u.) of 50 cells (per condition). C. WB shows H3K9ac levels of histone acidic extracts. VRK1, β-actin and histone H3 were used as knock-down and loading control, respectively. H3K9ac/H3 ratio is shown. Scale bar = 15 µm. ***: $p < 0.001$. a.u.: arbitrary units.

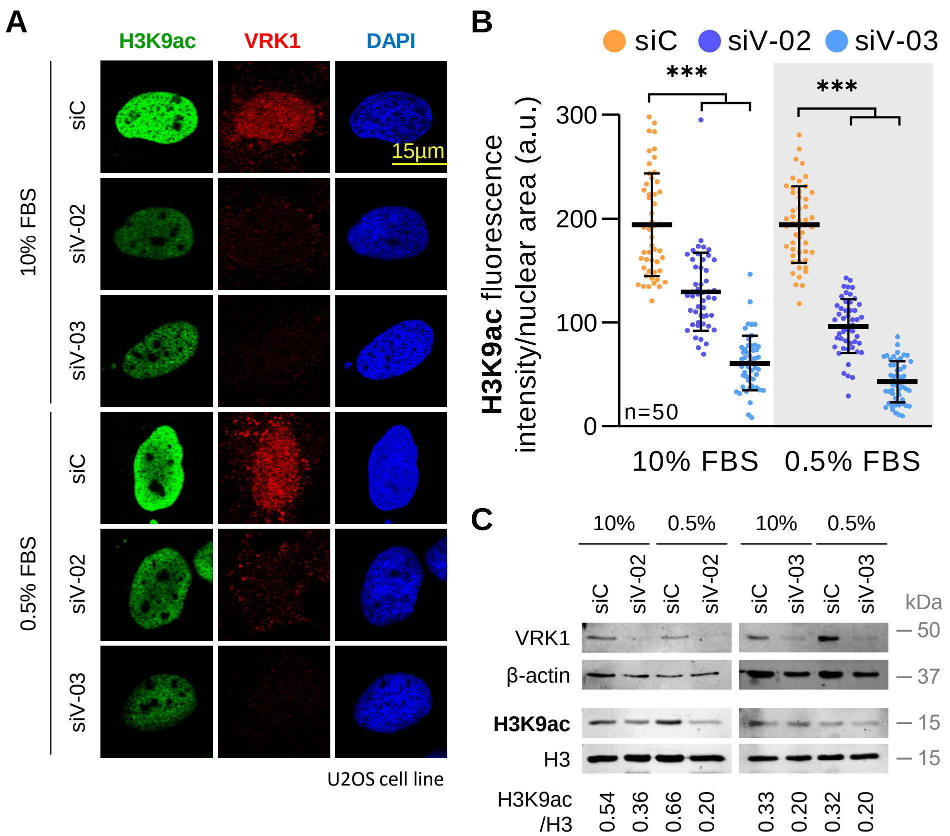

Figure 28. VRK1 depletion prevents H3K9 acetylation in U2OS cells. VRK1 was knocked down using two siRNA (siV-02 and siV-03) for 72 h. siC was used as off-target siRNA. Completed-serum (10% FBS) and reduced-serum (0.5% FBS) conditions were performed for 48 h. **A.** Image panels show acetylation of H3K9 and VRK1 levels stained by IF and detected using confocal microscopy. DAPI was used to stain the nuclei. **B.** H3K9ac fluorescence intensity per nuclear area (a.u.) quantification of 50 cells (per condition) is represented in a dot plot. **C.** WB represents H3K9ac levels of histone acidic extracts. VRK1, β-actin and histone H3 were used as knock-down and loading control, respectively. H3K9ac/H3 ratio is shown. Scale bar = 15 µm. ***: $p < 0.001$. a.u.: arbitrary units.

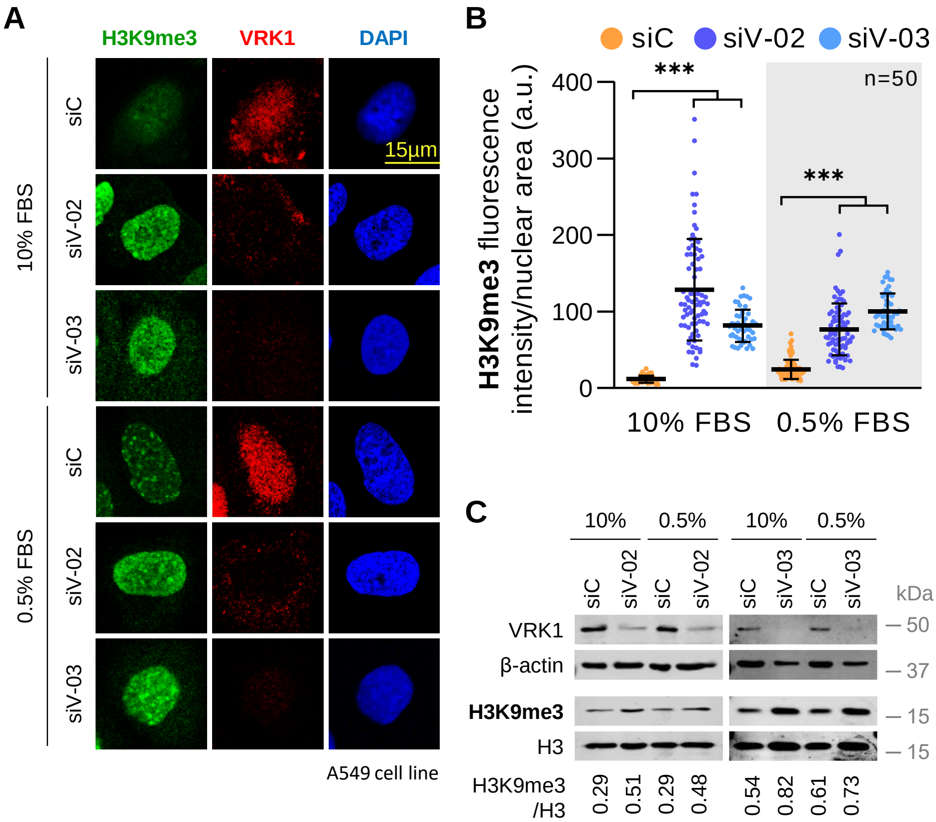

Figure 29. VRK1 depletion causes an increment of H3K9 trimethylation in A549 cells. VRK1 was depleted using two siRNAs (siV-02 and siV-03) for 72 h. siC was used as off-target siRNA. Cells were cultured with 10% or 0.5% of FBS for 48 h. **A.** Image panels show trimethylation of H3K9 and VRK1 levels stained by IF and detected using confocal microscopy. DAPI was used to stain the nuclei. **B.** H3K9me3 fluorescence intensity per nuclear area (a.u.) quantification of 50 cells (per condition) is represented in a dot plot. **C.** WB shows H3K9me3 levels of histone acidic extracts. VRK1, β-actin and histone H3 were used as knock-down and loading control, respectively. H3K9me3/H3 ratio is shown. Scale bar = 15 µm. ***: $p < 0.001$. a.u.: arbitrary units.

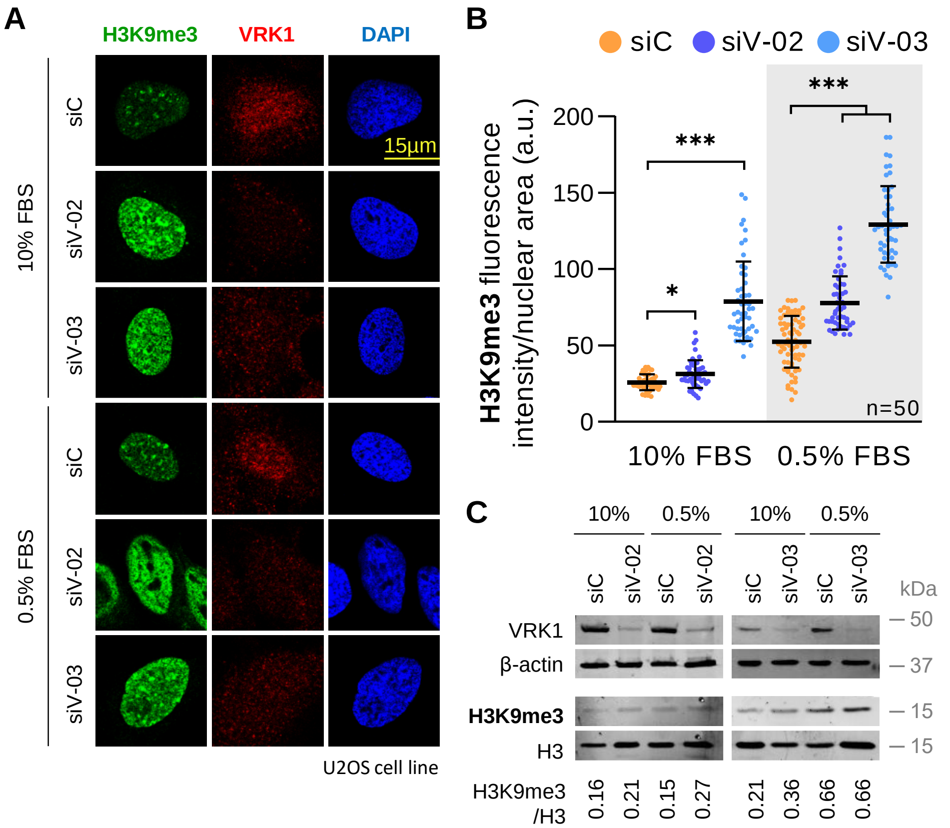

Figure 30. VRK1 knock-down promotes H3K9 trimethylation in U2OS cells. VRK1 was knocked down using two siRNA (siV-02 and siV-03) for 72 h. siC was used as off-target siRNA. Completed-serum (10% FBS) and reduced-serum (0.5% FBS) conditions were performed for 48 h. **A.** Panels show IF images of the levels of H3K9me3 detected using confocal microscopy. DAPI was used to stain the nuclei and VRK1 as knock-down control. **B.** Quantification of H3K9me3 fluorescence intensity per nuclear area (a.u.) of 50 cells (per condition). **C.** WB represents H3K9me3 levels of histone acidic extracts. VRK1, β-actin and histone H3 were used as knock-down and loading control, respectively. H3K9me3/H3 ratio is shown. Scale bar = 15 µm. *** = $p < 0.001$; *: $p < 0.05$. a.u.: arbitrary units.

4.1.3.2 The HDAC inhibitors SAHA, entinostat, panobinostat, and selisistat enhance H3K9ac and impair H3K9me3

As it has been described, H3K9 can be acetylated and methylated, which is regulated by different epigenetic enzymes. The balance between de- and acetylation is controlled by HDAC and HAT enzymes, while de- and methylation are regulated by KMTs and KDMs (**Figure 31**).

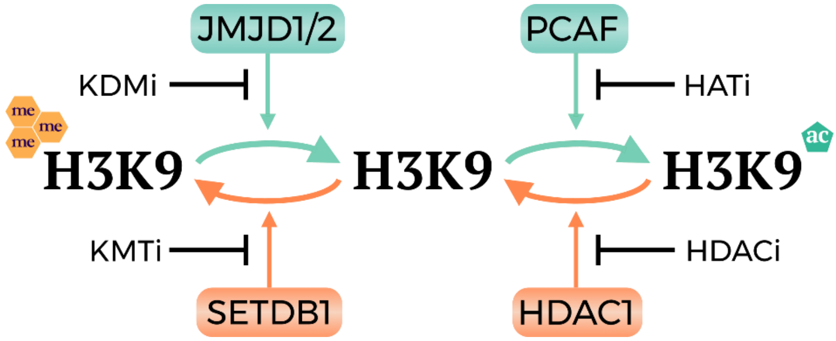

Figure 31. Regulation of H3K9 acetylation and trimethylation. Scheme of the likely regulation of the acetylation and trimethylation state of the H3K9 by PCAF, HDAC1, SETDB1 and JMJD1 or 2. Blue and orange arrows promote an acetylated and a trimethylated state respectively. Black lines indicate the steps that HATi, HDACi, KMTi and KDMi block. Blue pentagon (ac): acetylation; Yellow hexagon (me): methylation.

For this reason, we continued evaluating the effect of different HDAC inhibitors on the acetylation and methylation of H3K9. As mutually exclusive histone PTMs, we expected to see an increase on the acetylation levels as a result of blocking the deacetylase activity of the HDAC enzymes, preventing the deacetylation of this residue, and consequently a reduction of the methylation levels, which cannot occur. In our work, SAHA (a non-selective HDAC inhibitor), entinostat (HDAC1 and HDAC3 inhibitor), panobinostat (a non-selective HDAC inhibitor), and selisistat (SIRT1 inhibitor) were used to evaluate H3K9 PTMs.

For this aim, A549 and U2OS cells were treated with 5 µM SAHA, 5 µM entinostat, 50 nM panobinostat and 50 nM selisistat for 24 h. Using IF staining and WB, we quantified the levels of the acetylation on H3K9. We detected an increase in H3K9ac levels after HDACi treatments compared with non-treated cells, which was similar in A549 (**Figure 32**) and U2OS (**Figure 33**) cell lines.

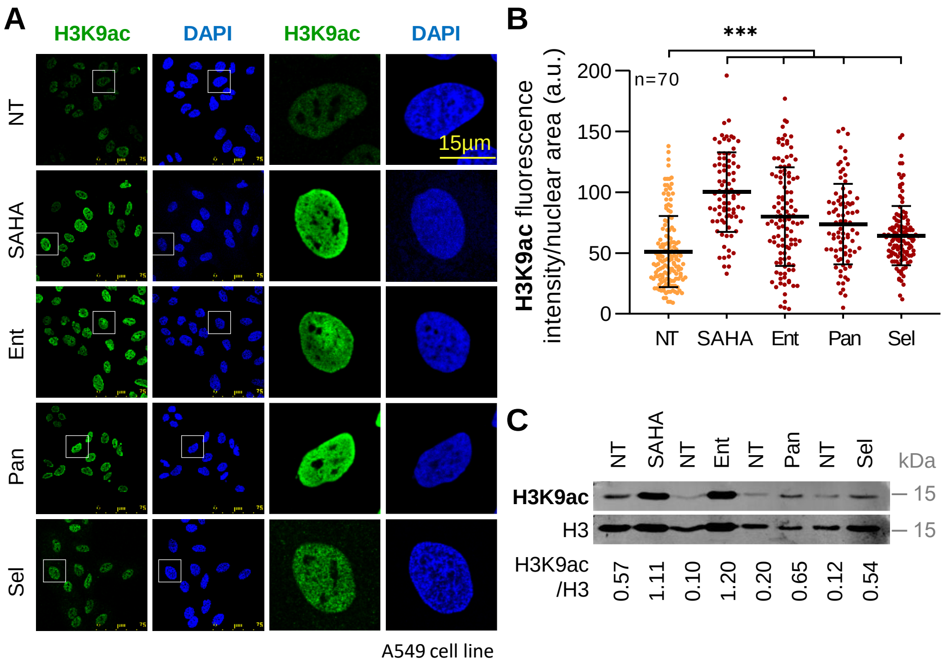

Figure 32. HDAC inhibitors promote H3K9 acetylation in A549 cells. Serum-reduced (0.5% FBS for 48 h) cells were treated with 5 µM SAHA, 5 µM entinostat, 50 nM panobinostat and 50 nM selisistat for 24 h. A. Panels show IF images of the levels of H3K9ac detected using confocal microscopy. DAPI was used to stain the nuclei. B. Quantification of H3K9ac fluorescence intensity per nuclear area (a.u.) of 70 cells (per condition). C. WB represents the levels of H3K9ac of histone acidic extracts. Histone H3 was used as loading control. H3K9ac/H3 ratio is shown. NT: Non-treated; Ent: Entinostat; Pan: Panobinostat; Sel: Selisistat. Scale bar = 15 µm. ***: $p < 0.001$. a.u.: arbitrary units.

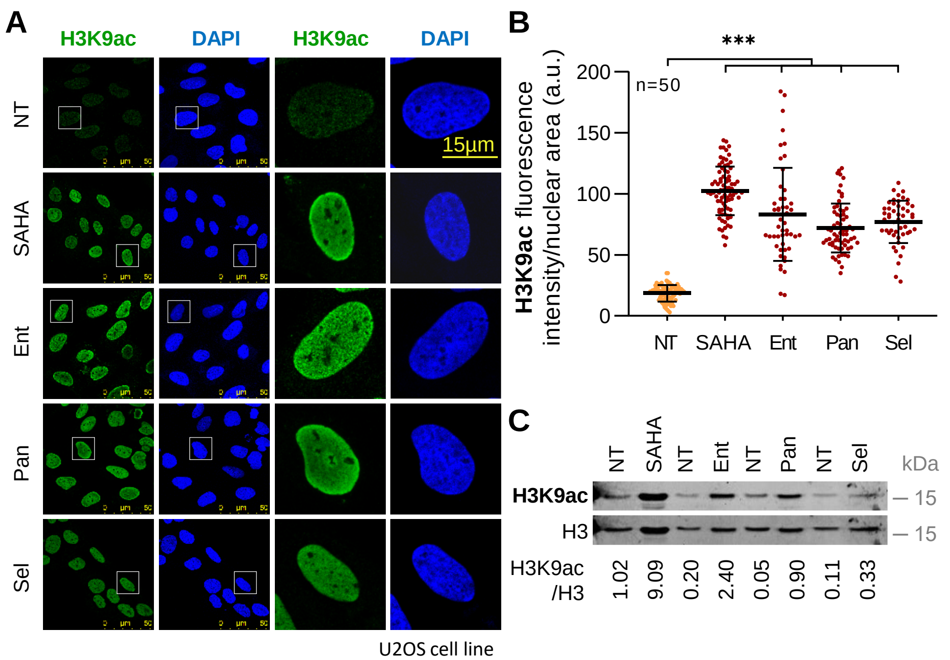

Figure 33. HDAC inhibitors enhance acetylated H3K9 in U2OS cells. Cells were cultured with 0.5% FBS for 48 h and treated with 5 µM SAHA, 5 µM entinostat (Ent), 50 nM panobinostat (Pan) and 50 nM selisistat (Sel) for 24 h. NT: Non-treated. **A.** Panels show IF images of H3K9ac levels detected using confocal microscopy. DAPI was used to stain the nuclei. Scale bar = 15 µm. **B.** H3K9ac fluorescence intensity per nuclear area (a.u.) quantification of 50 cells (per condition) is represented in a dot plot. *** = $p < 0.001$. **C.** H3K9ac acidic extracts detected by WB. Histone H3 was used as loading control. H3K9ac/H3 ratio is shown.

Additionally, we measured the methylation levels of H3K9. We noticed a significant reduction on H3K9me3 levels after HDACi treatments compared with non-treated samples, both by IF and by WB in A549 (**Figure 34**) and U2OS (**Figure 35**) cells.

This finding indicates that the absence of VRK1 produces opposite outcomes than HDACs inhibition, suggesting that VRK1 may inhibit HDAC activity.

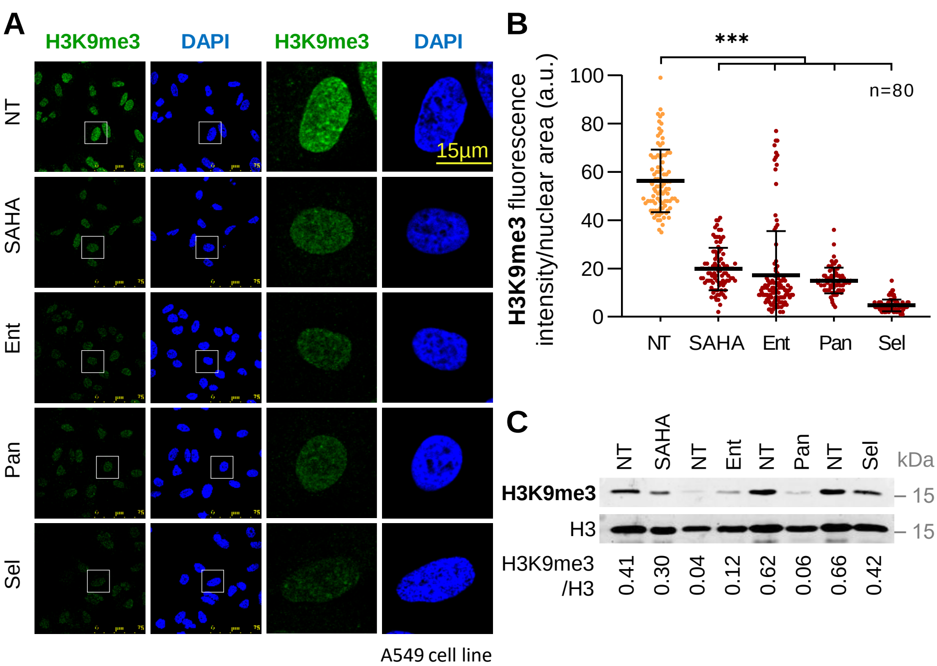

Figure 34. HDAC inhibitors produce a drop of H3K9 trimethylation in A549 cells. Cells were cultured with 0.5% FBS for 48 h and treated with 5 µM SAHA, 5 µM entinostat, 50 nM panobinostat nd 50 nM selisistat for 24 h. **A.** Panels show IF images of H3K9me3 levels detected using confocal microscopy. DAPI was used to stain the nuclei. **B.** H3K9me3 fluorescence intensity per nuclear area (a.u.) quantification of 80 cells (per condition) is represented in a dot plot. **C.** H3K9me3 acidic extracts detected by immunoblot. Histone H3 was used as loading control. H3K9me3/H3 ratio is shown. NT: Non-treated; Ent: Entinostat; Pan: Panobinostat; Sel: Selisistat. Scale bar = 15 µm. ***: $p < 0.001$. a.u.: arbitrary units.

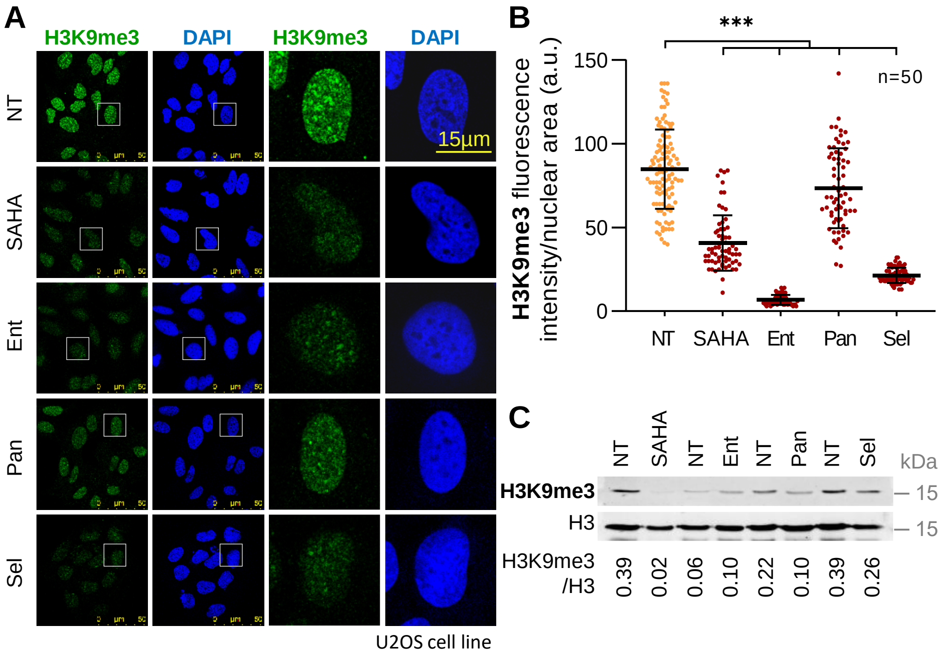

Figure 35. HDAC inhibitors reduce trimethylated H3K9 in U2OS cells. Serum-reduced (0.5% FBS for 48 h) cells were treated with 5 μM SAHA, 5 μM entinostat, 50 nM panobinostat and 50 nM selisistat for 24 h. **A.** Panels show IF images of the levels of H3K9me3 detected using confocal microscopy. DAPI was used to stain the nuclei. **B.** Quantification of H3K9me3 fluorescence intensity per nuclear area (a.u.) of 50 cells (per condition). **C.** WB shows H3K9me3 levels of histone acidic extracts. Histone H3 was used as loading control. H3K9me3/H3 ratio is shown. NT: Non-treated; Ent: Entinostat; Pan: Panobinostat; Sel: Selisistat. Scale bar = 15 μm. ***: $p < 0.001$. a.u.: arbitrary units.

4.1.3.3 The HAT inhibitor C646 causes a reduction of H3K9ac and an increment of H3K9me3 levels

To reach a deeper understanding of the H3K9 modifications, we study the effect of the HAT inhibitor C646. C646 is a reagent that inhibits the p300 acetyltransferase, which is associated with H3K9 and H3K27 acetylation[165].

For this aim, analyzing these PTMs via IF, we uncovered that the treatment with 5 μM C646 for 24 h caused a loss of acetylated H3K9 fluorescence levels as compared with the non-treated condition in A549 cells (**Figure 36**). To ensure this effect, we measured these acetylation levels by WB which demonstrated a significant drop in C646 treated cells.

This result was confirmed in U2OS cells, where C646 treatment had a similar effect and resulted in a notable reduction on H3K9ac, which were detected by IF and WB (**Figure 37**).

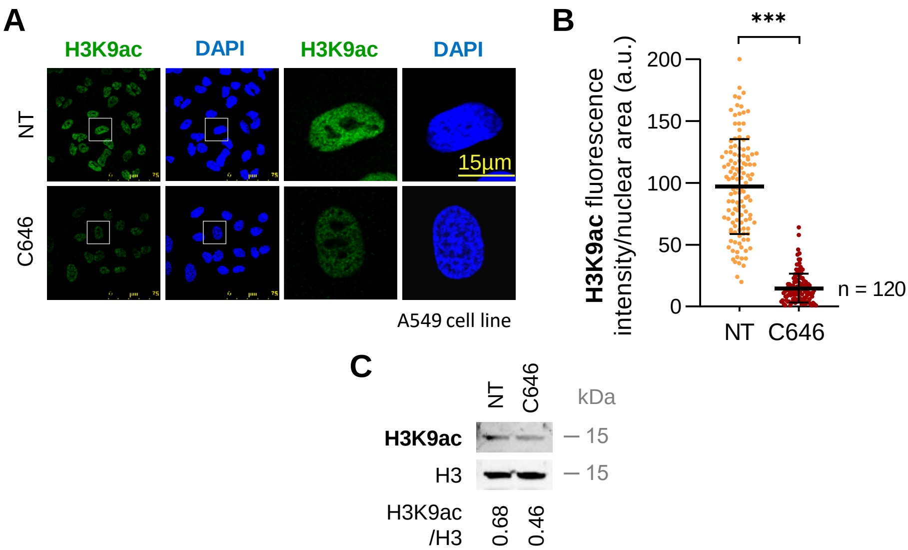

Figure 36. C646 reduces acetylated H3K9 in A549 cells. Cells were cultured with 0.5% FBS for 48 h and treated with 5 µM C646 for 24 h. **A.** Panels show IF images of the levels of H3K9ac detected using confocal microscopy. DAPI was used to stain the nuclei. **B.** Quantification of H3K9ac fluorescence intensity per nuclear area (a.u.) of 120 cells (per condition). **C.** WB shows H3K9ac levels of histone acidic extracts. Histone H3 was used as loading control. H3K9ac/H3 ratio is shown. NT: Non-treated. Scale bar = 15 µm. ***: $p < 0.001$. a.u.: arbitrary units.

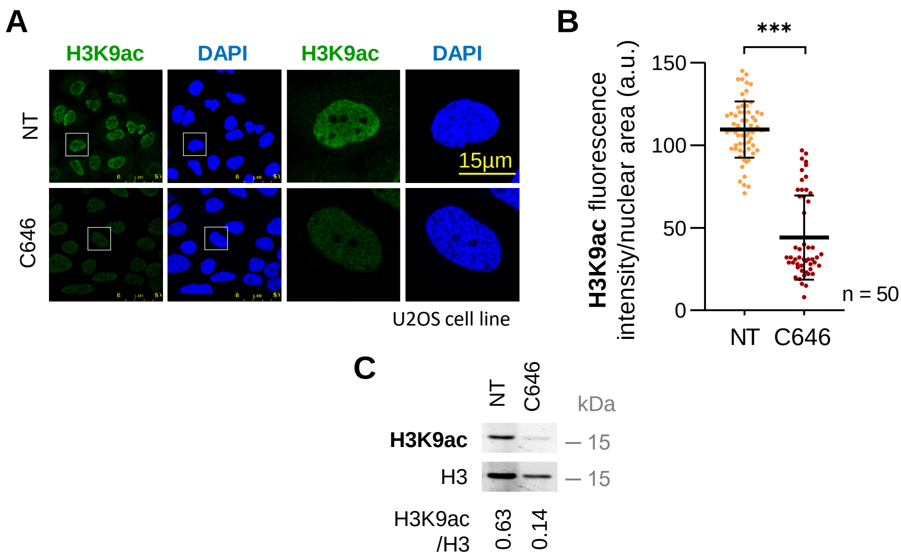

Figure 37. C646 impairs the acetylation of H3K9 in U2OS cells. Serum-deprived cells were treated with 5 µM C646 for 24 h. **A.** Image panels show acetylation of H3K9 levels stained by

IF and detected using confocal microscopy. DAPI was used to stain the nuclei. **B.** H3K9ac fluorescence intensity per nuclear area (a.u.) quantification of 50 cells (per condition) is represented in a dot plot. **C.** WB represents the levels of H3K9ac of histone acidic extracts. Histone H3 was used as loading control. H3K9ac/H3 ratio is shown. NT: Non-treated. Scale bar = 15 µm. ***: $p < 0.001$. a.u.: arbitrary units.

Additionally, we evaluated the trimethylation of H3K9 after C646 treatment. Unlike what happened with H3K9 acetylation, both A549 (**Figure 38**) and U2OS (**Figure 39**) cells showed a significant rise of the trimethylation, that were detected by IF and WB.

Thus, we concluded that C646 is able to alter chromatin structure through the inhibition of p300 and promotes a closed chromatin conformation, given that C646 causes a decrease of H3K9ac levels.

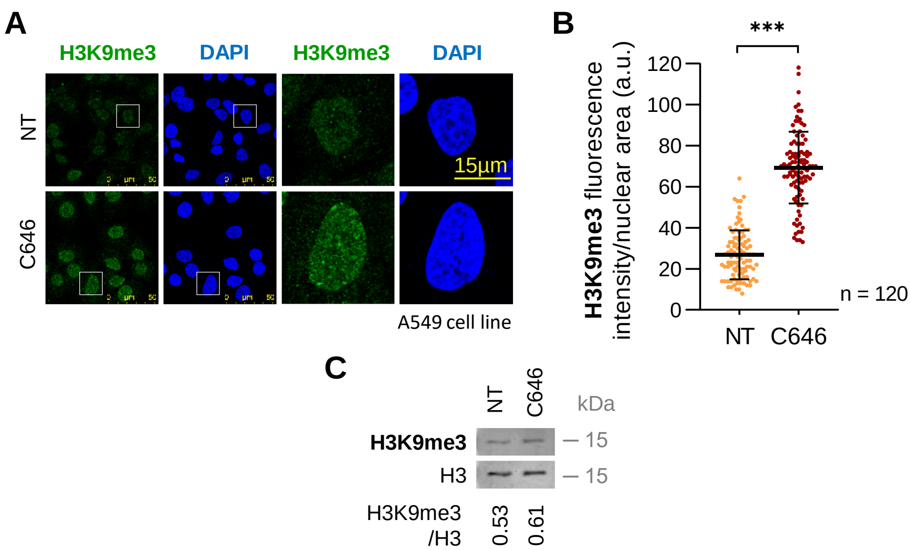

Figure 38. C646 causes an increase in trimethylated H3K9 in A549 cells. Cells were cultured with 0.5% FBS for 48 h and treated with 5 µM C646 for 24 h. **A.** Panels show IF images of the levels of H3K9me3 detected using confocal microscopy. DAPI was used to stain the nuclei. **B.** Dot plot represents the quantification of H3K9me3 fluorescence intensity per nuclear area (a.u.) of 120 cells (per condition). **C.** WB shows H3K9me3 levels of histone acidic extracts. Histone H3 was used as loading control. H3K9me3/H3 ratio is shown. NT: Non-treated. Scale bar = 15 µm. ***: $p < 0.001$. a.u.: arbitrary units.

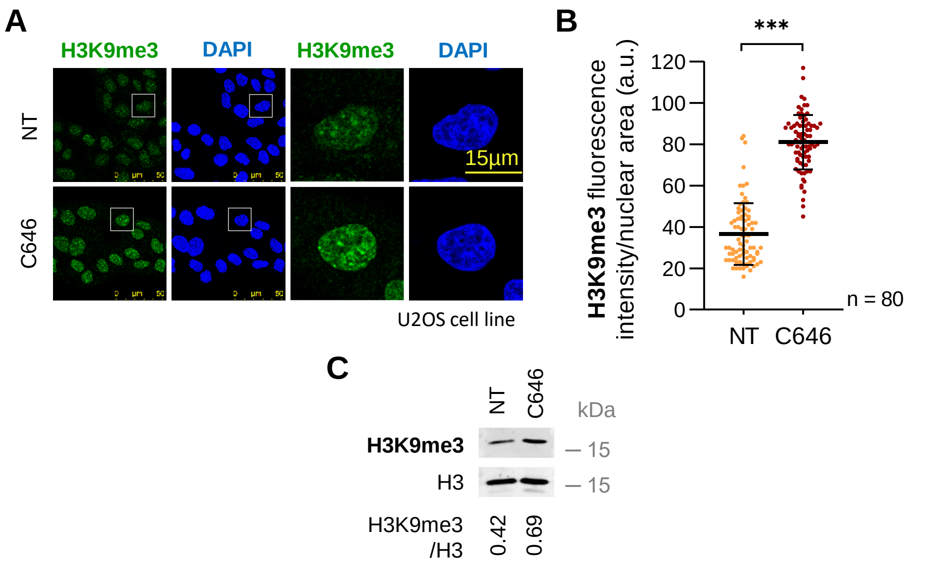

Figure 39. C646 enhances H3K9 trimethylation in U2OS cells. Cells were cultured with 0.5% FBS for 48 h and treated with 5 µM C646 for 24 h. **A.** Panels show IF images of H3K9me3 levels detected using confocal microscopy. DAPI was used to stain the nuclei. **B.** H3K9me3 fluorescence intensity per nuclear area (a.u.) quantification of 80 cells (per condition) is represented in a dot plot. **C.** H3K9me3 acidic extracts detected by immunoblot. Histone H3 was used as loading control. H3K9me3/H3 ratio is shown. NT: Non-treated. Scale bar = 15 µm. ***: $p < 0.001$. a.u.: arbitrary units.

4.1.3.4 **The KMT inhibitors chaetocin and tazemetostat promote H3K9ac and diminish H3K9me3**

Once we have demonstrated that HDAC and HAT inhibitors modify H3K9 PTM levels, our next step was to study methyltransferase epi-drugs chaetocin and the already mentioned tazemetostat. Chaetocin is a specific inhibitor of SUV39H1, the KDM responsible for H3K9 methylation, while tazemetostat inhibits EZH2, the KDM responsible for H3K27 methylation[102,166].

For this purpose, we assessed KMTi implication on H3K9 acetylation. After treating A549 cells with 100 nM chaetocin and 50 nM tazemetostat for 24 h, we detected a gain of this modification compared with non-treated cells by IF and WB (**Figure 40**). To confirm this result, we also quantified it in U2OS-treated cells, detecting an increase on H3K9ac levels after chaetocin and tazemetostat incubation (**Figure 41**).

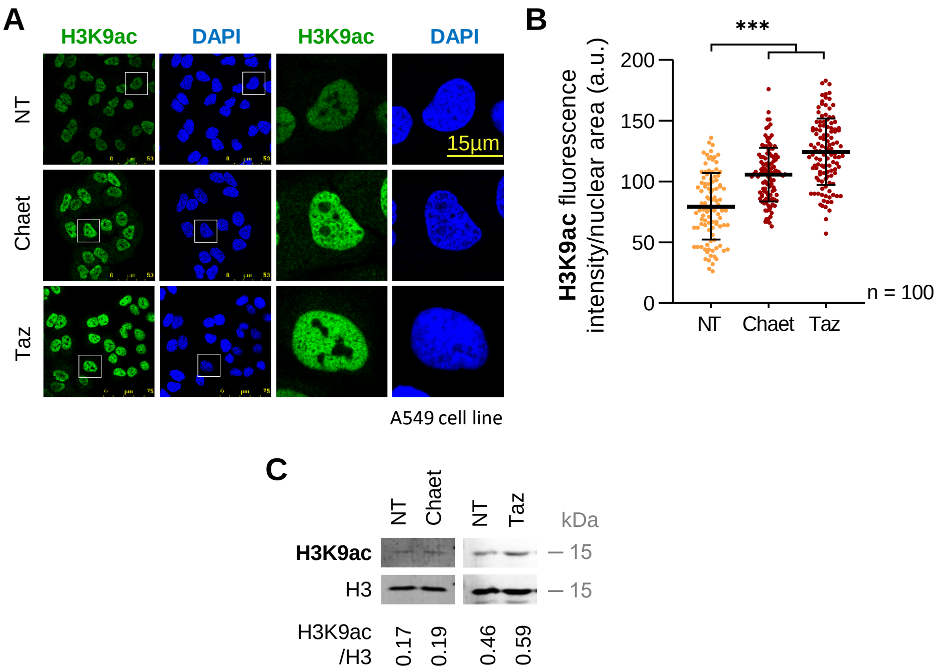

Figure 40. KMT inhibitors produce an accumulation of acetylated H3K9 in A549 cells. Cells were cultured with 0.5% FBS for 48h and treated with 100 nM chaetocin and 50 nM tazemetostat for 24 h. **A.** Panels show IF images of the levels of H3K9ac detected using confocal microscopy. DAPI was used to stain the nuclei. **B.** Quantification of H3K9ac fluorescence intensity per nuclear area (a.u.) of 100 cells (per condition). **C.** WB shows H3K9ac levels of histone acidic extracts. Histone H3 was used as loading control. H3K9ac/H3 ratio is shown. NT: Non-treated; Chaet: Chaetocin; Taz: Tazemetostat. Scale bar = 15 µm. ***: $p < 0.001$. a.u.: arbitrary units.

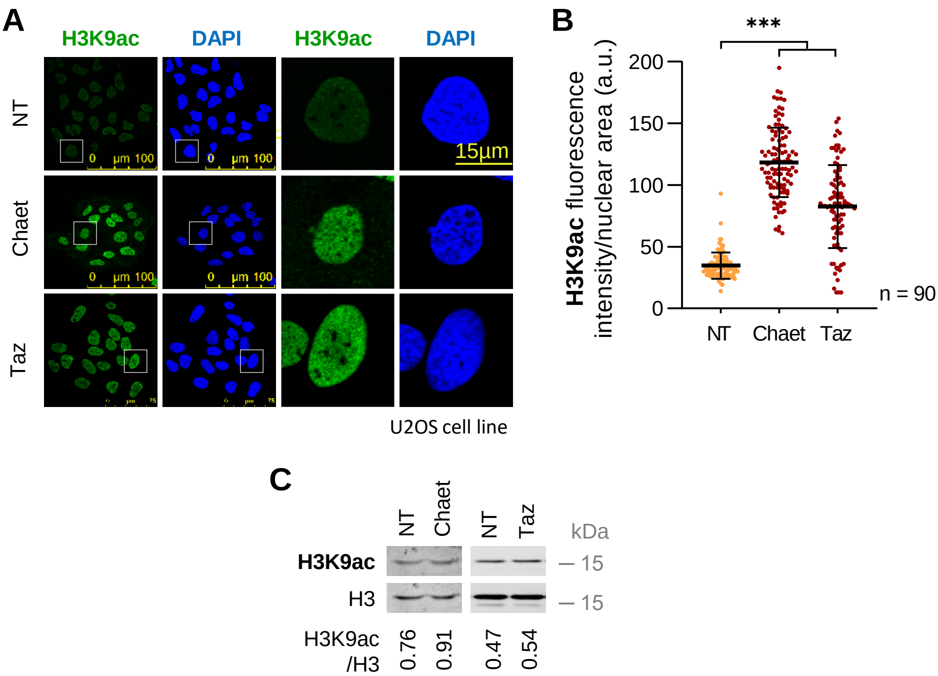

Figure 41. KMT inhibitors promote the acetylation of H3K9 in U2OS cells. Serum-deprived cells were treated with 100 nM chaetocin and 50 nM tazemetostat for 24 h. **A.** Image panels show acetylation of H3K9 levels stained by IF and detected using confocal microscopy. DAPI was used to stain the nuclei. **B.** H3K9ac fluorescence intensity per nuclear area (a.u.) quantification of 90 cells (per condition) is represented in a dot plot. **C.** H3K9ac acidic extracts detected by immunoblot. Histone H3 was used as loading control. H3K9ac/H3 ratio is shown. NT: Non-treated; Chaet: Chaetocin; Taz: Tazemetostat. Scale bar = 15 µm. ***: $p < 0.001$. a.u.: arbitrary units.

Once we had corroborated that KMTi were able to alter acetylation of H3K9, our next step was to examine H3K9 trimethylation. Following the same experimental procedure, chaetocin and tazemetostat treatments impaired H3K9me3 in A549 (**Figure 42**) and U2OS (**Figure 43**) cells compared with non-treated samples.

Thus, these findings suggest that KMTi promote acetylation and disrupt trimethylation on H3K9, mimicking the effect that VRK1 has on two different cell lines: maintaining higher levels of H3K9ac and lower levels of H3K9me3.

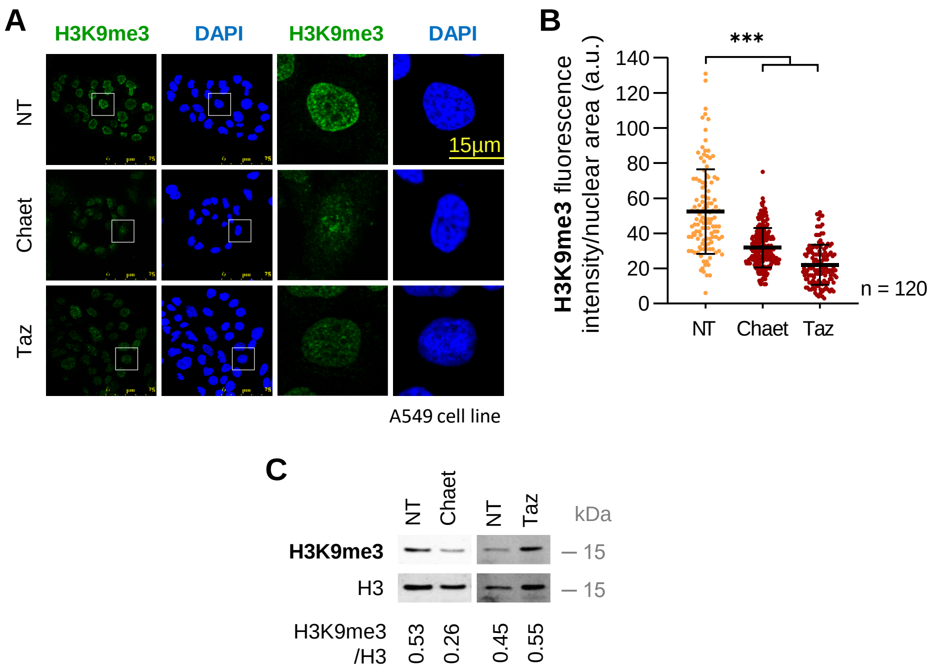

Figure 42. KMT inhibitors reduce the trimethylation of H3K9 in A549 cells. Serum-deprived cells were treated with 100 nM chaetocin and 50 nM tazemetostat for 24 h. **A.** Image panels show H3K9me3 levels stained by IF and detected using confocal microscopy. DAPI was used to stain the nuclei. **B.** Dot plot represents the quantification of H3K9me3 fluorescence intensity per nuclear area (a.u.) of 120 cells (per condition). **C.** WB represents the levels of H3K9me3 of histone acidic extracts. Histone H3 was used as loading control. H3K9me3/H3 ratio is shown. NT: Non-treated; Chaet: Chaetocin; Taz: Tazemetostat. Scale bar = 15 µm. ***: $p < 0.001$. a.u.: arbitrary units.

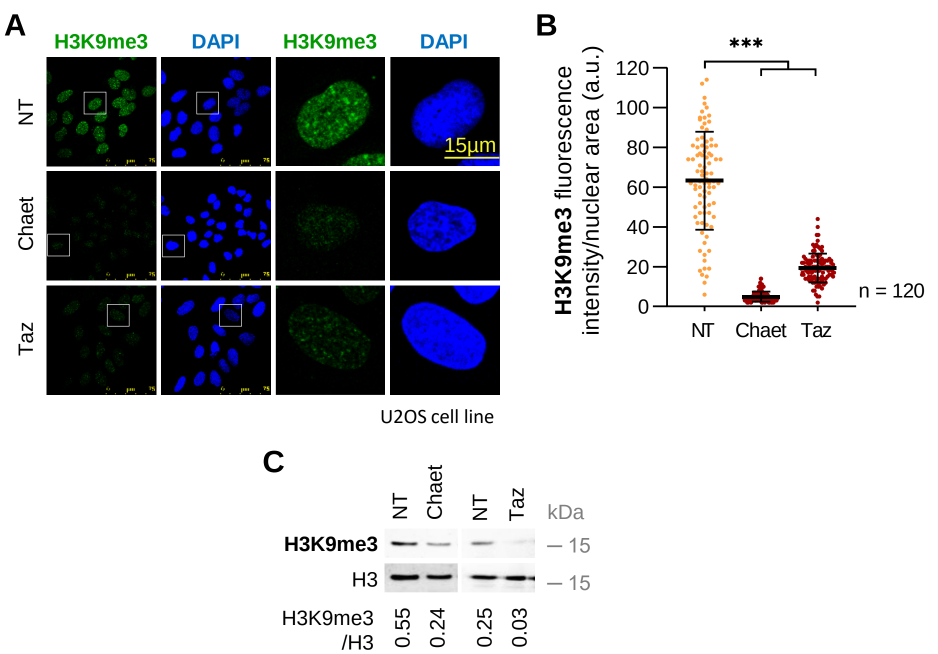

Figure 43. KMT inhibitors impair the trimethylation of H3K9 in U2OS cells. Serum-deprived cells were treated with 100 nM chaetocin and 50 nM tazemetostat for 24 h. A. Image panels show trimethylation of H3K9 levels stained by IF and detected using confocal microscopy. DAPI was used to stain the nuclei. B. H3K9me3 fluorescence intensity per nuclear area (a.u.) quantification of 120 cells (per condition) is represented in a dot plot. C. WB shows H3K9me3 levels of histone acidic extracts. Histone H3 was used as loading control. H3K9me3/H3 ratio is shown. NT: Non-treated; Chaet: Chaetocin; Taz: Tazemetostat. Scale bar = 15 μm. ***: $p < 0.001$. a.u.: arbitrary units.

4.1.3.5 The KDM inhibitors JMJD2i and ORY-1001 produce a decrease on H3K9ac and an increase on H3K9me3 levels

Finally, the last set of epigenetic enzymes evaluated that control H3K9 modifications are the demethylases. Thus, we studied JMJD2 inhibitor (JMJD2i) and the aforementioned ORY-1001. JMJD2i acts against JMJD2A, inhibiting its demethylase activity[167]. On the other hand, ORY-1001 inhibits another KDM related to the H3K4 methylation, LSD1.

We studied the acetylation and trimethylation of H3K9 after treating A549 and U2OS cells with 100 μM JMJD2i and 50 nM ORY-1001 for 24 h. In this case, giving that KDM activity was inhibited, A549 and U2OS treated cells showed a drop of the acetylation levels (**Figure 44** and **Figure 45**), both by IF and WB, compared with non-treated cells.

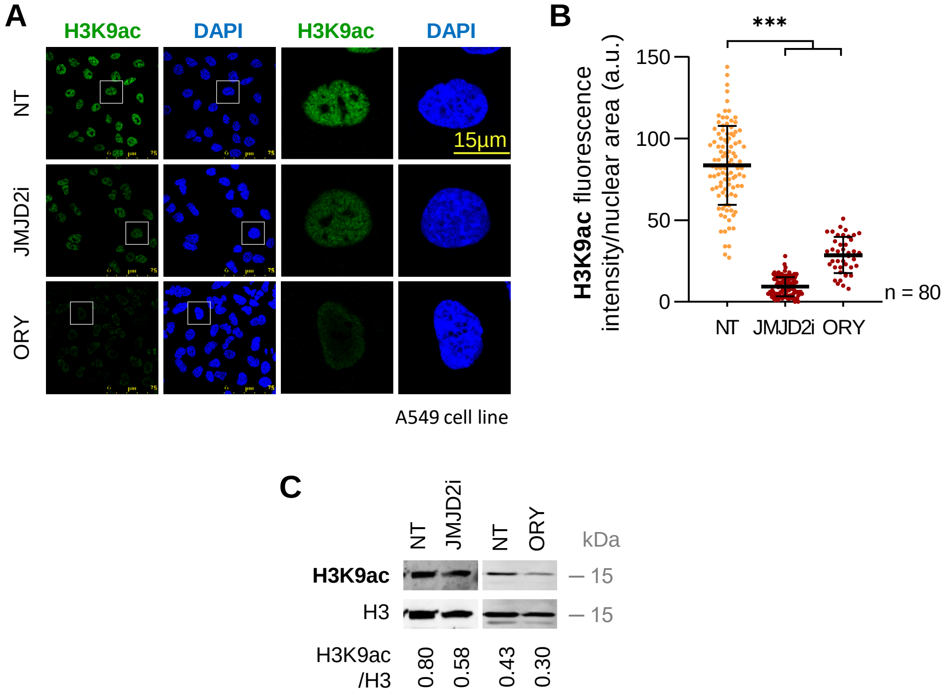

Figure 44. KDM inhibitors reduce H3K9 acetylation in A549 cells. Serum-deprived (0.5% FBS for 48 h) cells were treated with 100 µM JMJD2i and 50 nM ORY-1001 for 24 h. **A.** Image panels show H3K9ac levels stained by IF and detected using confocal microscopy. DAPI was used to stain the nuclei. **B.** Dot plot represents the quantification of H3K9ac fluorescence intensity per nuclear area (a.u.) of 80 cells (per condition). **C.** WB shows H3K9ac levels of histone acidic extracts. Histone H3 was used as loading control. H3K9ac/H3 ratio is shown. NT: Non-treated; ORY: ORY-1001. Scale bar = 15 µm. ***: $p < 0.001$. a.u.: arbitrary units.

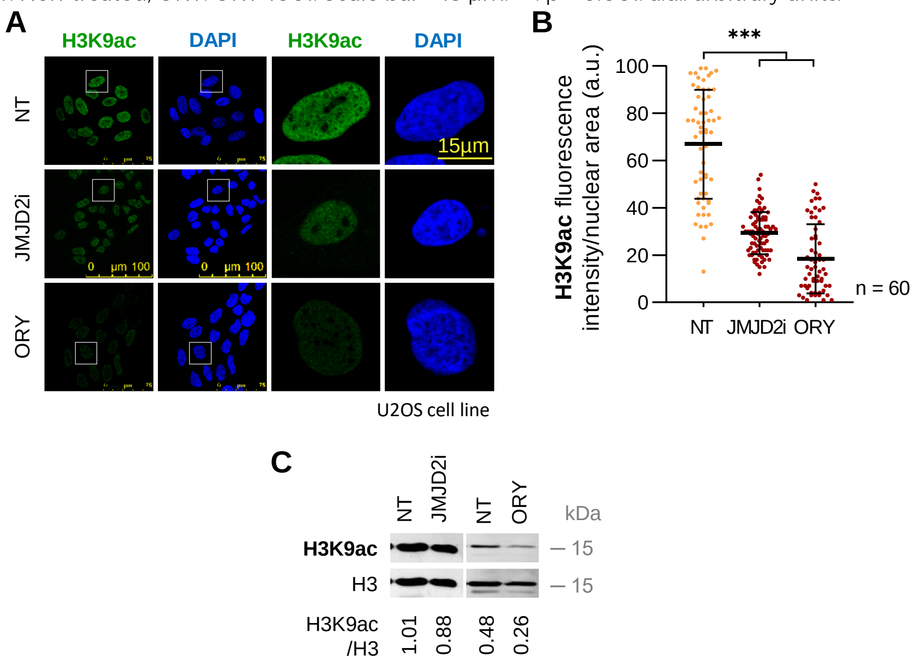

Figure 45. KDM inhibitors reduce the acetylation of H3K9 in U2OS cells. Serum-reduced (0.5% FBS for 48 h) cells were treated with 100 µM JMJD2i and 50 nM ORY-1001 for 24 h. **A.** Image panels show H3K9ac levels stained by IF and detected using confocal microscopy. DAPI was used to stain the nuclei. **B.** Dot plot represents the quantification of H3K9ac fluorescence intensity per nuclear area (a.u.) of 60 cells (per condition). **C.** H3K9ac acidic extracts detected by immunoblot. Histone H3 was used as loading control. H3K9ac/H3 ratio is shown. NT: Non-treated; ORY: ORY-1001. Scale bar = 15 µm. ***: $p < 0.001$. a.u.: arbitrary units.

By contrast, H3K9me3 levels boosted with both KDMi compared with non-treated A549 cells, assessed by IF and WB (**Figure 46**). Moreover, we checked this increase of H3K9me3 levels in U2OS, which showed similar results (**Figure 47**).

Therefore, we conclude that KDMi blocks the demethylation of H3K9 and VRK1 absence mimics their effect through impairing acetylation and promoting trimethylation.

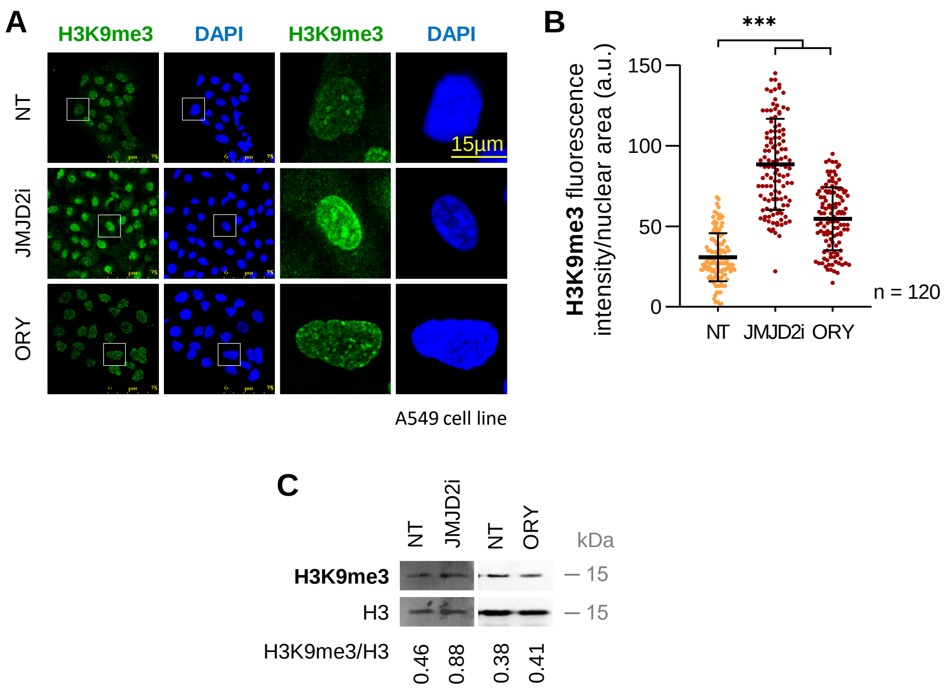

Figure 46. KDM inhibitors enhance H3K9 trimethylation in A549 cells. Cells were cultured with 0.5% FBS for 48 h and treated with 100 µM JMJD2i and 50 nM ORY-1001 for 24 h. **A.** Panels show IF images of H3K9me3 levels detected using confocal microscopy. DAPI was used to stain the nuclei. **B.** H3K9me3 fluorescence intensity per nuclear area (a.u.) quantification of 120 cells (per condition) is represented in a dot plot. **C.** H3K9me3 acidic extracts detected by immunoblot. Histone H3 was used as loading control. H3K9me3/H3 ratio is shown. NT: Non-treated; ORY: ORY-1001. Scale bar = 15 µm. ***: $p < 0.001$. a.u.: arbitrary units.

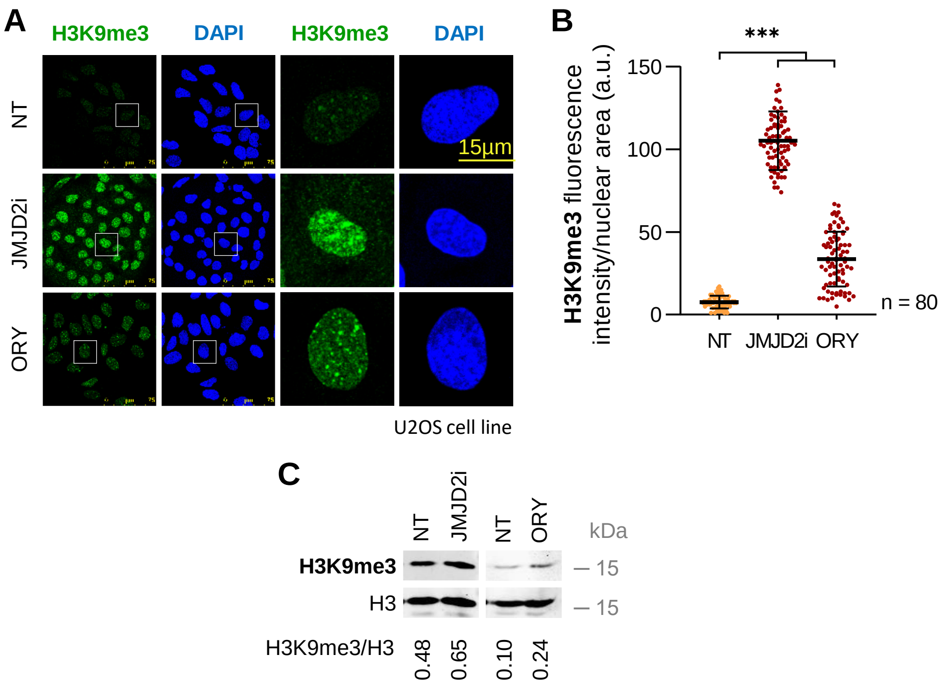

Figure 47. KDM inhibitors promote trimethylated H3K9 levels in U2OS cells. Cells were cultured with 0.5% FBS for 48 h and treated with 100 µM JMJD2i and 50 nM ORY-1001 for 24 h. **A.** Panels show IF images of H3K9me3 levels detected using confocal microscopy. DAPI was used to stain the nuclei. **B.** H3K9me3 fluorescence intensity per nuclear area (a.u.) quantification of 80 cells (per condition) is represented in a dot plot. **C.** WB shows H3K9me3 levels of histone acidic extracts. Histone H3 was used as loading control. H3K9me3/H3 ratio is shown. NT: Non-treated; ORY: ORY-1001. Scale bar = 15 µm. ***: $p < 0.001$. a.u.: arbitrary units.

4.1.4 VRK1 facilitates an open chromatin state, promoting H3K27ac and preventing H3K27me3

4.1.4.1 VRK1 depletion causes a reduction of H3K27ac and a rise of H3K27me3 levels

To address the role of the human VRK1 in the chromatin relaxation associated with histone PTMs, we evaluated PTMs on Lys 27 of histone H3. H3K27 acetylation is related with active enhancers, while methylation of this residue is associated with gene repression[12,42].

To study H3K27 modifications, A549 cells (siC, siV-02 and siV-03) were cultured in media containing 10% or 0.5% FBS. VRK1-depleted cells showed an increase on H3K27 acetylated levels as compared with siC samples (**Figure 48**). To confirm this result, VRK1 was depleted in U2OS cells. Similarly, VRK1-knocked-down cells responded preventing H3K27 acetylation in both serum-completed and -reduced conditions (**Figure 49**). Likewise, the trimethylation levels of H3K27 were evaluated. By contrary of H3K27ac, a strong increase on the trimethylation levels were detected in A549 (**Figure 50**) and U2OS (**Figure 51**) cells by IF. However, these differences were not always clearly seen by WB. These data show that VRK1 depletion significantly impairs chromatin relaxation due to impairment of H3K27ac, favoring H3K27me3.

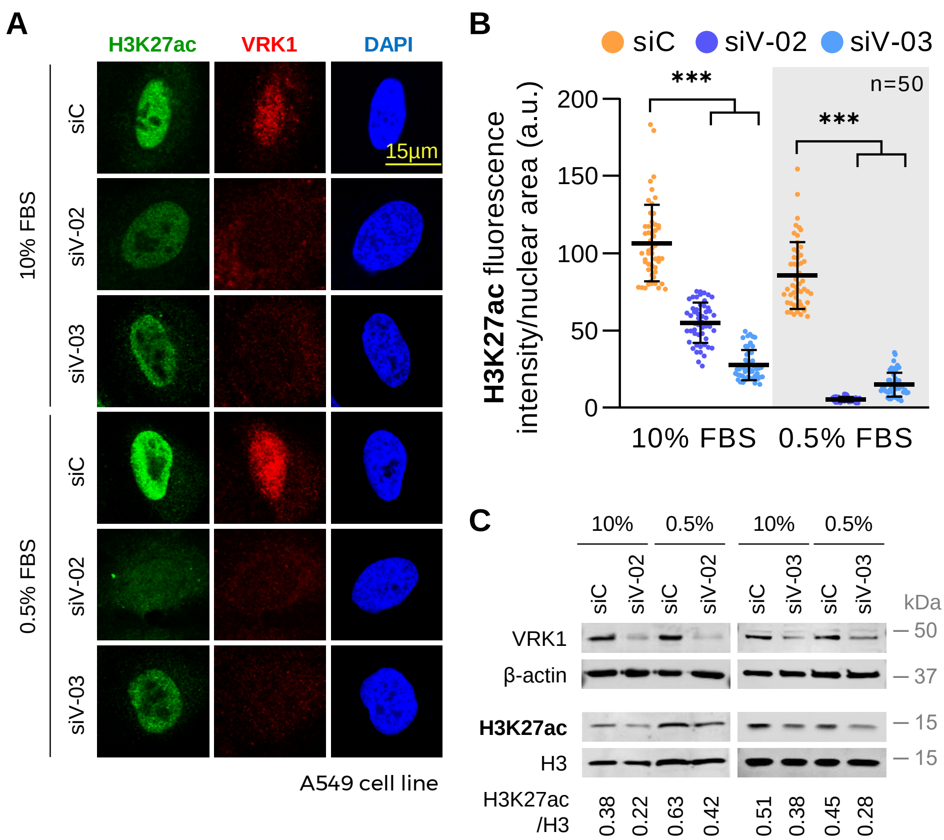

Figure 48. VRK1 depletion causes a reduction of H3K27 acetylation in A549 cells. VRK1 was depleted using two siRNAs (siV-02 and siV-03) for 72 h. siC was used as off-target siRNA. Cells were cultured with 10% or 0.5% of FBS for 48 h. **A.** Panels show IF images of the levels of H3K27ac detected using confocal microscopy. DAPI was used to stain the nuclei and VRK1 as knock-down control. **B.** H3K27ac fluorescence intensity per nuclear area (a.u.)

quantification of 50 cells (per condition) is represented in a dot plot. **C.** WB shows H3K27ac levels of histone acidic extracts. VRK1, β-actin and histone H3 were used as knock-down and loading control, respectively. H3K27ac/H3 ratio is shown. Scale bar = 15 µm. ***: $p < 0.001$. a.u.: arbitrary units.

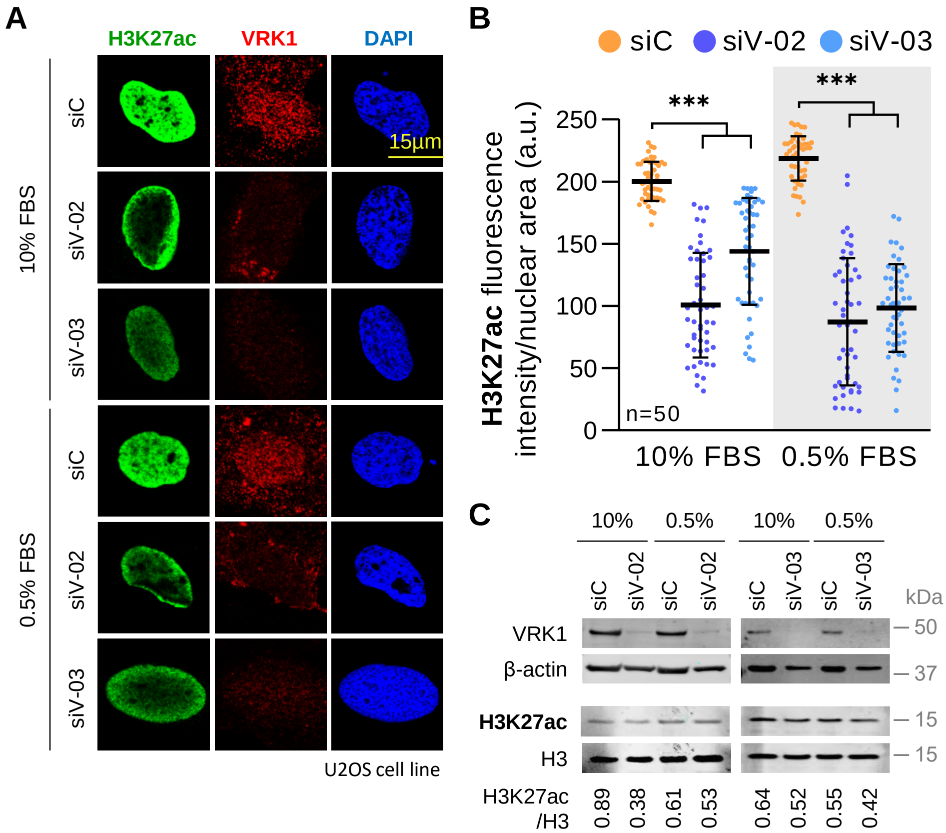

Figure 49. VRK1 depletion produces a reduction in the acetylation of H3K27 in U2OS cells. VRK1 was depleted using two siRNAs (siV-02 and siV-03) for 72 h. siC was used as off-target siRNA. Cells were cultured with 10% or 0.5% of FBS for 48 h. **A.** Image panels show acetylation of H3K27 and VRK1 levels stained by IF and detected using confocal microscopy. DAPI was used to stain the nuclei. **B.** Quantification of H3K27ac fluorescence intensity per nuclear area (a.u.) of 50 cells (per condition). **C.** WB shows H3K27ac levels of histone acidic extracts. VRK1, β-actin and histone H3 were used as knock-down and loading control, respectively. H3K27ac/H3 ratio is shown. Scale bar = 15 µm. ***: $p < 0.001$. a.u.: arbitrary units.

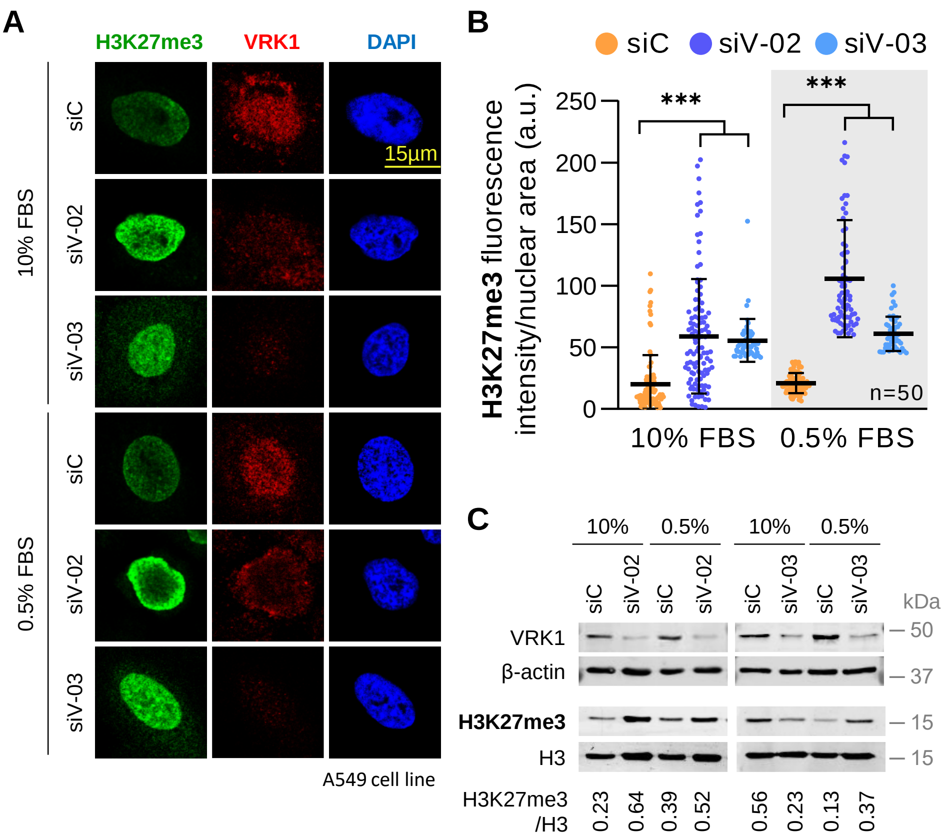

Figure 50. VRK1 knock-down promotes the trimethylation of H3K27 in A549 cells. VRK1 was knocked down using two siRNA (siV-02 and siV-03) for 72 h. siC was used as off-target siRNA. Completed-serum (10% FBS) and reduced-serum (0.5% FBS) conditions were performed for 48 h. **A.** Image panels show trimethylation of H3K27 and VRK1 levels stained by IF and detected using confocal microscopy. DAPI was used to stain the nuclei. **B.** Quantification of H3K27me3 fluorescence intensity per nuclear area (a.u.) of 50 cells (per condition). **C.** WB represents H3K27me3 levels of histone acidic extracts. VRK1, β-actin and histone H3 were used as knock-down and loading control, respectively. H3K27me3/H3 ratio is shown. Scale bar = 15 µm. ***: $p < 0.001$. a.u.: arbitrary units.

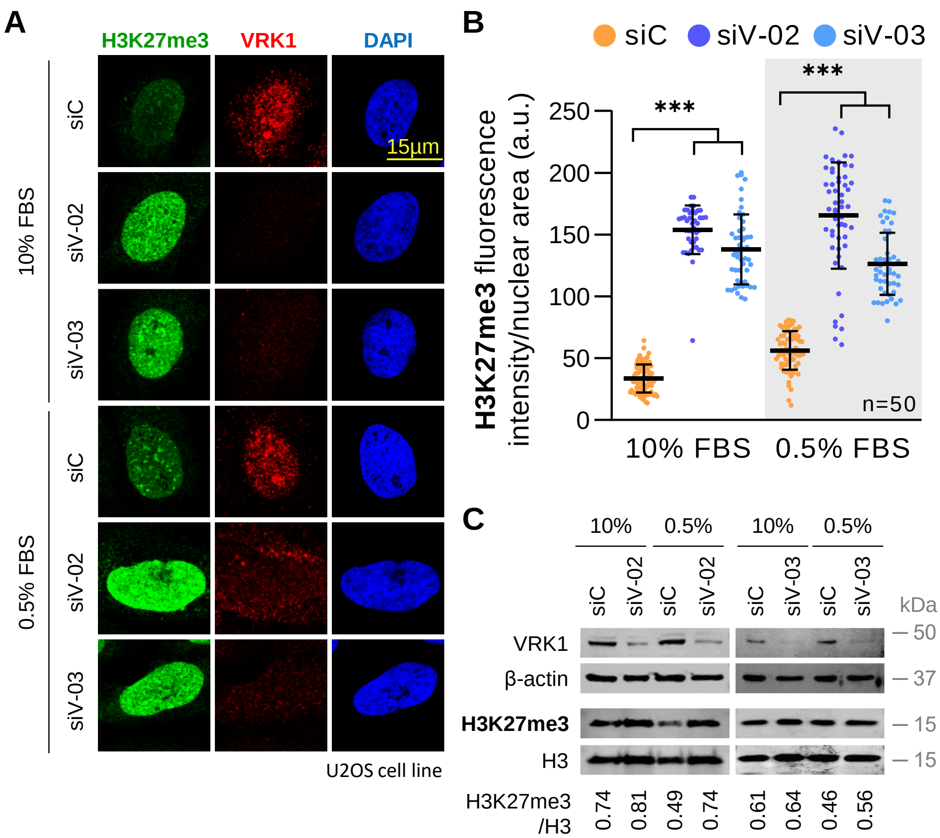

Figure 51. VRK1 knock-down causes an increment of H3K27 trimethylation in U2OS cells. VRK1 was knocked down using two siRNA (siV-02 and siV-03) for 72 h. siC was used as off-target siRNA. Completed-serum (10% FBS) and reduced-serum (0.5% FBS) conditions were performed for 48 h. **A.** Image panels show trimethylation of H3K27 and VRK1 levels stained by IF and detected using confocal microscopy. DAPI was used to stain the nuclei. **B.** Quantification of H3K27me3 fluorescence intensity per nuclear area (a.u.) of 50 cells (per condition). **C.** WB shows H3K27me3 levels of histone acidic extracts and VRK1 as knock-down control. β-actin and histone H3 were used as loading control. H3K27me3/H3 ratio is shown. Scale bar = 15 µm. ***: $p < 0.001$. a.u.: arbitrary units.

4.1.4.2 **The HDAC inhibitors SAHA, entinostat, panobinostat and selisistat increase H3K27ac and decrease H3K27me3 levels**

As occurring with H3K9 modifications, H3K27 can be acetylated and methylated and the HDAC, HAT, KMTs and KDMs epigenetic enzymes regulate these two actions (**Figure 52**). For this reason, we studied the effect of the HDAC inhibitors that were previously mentioned on H3K9 section (**Section 4.1.3.2**). As before, we expected contrary results between the acetylation and the trimethylation of H3K27 after treating cells with HDACi, with a gain on the H3K27ac as a result of blocking the deacetylase activity of the HDAC enzymes, which would prevent the deacetylation of this residue.

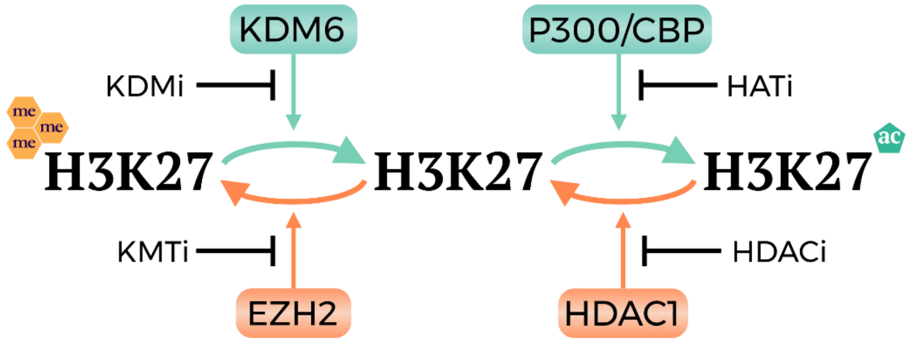

Figure 52. Regulation of H3K27 acetylation and trimethylation. Scheme of the likely regulation of the acetylation and trimethylation state of the H3K27 by P300/CBP, HDAC1, EZH2 and KDM6. Blue and orange arrows promote an acetylated and a trimethylated state, respectively. Black lines indicate the steps that HATi, HDACi, KMTi and KDMi block. Blue pentagon (ac): acetylation; Yellow hexagon (me): methylation.

For this aim, we treated A549 and U2OS cells with HDACi, under serum-depleted conditions, for 24 h. Then, acetylated and trimethylated H3K27 levels were detected by WB and IF. On one hand, we perceived an important increase on acetylation levels of H3K27 in both A549 (**Figure 53**) and U2OS (**Figure 54**) cell lines after 5 µM SAHA, 5 µM entinostat, 50 nM panobinostat and 50 nM selisistat treatments.

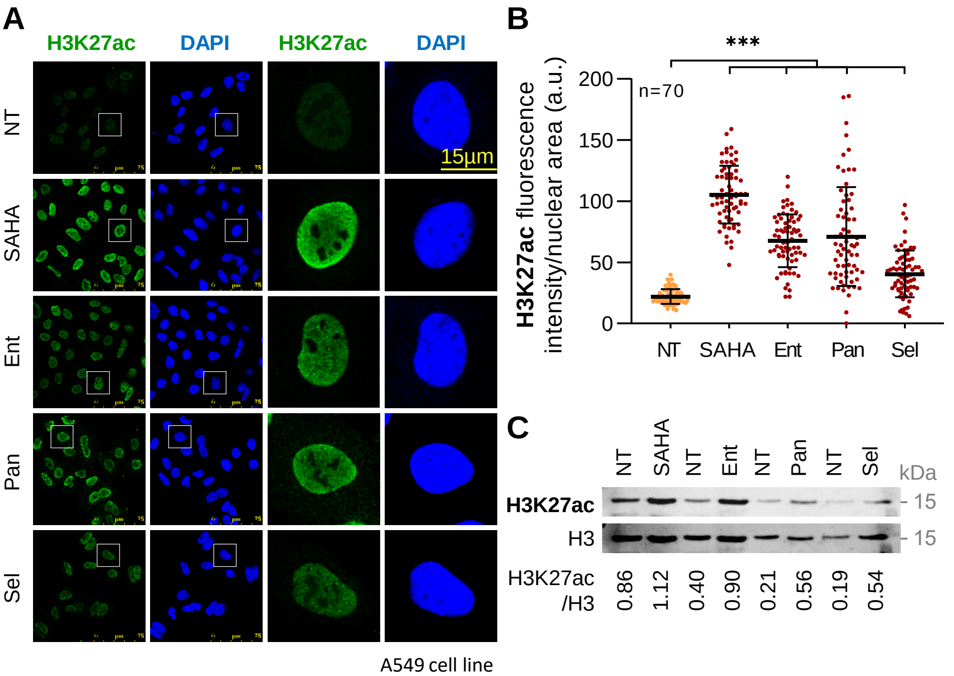

Figure 53. HDAC inhibitors enhance H3K27 acetylation in A549 cells. Cells were cultured with 0.5% FBS for 48 h and treated with 5 µM SAHA, 5 µM entinostat, 50 nM panobinostat and 50 nM selisistat for 24 h. **A.** Image panels show acetylation of H3K27 levels stained by IF and detected using confocal microscopy. DAPI was used to stain the nuclei. **B.** Dot plot illustrates quantification of H3K27ac fluorescence intensity per nuclear area (a.u.) of 70 cells (per condition). **C.** WB represents H3K27ac of histone acidic extracts. Histone H3 was used as loading control. H3K27ac/H3 ratio is shown. NT: Non-treated; Ent: Entinostat; Pan: Panobinostat; Sel: Selisistat. Scale bar = 15 µm. ***: $p < 0.001$. a.u.: arbitrary units.

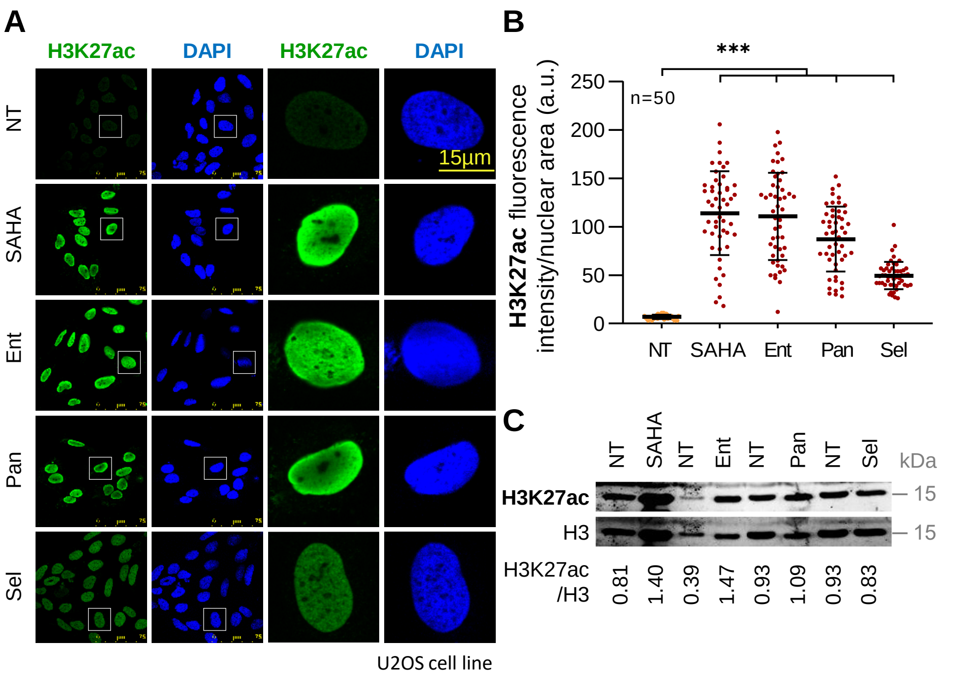

Figure 54. HDAC inhibitors cause an accumulation of acetylated H3K27 in U2OS cells. Cells were cultured with 0.5% FBS for 48 h and treated with 5 μM SAHA, 5 μM entinostat, 50 nM panobinostat and 50 nM selisistat for 24 h. **A.** Panels show IF images of H3K27ac levels detected using confocal microscopy. DAPI was used to stain the nuclei. **B.** H3K27ac fluorescence intensity per nuclear area (a.u.) quantification of 50 cells (per condition) is represented in a dot plot. **C.** WB shows H3K27ac levels of histone acidic extracts. Histone H3 was used as loading control. H3K27ac/H3 ratio is shown. NT: Non-treated; Ent: Entinostat; Pan: Panobinostat; Sel: Selisistat. Scale bar = 15 μm. ***: $p < 0.001$. a.u.: arbitrary units.

On the other hand, the opposite modification of this residue, the trimethylation, revealed a strong decrease compared with non-treated A549 (**Figure 55**) and U2OS (**Figure 56**) cells. The fact that cells show an increase on H3K27ac and a decrease on H3K27me3 levels confirms that HDACis promote relaxed chromatin and active enhancers through inhibiting HDAC activity and preventing the deacetylation of this residue.

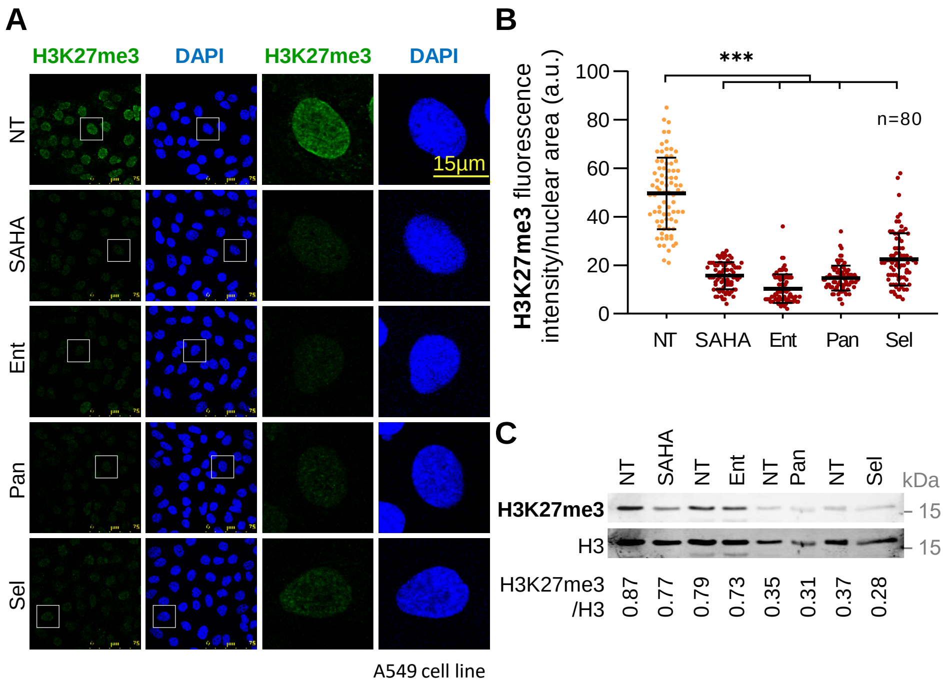

Figure 55. HDAC inhibitors cause a reduction of H3K27 trimethylation in A549 cells. Serum-reduced (0.5% FBS for 48 h) cells were treated with 5 μM SAHA, 5 μM entinostat, 50 nM panobinostat and 50 nM selisistat for 24 h. **A.** Image panels show H3K27me3 levels stained by IF and detected using confocal microscopy. DAPI was used to stain the nuclei. **B.** H3K27me3 fluorescence intensity per nuclear area (a.u.) quantification of 80 cells (per condition) is represented in a dot plot. **C.** WB shows H3K27me3 levels of histone acidic extracts. Histone H3 was used as loading control. H3K27me3/H3 ratio is shown. NT: Non-treated; Ent: Entinostat; Pan: Panobinostat; Sel: Selisistat. Scale bar = 15 μm. ***: $p < 0.001$. a.u.: arbitrary units.

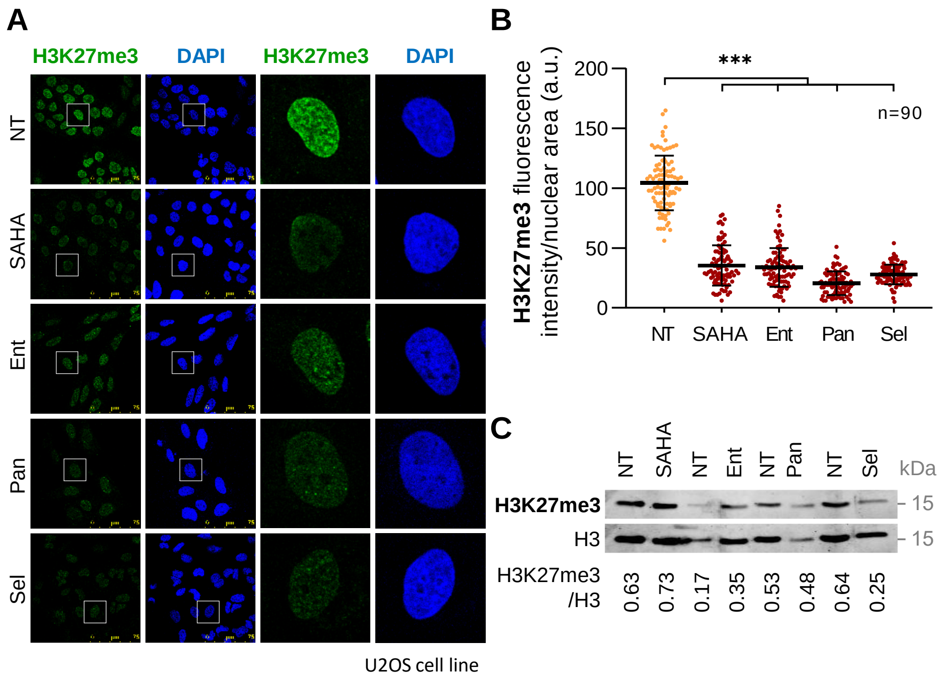

Figure 56. HDAC inhibitors cause a drop on H3K27 trimethylation in U2OS cells. Serum-reduced (0.5% FBS for 48 h) cells were treated with 5 μM SAHA, 5 μM entinostat, 50 nM panobinostat and 50 nM selisistat for 24 h. **A.** Panels show IF images of the levels of H3K27me3 detected using confocal microscopy. DAPI was used to stain the nuclei. **B.** Dot plot illustrates quantification of H3K27me3 fluorescence intensity per nuclear area (a.u.) of 90 cells (per condition). **C.** WB represents the levels of H3K27me3 of histone acidic extracts. Histone H3 was used as loading control. H3K27me3/H3 ratio is shown. NT: Non-treated; Ent: Entinostat; Pan: Panobinostat; Sel: Selisistat. Scale bar = 15 μm. ***: $p < 0.001$. a.u.: arbitrary units.

4.1.4.3 The HAT inhibitor C646 decreases H3K27ac and increases H3K27me3 levels

On the other hand, we determined the effect of inhibiting HAT enzymes on H3K27 modifications. For this aim, we used again the C646 inhibitor, which is used to inhibit p300 activity[165].

We evaluated the H3K27 acetylation levels after treating the cells with 5 μM C646 for 24 h. The C646-treated A549 cells responded with an increase on acetylation levels in H3K27 as compared with non-treated cells. This rise was identified by both IF and WB techniques in A549 (**Figure 57**). Likewise, treating U2OS with the C646 inhibitor resulted in a strong increase of H3K27ac levels that were detected by IF and WB (**Figure 58**).

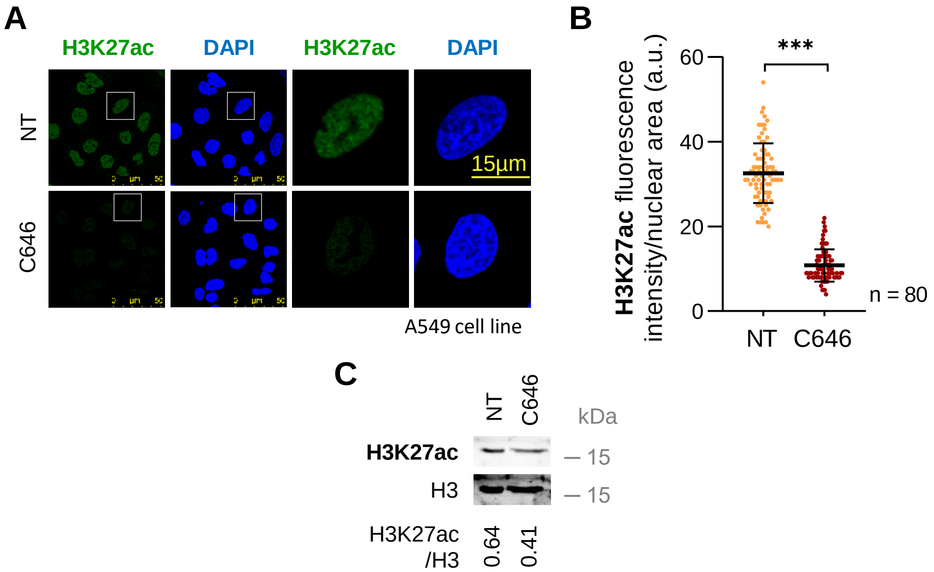

Figure 57. C646 treatment impairs acetylation of H3K27 in A549 cells. Cells were cultured with 0.5% FBS for 48 h and treated with 5 µM C646 for 24 h. **A.** Image panels show acetylation of H3K27 levels stained by IF and detected using confocal microscopy. DAPI was used to stain the nuclei. **B.** H3K27ac fluorescence intensity per nuclear area (a.u.) quantification of 80 cells (per condition) is represented in a dot plot. **C.** WB represents H3K27ac levels of histone acidic extracts. Histone H3 was used as loading control. H3K27ac/H3 ratio is shown. NT: Non-treated. Scale bar = 15 µm. ***: $p < 0.001$. a.u.: arbitrary units.

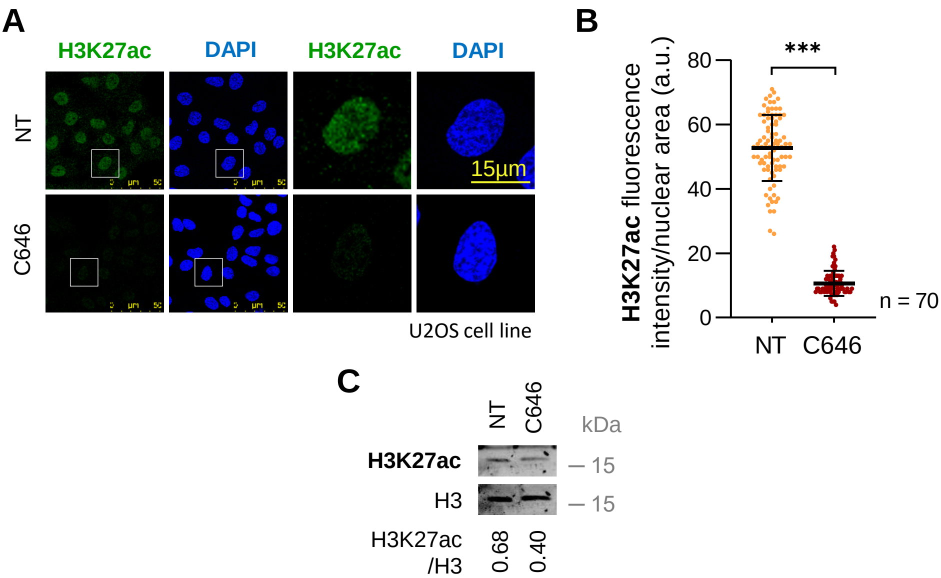

Figure 58. C646 inhibitor causes a reduction of acetylated H3K27 in U2OS cells. Cells were cultured with 0.5% FBS for 48 h treated with 5 µM C646 for 24 h. **A.** Panels show IF images of the levels of H3K27ac detected using confocal microscopy. DAPI was used to stain the

nuclei. B. Dot plot shows quantification of H3K27ac fluorescence intensity per nuclear area (a.u.) of 70 cells (per condition). C. WB represents H3K27ac levels of histone acidic extracts. Histone H3 was used as loading control. H3K27ac/H3 ratio is shown. NT: Non-treated. Scale bar = 15 µm. ***: p < 0.001. a.u.: arbitrary units.

Moreover, to check if C646 had the same effect on the trimethylation of H3K27, we analyzed the methylation levels after the treatment with this inhibitor. As we expected due to the HAT inhibition and the previous results on acetylation, H3K27me3 levels increased after the C646 treatment in A549 cells, assessed by IF and WB (**Figure 59**). This result was confirmed in U2OS, detecting a similar trend (**Figure 60**). This out-turn contributes to H3K9 results of C646 inhibitor, which can alter chromatin structure through the inhibition of p300 and promote a closed chromatin conformation thanks to an increase of H3K27me3 levels.

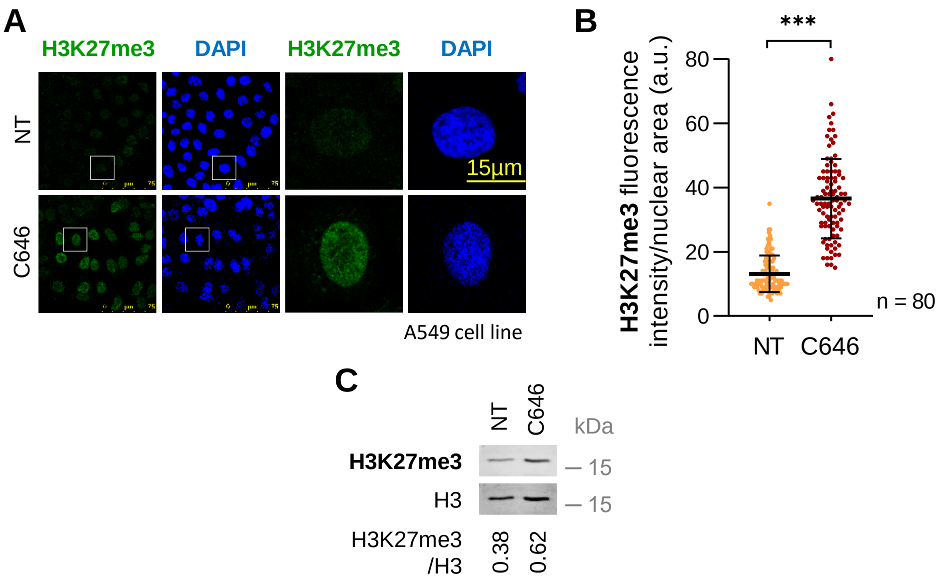

Figure 59. C646 promotes trimethylation of H3K27 in A549 cells. Serum-reduced (0.5% FBS for 48 h) cells were treated with 5 µM C646 for 24 h. A. Panels show IF images of the levels of H3K27me3 detected using confocal microscopy. DAPI was used to stain the nuclei. B. H3K27me3 fluorescence intensity per nuclear area (a.u.) quantification of 80 cells (per condition) is represented in a dot plot. C. WB shows H3K27me3 levels of histone acidic extracts. Histone H3 was used as loading control. H3K27me3/H3 ratio is shown. NT: Non-treated. Scale bar = 15 µm. ***: p < 0.001. a.u.: arbitrary units.

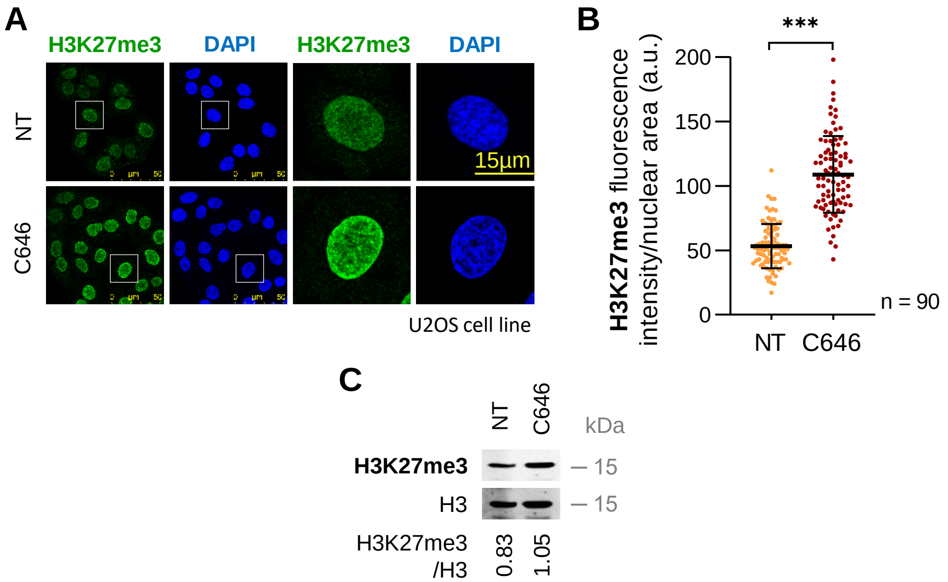

Figure 60. C646 treatment enhances H3K27 trimethylation in U2OS cells. Serum-deprived (0.5% FBS for 48 h) cells were treated with 5 µM C646 for 24 h. **A.** Image panels show trimethylation of H3K27 levels stained by IF and detected using confocal microscopy. DAPI was used to stain the nuclei. **B.** Dot plot represents quantification of H3K27me3 fluorescence intensity per nuclear area (a.u.) of 90 cells (per condition). **C.** WB shows H3K27me3 levels of histone acidic extracts. Histone H3 was used as loading control. H3K27me3/H3 ratio is shown. NT: Non-treated. Scale bar = 15 µm. ***: $p < 0.001$. a.u.: arbitrary units.

4.1.4.4 The KMT inhibitors chaetocin and tazemetostat decrease H3K27ac levels and increase H3K27me3 levels

Following with the inhibition of the epigenetic enzymes that regulate H3K27 modifications, we reviewed the repression of methylase activity of two KMTs. To achieve this objective, chaetocin and tazemetostat (KMT inhibitors used in section 4.1.3.4) were used again to determine H3K27 acetylation and trimethylation levels.

For this aim, A549 and U2OS cells were treated with 100 nM chaetocin and 50 nM tazemetostat for 24 h and H3K27ac levels were evaluated. Treated-cells showed a significant increase of H3K27ac levels compared with non-treated cells by IF and WB in most of the cases (**Figure 61** and **Figure 62**). However, the acidic extract of the chaetocin-treated A549 cells did not show this increase.

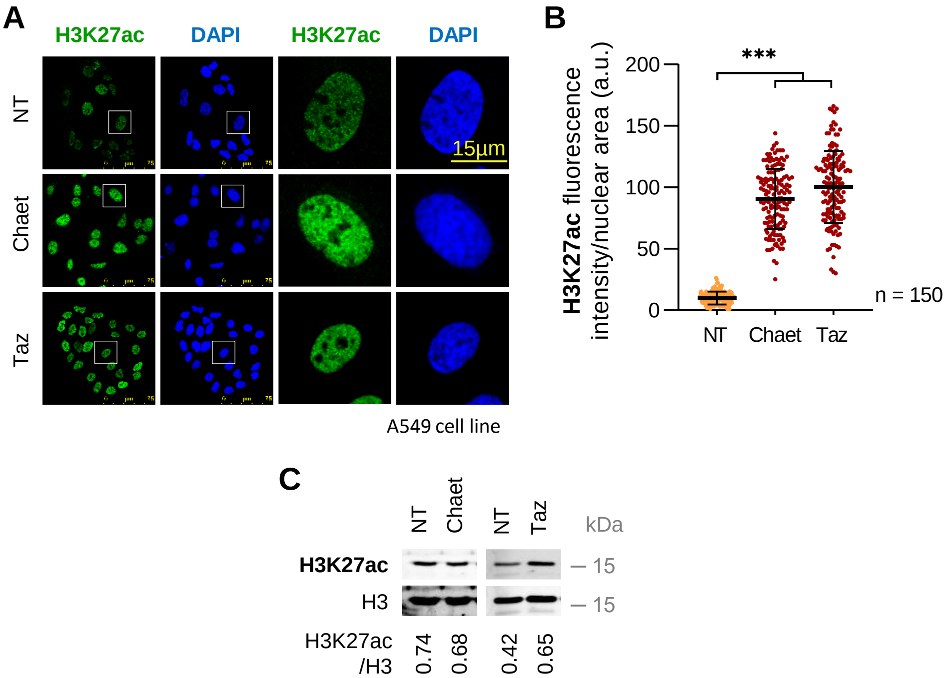

Figure 61. KMT inhibitors enhance the acetylation of H3K27 in A549 cells. Cells were cultured with 0.5% FBS for 48h and treated with 100 nM chaetocin and 50 nM tazemetostat for 24 h. **A.** Image panels show acetylation of H3K27 levels stained by IF and detected using confocal microscopy. DAPI was used to stain the nuclei. **B.** H3K27ac fluorescence intensity per nuclear area (a.u.) quantification of 150 cells (per condition) is represented in a dot plot. **C.** WB represents the levels of H3K27ac of histone acidic extracts. Histone H3 was used as loading control. H3K27ac/H3 ratio is shown. NT: Non-treated; Chaet: Chaetocin; Taz: Tazemetostat. Scale bar = 15 µm. ***: $p < 0.001$. a.u.: arbitrary units.

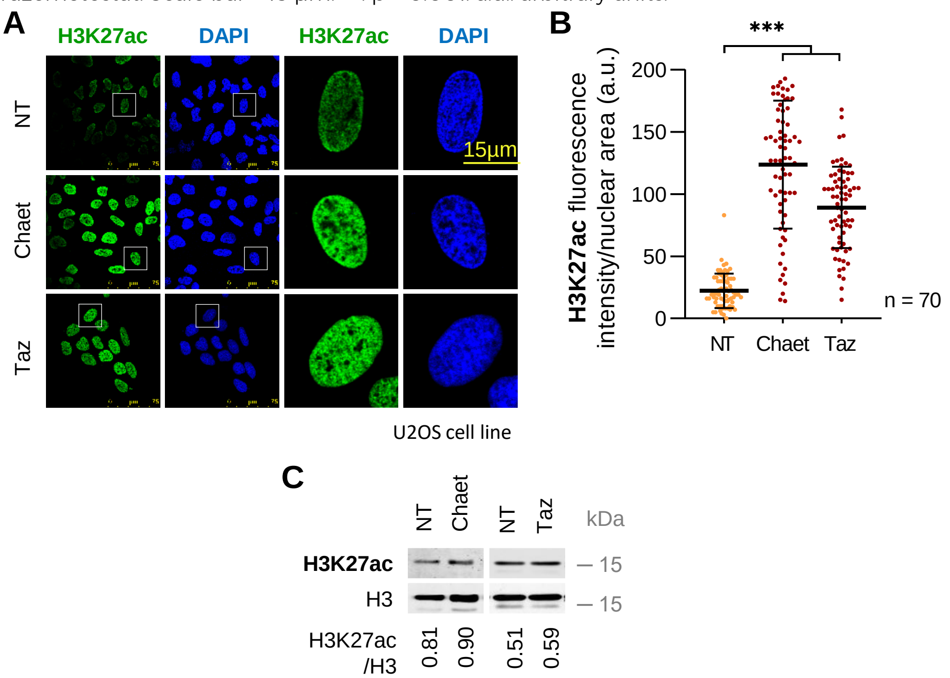

Figure 62. KMT inhibitors promote an increment of H3K27 acetylation in U2OS cells. Serum-deprived cells (0.5% FBS for 48 h) were treated with 100 nM chaetocin and 50 nM tazemetostat for 24 h. **A.** Panels show IF images of the levels of H3K27ac detected using confocal microscopy. DAPI was used to stain the nuclei. **B.** Dot plot illustrates quantification of H3K27ac fluorescence intensity per nuclear area (a.u.) of 70 cells (per condition). **C.** WB shows H3K27ac levels of histone acidic extracts. Histone H3 was used as loading control. H3K27ac/H3 ratio is shown. NT: Non-treated; Chaet: Chaetocin; Taz: Tazemetostat. Scale bar = 15 µm. ***: $p < 0.001$. a.u.: arbitrary units.

We also analyzed the trimethylation levels after treating cells with the KMTi. H3K27me3 levels experienced a significant drop after the KMTi treatments in A549 cells (**Figure 63**), detected by IF and WB. Moreover, we confirmed this reduction in U2OS cells (**Figure 64**). Thus, we conclude that KMTi weaken H3K27me3 levels and VRK1 mimics their effect through promoting acetylation and impairing trimethylation of H3K27.

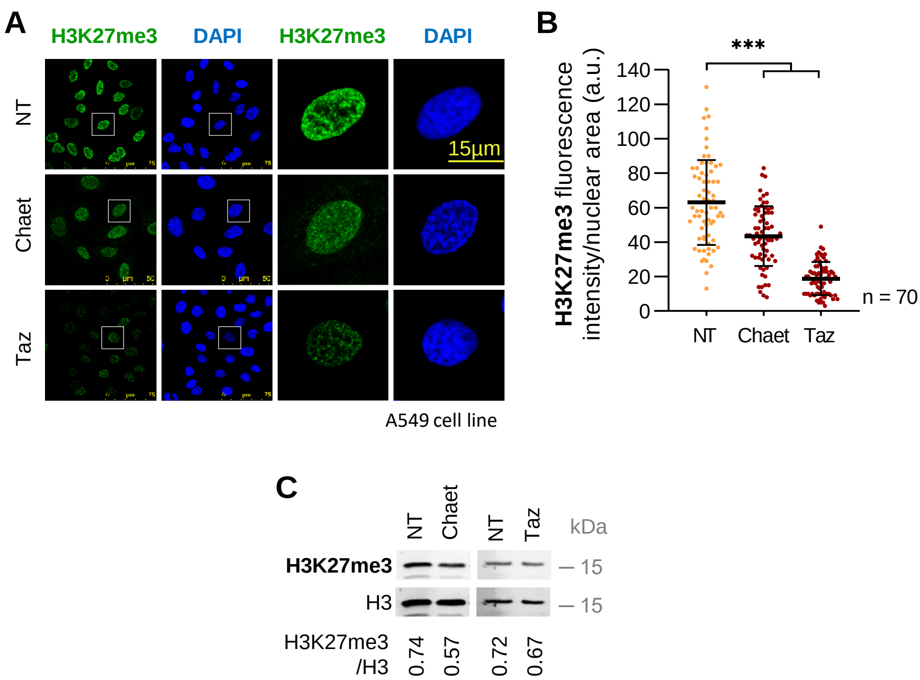

Figure 63. KMT inhibitors produce a drop on the trimethylation of H3K9 in A549 cells. Serum-deprived cells (0.5% FBS for 48 h) were treated with 100 nM chaetocin and 50 nM tazemetostat for 24 h. **A.** Panels show IF images of the levels of H3K27me3 detected using confocal microscopy. DAPI was used to stain the nuclei. **B.** Dot plot illustrates quantification of H3K27me3 fluorescence intensity per nuclear area (a.u.) of 70 cells (per condition). **C.** WB shows H3K27me3 levels of histone acidic extracts. Histone H3 was used as loading control. H3K27me3/H3 ratio is shown. NT: Non-treated; Chaet: Chaetocin; Taz: Tazemetostat. Scale bar = 15 µm. ***: $p < 0.001$. a.u.: arbitrary units.

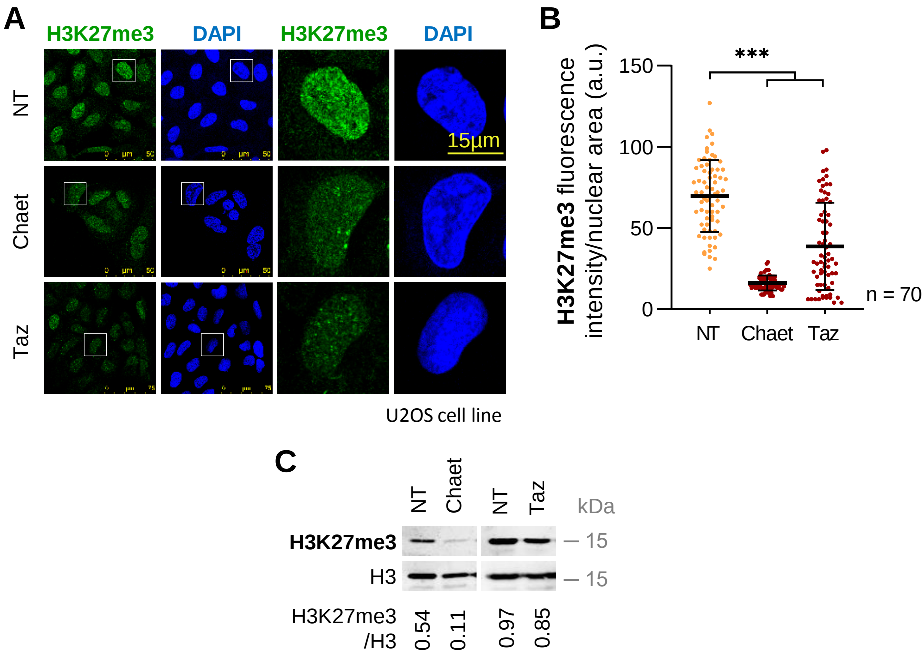

Figure 64. KMT inhibitors reduce trimethylated H3K27 in U2OS cells. Cells were cultured with 0.5% FBS for 48h and treated with 100 nM chaetocin and 50 nM tazemetostat for 24 h. A. Image panels show trimethylation of H3K27 levels stained by IF and detected using confocal microscopy. DAPI was used to stain the nuclei. B. H3K27me3 fluorescence intensity per nuclear area (a.u.) quantification of 70 cells (per condition) is represented in a dot plot. C. WB shows H3K27me3 levels of histone acidic extracts. Histone H3 was used as loading control. H3K27me3/H3 ratio is shown. NT: Non-treated; Chaet: Chaetocin; Taz: Tazemetostat. Scale bar = 15 µm. ***: $p < 0.001$. a.u.: arbitrary units.

4.1.4.5 The KDM inhibitors JMJD2i and ORY-1001 increase H3K27ac levels and decrease H3K27me3 levels

Finally, we evaluated KDMi effect on H3K27 modifications. JMJD2i and ORY-1001 were used for this purpose. As it was previously mentioned, JMJD2i inhibits the KDM JMJD2A, while ORY-1001 acts against LSD1.

We analyzed H3K27 acetylation after treating cells with 100 µM JMJD2i and 50 nM ORY-1001 for 24 h. We measured this mark by IF and WB in A549 and U2OS cell lines. The treatment with KDMi caused a significant decrease on H3K27ac levels compared with the non-treated cells by both techniques mentioned above in A549 (**Figure 65**). KDMi had a similar effect in U2OS cells, resulting in a significant reduction of H3K27ac detected by IF (**Figure 66**). However, the drop of this PTM was only perceived by WB with ORY-1001 treatment, since JMJD2i did not show any differences compared with the non-treated sample (**Figure 66**).

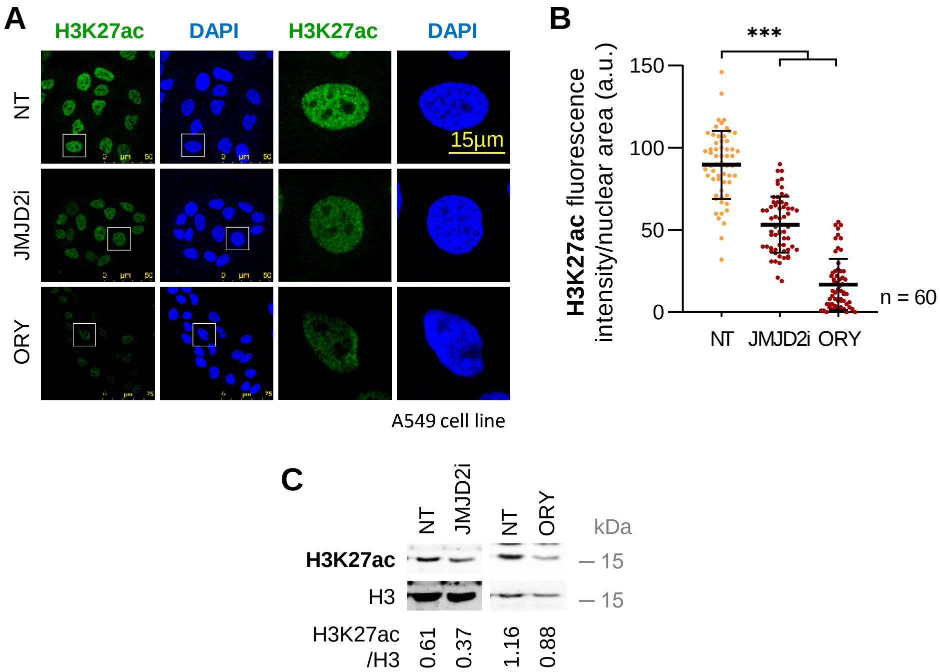

Figure 65. KDM inhibitors reduce the acetylation of H3K27 in A549 cells. Serum-deprived (0.5% FBS for 48 h) cells were treated with 100 µM JMJD2i and 50 nM ORY-1001 for 24 h. A. Image panels show acetylation levels of H3K27 stained by IF and detected using confocal microscopy. DAPI was used to stain the nuclei. B. H3K27ac fluorescence intensity per nuclear area (a.u.) quantification of 60 cells (per condition) is represented in a dot plot. C. WB shows H3K27ac levels of histone acidic extracts. Histone H3 was used as loading control. H3K27ac/H3 ratio is shown. NT: Non-treated; ORY: ORY-1001. Scale bar = 15 µm. ***: $p < 0.001$. a.u.: arbitrary units.

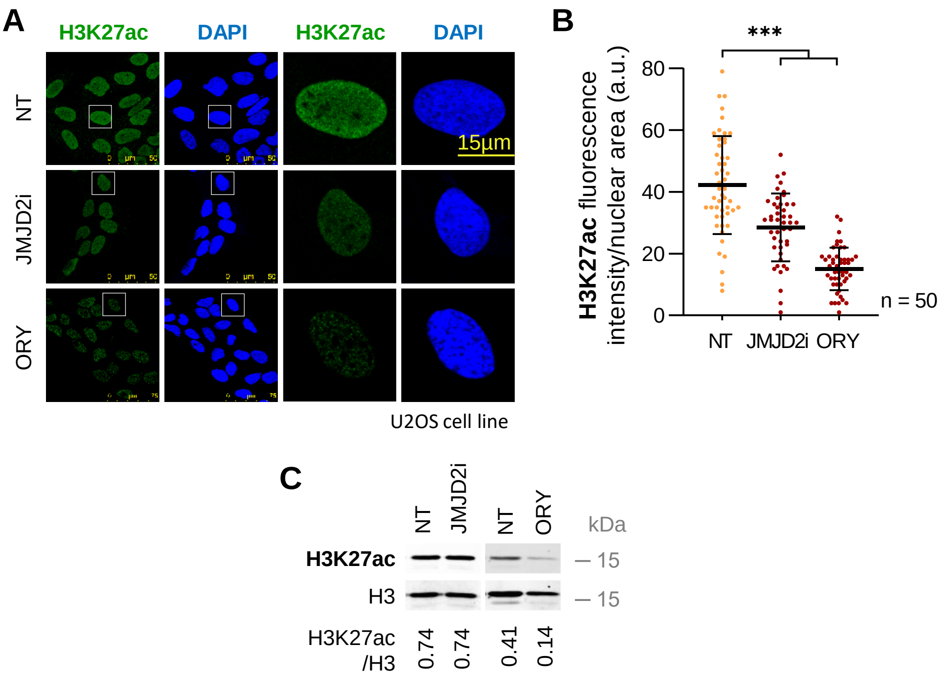

Figure 66. KDM inhibitors cause a drop on the acetylation of H3K27 in U2OS cells. Serum-reduced (0.5% FBS for 48 h) cells were treated with 100 µM JMJD2i and 50 nM ORY-1001 for 24 h. **A.** Panels show IF images of the levels of H3K27ac detected using confocal microscopy. DAPI was used to stain the nuclei. **B.** Dot plot shows quantification of H3K27ac fluorescence intensity per nuclear area (a.u.) of 50 cells (per condition). **C.** WB represents the levels of H3K27ac of histone acidic extracts. Histone H3 was used as loading control. H3K27ac/H3 ratio is shown. NT: Non-treated; ORY: ORY-1001. Scale bar = 15 µm. ***: $p < 0.001$. a.u.: arbitrary units.

Once we verified that KDMi altered the acetylation of H3K27, our next step was to examine their effect on H3K27 trimethylation levels. JMJD2i treatment promoted H3K27me3 compared with non-treated samples in A549 (**Figure 67**) and U2OS (**Figure 68**) cells. On the other hand, ORY-1001 treatment only showed differences in A549 cells (**Figure 67**) but did not reveal changes in U2OS cells (**Figure 68**).

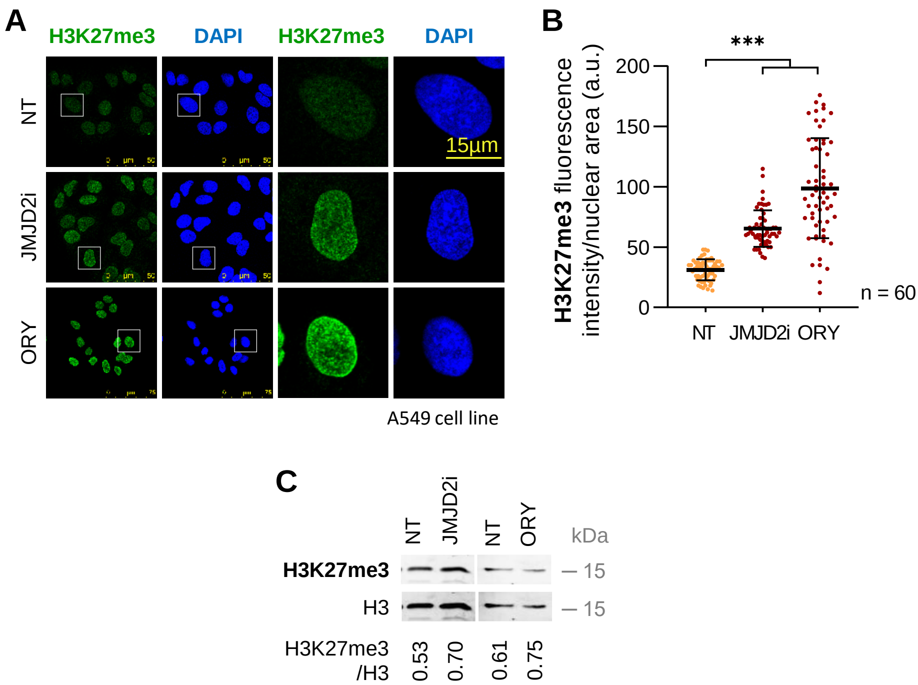

Figure 67. KDM inhibitors promote H3K27 trimethylation in A549 cells. Cells were cultured with 0.5% FBS for 48 h and treated with 100 µM JMJD2i and 50 nM ORY-1001 for 24 h. **A.** Panels show H3K27me3 levels stained by IF and detected using confocal microscopy. DAPI was used to stain the nuclei. **B.** Dot plot illustrates quantification of H3K27me3 fluorescence intensity per nuclear area (a.u.) of 60 cells (per condition). **C.** WB represents H3K27me3 levels of histone acidic extracts. Histone H3 was used as loading control. H3K27me3/H3 ratio is shown. NT: Non-treated; ORY: ORY-1001. Scale bar = 15 µm. ***: $p < 0.001$. a.u.: arbitrary units.

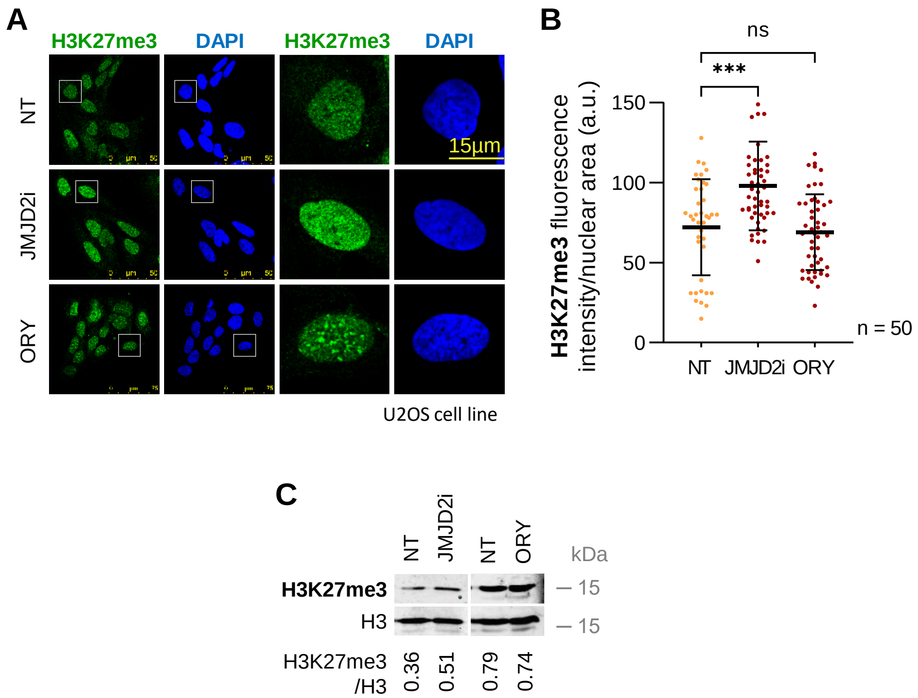

Figure 68. KDM inhibitors cause an increase of trimethylated H3K27 levels in U2OS cells. Cells were cultured with 0.5% FBS for 48 h and treated with 100 μM JMJD2i and 50 nM ORY-1001 for 24 h. A. Panels show IF images of the levels of H3K27me3 detected using confocal microscopy. DAPI was used to stain the nuclei. B. H3K27me3 fluorescence intensity per nuclear area (a.u.) quantification of 50 cells (per condition) is represented in a dot plot. C. WB shows H3K27me3 levels of histone acidic extracts. Histone H3 was used as loading control. H3K27me3/H3 ratio is shown. NT: Non-treated; ORY: ORY-1001. Scale bar = 15 μm. ***: $p < 0.001$; ns: non-significant. a.u.: arbitrary units.

4.1.5 VRK1 promotes an open chromatin state, facilitating H3K79me2

4.1.5.1 VRK1 knock down prevents H3K79me2

Finally, we tested H3K79me2 levels, another histone PTM linked to open chromatin. In this case, this modification is intimately related whit the acetylation of H4K16. In yeast, acetylation of histone H4 allosterically stimulates Dot1, the KMT responsible for H3K79[23]. Since we demonstrated that VRK1 alters H4K16ac, our next aim was to assess H3K79me2 levels in presence and absence of VRK1.

For this aim, it was determined whether H3K79me2 was influenced by VRK1 depletion. For this, we silenced VRK1 expression with two siRNA (siV-02 and siV-03), under both serum-completed and serum-reduced conditions. In A549 cells, we detected a reduction of H3K79me2 levels in absence of VRK1 (**Figure 69**) by IF and WB. This data indicates that VRK1 is able to modulate the dimethylation of H3K79, as VRK1 down expression causes a drop on this modification independently of mitogenic signals.

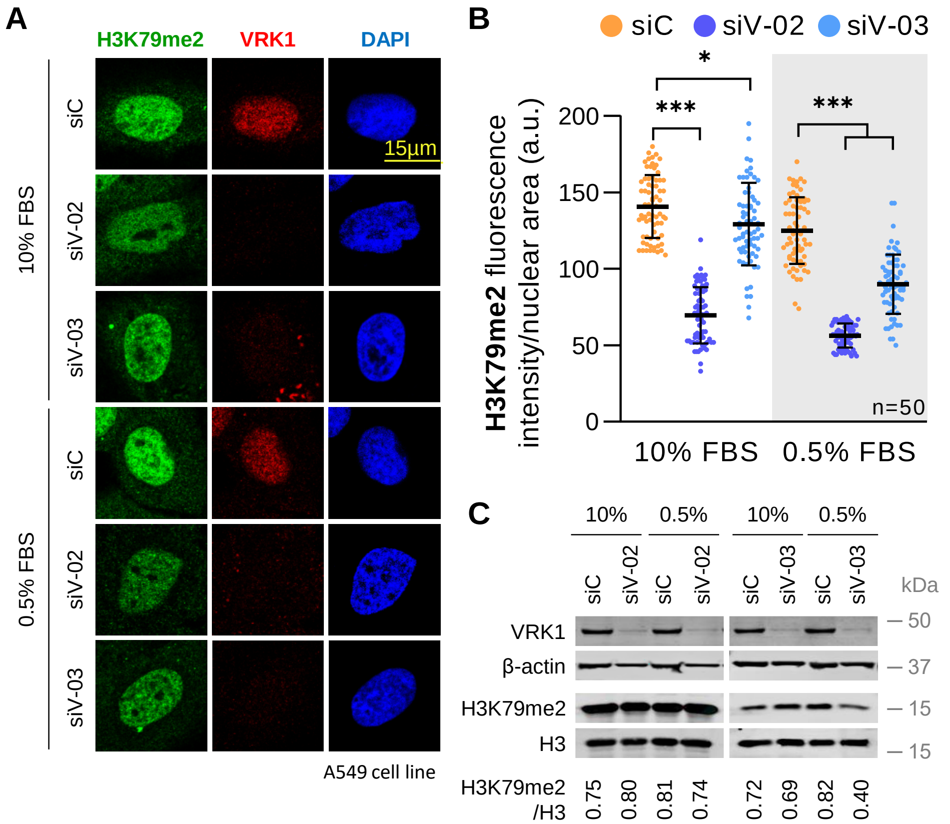

Figure 69. VRK1 depletion prevents H3K79 dimethylation in A549 cells. VRK1 was depleted using two siRNAs (siV-02 and siV-03) for 72 h. siC was used as off-target siRNA. Cells were cultured with 10% or 0.5% of FBS for 48 h. **A.** Panels show IF images of the levels of H3K79me2 detected using confocal microscopy. DAPI was used to stain the nuclei and VRK1 as knock-down control. **B.** H3K79me2 fluorescence intensity per nuclear area (a.u.) quantification of 50 cells (per condition) is represented in a dot plot. **C.** WB represents H3K79me2 levels of histone acidic extracts. VRK1, β-actin and histone H3 were used as knock-down and loading control, respectively. H3K79me2/H3 ratio is shown. Scale bar = 15 µm. ***: $p < 0.001$; *: $p < 0.05$. a.u.: arbitrary units.

4.1.5.2 The KMT inhibitor EPZ004777 impairs H3K79me2 levels

To continue with this modification, we explore the role of different treatments that target the enzymes that control this PTM. H3K79 methylation is regulated by DOT1L. However, the histone-modifying enzyme that demethylated this residue is still unknown (**Figure 70**). For this reason, we studied H3K79me2 levels after the KMT inhibitor EPZ004777 treatment. This drug blocks the activity of the methyltransferase DOT1L and, consequently, the H3K79 methylation[168].

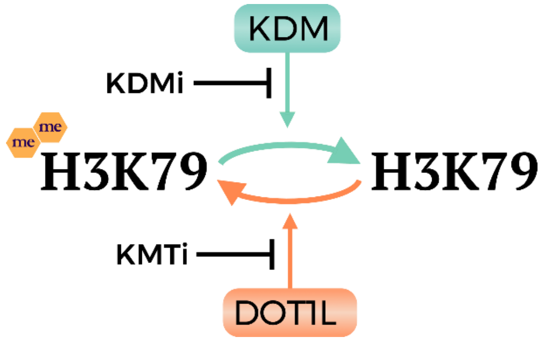

Figure 70. Regulation of H3K79 dimethylation. Scheme of the principal regulation of the H3K79 dimethylation by DOT1L and some KDM. Blue and orange arrows promote a demethylated and a dimethylated state, respectively. Black lines indicate the steps that KMTi and KDMi block. Yellow hexagon (me): methylation.

To achieve this aim, A549 cells were incubated with 80 nM of EPZ004777 for 24 h. H3K79me2 levels showed a significant drop after EPZ004777 treatment compared with non-treated cells by IF and WB (**Figure 71**). This result suggests that the inhibition of DOT1L activity has the same effect of the down regulation of VRK1 expression.

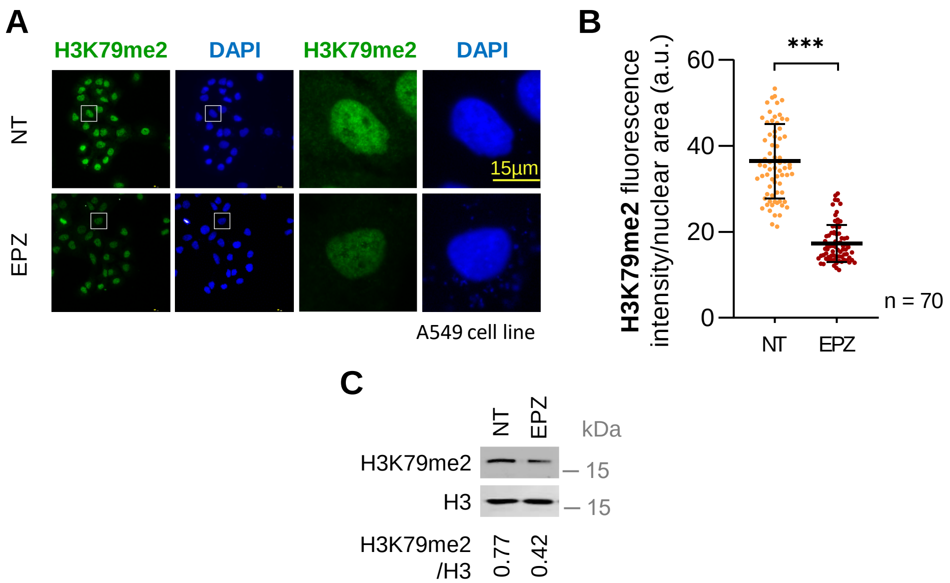

Figure 71. KMT inhibitor EPZ004777 produces a decrease on H3K79 dimethylation in A549 cells. Cells were cultured with 0.5% FBS for 48h and treated with 80 nM EPZ004777 for 24 h. A. Panels show H3K79me2 levels stained by IF and detected using confocal microscopy. DAPI was used to stain the nuclei. B. H3K79me2 fluorescence intensity per nuclear area (a.u.) quantification of 70 cells (per condition) is represented in a dot plot. C. WB represents H3K79me2 levels of histone acidic extracts. Histone H3 was used as loading

control. H3K79me2/H3 ratio is shown. NT: Non-treated; EPZ: EPZ004777. Scale bar = 15 μm. ***: $p < 0.001$. a.u.: arbitrary units.

4.1.5.3 The HAT inhibitor MG149 produces a reduction of H3K79me2 levels

To further characterize the regulation of H3K79, we sought to compare EPZ004777-mediated inhibition of DOT1L (KMT responsible for H3K79 methylation) and MG149-mediated inhibition of TIP60 (HAT responsible for H4K16 acetylation), given the relationship between them[23]. Moreover, since we demonstrated in prior sections of this work that VRK1 is able to modulate these two PTMs, we included two additional conditions to the previous experiment: VRK1 depletion and MG149 treatment.

For this aim, VRK1 was depleted using the siRNA siV-02. Then, cells were treated with 80 nM of EPZ004777 or 1 µM MG149 for 24 h and H4K16ac and H3K79me2 levels were analyzed by IF. Firstly, we confirmed that MG149 and VRK1 depletion both impaired H4K16ac (**Figure 72 A**). Moreover, H4K16ac levels showed a decrease when siC-cells were treated with EPZ004777 and this decrease was higher when VRK1 was knocked-down (**Figure 72 A**). Secondly, we verified our prior result about the impact of VRK1 absence and EPZ004777 treatment on H3K79me2 (**Figure 72 B**). Furthermore, siC-cells treated with MG149, which have TIP60 inactive and DOT1L active, showed a decrease on H3K79me2 (**Figure 72 B**). In the case of VRK1-depleted cells treated with MG149, we observed similar results.

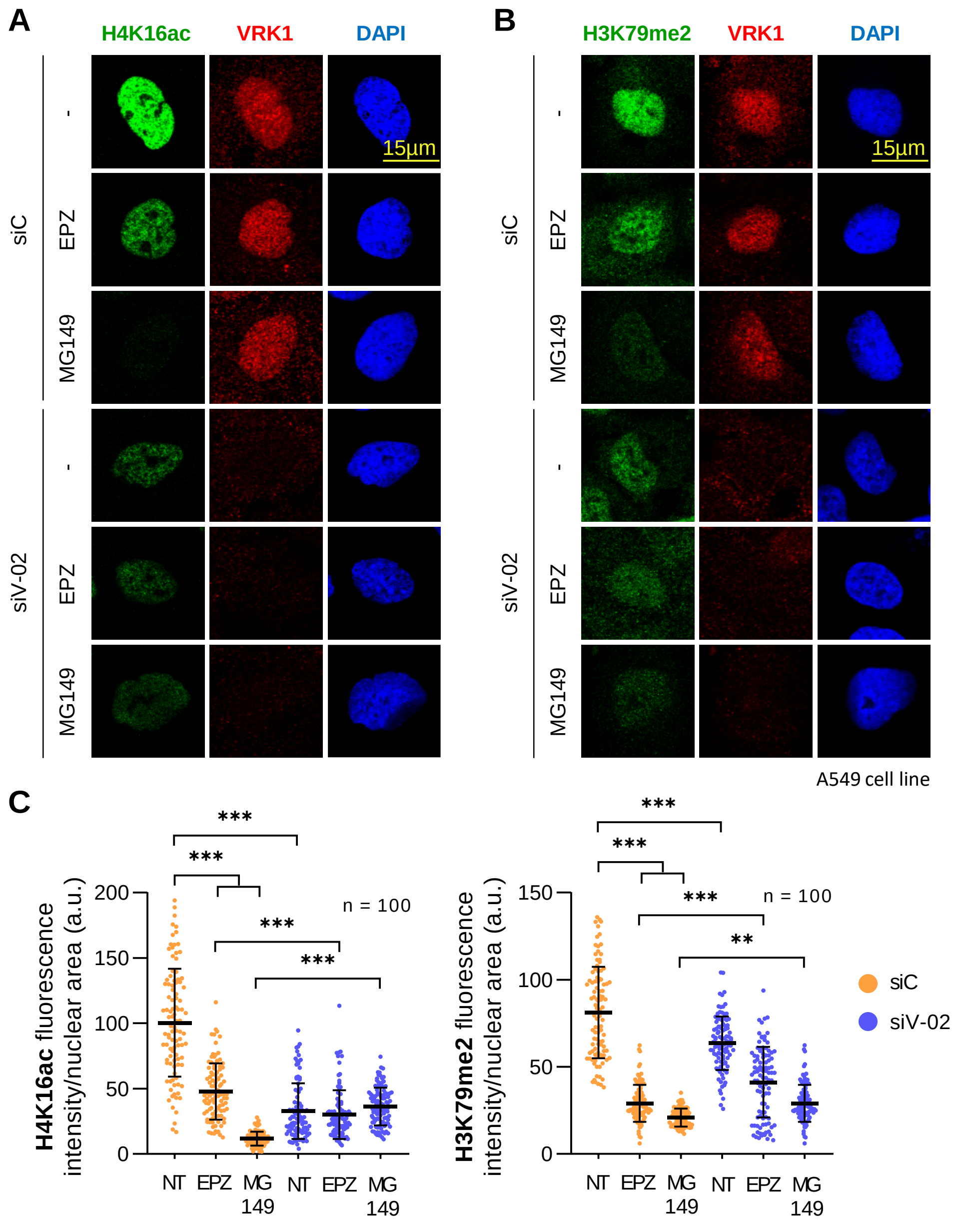

Figure 72. MG149 treatment impairs H4K16ac and, consequently, H3K79me2 levels in A549 cell line. Cells were cultured with 0.5% FBS for 48 h and treated with 80nM EPZ004777 or 1 µM MG149 for 24 h. **A, B.** Image panels show acetylation of H4K16 (A) and dimethylation of H3K79 (B) levels stained by IF and detected using confocal microscopy. DAPI was used to stain the nuclei. Scale bar = 15 µm. **C, D.** H4K16ac (C) and H3K79me2 (D) fluorescence intensity per nuclear area (a.u.) quantification of 100 cells (per condition) is represented in a dot plot. NT: Non-treated; EPZ: EPZ004777. Scale bar = 15 µm. ***: $p < 0.001$; **: $p < 0.01$. a.u.: arbitrary units.

4.2 VRK1 interacts with epigenetic enzymes

After we demonstrated that VRK1 can alter chromatin structure and PTMs pattern, we sought to investigate its implication in the modulation of writer and eraser enzymes that control these PTMs. For this reason, our next step was to identify the possible interactions of VRK1 with different epigenetic enzymes.

4.2.1 VRK1 interacts with the acetyltransferase PCAF

Among all the HATs, PCAF is one of the enzymes described as a modulator of H3K9 acetylation (**Figure 31**)[27]. To study the potential interaction of VRK1 with this acetyltransferase, an *in vitro* interaction experiment was performed using a fragment of PCAF (residues from 352 to 832) fusion with GST. For that purpose, we incubated a constant amount of 1 µg VRK1-His and increasing amounts of GST-PCAF(352-832) overnight at 4ºC. Then, we performed GST-PCAF pull-down. Finally, we observed that PCAF is able to interact with VRK1 *in vitro* in a dose-dependent manner (**Figure 73 A**). This indicated that both proteins are able to form a direct stable complex by themselves *in vitro*. To confirm this interaction *in vivo*, HEK293T cells were transfected with PCAF-Flag plasmid that express its human protein, and a reciprocal immunoprecipitation of PCAF and endogenous VRK1 was performed. The PCAF-VRK1 complex was detected in both immunoprecipitations indicating PCAF and VRK1 can interact in cells (**Figure 73 B**). In addition, we determined this interaction by transfecting both tagged proteins, PCAF-Flag and VRK1-HA. The tagged proteins were immunoprecipitated and VRK1-HA and PCAF-Flag were detected in both precipitations confirming the aforementioned results (**Figure 73 C**).

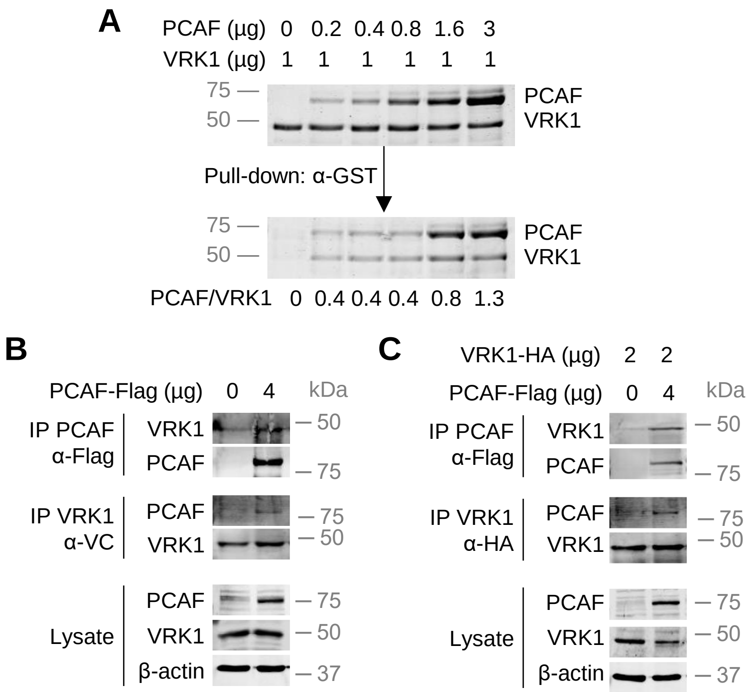

Figure 73. VRK1 directly interacts with PCAF *in vitro* and *in vivo*. A. WB shows the concentration dependent *in vitro* interaction between bacterially expressed and purified VRK1-His protein and increasing amounts of purified GST-PCAF (352-832 aa) in a GST pulldown *in vitro* assay. 1 µg VRK1-His and the indicated amounts of GST-PCAF were mixed and incubated overnight at 4°C. GST-PCAF pull-down was performed using glutathione beads. At the bottom is shown the quantification of the interaction. Empty-GST protein was used as negative control. The upper WB shows the control loading proteins. B. Interaction of endogenous VRK1 with tagged PCAF-Flag in HEK293T cells. The interaction was detected by reciprocal immunoprecipitations with anti-VRK1 and anti-Flag rabbit antibodies. C. Interaction of VRK1-HA and PCAF-Flag expressed from plasmids and transfected in HEK293T cells. The interaction was detected by reciprocal immunoprecipitations with anti-HA and anti-Flag rabbit antibodies.

4.2.2 VRK1 interacts with the histone deacetylases HDAC1, SIRT1 and SIRT2

Continuing with another group of epigenetic enzymes, HDACs are responsible for histone deacetylation. In this case, HDAC1 is relatively low substrate-specific and a possible candidate to deacetylate different histone residues (**Figure 31** and **Figure 52**), while SIRT1 and SIRT2 have been described as specific enzymes for H4K16 deacetylation (**Figure 12**)[34,169].

Firstly, we aimed to analyze HDAC1 and VRK1 interaction by reciprocal immunoprecipitations. For that purpose, HEK293T cells were transfected to express HDAC1-Flag protein. Then, HDAC1 or endogenous VRK1 were immunoprecipitated and the interaction of both proteins was assessed via immunoblot (**Figure 74 A**). To confirm this result, this interaction was evaluated with both tagged proteins (HDAC1-Flag and VRK1-HA) in HEK293T. The HDAC1-VRK1 complex was detected in both immunoprecipitations demonstrating that HDAC1 and VRK1 can interact (**Figure 74 B**).

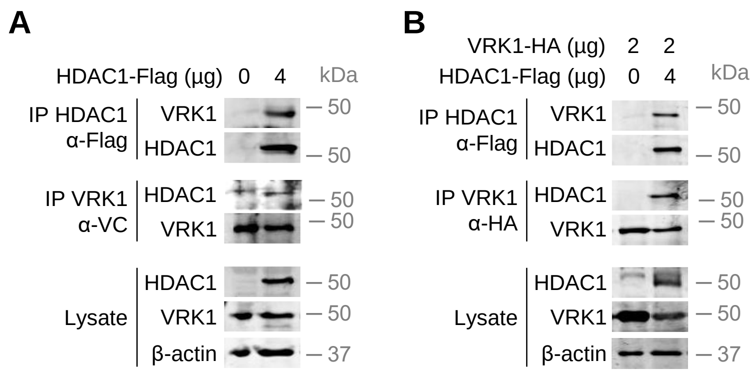

Figure 74. VRK1 interacts with HDAC1. A. Interaction of endogenous VRK1 with tagged HDAC1-Flag in HEK293T cells. The interaction was detected by reciprocal immunoprecipitations with anti-VRK1 and anti-Flag rabbit antibodies. B. Interaction of VRK1-HA and HDAC1-Flag expressed from plasmids and transfected in HEK293T cells. The interaction was detected by reciprocal immunoprecipitation with anti-HA and anti-Flag rabbit antibodies.

We also studied the relationship between SIRT1 and VRK1. We performed an IP assay between SIRT1-Flag and endogenous VRK1 in HEK293T. The experiment demonstrated how both proteins interact because both of them were detected in the corresponding immunoblot (**Figure 75 A**). Moreover, these reciprocal IPs were carried out with tagged VRK1-HA, which confirmed the previous outcome due to the detection of SIRT1 and VRK1 in the corresponding IP (**Figure 75 B**).

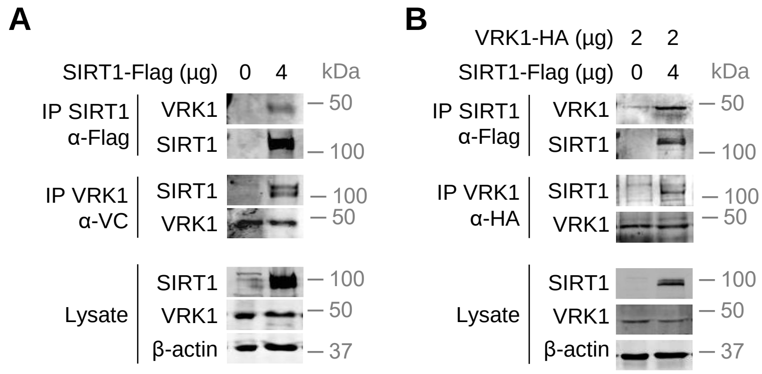

Figure 75. VRK1 interacts with SIRT1. A. Interaction of endogenous VRK1 with tagged SIRT1-Flag in HEK293T cells. The interaction was detected by reciprocal immunoprecipitations with anti-VRK1 and anti-Flag rabbit antibodies. B. Interaction of VRK1-HA and SIRT1-Flag expressed from plasmids and transfected in HEK293T cells. The interaction was detected by reciprocal immunoprecipitation with anti-HA and anti-Flag rabbit antibodies.

Finally, we studied whether VRK1 and SIRT2 were able to form a stable protein complex. For this aim, we first determined the in vitro interaction between tagged GST-VRK1 and SIRT2-His, using bacterially expressed and purified proteins, which allows us to detect a direct and stable protein interaction. SIRT2 directly and stably interacted with VRK1 in a dose dependent manner (**Figure 76 A**). Next, to identify what VRK1 region is interacting with SIRT2, several GST-VRK1 constructs spanning different regions of VRK1 were expressed in bacteria, and purified fusion proteins were used in pulldown assays with SIRT2-His as target. These constructs corresponded to VRK1 catalytic site (residues 1 to 332), C-terminal domain (residues 227 to 396) and a truncated variant at C-terminal that does not allow for proper folding (VRK1[R358X]). The common region of interaction of VRK1 corresponds to residues 1-262, which comprise kinase domain, and includes both the ATP binding site and the catalytic site[126]. We saw that SIRT2 interacted with the catalytic site and the truncated variant, while it did not interact with the low complexity C-terminal VRK1 regulatory domain (**Figure 76 B**).

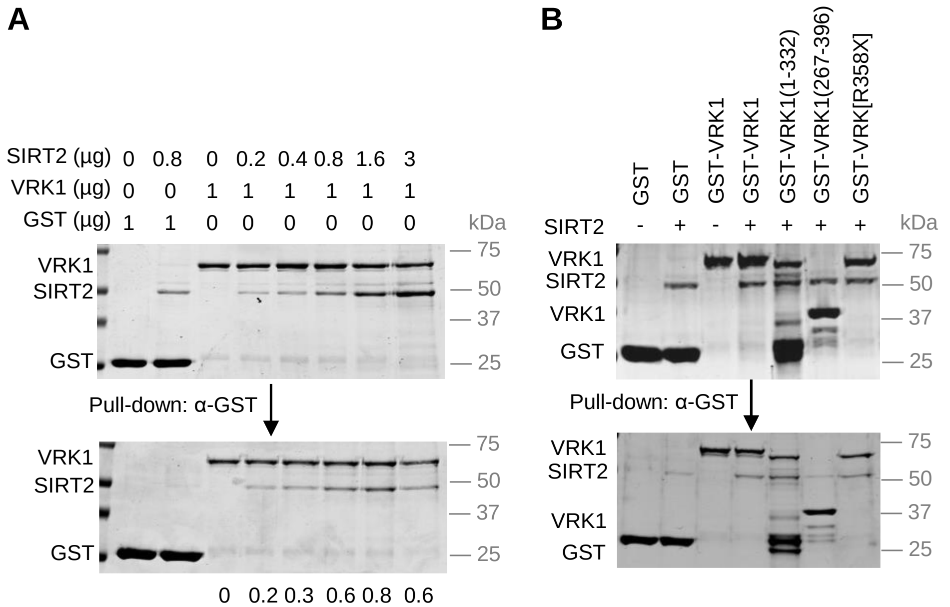

Figure 76. VRK1 directly interacts with SIRT2 *in vitro*. A. WB shows the concentration dependent *in vitro* interaction between bacterially expressed and purified GST-VRK1 protein and increasing amounts of purified His-SIRT2 in a GST pulldown *in vitro* assay. GST-VRK1 and the indicated amounts of His-SIRT2 were mixed and incubated overnight at 4°C. GST-VRK1 pull-down was performed using glutathione beads. In the bottom of WB, it is shown the SIRT2 levels per VRK1 quantification. Empty-GST protein was used as negative control. The upper WB shows the control loading proteins. B. Detection of the VRK1 region of interaction with SIRT2. 2µg of His-SIRT2 and different GST-VRK1 constructs were used in the pulldown assay as described in A.

To confirm the VRK1-SIRT2 interaction *in vivo*, HEK293T cells were transfected to express SIRT2-Flag, which was able to interact with the endogenous VRK1 in reciprocal IP experiments (**Figure 77 A, top WB**). The IP of the endogenous VRK1 protein with an antibody targeting its C-terminus confirmed that this region of VRK1 is not involved in the interaction, and thus the N-terminus is available for recognition and interaction with SIRT2-Flag (**Figure 77 A, center WB**). In addition, we checked whether SIRT2 and VRK1 colocalize in the nucleus, which was confirmed by IF in A549 cells (**Figure 78**). This VRK1-SIRT2 interaction was further confirmed when cells were transfected to express both tagged proteins and detected in reciprocal immunoprecipitation experiments (**Figure 77 B**). Furthermore, HEK293T cells were transfected to express

SIRT2-HA variants with a mutation in a known phosphorylation site that participates in the regulation of the cell cycle progression (residue 368)[34]. We carried out IP experiments and observed that VRK1-SIRT2 interaction is independent of the SIRT2-S368 mutation to either Ala (phosphorylation-null mutant) or Glu (phosphorylation-mimetic mutant) (**Figure 77** C).

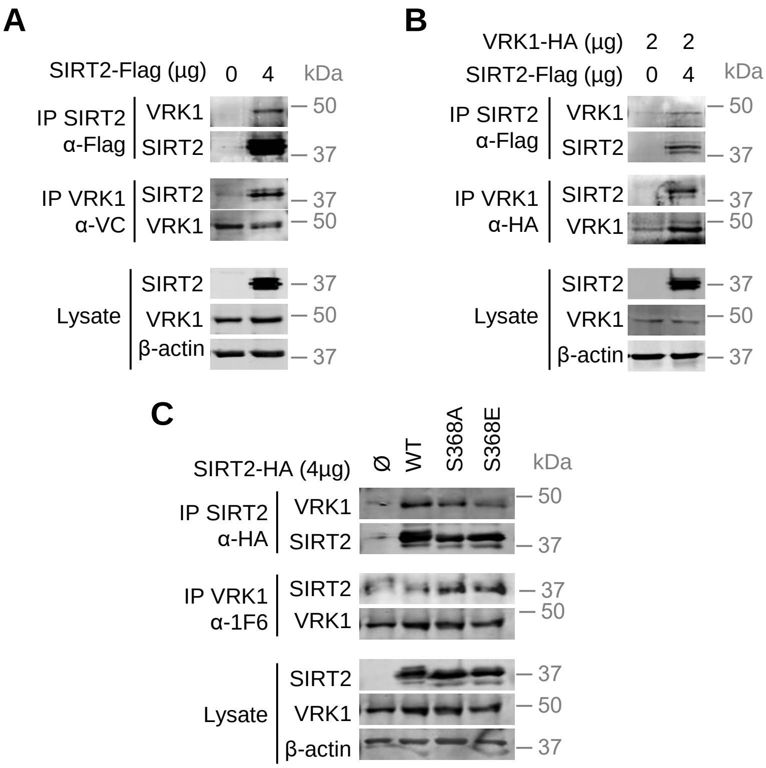

Figure 77. VRK1 interacts with SIRT2 *in vivo*. A. Interaction of endogenous VRK1 with a transfected and tagged SIRT2-flag in HEK293T cells. The interaction was detected by reciprocal immunoprecipitation with anti-VRK1 and anti-Flag rabbit antibodies. B. Interaction of VRK1-HA and SIRT2-flag expressed from plasmids transfected in HEK293T cells that were detected in reciprocal immunoprecipitations with anti-HA and anti-Flag rabbit antibodies. C. Interaction of endogenous VRK1 and SIRT2-HA mutants expressed from plasmids transfected in HEK293T cells that were detected in reciprocal immunoprecipitation with anti-VRK1 and anti-HA rabbit antibodies.

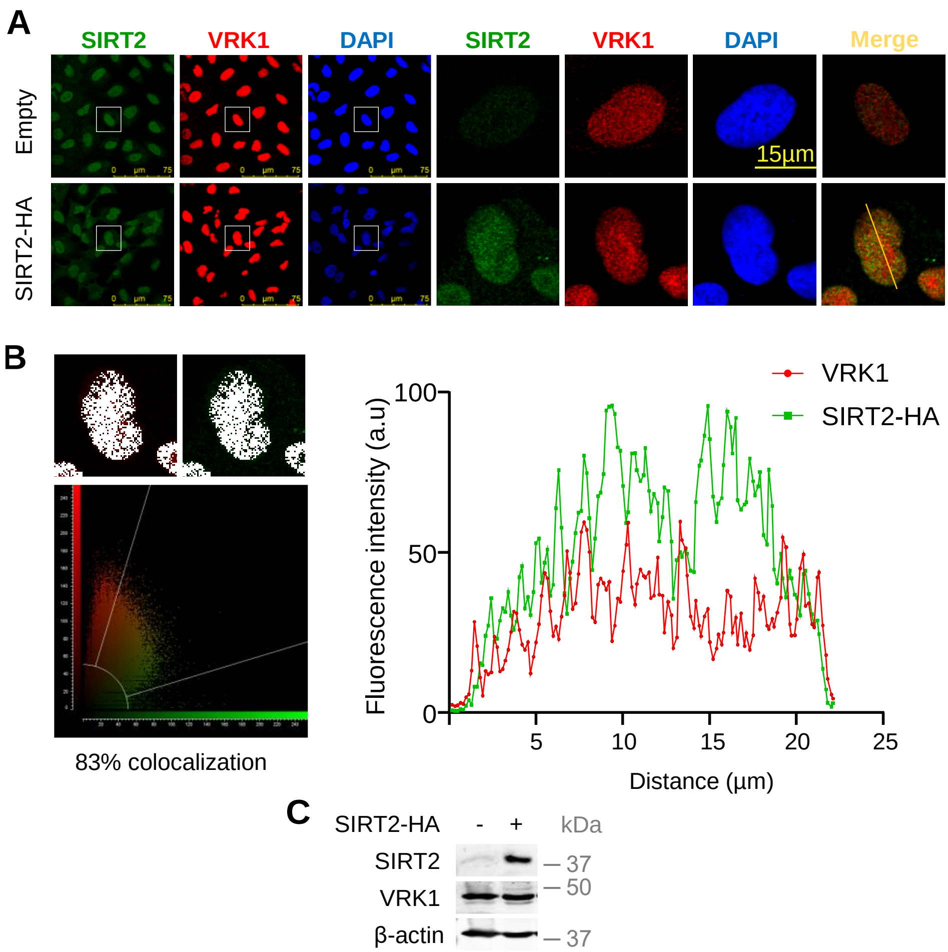

Figure 78. Nuclear colocalization of VRK1 and SIRT2 proteins. A. Fluorescence images show colocalization of endogenous VRK1 and transfected SIRT2-HA in A549 cells. Field images are shown on the left and the selected individual cell to show detail is marked by a box and shown on the right. B. Overlap of the immunofluorescence signals of VRK1 (red) and SIRT2 (green) along the plane (line) indicated in the merged image at the right. C. Immunoblot showing the expression of endogenous VRK1 and transfected SIRT2-HA in A549 cells. β-actin was used as loading control.

4.2.2.1 SIRT2 inhibits the kinase activity of VRK1 *in vitro*

Once we verified that VRK1 and SIRT2 are able to form a stable complex and due to them having opposite roles on H4K16 acetylation, it is likely that there is a relationship between these two enzyme activities. Therefore, we tested whether VRK1 or SIRT2 activity could be altered as a result of their interaction, and thus permitting the deacetylation of H4K16 mediated by SIRT2. One hypothesis is that VRK1 losses its activity, since SIRT2 interacts with the catalytic domain of VRK1. To achieve this aim, we performed an initial *in vitro* kinase assay with both proteins expressed and purified in bacteria. VRK1 by itself has a strong autophosphorylation activity that was inhibited in the presence of SIRT2 (**Figure 79 A**). Next, we tested different concentrations of SIRT2 to detect both the inhibitory effect on VRK1 autophosphorylation, and on H3 phosphorylation, which is a direct target of VRK1[136]. SIRT2 inhibited both the VRK1 autophosphorylation as well as the phosphorylation of histone H3 in a dose-dependent manner with an IC_{50} of 190 nM and 150 nM, respectively (**Figure 79 B**).

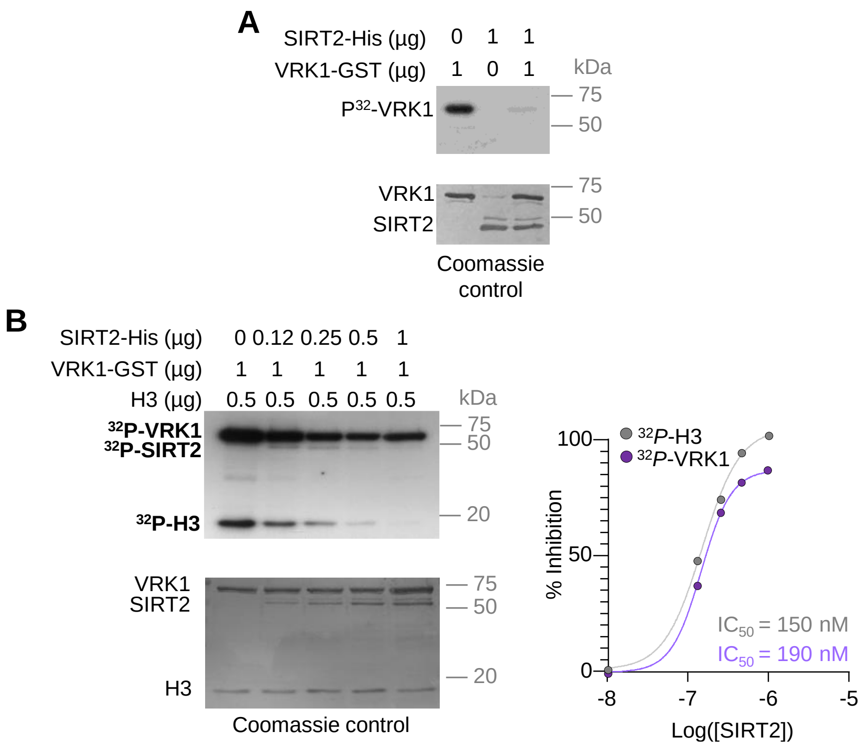

Figure 79. Inhibition of VRK1 kinase activity by SIRT2. A. SIRT2 inhibits the autophosphorylation of VRK1. *In vitro* kinase assay was performed for 45 min at 37 °C to detect the phosphorylation of VRK1 purified protein. The exposure time to detect the autophosphorylation VRK1 is two h. **B.** SIRT2 dose-dependent inhibition of the kinase activity of VRK1 in autophosphorylation and transphosphorylation with histone H3 as substrate. The exposure time to detect the autophosphorylation VRK1 and H3 phosphorylation is forty-eight h. Below the WB, the IC_{50} for both activities is shown.

4.2.3 VRK1 interacts with the methyltransferase SETDB1

Following the identification of possible VRK1 interactors, we studied the methyltransferase SETDB1. This KMT is responsible for the H3K9 methylation (**Figure 31**)[170]. To establish if VRK1 and SETDB1 are able to interact, we performed an *in vivo* interaction assay by reciprocal immunoprecipitation of endogenous VRK1 and SETDB1-Flag in HEK293T. VRK1 was detected in the SETDB1 immunoprecipitated, while SETDB1 was observed in the VRK1 immunoprecipitated (**Figure 80 A**). Furthermore, these reciprocal immunoprecipitations were carried out with tagged VRK1-HA and SETDB1-Flag. SETDB1 tagged protein was detected in the VRK1-HA immunoprecipitation (**Figure 80 B**), confirming the previous results that VRK1 and SETDB1 could be interacting, being part of an enzymatic complex. However, the recognition of VRK1-HA in the SETDB1-Flag immunoprecipitation was not clear.

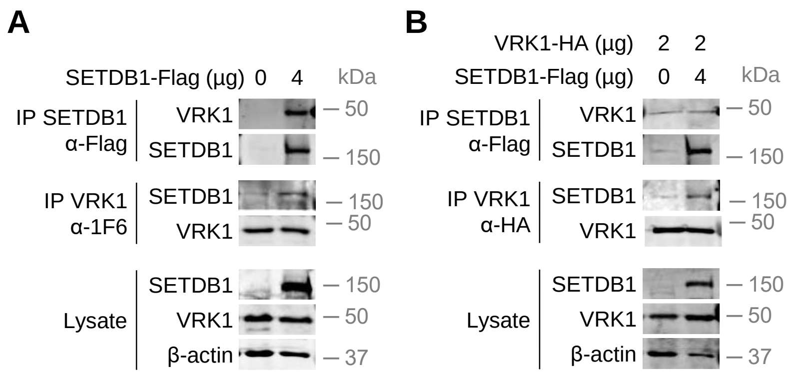

Figure 80. VRK1 interacts with SETDB1. A. Interaction of endogenous VRK1 with tagged SETDB1-Flag in HEK293T cells. The interaction was detected by reciprocal immunoprecipitations with anti-VRK1 and anti-Flag rabbit antibodies. B. Interaction of VRK1-HA and SETDB1-Flag expressed from plasmids and transfected in HEK293T cells. The interaction was detected by reciprocal immunoprecipitation with anti-HA and anti-Flag rabbit antibodies. β-actin was used as loading control.

4.2.4 VRK1 interacts with the demethylases LSD1, JMJD1A, JMJD2A

To further elucidate the interactions of VRK1, we aimed to identify demethylase enzymes that can participate together with VRK1 in the control of histone PTMs. In this case, LSD1, JMJD1A and JMJD2A, associated with H3K4 and H3K9 (**Figure 31**) demethylation, were the chosen enzymes for this purpose[171]. We expressed increasing amounts of Myc-tagged LSD1 in HEK293T cells and performed Myc-tag and endogenous VRK1 immunoprecipitations. These immunoprecipitations coupled to WB analysis confirmed that Myc-tagged LSD1 interacted with endogenous VRK1 in a dose-dependent manner (**Figure 81 A, top WB**) and reciprocal immunoprecipitation of endogenous VRK1 revealed this interaction with Flag-tagged LSD1 (**Figure 81 A, center WB**). Likewise, we also studied the interaction of LSD1-Myc and VRK1-HA, detecting both proteins in reciprocal immunoprecipitations, again in a dose-dependent manner (**Figure 81 B**).

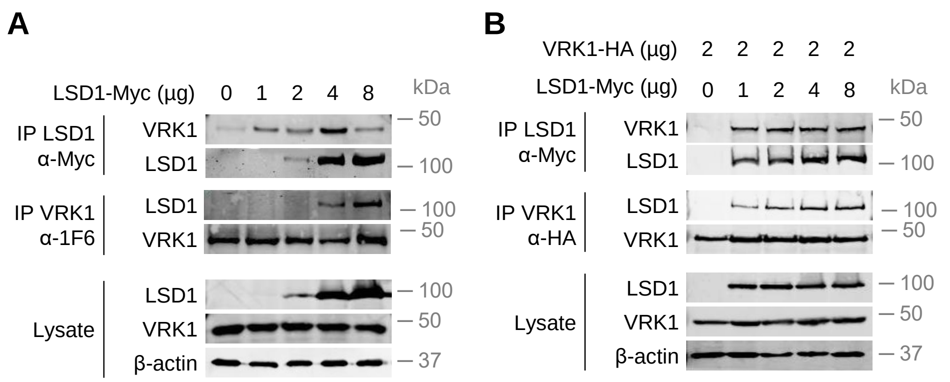

Figure 81. VRK1 interacts with LSD1. A. Concentration-dependent interaction between endogenous VRK1 with tagged LSD1-Myc in HEK293T cells. The interaction was detected by reciprocal immunoprecipitations with anti-VRK1 and anti-Myc rabbit antibodies. B. Concentration-dependent interaction of VRK1-HA and LSD1-Myc expressed from plasmids and transfected in HEK293T cells. The interaction was detected by reciprocal immunoprecipitation with anti-HA and anti-Myc rabbit antibodies.

To investigate a potential interplay between JMJD1A and VRK1, we analyzed whether they interact in an immunoprecipitation assay. For this aim, HEK293T cells were transfected to express JMJD1A-V5 and we carried out reciprocal IPs of both VRK1 and JMJD1A-V5 proteins. VRK1 was detected in JMJD1A immunoprecipitation, while JMJD1A was detected in the VRK1 immunoprecipitation (**Figure 82 A**). To further characterize this interaction, we performed the same experiment, but using HA-tagged VRK1. In this case, the interaction was again detected in both immunoprecipitations, demonstrating that JMJD1A and VRK1 can interact (**Figure 82 B**).

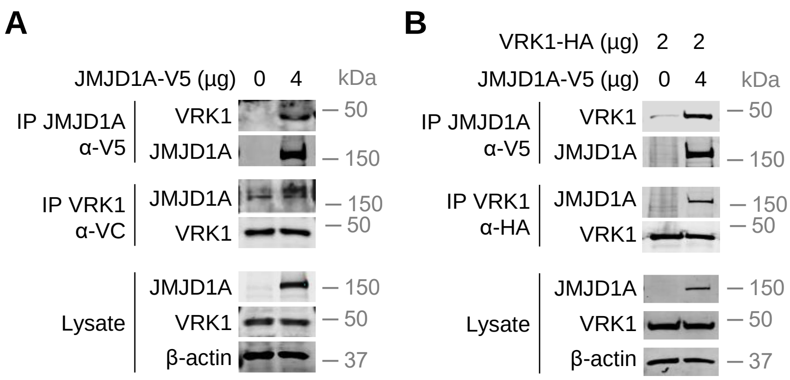

Figure 82. VRK1 interacts with JMJD1A. A. Interaction of endogenous VRK1 with a transfected and tagged JMJD1A-V5 plasmid in HEK293T cells. The interaction was detected by reciprocal immunoprecipitations with anti-VRK1 and anti-V5 rabbit antibodies. B. Interaction of VRK1-HA and JMJD1A-V5 expressed from plasmids and transfected in HEK293T cells. The interaction was detected by reciprocal immunoprecipitation with anti-HA and anti-V5 rabbit antibodies.

Finally, we analyzed the possible interaction of VRK1 with the KDM JMJD2A. To decipher its interaction *in vivo*, reciprocal immunoprecipitations of HA-tagged JMJD2A and endogenous VRK1 were performed with HEK293T cells. VRK1 seemed to be detected in the HA immunoprecipitation, indicating that JMJD2A and VRK1 may interact (**Figure 83 A, top WB**). However, the detection of JMJD2A in the VRK1 immunoprecipitated was less clear (**Figure 83 A, center WB**). In addition, we determined this interaction transfecting both tagged proteins, JMJD2A-HA and VRK1-Myc. The tagged proteins were immunoprecipitated and both VRK1-Myc and JMJD2A-HA were detected in both immunoprecipitations, confirming the previous result (**Figure 83 B**).

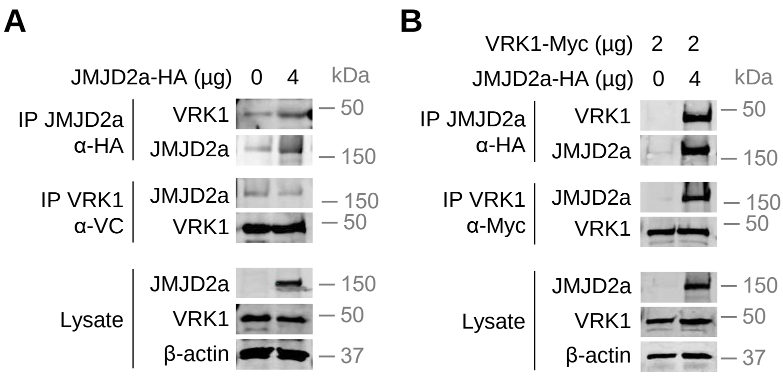

Figure 83. VRK1 interacts with JMJD2A. A. Interaction of endogenous VRK1 with a transfected and tagged JMJD2A-HA plasmid in HEK293T cells. The interaction was detected by reciprocal immunoprecipitations with anti-VRK1 and anti-HA rabbit antibodies. B. Interaction of VRK1-Myc and JMJD2A-HA expressed from plasmids and transfected in HEK293T cells. The interaction was detected by reciprocal immunoprecipitation with anti-Myc and anti-HA rabbit antibodies.

4.3 Characterization of VRK-IN-1, a VRK1 inhibitor

4.3.1 VRK-IN-1 inhibitor impairs the VRK1 kinase activity

To alter the activity of VRK1, the development of specific inhibitors is necessary. Because of its structural characteristics, VRK1 is not inhibited by existing inhibitors targeting different kinase families of the human kinome. VRK-IN-1 is a novel inhibitor recently developed with a structure based on an aminopyridine scaffold that has a high affinity for VRK1[157].

To test if this inhibitor is able to block the kinase activity of VRK1, we carried out an *in vitro* kinase assay using two of the known proteins that are phosphorylation targets of VRK1, histone H3 and p53. Thus, purified

VRK1-GST and human histone H3 were incubated with increasing concentrations of VRK1-IN-1 for 2 h and then an *in vitro* kinase assay was performed. The results show that VRK-IN-1 blocked the specific phosphorylation of histone H3 in Thr3 (**Figure 84 A**) in a dose-dependent manner with an IC_{50} of 250 nM. In the same way, purified GST-VRK1 and GST-P53[1-84] were incubated with increasing concentrations of VRK1-IN-1 for 2 h and then an *in vitro* kinase assay was made, confirming that VRK-IN-1 blocked the specific phosphorylation of P53 in Thr18 (**Figure 84 B**) in a dose-dependent manner with an IC_{50} of 340 nM.

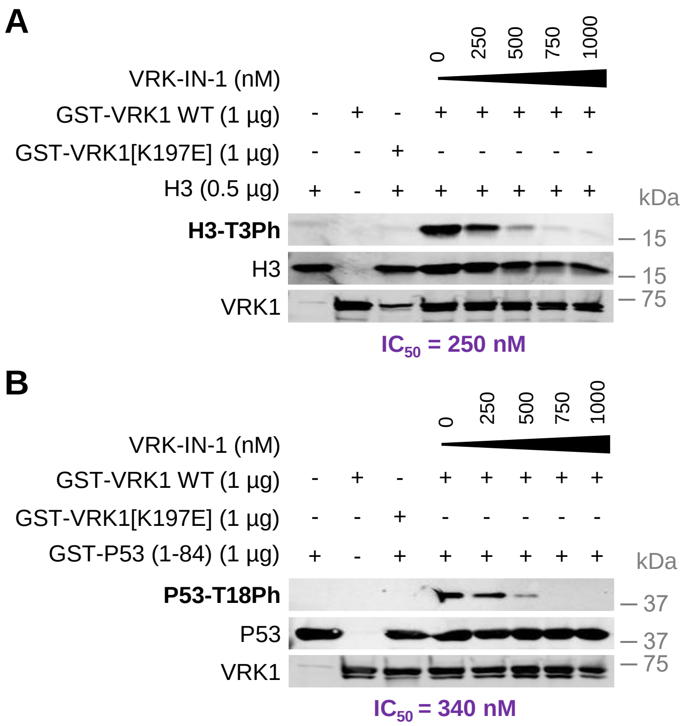

Figure 84. Effect of the VRK-IN-1 inhibitor on the phosphorylation of histone H3 and p53 *in vitro*. A. GST- VRK1 and human histone H3 were incubated with increasing concentrations of the VRK-IN-1 inhibitor (0-1 µM) for 2 h at 37 °C. Then, an in vitro kinase assay was carried out and phospho-specific signal was identified by WB. As negative control a kinase-dead VRK1 (K179E) was used. B. GST-VRK1 and GST-P53 (1-84) were incubated with increasing concentrations of the VRK-IN-1 inhibitor (0-1 µM) for 2 h at 37 °C. Consecutively, an in vitro kinase assay was performed, and phospho-specific signal was detected by WB. As negative control a kinase-dead VRK1 (K179E) was used.

Then, we also tested whether VRK-IN-1 is capable of inhibiting VRK1 kinase activity *in vivo* and consequently, opening the possibility of its use in cells, with potential for clinical applications in the future. We analyzed the phosphorylation of P53 in Thr18 and histone H3 in Thr3 with phosphospecific antibodies. A549 cells were cultured in serum-deprived conditions and treated with different concentrations of VRK-IN-1 for 24 h. VRK1-knocked-down cells were used as control for VRK1 kinase activity inactivation. Cells exhibited a decrease in both P53 in Thr18 and H3 in Thr3 phosphorylation compared with non-treated cells (**Figure 85**). These results demonstrated that the VRK-IN-1 treatment is able to inhibit the kinase activity of VRK1 *in vitro* and *in vivo*.

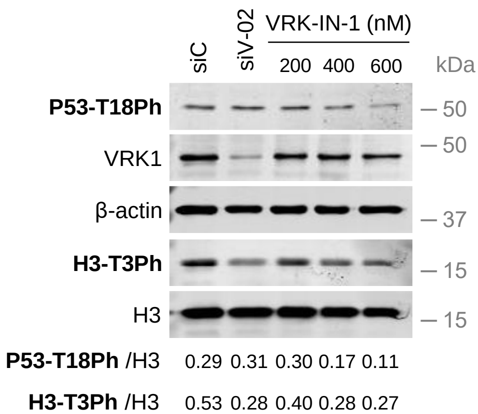

Figure 85. Effect of VRK-IN-1 treatment on P53 and histone H3 phosphorylation *in vivo*. VRK1 was knocked down in A549 cells using a specific siRNA (siV-02) for 72 h. Then, A549 cells were deprived of serum for 48 h, and incubated with different concentrations of VRK-IN-1 as indicated for 24 h. WB shows the levels of P53-T18Ph and H3-T3Ph of the whole protein extract. H3 was used as loading control. P53-T18Ph/H3 and H3-T3Ph/H3 are shown.

4.3.2 VRK-IN-1 inhibitor blocks cell migration

Once we have demonstrated that VRK-IN-1 inhibitor works by blocking the kinase activity of VRK1, we wanted to check if VRK-IN-1 treatment is able to inhibit other functions of VRK1. Since VRK1 is necessary for migration[124,172], we performed wound healing assays to validate the potential effect of VRK-IN-1.

To study this effect, A549 and U2OS cells were treated with 600 nM VRK-IN-1 and then wound healings were performed. VRK1 knocked down cells were used as a positive control. We measured the wound area at different times to calculate the wounding area coverage percent. In this way, we checked that VRK1 inhibition resulted in significantly decreased migration speed compared with non-treated cells both in A549 (**Figure 86**) and U2OS (**Figure 87**) cell lines, because wounds were not able to close after 42 h. Videos of the process of cell migration were made using photos at different time points (**Supplementary Figure S1**). These results confirm that VRK1 is necessary for cell migration and demonstrate that VRK-IN-1 disrupts cell motility via VRK1 inhibition.

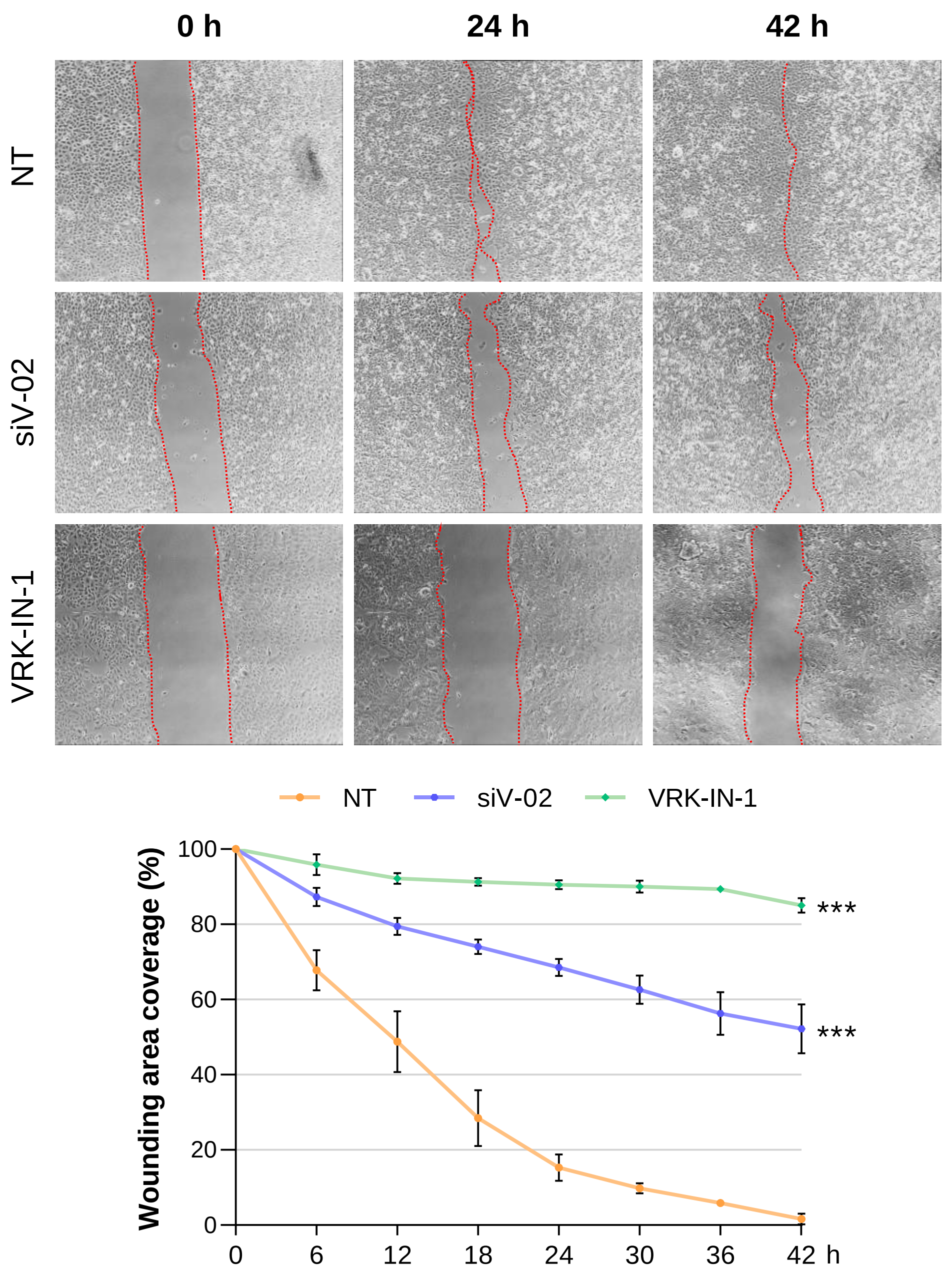

Figure 86. VRK-IN-1 inhibitor impairs cell migration in A549 cells. Wound healing assay was performed for 42 h to study cell migration in A549 cell line. VRK1 was knocked down using a siRNA (siV-02) for 72 h and the corresponding cells were treated with 600 nM VRK-IN-1 before wound healings were performed. Images were captured each 15 min for 42 h after wounding. Representative bright-field images are shown from one of three independent experiments. Graphics shows values of percentage wound closure ± SD (n = 3). NT: Non-treated. *** = $p < 0.001$.

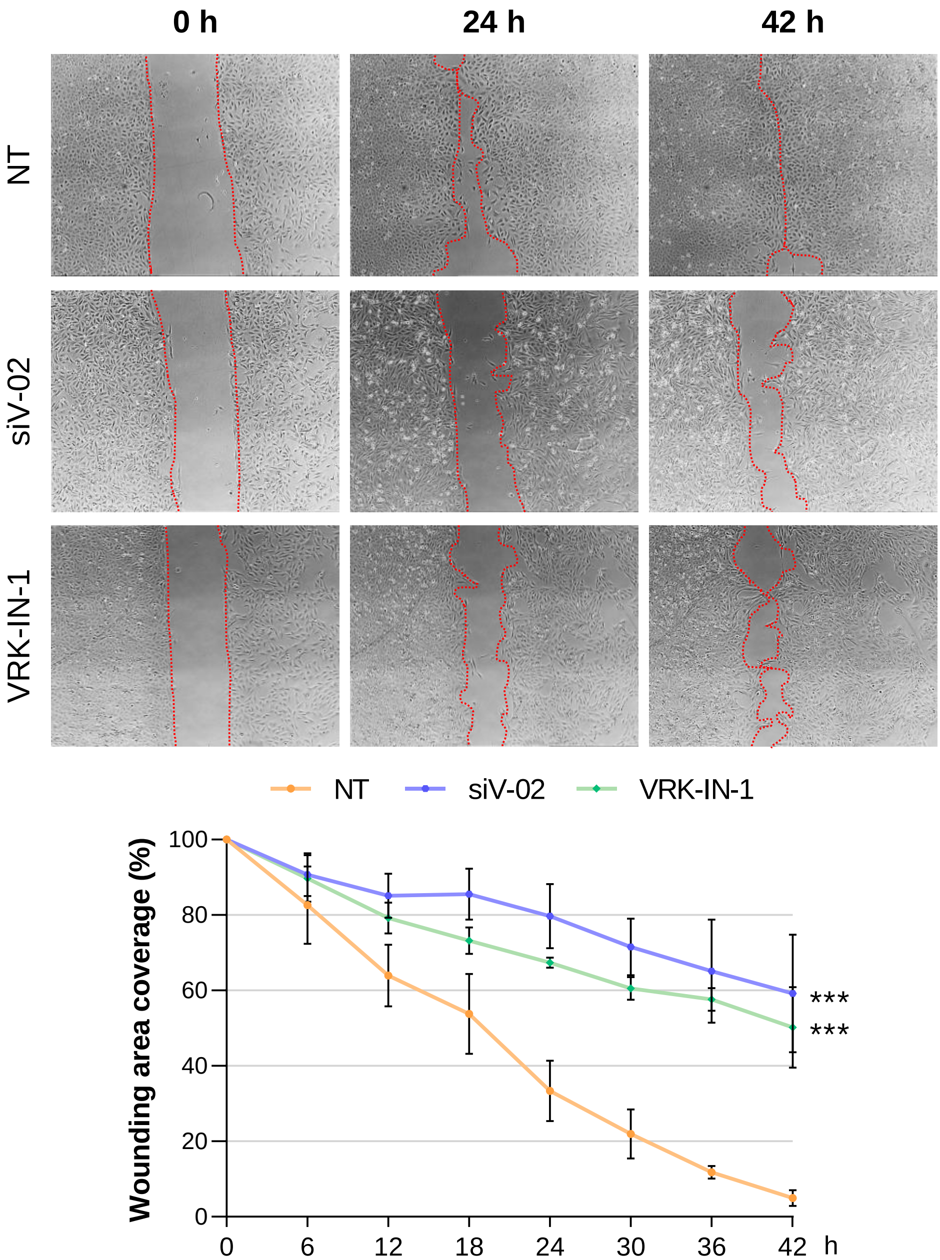

Figure 87. VRK-IN-1 treatment alters cell migration in U2OS cells. Wound healing assay was performed for 42 h to study cell migration in U2OS cell line. VRK1 was knocked down using a siRNA (siV-02) for 72 h and the corresponding cells were treated with 600 nM VRK-IN-1 before wound healings were performed. Images were captured each 15 min for 42 h after wounding. Representative bright-field images are shown from one of three independent experiments. Graphics shows values of percentage wound closure ± SD (n = 3). NT: Non-treated. *** = $p < 0.001$.

4.3.3 VRK-IN-1 inhibitor alters histone PTM pattern, promoting closed chromatin PTMs

Following with the characterization of VRK-IN-1 and its effect *in vivo*, we aimed to study its effect in chromatin remodeling and in the PTMs pattern changes. Given that VRK1 down expression promotes histone PTMs associated with a closed chromatin state, we hypothesized that VRK-IN-1 could have a similar effect.

To confirm it, we analyzed the H4K16 acetylation after treating the cells with different concentrations of VRK-IN-1 for 24 h. VRK1 positive control cells were obtained by using the siRNA siV-02 for 72 h. A549 cells showed a decrease in H4K16ac levels after VRK-IN-1 treatment compared with non-treated cells (**Figure 88**). Moreover, the drop on this PTM was similar to VRK1-depletion on higher doses of the inhibitor (600 nM). Therefore, this concentration was used in the next experiments. Then, we checked the VRK-IN-1 effect on U2OS cell line, obtaining a similar reduction of H4K16ac levels when cells were treated with 600 nM VRK-IN-1 for 24 h (**Figure 89**). These results indicate that VRK-IN-1 has comparable outcomes to VRK1 depletion in H4K16 regulation in cells.

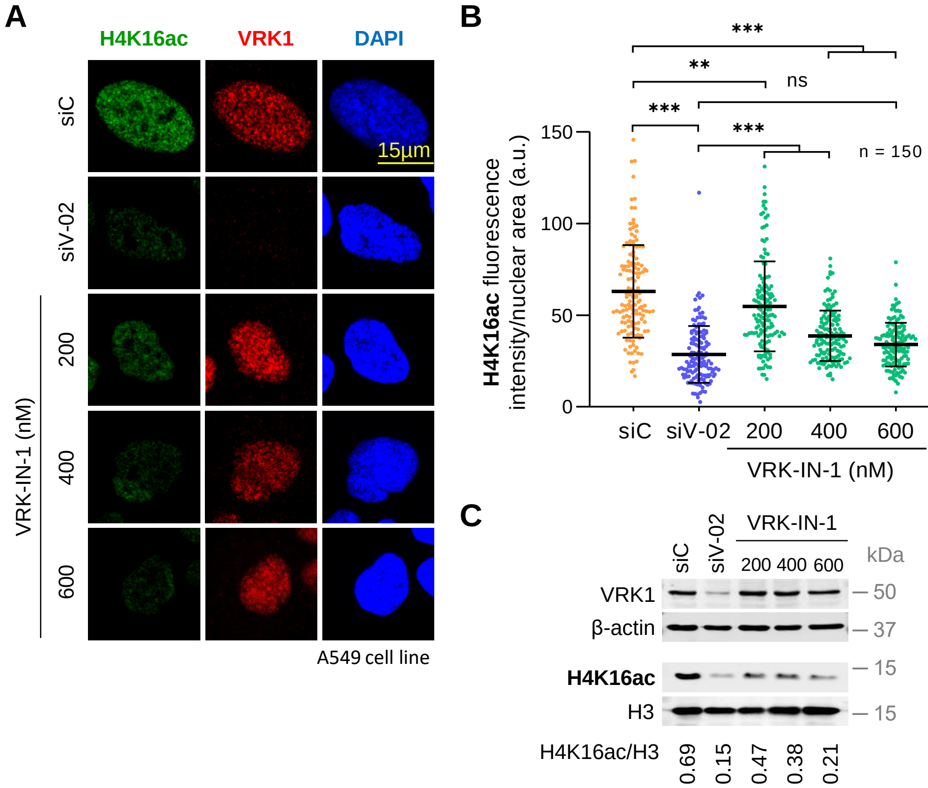

Figure 88. VRK1 depletion or inhibition with VRK-IN-1 reduces H4K16 acetylation levels in A549 cells. VRK1 was knocked down in A549 cells using a specific siRNA (siV-02) for 72 h. Cells were serum-deprived for 48 h and incubated with different concentrations of VRK-IN-1 for 24 h. **A**. Panels show IF images of the levels of H4K16ac detected using confocal microscopy. DAPI was used to stain the nuclei. **B.** Quantification of H4K16ac fluorescence intensity per nuclear area (a.u.) of 150 cells (per condition). **C.** WB shows H4K16ac levels of histone acidic extracts. VRK1, β-actin and histone H3 were used as knock-down and loading control, respectively. H4K16ac/H3 ratio is shown. Scale bar = 15 µm. ***: $p < 0.001$; **: $p < 0.01$; *: $p < 0.05$. a.u.: arbitrary units.

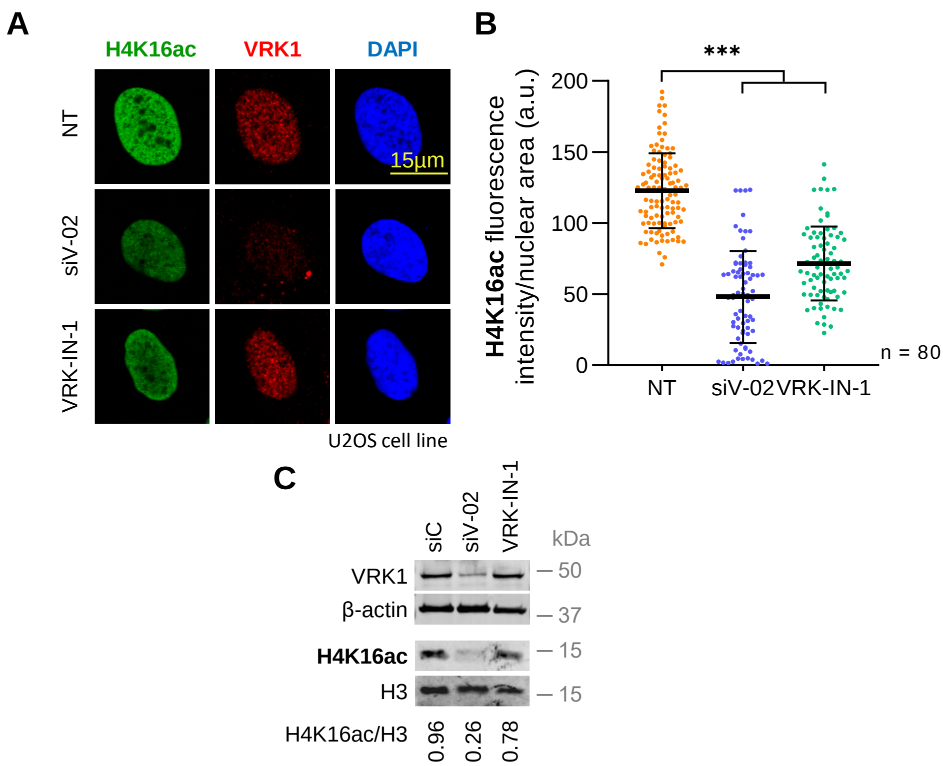

Figure 89. VRK1 depletion or inhibition with VRK-IN-1 reduces H4K16 acetylation levels in U2OS cells. U2OS VRK1-depleted cells were serum-deprived for 48 h and incubated with 600 nM VRK-IN-1 for 24 h. **A.** IF images of H4K16ac levels detected using confocal microscopy. DAPI was used to stain the nuclei. **B.** Dot plot shows the H4K16ac fluorescence intensity quantification per nuclear area (a.u.) of 80 cells (per condition). **C.** WB shows H4K16ac levels of histone acidic extracts. VRK1, β-actin and histone H3 were used as knock-down and loading control, respectively. H4K16ac/H3 ratio is shown. Scale bar = 15 µm. ***: $p < 0.001$. a.u.: arbitrary units.

To further analyze the effect of VRK-IN-1 on chromatin remodeling, several histone epigenetic modifications altered by VRK1 absence were studied: H3K4me3, H3K9ac/me3, and H3K27ac/me3.

Both A549 and U2OS cells were treated with 600 nM VRK-IN-1 for 24 h. Then, H3K4me3, H3K9ac, H3K9me3, H3K27ac, and H3K27me3 levels were detected by IF and WB. H3K4me3 (**Figure 90**), H3K9ac (**Figure 91**), and H3K27ac (**Figure 92**) levels decreased, while H3K9me3 (**Figure 93**) and H3K27me3 (**Figure 94**) levels increased when cells were treated with VRK-IN-1. Altogether, these findings suggest that VRK-IN-1 suppresses VRK1 function completely altering histone PTMs landscape. Moreover, the role of VRK1 as an orchestrator of chromatin remodeling depends on part of its kinase activity and its possible regulations of the histone-modifying enzymes.

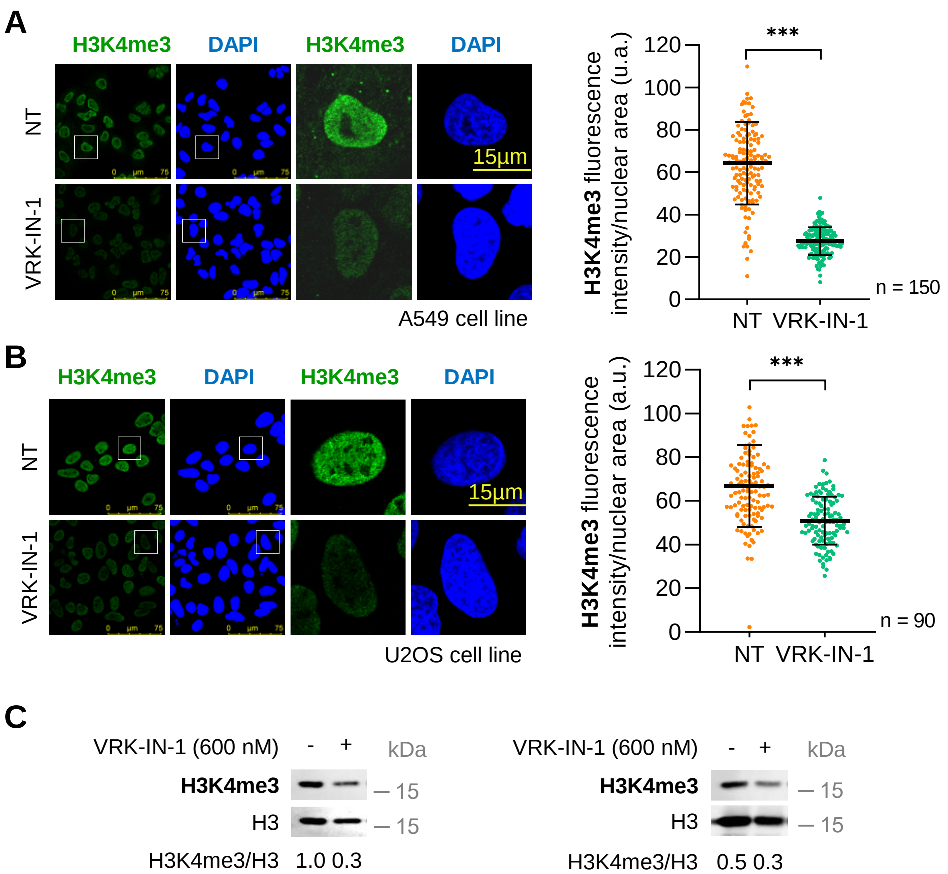

Figure 90. The VRK-IN-1 inhibitor reduces H3K4 trimethylation levels. A549 (A) and U2OS (B) cells were serum-deprived for 48 h, and incubated with 600 nM of VRK-IN-1 for 24 h. **A, B.** Panels show IF images of the levels of H3K4me3 detected using confocal microscopy. DAPI was used to stain the nuclei. On the right, dot plots show the quantification of H3K4me3 fluorescence intensity per nuclear area (a.u.) of 150 and 90 cells (per condition), respectively. **C.** WB shows H3K4me3 levels of histone acidic extracts of A549 (left) and U2OS (right) cells. Histone H3 was used as loading control. H3K4me3/H3 ratio is shown. NT: Non-treated. Scale bar = 15 µm. ***: $p < 0.001$. a.u.: arbitrary units.

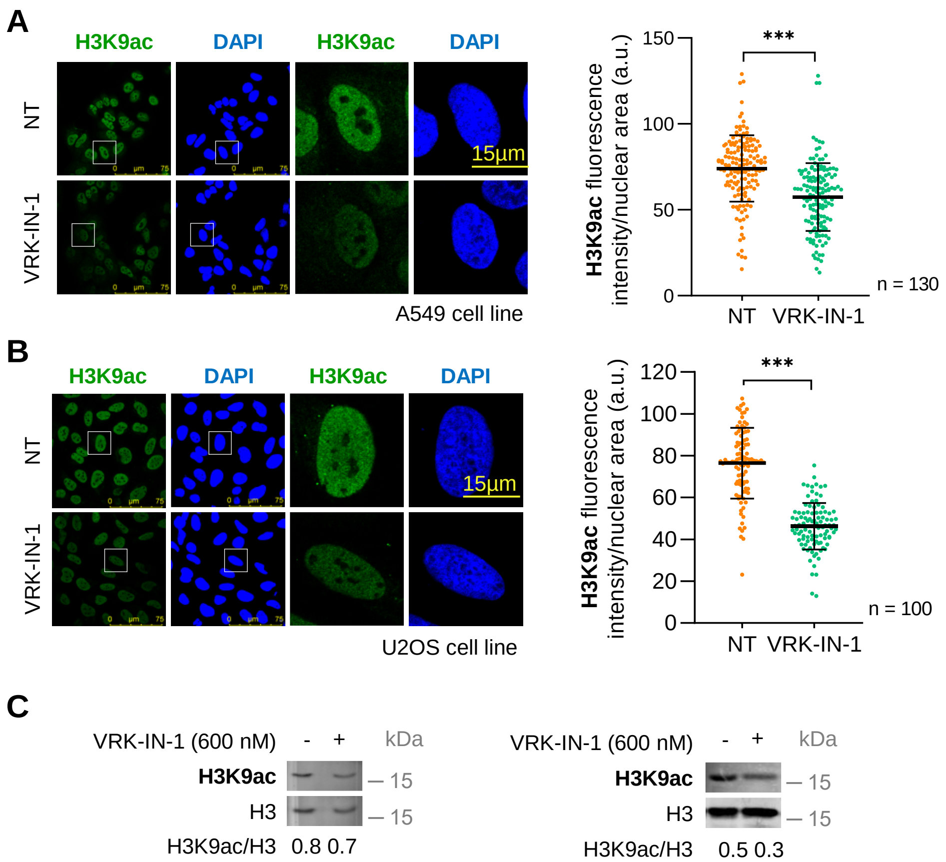

Figure 91. VRK-IN-1 treatment impairs acetylation levels of H3K9. A549 (A) and U2OS (B) cells were serum-deprived for 48 h, and incubated with 600 nM of VRK-IN-1 for 24 h. A, B. Panels show IF images of the levels of H3K9ac detected using confocal microscopy. DAPI was used to stain the nuclei. Quantification of H3K9ac fluorescence intensity per nuclear area (a.u.) of 130 and 100 cells (per condition) respectively were shown in dot plots. C. WB shows H3K9ac levels of histone acidic extracts of A549 (left) and U2OS (right) cells. Histone H3 was used as loading control. H3K9ac/H3 ratio is shown. NT: Non-treated. Scale bar = 15 µm. ***: $p < 0.001$. a.u.: arbitrary units.

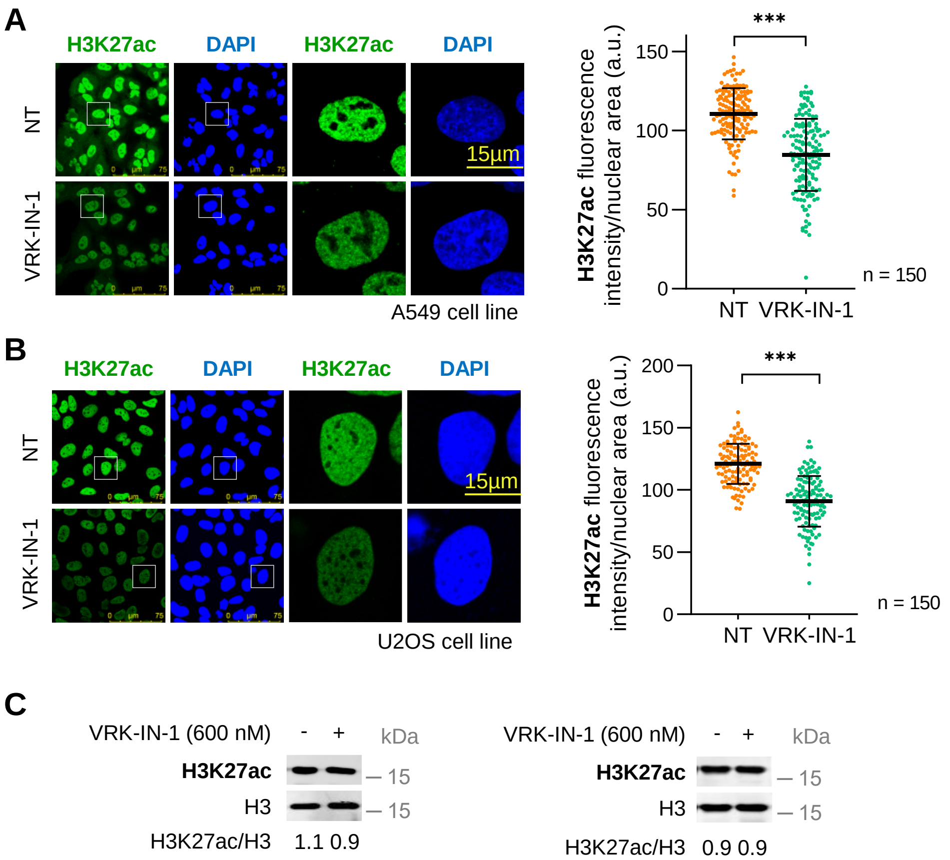

Figure 92. The VRK-IN-1 inhibitor reduces H3K27 acetylation levels. A549 (A) and U2OS (B) cells were serum-deprived for 48 h, and incubated with 600 nM of VRK-IN-1 for 24 h. **A, B.** Panels show IF images of the levels of H3K27ac detected using confocal microscopy. DAPI was used to stain the nuclei. Quantification of H3K27ac fluorescence intensity per nuclear area (a.u.) of 150 and 100 cells (per condition) respectively were shown in dot plots. **C.** WB shows H3K27ac levels of histone acidic extracts of A549 (left) and U2OS (right) cells. Histone H3 was used as loading control. H3K27ac/H3 ratio is shown. NT: Non-treated. Scale bar = 15 µm. ***: $p < 0.001$. a.u.: arbitrary units.

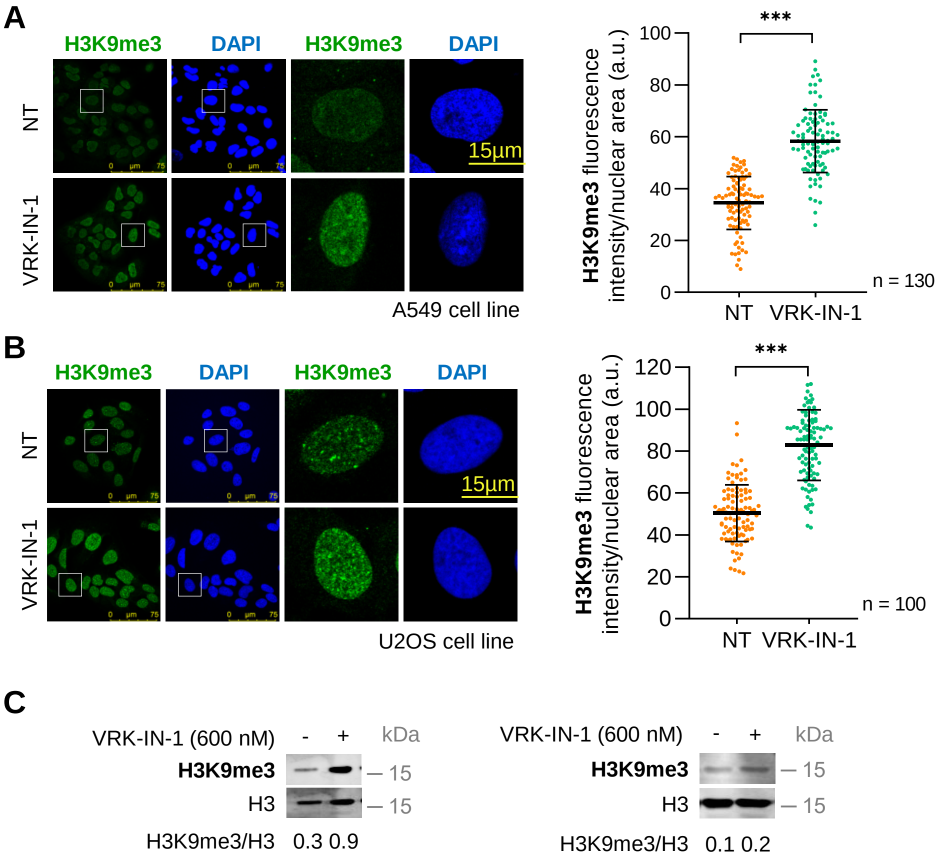

Figure 93. VRK-IN-1 treatment promotes H3K9 trimethylation levels. A549 (A) and U2OS (B) cells were serum-deprived for 48 h, and incubated with 600 nM of VRK-IN-1 for 24 h. **A, B.** Panels show IF images of the levels of H3K9me3 detected using confocal microscopy. DAPI was used to stain the nuclei. Dot plots show the quantification of H3K9me3 fluorescence intensity per nuclear area (a.u.) of 130 and 100 cells (per condition) respectively. **C.** WB shows H3K9me3 levels of histone acidic extracts of A549 (left) and U2OS (right) cells. Histone H3 was used as loading control. H3K9me3/H3 ratio is shown. NT: Non-treated. Scale bar = 15 µm. ***: $p < 0.001$. a.u.: arbitrary units.

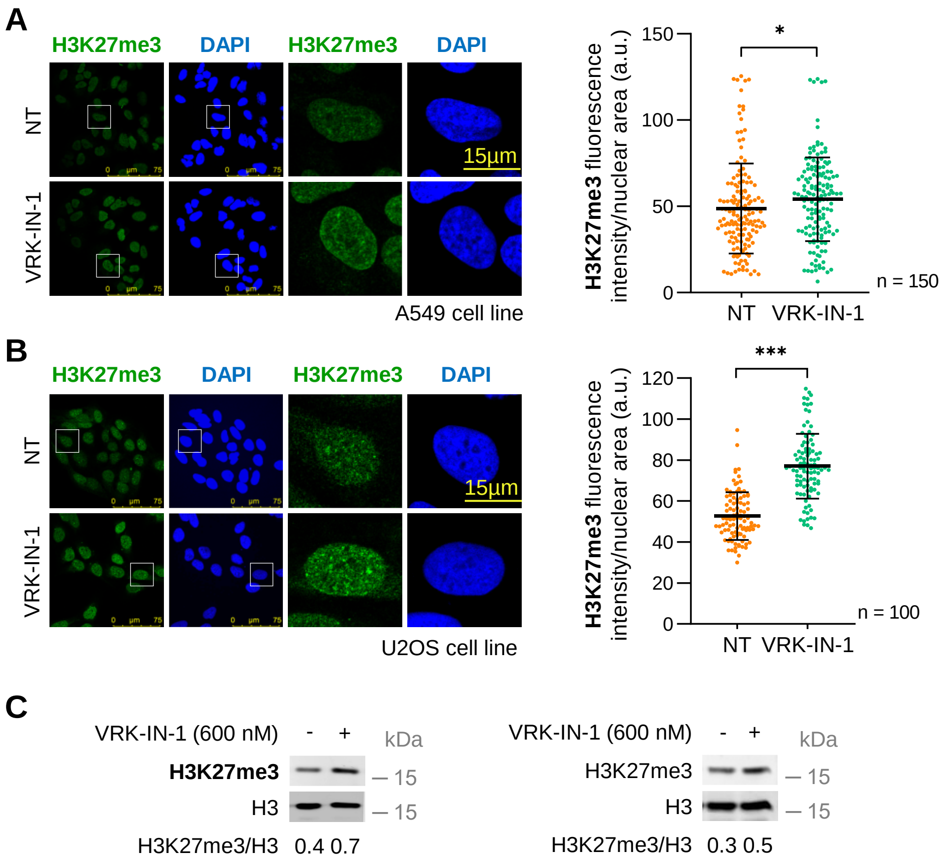

Figure 94. VRK-IN-1 treatment promotes H3K27 trimethylation levels. A549 (A) and U2OS (B) cells were serum-deprived for 48 h, and incubated with 600 nM of VRK-IN-1 for 24 h. A, B. Panels show IF images of the levels of H3K27me3 detected using confocal microscopy. DAPI was used to stain the nuclei. Dot plots show the quantification of H3K27me3 fluorescence intensity per nuclear area (a.u.) of 150 and 100 cells (per condition) respectively. C. WB shows H3K27me3 levels of histone acidic extracts of A549 (left) and U2OS (right) cells. Histone H3 was used as loading control. H3K27me3/H3 ratio is shown. NT: Non-treated. Scale bar = 15 µm. ***: $p < 0.001$; *: $p < 0.05$. a.u.: arbitrary units.

4.3.4 VRK1 absence, but not VRK1 inhibition, provokes widespread chromatin compaction

Since we observed that VRK1 absence produces global changes in chromatin accessibility, we aim to further identify the specific nature of theses epigenetic changes. For this purpose, we performed an ATAC-seq assay to determine accessible chromatin sites on A549 cells when VRK1 expression is knocked down or its kinase activity is inhibited.

VRK1 was depleted using siVRK1-02 for 72 h or cells were treated with 600 nM VRK-IN-1 for 24 h prior to ATAC-seq protocol. Histone PTM pattern and knock-down quality controls (QCs) are represented in **Supplementary Figure S2**. The collective datasets of ATAC-seq assay yielded around 16,600,000 alignments and fraction of reads in peaks (FRIP) score was higher than 30% for all samples, indicative of good QC.

In total, 69,285, 53,759 and 75,076 significative peaks were identified from NT, siV-02 and VRK-IN-1 samples, respectively (**Figure 95 A**). It indicates a reduction in chromatin accessibility by VRK1 depletion, but not by VRK-IN-1 treatment. Moreover, the analysis showed that ATAC signals were mostly distributed 0–2 kb upstream of the TSS of genes (**Figure 95 B**). The differences in peak number between NT and siV-02 comparison are mainly in proximal promoters (NT: 10,877and siV-02: 8,734) and gene bodies (NT: 45,733 and siV-02: 33,177). To get a better understanding of the functional differences in chromatin accessibility, Web-Gestalt (WEB-based GEne SeT AnaLysis Toolkit) was used to perform Gene Ontology (GO Biological Process) analysis on the genes associated with the nearest peaks. As shown in **Figure 95 C**, cellular response to tumor cell was enriched in VRK1-depleted condition compared with NT. KLRC4 and KLRK1 genes were identified in this biological process. However, there were no biological processes significantly enriched in VRK1-IN-1 treated-cells compared to NT cells or to siV-02 (**Supplementary Figure S3**).

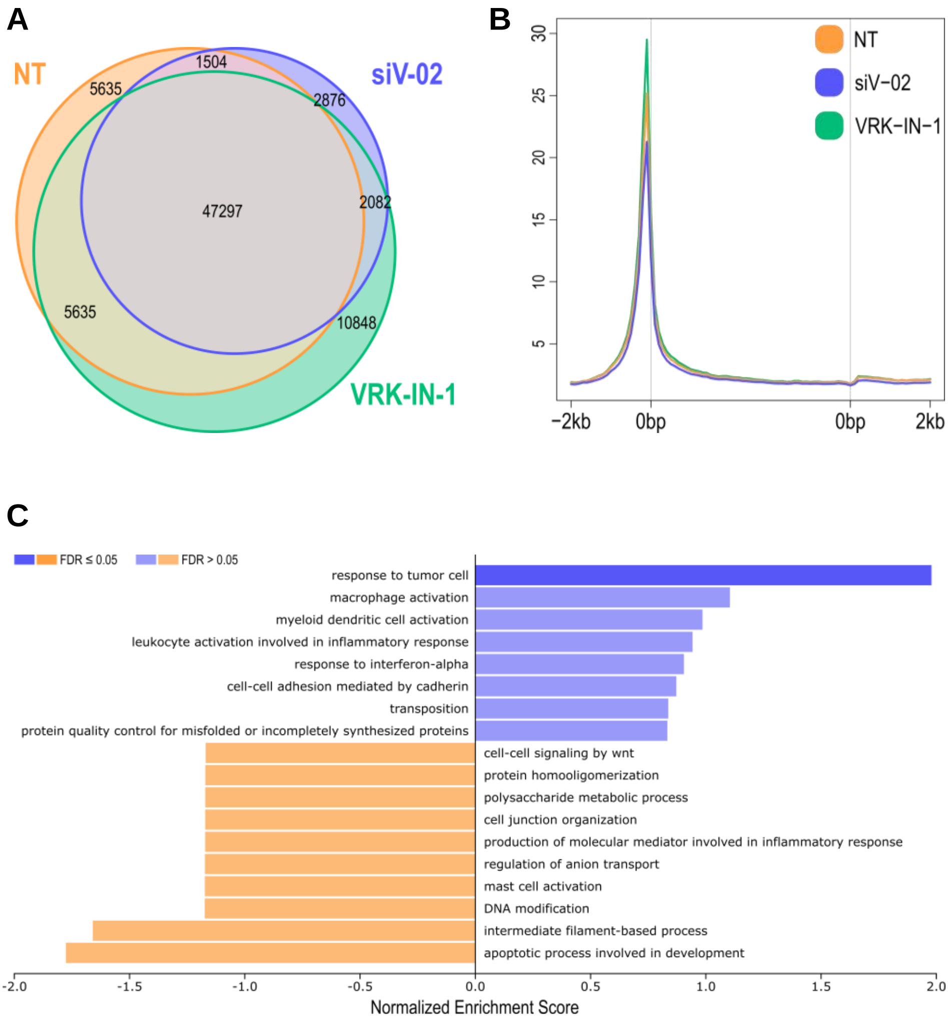

Figure 95. Chromatin accessibility profiling in A549 cells after VRK1 depletion or inhibition. A. Venn diagram of the number of ATAC-seq peaks that are unique or overlapping between NT, siV02 and VRK-IN-1 samples. B. ATAC-seq peak density distributions. C. Gene ontology analysis of genes associated with ATAC-seq peaks based on association by proximity. Purple is associated with enriched processes in siV-02 condition and orange is linked to enriched processes in NT.

Focusing on the differentially accessible regions (DARs) of NT and siV-02 comparison, ATAC-seq signal showed an increase in 353 regions rather than a decrease (150 regions) after VRK1 depletion (**Supplementary Figure S4**). g:GOST toll on g:Profiler website was used to carry out functional enrichment analysis of the down DARs of the siV-02 compared to the NT sample. After VRK1 depletion, actin and integrin binding and regulation of cell migration are two of the main affected function. Moreover, some interesting less accessible regions are detected in nuclear receptor subfamily 4 group A member 1 (NR4A1), mitogen-activated protein 3 kinase 9 (MAP3K9), early growth response protein 1 (EGR1), and VRK1 promoter (**Figure 96**, **Supplementary Figure S5**). These data also showed less accessible regions in genes that codified for some epigenetic enzymes such as KAT2 and KAT6, various HDACs and SIRTs, KMT2 and KDM1, KDM4 and JARID2, and which confirm that VRK1 absence can modulate chromatin remodeling (**Figure 96, Supplementary Figure S5**). However, there were not DARs between non- and VRK-IN-1-treated cells (**Supplementary Figure S4**). Moreover, VRK1 absence or inhibition had different outcome in cells, with chromatin being more open in 637 regions and less accessible in 198 regions after VRK1 depletion compared with VRK-IN-1 treatment (**Supplementary Figure S4**). The vast majority of up- and down-DARs correspond with the same DARs than the siV-02 VS NT comparison and some non-coding domains.

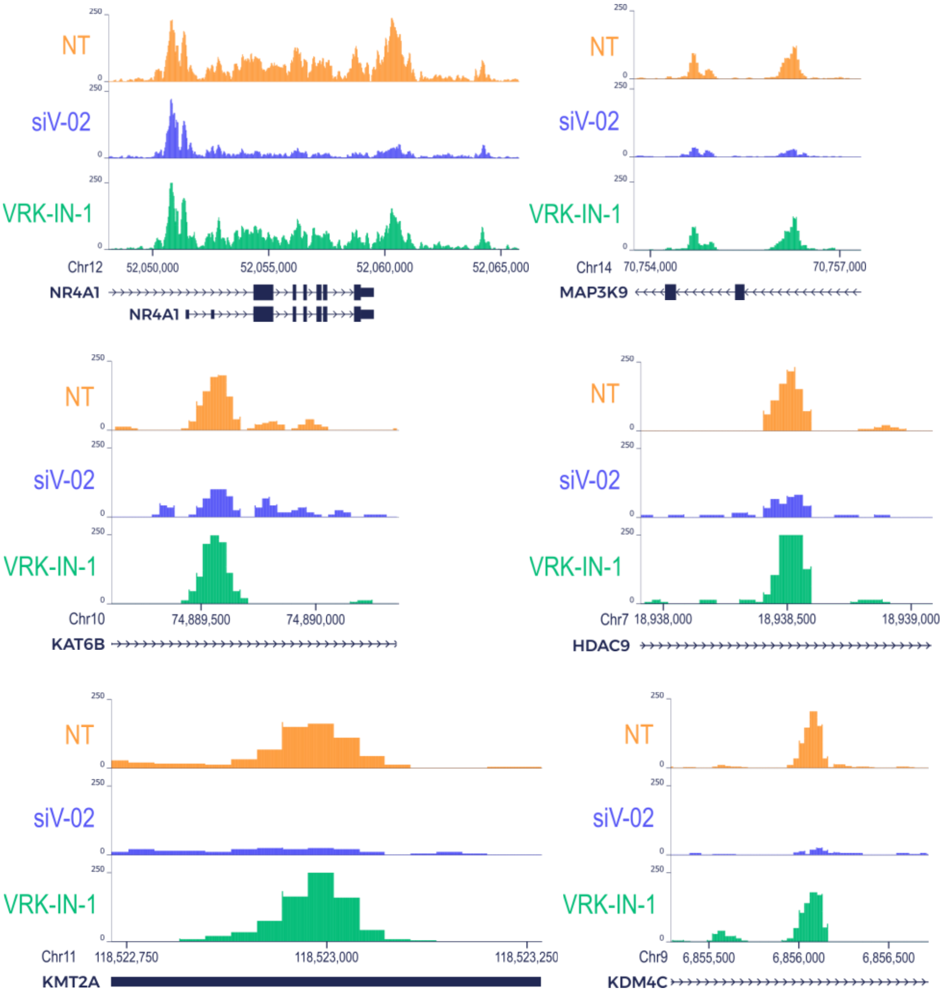

Figure 96. ATAC-seq signal distribution in A549 cells after VRK1 depletion or inhibition. Screen shot of ATAC signal of NT (orange), siV-02 (purple) and VRK1-IN-1-treated (green) cells in different chromosome regions. Human protein-coding genes taken from the NCBI RNA reference sequences collection (RefSeq) are shown (NR4A1, MAP3K9, KAT6B, HDAC9, KMT2A and KDM4C).

Open chromatin states allow TFs to bind to specific sequences of the genome and facilitate their transcription. These sequences are known as motifs and the binding positions are called TF binding sites[173]. Therefore, after identifying genomic regions with differential ATAC-seq signal, we wanted to find what TF binding motifs are present at those sites by performing a HOMER motif analysis. It is a differential motif discovery algorithm that takes two sets of sequences and tries to identify the regulatory elements that are specifically enriched in one set relative to the other. The most enriched binding motifs in VRK1 depletion compared with non-treated cells are activator protein-1 (AP-1), a key regulator of differentiation, proliferation and apoptosis, and NR4A1, which plays an important role in processes such as metabolism, proliferation and apoptosis (**Figure 97**, **Supplementary Figure S6**)[174,175]. Given that there were not differences between non- and VRK-IN-1-treated cells, any TF binding sites were significantly identified. On the other hand, the principal enriched binding motifs after VRK-IN-1 treatment compared with VRK1 absence are the binding motif of the forkhead box protein O3 (FOXO3), a well know TF important for cellular homeostasis[176], and the nuclear factor kappa B (NF-κB), which is involved in cellular differentiation, proliferation, and survival in almost all multicellular organisms (**Figure 97**, **Supplementary Figure S6**)[177].

Motif	TFs	P-value	Functions
TGTGACTCAT	AP-1	1e-76	Differentiation, proliferation and apoptosis
TGACCTTTTA	NR4A1	1e-18	Metabolism, proliferation and apoptosis
GTAAACAA	FOXO3	1e-17	Cell homeostasis
GGAATTTGCC	NF-kB	1e-13	Proliferation and cell survival

Figure 97. TF binding motifs enriched in A549 cells VRK1 depletion or inhibition. HOMER motif analysis identifies the binding sequence of specific regulatory elements that are specifically enriched after VRK1 depletion by siV-02 (Purple; compared with NT) or 600 nM VRK-IN-1 treatment (Green; compared with siV-02).

4.3.5 VRK-IN-1 inhibitor impairs the DNA damage response induced by doxorubicin and facilitates the accumulation of endogenous DNA strand breaks

VRK1 also plays several roles in DDR, processes which require a local and dynamic coordination of chromatin reorganization[32,178]. The use of VRK1 inhibitor, which are expected to prevent the activation of TIP60 and avoid the recruitment of DNA repair proteins, should cause an increase in the accumulation of DNA damage, by impairing a local open chromatin organization and DDR progression. Therefore, we studied the effect of the VRK-IN-1 inhibitor in A549 cells to determine its effect on the accumulation of DNA damage induced by doxorubicin.

Firstly, we assessed VRK-IN-1 ability to induce DNA damage in A549 cells. We used terminal deoxynucleotidyl transferase dUTP nick end labeling (TUNEL) assay. Briefly, this assay stains 3'-OH DNA ends as a DNA damage biomarker. We observed that DNA damage accumulation increased after doxorubicin treatment compared with non-treated cells and the VRK-IN-1 inhibitor caused a similar level of DNA damage (**Figure 98**). Moreover, the combination of doxorubicin and VRK-IN-1 caused a significant increment in free-DNA ends levels. This result suggests that the inhibition of VRK1 combined with DNA damaging agents could lead to the accumulation of unrepaired DNA breaks and, thus, induce tumor cell death.

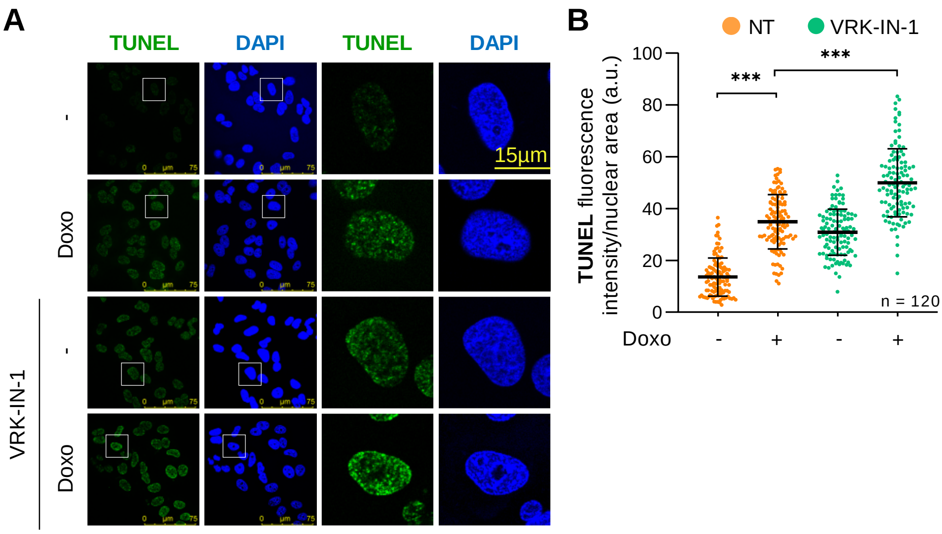

Figure 98. VRK1 inhibition with VRK-IN-1 induces DNA damage accumulation. A549 were treated with 600 nM VRK-IN-1 for 24h. DNA damage was induced by 3 µM of doxorubicin for 2 h. **A.** Image panels showing TUNEL levels. DAPI was used to stain the nuclei. **B.** Dot-plot representing the quantification of TUNEL levels (a.u) per nuclear area of 120 cells (per condition). Control: Non-treated; Doxo: Doxorubicin. Scale bar = 15 µm. ***: $p < 0.001$. a.u.: arbitrary units.

Secondly, we measured the levels of H4K16ac reflecting the early response to damage mediated by TIP60. Using IF staining, we quantified H4K16ac levels, a PTM necessary for chromatin relaxation before the repair. We detected an increase in H4K16ac levels after doxorubicin treatment, which was impaired by VRK-IN-1 inhibitor (**Figure 99**). This result indicates that the activation of TIP60 was impaired by VRK-IN-1 after DNA damage and, thus, is unable to recruit repair proteins.

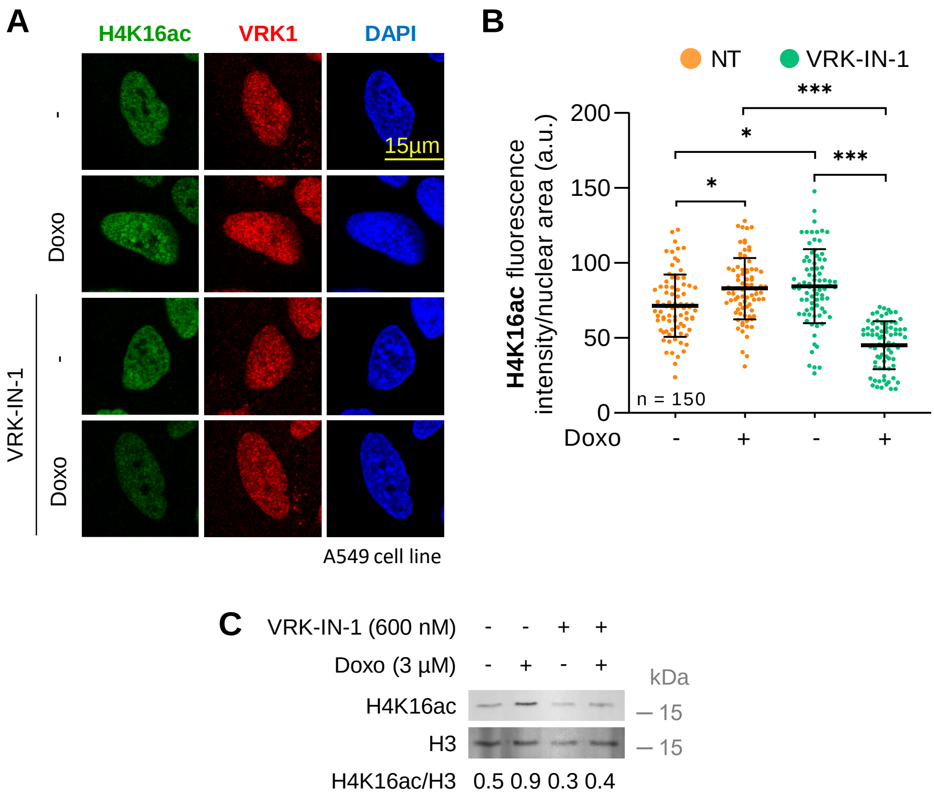

Figure 99. VRK-IN-1 treatment diminishes acetylation on H4K16 after DNA damage. A549 were treated with 600 nM VRK-IN-1 for 24h. DNA damage was induced by 3 µM of doxorubicin for 2 h. **A.** Panels show IF images of the levels of H4K16ac detected using confocal microscopy. DAPI was used to stain the nuclei. **B.** Quantification of H4K16ac fluorescence intensity per nuclear area (a.u.) of 150 cells (per condition). Doxo: Doxorubicin. Scale bar = 15 µm. ***: $p < 0.001$; *: $p < 0.05$. a.u.: arbitrary units.

Finally, we analyzed γH2A.X and 53BP1 foci, two biomarkers that reflect DNA damage repair. Whereas γH2A.X (phosphorylated H2A.X) acts as a damage sensor, 53BP1 is implicated in the NHEJ pathway, both aggregating and forming foci at the damage sites. We observed that VRK-IN-1 treatment reduced both the formation of 53BP1 and γH2A.X foci induced in response to doxorubicin (**Figure 100**), indicating that the activation of the NHEJ repair pathway was defective.

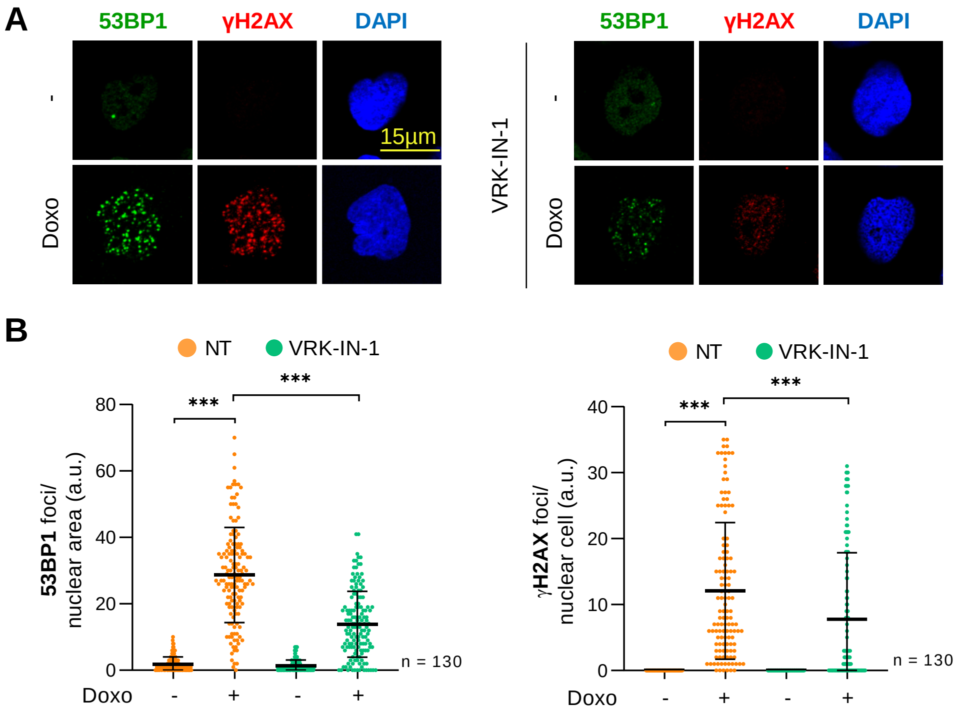

Figure 100. VRK-IN-1 treatment impairs 53BP1 and γH2A.X foci formation after DNA damage. Serum-deprived A549 cells were treated with 600 nM VRK-IN-1 for 24h. DNA damage was induced by 3 µM of doxorubicin for 2 h. **A.** Image panels showing 53BP1 and γH2A.X foci levels. DAPI was used to stain the nuclei. **B.** 53BP1 (left) and γH2A.X (right) foci levels (a.u) per nuclear area of 130 cells (per condition) were represented in dot-plots. Doxo: Doxorubicin. Scale bar = 15 µm. ***: $p < 0.001$. a.u.: arbitrary units.

Discussion

5 Discussion

In eukaryotic cells, DNA organization is essential for proper chromatin packaging and necessary to facilitate different processes that require dynamic chromatin remodeling, which are adapted to the specific need of a particular region[2]. Epigenetic alterations can control DNA accessibility and their deregulation drives several human pathologies, including cancer[8,179]. Post-translational modifications (PTMs) of the N-terminal tails of histones play a key role in this context and, consequently, regulates DNA access[1,14]. Importantly, histone PTMs are reversible and their coordination requires the tight regulation of multiple epigenetic enzymes, known as writers (enzymes that add an epigenetic mark) and erasers (enzymes that remove an epigenetic mark)[1]. Acetylation and methylation deserve specific mention among the various possible PTMs, as they have been extensively investigated in relation to cancer and response to therapy.[26]

Furthermore, chromatin can be broadly divided into open chromatin (euchromatin) domains, which are accessible regions to nuclear proteins like TFs characterized by high levels of H3K4me3, H3K9ac, H3K27ac and H4K16ac, and closed chromatin (heterochromatin) domains, which are repressive regions characterized by high levels of H3K9me3 and H3K27me3, among other histone PTMs[11,14,12].

VRK1 (Vaccinia-related kinase 1) is a kinase implicated in different cellular processes. VRK1 is associated with the activation of TFs such as c-Jun[180], CREB[128], ATF2[181], p53[130,142], as well as proteins implicated in DDR such as H2AX[16], NBS1[140], and 53BP1[97]. The location of VRK1 as a nucleus-resident kinase[16,32] and all the evidence mentioned above make it a suitable candidate to coordinate and organize the signals involved in chromatin remodeling and, thus, being able to indirectly alter some histone PTMs that are necessary for a relaxed chromatin conformation and proper cell viability.

In this work, we have studied different histone PTMs (H3K4, H3K9, H3K27, H3K79 and H4K16 acetylation and methylation) and their behavior upon VRK1 depletion. Low levels of VRK1 or its kinetic inhibition by VRK-IN-1 cause a decrease of H3K4me3, H3K9ac, H3K27ac, H3K79me2 and H4K16ac levels, and an increase of H3K9me3 and H3K27me3 in lung adenocarcinoma and osteosarcoma cells (**Figure 101**)[182]. In addition, Valbuena *et al.* described that mRNA levels of VRK1 decreased after 48 h of serum withdrawal[124], but we observed that the protein levels remained unaffected and the pattern of PTMs did not change. These data indicate that VRK1 protein levels and its kinase activity remain high during this time of cell starvation. Thus, VRK1 may be disrupting chromatin structure and maintaining some marks associated with relaxed chromatin under different conditions, independently of mitogenic signals.

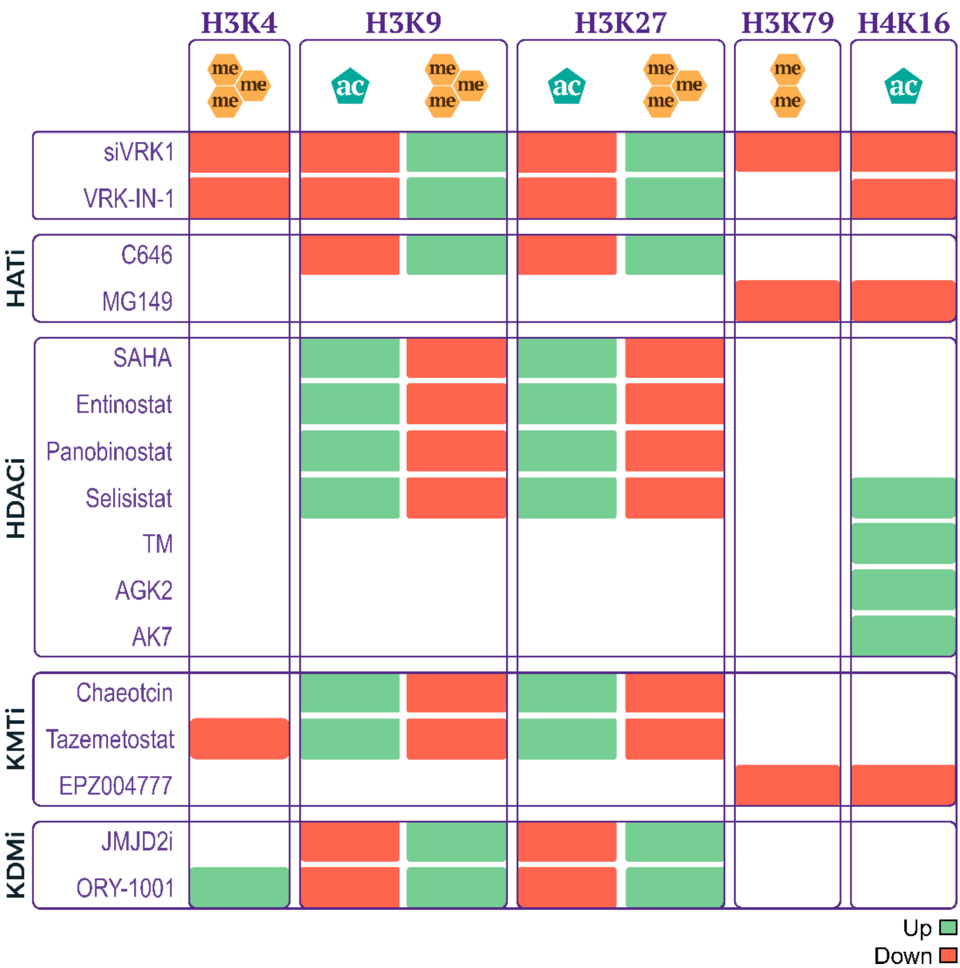

Figure 101. PTMs changes in A549 and U2OS cells. VRK1 depletion, VRK-IN-1, HATi, HDACi, KMTi and KDMi effect in the PTMs studied in this work. Green and red indicate that PTM levels increase and decrease, respectively, compared with siC or non-treated cells. Blanks indicate that this effect has not been studied on the corresponding PTM.

These PTMs are commonly dysregulated in cancer and partly allow tumor cells to adapt to their immunologic milieu. These alterations have been linked to abnormal cellular proliferation, invasiveness, metastatic progression, and therapy resistance. For example, H3K4me3 levels are enriched in pancreatic tumor cells and activate the transcription of programmed death-ligand 1 (PD-L1), a membrane protein that is considered an inhibitory checkpoint of the immune response[52]. JMJD1A overexpression provokes a reduction in H3K9me3 levels in breast cancer[53].

In osteosarcoma, H3K27ac upregulates the expression of COL6A1, responsible for cell migration and invasion[183]. Therefore, we propose that VRK1 depletion, or specific inhibition of its kinase activity, can be exploited for therapeutic applications of different tumor types in order to disrupt these histone PTMs. However, further studies clarifying the role of VRK1 on histone modification regulation would help to tailor more efficient strategies for cancer therapy and prevention.

Histone acetylation is dynamically regulated by the epigenetic enzymes HATs and HDACs, while histone methylation is regulated by KMTs and KDMs[25]. However, the coordination of these epigenetic enzymes and the differential histone PTM changes that must occur for proper genomic stability remains unclear. Thus, it is crucial to understand the major mechanisms that mediate their coordination. In this work, we demonstrate that VRK1 is able to interact with various epigenetic enzymes, possibly activating or inactivating them through phosphorylation (PCAF, HDAC1, SIRT1-2, SETDB1, LSD1 and JMJD1-2)[182]. This indicate that VRK1 could be a component of chromatin-remodeling complexes and regulate the activity of some subunits. However, the ability of VRK1 to phosphorylate these histone-modifiers remains unknown (**Figure 102**). It could be interesting to perform a proteomic analysis to identify VRK1-proteins interactions by mass spectrometry techniques, which would allow us to identify proteins that are within the same complex and provides structural information by detecting proximate amino acid pairs[184]. Furthermore, future studies of VRK1 phosphorylation pattern on epigenetic enzymes would assist in deciphering the histone code. Moreover, it is believed that malfunction of this epigenetic machinery disrupts the pattern and levels of histone marks and consequently deregulates the control of chromatin-based processes, ultimately leading to carcinogenesis and tumor progression[8,25]. For this reason, different drugs targeting epigenetic enzymes are currently in use as therapeutic drugs[26]. In this work, we compared the lack of VRK1 with some epidrugs that are likely candidates for cancer treatment (**Table 1**) and PTMs changes were comparable after different treatments (**Figure 101**), proposing VRK1 as a potential pharmacological target.

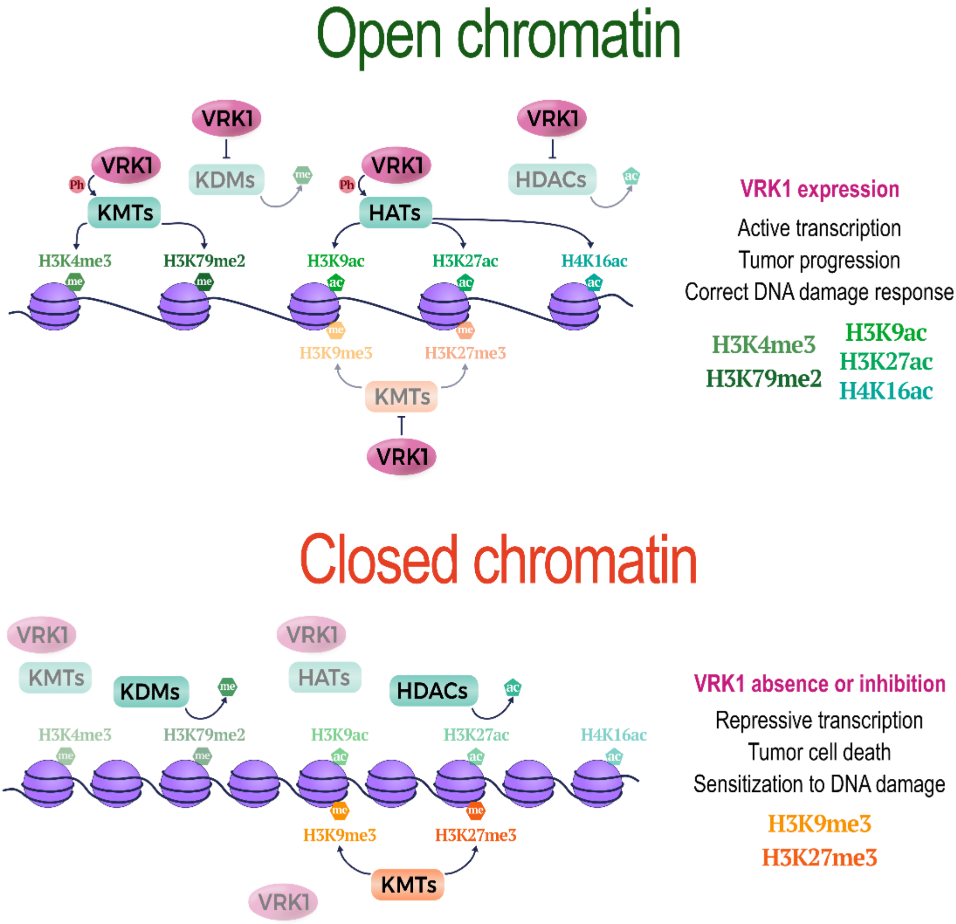

Figure 102. The possible involvement of VRK1 in chromatin remodeling. Chromatin landscape showing the potential regulation of epigenetic enzymes by VRK1. These epigenetic enzymes control the post-translational modifications associated with open and closed chromatin and their biological impact.

Focusing on H4K16, this Lys can be acetylated by the HAT TIP60 and deacetylated by the HDACs SIRT1/2[32,36,62]. Previous projects in our laboratory demonstrate that VRK1 is able to interact and directly phosphorylate TIP60 after DNA damage, leading to its translocation from the nucleoplasm to the chromatin, activating its acetylase activity and finally promoting H4K16 acetylation[32,178]. Moreover, it is described that the lack of VRK1 sensitizes glioblastoma cells to DNA damage, facilitating tumor cell death[151]. In this work, we corroborate that MG149 treatment, which inactivates TIP60, induces a reduction of H4K16ac levels in A549 and U2OS cells, confirming that this histone-modifying enzyme plays a key role in H4K16 acetylation. Moreover, H4K16ac levels quantification reveals that VRK1 absence or VRK-IN-1 treatment mimics the effect of TIP60 inhibition by MG149, emphasizing that VRK1 may be involved in TIP60 activity.

Furthermore, inhibition of SIRT1 or SIRT2 causes an increase in H4K16ac levels, which confirm previous reports that described these epigenetic enzymes as responsible for this deacetylation reaction (**Figure 101**)[35,36,182]. We also identified a probable interaction between VRK1 and SIRT1 and SIRT2. Besides, we observed that when SIRT2 interacts with VRK1, its kinase activity is inhibited[185]. This VRK1 inhibition could be favoring H4K16 deacetylation by the HDACs SIRT1 and SIRT2 and, at the same time, blocking H4K16 acetylation, because VRK1 cannot phosphorylate TIP60 (**Figure 103**). Consequently, we have found a mechanism in which there can be a crosstalk between the two activities, acetylase and deacetylase. Functionally and considering the role of H4K16ac in the DNA damage response, the loss of TIP60 activation by VRK1 inactivation will result in an impaired recruitment of sensor and repair proteins of DDR such as 53BP1 or NBS1. Moreover, SIRT1 and SIRT2 inhibition with different drugs, such as selisistat, TM, AGK2 and AK7, which produce an accumulation of H4K16ac, will disrupt the progression of the DNA repair pathway, because of the block of the dynamic regulation by keeping H4K16 in an acetylated state[14,32,185]. Likewise, SIRT2 participates in genome stability and cell-cycle progression. Reduction of SIRT2 levels produces an increase in H4K16ac levels, which is necessary to enter S-phase[36]. However, the relationship between abnormal expression of SIRT2 and tumorigenesis is still complicated given the given the wide variety of results. In NSCLC cells, SIRT2 inhibits JMJD2A expression, thereby weakening cell proliferation and tumor growth[186]. SIRT2 also enhances the sensitivity of breast cancer cells to DNA damage induced by reactive oxygen species (ROS) and promotes apoptosis[187]. On the other hand, SIRT2 plays a key role in glioma cell survival because its downregulation induces caspase-3 dependent apoptosis[188]. Thus, in cases where SIRT2 is linked to tumor progression, the combination of VRK1 and SIRT2 inhibition could be a potential approach for cancer therapy.

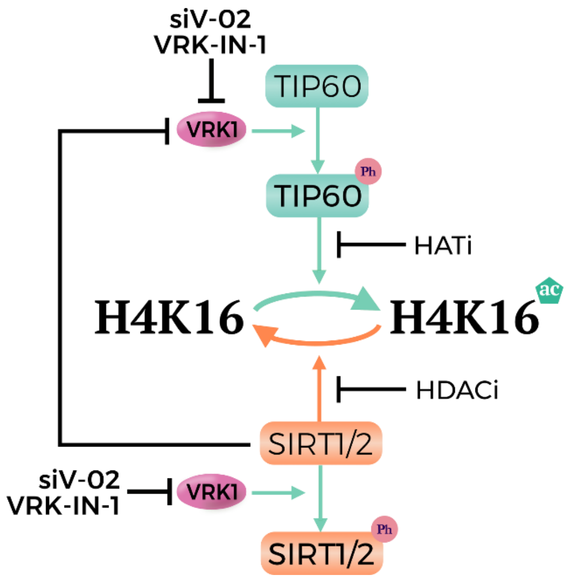

Figure 103. Hypothetical model of H4K16 regulation. Proposed diagram of the interplay between TIP60, SIRT1/2 and VRK1 regulating the levels of H4K16 acetylation and their manipulation by different types of inhibitors. Blue arrows indicate a boost in H4K16 acetylation, while orange arrows represent its impairment. siV-02: siRNA targeting VRK1; VRK-IN-1: VRK1 inhibitor; HATi: HAT inhibitor (TIP60 inhibitor: MG149); HDACi: HDAC inhibitors

(SIRT2 inhibitors: Thiomyristoyl, AGK2, AK7; SIRT1 inhibitor: Selisistat); ac: acetylation; Ph: phosphorylation.

The interrelationship between VRK1, TIP60 and SIRT2 in the context of H4K16 (de)acetylation provides an opportunity for pharmacological intervention through different approaches. H4K16ac impairment by VRK1 and TIP60 inhibition will disrupt a proper DDR and trigger cell death. An alternative effect would be the accumulation of DNA damage resulted from an opened-chromatin state caused by SIRT1 and SIRT2 inhibition. This would facilitate access to genotoxic agents such as oxidative stress by chemotherapeutic drugs, compromising tumor cell viability[189,190]. Moreover, combination of SIRT2 and VRK1 inhibition in gliomas can help to disrupt cell proliferation and induce apoptosis of tumor cells. Contrary, in tumors where SIRT2 prevent tumor progression, such as lung and breast cancer, it can inhibit VRK1 kinase activity and, consequently, prevent tumor cell growth.

Attending to H3K4, the methylation of this residue at transcription start sites (TSS) provides information about active gene transcription[191,192]. H3K4me3-marked promoters are enriched in RNA polymerase II, which recruits the KMT SETD1A that establishes H3K4me3[192,193]. The dysregulation of SETD1A, a component of the COMPASS complex that regulates this modification, is frequently related with poor prognosis in many types of cancer. It methylates YAP, resulting in an increase of cell proliferation and tumorigenesis, and exhibits stronger binding to the EGF promoter, enhancing cell migration and invasion[194,195]. This protein complex is also necessary for proper DNA replication and contributes to the restoration of this mark on newly synthesized histones during the cell cycle progression[196]. Moreover, a sustained high H3K4me3 levels are linked to carcinogenesis[52,54,197,198,195]. Conversely, LSD1 specifically catalyzes the demethylation of H3K4me and -me2[43], while JARID1 specifically demethylates H3K4me2 and -me3[44,45]. For instance, LSD1 inhibition has been proved to abrogate the malignant phenotype of solid tumors and to improve the efficacy of tumor immunotherapy, directly downregulating CD47 and PD-L1 expression through elevated H3K4me2 levels[199]. In leukemias, downregulation of JARID1B allows to maintain H3K4me3 hypermethylation driven by the MLL methytransferases[200]. Furthermore, JARID1D causes transcriptional repression of androgen receptor genes in hormone-sensitive prostate cancers[201].

We noticed that VRK1 depletion or its kinase activity inhibition by VRK-IN-1 impaired the trimethylation of H3K4 in A549 and U2OS cell lines (**Figure 101**)[182]. Thus, VRK1 could be promoting this mark and, as a result, affecting the transcription process. This would mean that VRK1 activates the KMTs or inactivates the KDMs responsible for this modification (**Figure 104**). Taking into consideration the role of VRK1 in the cell cycle progression, VRK1 inactivation could affect H3K4 methylation through the COMPASS complex and disrupt DNA replication[196]. Given that VRK1 absence or VRK-IN-1 treatment reduces cell proliferation and migration, it indicates that the inhibition of VRK1 may be used to reduce tumor growth and progression in H3K4me3 enrichment tumors[52,54,197,198,195]. Besides, the impairment of this mark suppresses the recruitment of the SAGA complex and the acetylation of histone H3 and H4, also leading to inefficient transcription[48].

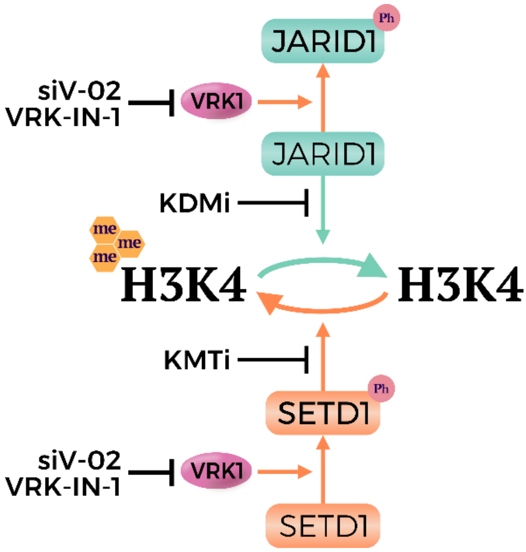

Figure 104. Hypothetical model of H3K4 regulation. Possible interaction between JARID1, SETD1 and VRK1 regulating the levels of H3K4 trimethylation and their manipulation by different types of inhibitors. Orange arrows indicate a boost in H3K4 trimethylation, while blue arrows indicate its impairment. siV-02: siRNA targeting VRK1; VRK-IN-1: VRK1 inhibitor; KMTi: KMT inhibitor (EZH2 inhibitor: Tazemetostat); KDMi: KDM inhibitor (LSD1 inhibitor: ORY-1001); me: methylation; Ph: phosphorylation.

We also observed that the KMT inhibitor tazemetostat produces a decrease in H3K4me3 levels, while the KDM inhibitor ORY-1001 boosts H3K4me3 levels (**Figure 101**)[182]. These drugs do not target the epigenetic enzymes responsible for this PTM, confirming the existence of a crosstalk between histone marks[102,164]. In this case, blocking the activity of EZH2 (by tazemetostat) and LSD1 (by ORY-1001), which regulate H3K27me3[42] and H3K4me1/2[43] respectively, affects the trimethylation of H3K4. SETD1A promotes EZH2 transcription in an H3K4me3-dependent manner and activates the Wnt/β-catenin pathway in NSCLC cells, which verifies the relationship between them[194]. Moreover, VRK1 and LSD1 are able to directly or indirectly interact in cells, so we speculated that VRK1 most likely alters LSD1 activity. We hypothesize that VRK1 activates LSD1 (which allows H3K4me2 demethylation) and SETD1 (that performs H3K4me3 methylation) and, subsequently, inhibits JARID1, maintaining high H3K4me3 levels by its demethylase activity inhibition. Thus, VRK1 inhibition would impair SETD1 and LSD1 activity and allow JARID1 demethylates H3K4me3. However, the relationship between VRK1 and these epigenetic enzymes needs to be further investigated.

Continuing with H3K9, this residue can be acetylated or mono-, di- and trimethylated, resulting in opposing transcriptional readouts[14]. H3K9me3 is a common marker of heterochromatin domains that is recognized by HP1. Together, they are responsible for the recruitment of other heterochromatic proteins that reinforce gene silencing[202,203]. Lower H3K9me3 levels grant permissibility for TFs-mediated gene activation and, in that case, H3K9ac allows the transition from transcription initiation to elongation[204,205]. The fact that both A549 and U2OS cells with low levels of VRK1 or treated with VRK-IN-1 showed a decrease in H3K9ac and an increase in H3K9me3 levels (**Figure 101**) supports the idea that VRK1 partakes in chromatin remodeling and promotes open chromatin and gene transcription[182]. Consequently, specific VRK1 inhibition can be used as a therapeutic tactic since it would disrupt transcription elongation and lead to genomic instability and cell death.

Our findings reveal that VRK1 absence has a similar effect to HAT and KDM inhibition and an opposite effect to HDACs and KMTs inhibition, promoting H3K9 methylation and blocking its acetylation (**Figure 101**)[182]. Not all these drugs target the above-mentioned enzymes, evidencing the existence of a crosstalk between H3K4, H3K9 and H3K27 modifications. LSD1 inhibition, by ORY-1001[164], causes an increment of H3K4 methylation levels, and also produces an increment of H3K9me3 levels. On the other hand, P300 acetyltransferase activity inhibition by C646, responsible for H3K27 acetylation[165], reduces H3K9ac levels. Therefore, the loss of H3K27ac can be affecting H3K9ac. Likewise, EZH2 inhibition by tazemetostat[102], which is the KMT linked to H3K27 methylation, has a similar effect to SUV39H1 inhibition by chaetocin[166], a KMT linked to H3K9 methylation. This reaffirms the likely crosstalk between H3K9 and H3K27 modifications.

The balance between acetylated and trimethylated states can be controlled by PCAF, HDAC1, SETDB1 and JMJD1 or JMJD2, among other epigenetic enzymes[27,33,206–208]. Our results also indicate that VRK1 might activate the HAT and KDMs linked to H3K9 epigenetic regulation. On the other hand, VRK1 might abrogate the deacetylase or methyltransferase activity of some HDACs and KMTs responsible for H3K9 control (**Figure 105**). In this work, we detected by IP that VRK1 is able to interact with PCAF, HDAC1, SETDB1, JMJD1 and JMJD2A in cells, possibly through forming a multiprotein complex that regulates the PTMs of H3K9. These results support the role of VRK1 in chromatin remodeling through epigenetic enzyme modulation.

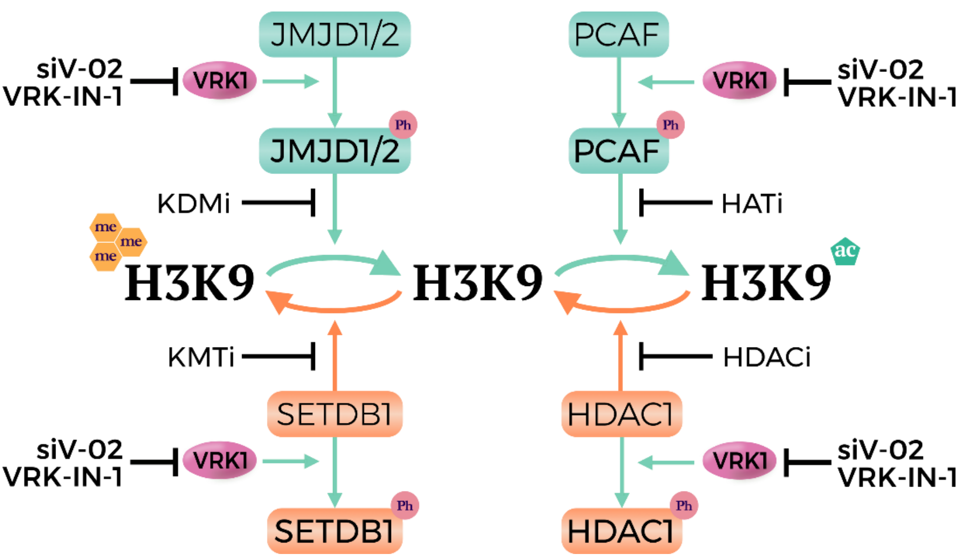

Figure 105. Proposed model of H3K9 regulation. Illustration of the probable relationship between PCAF, HDAC1, SETDB1, JMJD1/2 and VRK1 regulating the levels of H3K9 acetylation and trimethylation and their manipulation by different types of inhibitors. Blue arrows indicate a boost in H3K9 acetylation, while orange arrows represent a boost in H3K9 methylation. siV-02: siRNA targeting VRK1; VRK-IN-1: VRK1 inhibitor; HATi: HAT inhibitor (P300

inhibitor: C646); HDACi: HDAC inhibitors (Pan-HDAC inhibitors: SAHA, entinostat, panobinostat; SIRT1 inhibitor: Selisistat); KMTi: KMT inhibitors (SUV39H1 inhibitor: Chaetocin; EZH2 inhibitor: Tazemetostat); KDMi: KDM inhibitors (JMJD inhibitor: JMJD2i; LSD1 inhibitor: ORY-1001); ac: acetylation; me: methylation; Ph: phosphorylation.

HATs activity is deregulated in cancer but their precise regulation remains elusive, as several studies have implicated them as both oncogenes and tumor suppressors. HAT inhibitors are available, but they have several drawbacks such as low potency or lack of selectivity[209]. Apart from histones, HATs are able to acetylate TFs. PCAF acetylates c-Myc, which boosts cancer progression[210]. Our results indicate that PCAF can be likely positively regulated by VRK1, so its suppression can weaken H3K9 acetylation and other TFs and proteins activation, such as c-Myc, and subsequently - as we observed in the wound healing assays - block tumor expansion.

JMJD1 and JMJD2 family enzymes, which demethylate H3K9, are up-regulated in many cancer types and thus, they have emerged as potential therapeutic targets. Their overexpression deregulates heterochromatin and enhances gene transcription, promoting cancer progression[207,208]. For instance, JMJD1A is required for breast tumor growth and promotes chemoresistance by inhibiting apoptosis through p53 demethylation[211]. JMJD2A activates gene transcription of the AP-1 family members by removing H3K9me3, and promotes invasion and metastasis in squamous cell carcinoma[212]. Therefore, impairing H3K9 demethylation or acetylation through VRK1, KDMs or HATs inhibition can epigenetically reverse the transcriptional landscape of cancer cells and offer new strategies for treating these cancers that have an overexpression of these enzymes.

By contrast, HDACs and KMTs are also involved in the regulation of gene expression by modulating the chromatin conformation regulation and prompting cancer progression. HDAC1 overexpression is associated with poor prognosis of multiple myeloma, ovarian and gastric cancer[59–61,213]. SETDB1 promotes Akt hyperactivation and therapy resistance in breast and lung cancer, resulting in tumor progression[214,215]. We observed that VRK1 interacts with both of them by immunoprecipitation. However, our results indicate that VRK1 should prevent deacetylase activity of HDAC1 and methyltransferase activity of SETDB1, given that H3K9ac and H3K9me3 levels decrease and increase, respectively, after VRK1 depletion. Therefore, we hypothesize that they could form a protein complex in which their activities are altered. On one hand, HDAC1 and SETDB1 inactivation by VRK1 can prevent H3K9me3 methylation in specific oncogenes triggering its expression. On the other hand, HDAC1 and SETDB1 can enhance H3K9me3 in broader chromatin domains to prevent tumor-suppressing gene expression when VRK1 does not form part of the complex, as in the case of FOXA2 (a crucial tumor and metastasis suppressor) in NSCLC[216]. However, the mechanisms by which VRK1 modulates the activity of the epigenetic enzymes that control H3K9 PTMs remain elusive, making necessary further research to unveil the relationship between all these enzymes and cancer development.

Regarding H3K27, this Lys can be exclusively acetylated or methylated and changes in its pattern have been implicated in different cancer types[217]. For instance, H3K27ac is associated with cell migration and invasion in osteosarcoma[183] and low levels of H3K27me3 are correlated with shorter overall survival in breast, ovarian and pancreatic cancer[55,56]. Similarly to H3K9 modifications, our results showed that VRK1 absence or VRK-IN-1 treatment produce a decrease in acetylation and an increase in trimethylation levels of H3K27 (**Figure 101**)[182]. This reinforces our hypothesis of VRK1 participation in the regulation of chromatin structure and, according to the role of H3K27, VRK1 inhibition can epigenetically silence specific oncogenes expression of some tumor types.

We observed that VRK1 absence or inhibition mimics the effect of KDMi and HATi, which block the H3K27 demethylation and acetylation, and has the opposite effect of HDACi and KMTi, which impair H3K27 methylation and deacetylation (**Figure 101**)[182]. This is another example of how one mark can affect other modifications. Accordingly, VRK1 would be a good target in those tumors with VRK1 overexpression and high levels of H3K27ac, so its inhibition could help to revert its condition of poor prognosis biomarker and enhance closed chromatin state through H3K27me3.

The balance between these two possible states can be controlled by P300/CBP, HDACs, EZH2 and KDM6[217,218]. In that case, we only have evidence that VRK1 can interact with HDAC1, but we do not know whether VRK1 is able to interact with the other epigenetic enzymes that modulate H3K27 modifications. For that reason, it would be interesting to examine if VRK1 can cooperate with P300 or CBP, some HDAC, the PRC2 complex and KDM6 (**Figure 106**).

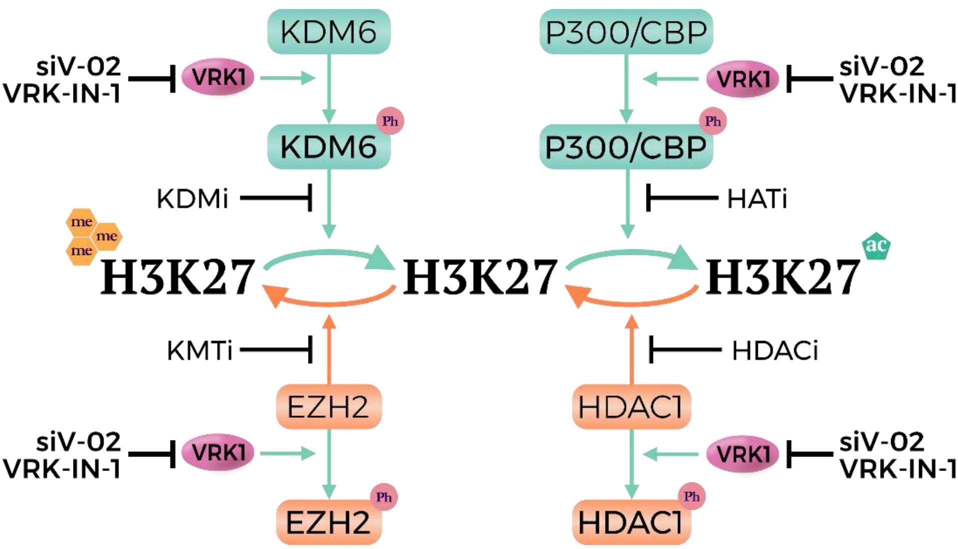

Figure 106. Hypothetical model of H3K27 regulation. Proposed diagram of the interplay between P300/CBP, HDAC1, EZH2, KDM6 and VRK1 regulating the levels of H3K27 acetylation and trimethylation and their manipulation by different types of inhibitors. Blue arrows represent a boost in H3K27 acetylation, while orange arrows indicate a boost in H3K27 methylation. siV-02: siRNA targeting VRK1; VRK-IN-1: VRK1 inhibitor; HATi: HAT inhibitor (P300 inhibitor: C646); HDACi: HDAC inhibitors (Pan-HDAC inhibitors: SAHA, entinostat, panobinostat; SIRT1 inhibitor: Selisistat); KMTi: KMT inhibitors (SUV39H1 inhibitor: Chaetocin; EZH2 inhibitor: Tazemetostat); KDMi: KDM inhibitors (JMJD inhibitor: JMJD2i; LSD1 inhibitor: ORY-1001); ac: acetylation; me: methylation; Ph: phosphorylation.

Regarding H3K79, this residue can be methylated by the KMT DOT1L, while the enzyme responsible for its demethylation remain unknown[22]. It is a common modification at the TSS of active genes and is implicated in transcriptional elongation, cell cycle regulation and DDR[22]. The recruitment of DOT1L results in the deposition of activating methyl groups in H3K79 in mixed lineage leukemia and solid tumors[219–221]. DOT1L inhibition blocks cell proliferation of tumors inducing cell-cycle arrest at G_1 phase and significantly downregulates CDK4 and CDK6 protein levels, and Myc expression[219].

We observed that VRK1 is able to modulate H3K79me2 levels, because there is a decrease in this PTM levels after VRK1 depletion or DOT1L inhibition by EPZ004777 treatment (**Figure 101**). Based on the knowledge that H4K16ac can regulate H3K79me2 and that VRK1 controls H4K16ac, we studied their possible crosstalk[23,32,185]. The results of this work suggest that DOT1L might need H4K16 acetylation for exerting its activity and to methylate H3K79. Therefore, the loss of H3K79me2 would be a consequence of the impairment of H4K16ac through the inactivation of TIP60 by VRK1 depletion (**Figure 107**). Lower levels of these two modifications prompted by the lack of VRK1, combined with TIP60 and DOT1L inhibitors, might have antitumor activity through cell-cycle arrest and a deficient DDR.

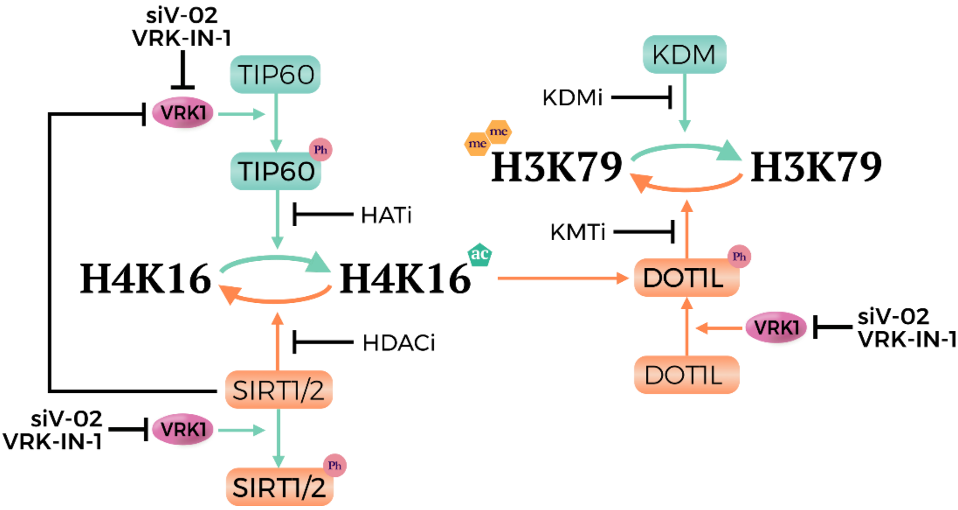

Figure 107. Proposed model of H3K79 regulation. Diagram of the possible interplay between DOT1L, VRK1 and H4K16ac regulating the levels of H3K79 dimethylation and their manipulation by different types of inhibitors. Orange arrows promote H3K79 dimethylation, while blue arrows represent its impairment. siV-02: siRNA targeting VRK1; VRK-IN-1: VRK1 inhibitor; HATi: HAT inhibitor (TIP60 inhibitor: MG149); HDACi: HDAC inhibitors (SIRT2 inhibitors: Thiomyristoyl, AGK2, AK7; SIRT1 inhibitor: Selisistat); KMTi: KMT inhibitor (DOT1L inhibitor: EPZ004777); KDMi: KDM inhibitors; ac: acetylation; me: methylation; Ph: phosphorylation.

In the context of gene expression, chromatin is required to be accessible, for which histone PTMs play an important role by providing access to transcription factors, RNA-polymerases and other gene regulators[10]. A common approach to identify these regulatory elements is studying the combination of different histone marks using multiomic techniques. While ChIP-seq requires millions of cells and requires a high cost of analysis, ATAC-seq is a good approach for an initial study of chromatin accessibility needing low input material.

We provide here a comprehensive genome-wide chromatin accessibility landscape analysis of VRK1 depletion and VRK-IN-1 treatment using A549 cells ATAC-seq data. The enrichment results of the ATAC-seq analysis show a correlation between close chromatin upstream of the TSS of genes upon VRK1 absence, which is also associated with high H3K9me3 levels[11,14]. However, VRK-IN-1 treatment did not show the same global effect in chromatin accessibility. Our findings support that VRK-IN-1 suppresses VRK1 function by impairing the phosphorylation of known substrates and altering some levels of histone PTMs. However, ATAC-seq analysis also suggests that the role of VRK1 as an orchestrator of chromatin remodeling depends not only on its kinase activity, but also on the presence of the protein. This may happen because VRK1 could form part of some chromatin remodeling complex and affect the activity of the epigenetic enzymes independently of its kinase activity. Moreover, VRK-IN-1 effect seems to be less effective than the lack of VRK1 in chromatin remodeling, so higher concentration or treatment time can be necessary. Thus, future work is needed to develop VRK1 inhibitors that not only inhibit VRK1 activity, but also disrupt its 3D structure or even degrade it, as is the case of inhibitor mediated protein degradation

GO analysis of the genes associated with the nearest peaks reveals that VRK1 absence upregulates genes related with response to tumorigenesis, such as *KLRK1* and *KLRC4* genes. They encode for two membrane receptors of NK and T cells that control tumor growth and metastasis. Moreover, their expression improve the overall survival of cancer patients and inhibit tumor cell proliferation and migration[222–224]. This would indicate that VRK1 can be a potential target in immune cells by increasing *KLRK1* and *KLRC4* expression, leading to the control of cancer through immunosurveillance.

Functional enrichment profiling of differentially accessible regions (differential peaks between two groups of ATAC-seq datasets) showed that actin and integrin binding and regulation of cell migration are two of the main functions affected. This data correlates with the cell migration disruption that we observed after VRK1 silencing or VRK-IN-1 treatment in the wound healing assays. For that reason, VRK1 inhibition can prevent cell migration in tumor cells by disturbing actin and integrin functions.

The ATAC signals of the siV-02 sample showed a decrease in genes such as *MAP3K9*, *NR4A1*, *EGR1*. MAP3K9, also known as mixed lineage kinase I (MLK1), is a Ser/Thr kinase that acts as an essential component of the MAP kinase signal transduction pathway and as an upstream activator of the MKK/JNK signal transduction cascade[225]. Previous reports suggest that MAP3K9 is involved in the pathogenesis of some cancer types such as pancreatic, prostate and hepatocellular carcinoma[226,227]. In lung cancer cells, a gain-of-function mutation of MAP3K9 leads to the increased activation of downstream pathways and its targeted depletion potentially inhibits tumor proliferation[228]. MAP3K9 reactivates the MEK/ERK pathway in melanoma cells and contributes to resistance of RAF inhibitors, promoting cell survival[229].

NR4A1 encodes a member of the steroid-thyroid hormone-retinoid receptor superfamily, also named as nuclear hormone receptor NUR/77 (Nur77)[174]. Its transcription is controlled by external stimuli. The principal mechanism to repress it is the recruitment of HDAC to its promoter, while its positive regulation is done by CREB and CBP recruitment[174]. VRK1 is able to phosphorylate CREB and we demonstrated here that VRK1 also interact with HDAC1[128]. Therefore, they might interact to control the *NR4A1* expression. Moreover, Nur77 is considered a carcinogenic survival factor when it is located in the nucleus, directly promoting cell growth. Its inactivation inhibits pancreatic, breast, lung, and liver tumor cell proliferation[230,231].

EGR1 is a TF closely related to carcinogenesis. Its expression is controlled by external stimuli like serum growth factors and can be promoted by MAPK signaling pathways. Previous reports have associated its expression with the development of prostate, gastric, glioma, lung and gastrointestinal tumors, and melanoma[232]. EGR1 can bind to the cyclin D1 promoter, activating the expression of cyclin D1, and promoting cell cycle progression by advancing cells from the G1 to S phase[233]. Moreover, VRK1 overexpression correlates with high levels of proliferative markers in tumor cells, including cyclins A and B1, CDK1 and CDK2[127,129]. This suggests that both VRK1 and EGR1 are necessary for proper cell cycle progression. Therefore, VRK1 depletion could alter EGR1 expression and, subsequently, the levels of cell cycle checkpoint proteins, which would ultimately disrupt tumor cell proliferation.

In addition, these data also showed less accessible regions in genes that encoded for some epigenetic enzymes which would explain why the PTM pattern is altered after VRK1 depletion. Moreover, overexpression or aberrant catalytic activity of these enzymes are related to different cancers, so their subsequent underexpression due to VRK1 absence could contribute to slowing down tumor progression. For example, the catalytic inactivation of KAT2 (or MOZ) or the disruption of its interaction with other proteins significantly interrupts gastrointestinal tumor growth[234]. HDAC4 and HDAC9 knockdown in leiomyosarcoma cells have increased H3K27ac levels around the TSS of repressed genes associated with programmed cell death and negative regulators of cell migration, which trigger cell adhesion, morphology and motility deficit and impair cell survival[235]. KMT2A (or MLL1), the catalytic subunit of the MLL1/MLL complex that mediates methylation of H3K4, directly activates PD-L1 transcription in pancreatic tumor cells[52]. KDM1A (or LSD1) overexpression has been identified in various sarcomas, which makes it an oncogenic driver[68]. KDM4 family proteins (or JMJD2) are highly expressed in several diseases, including breast, gastric, liver and colorectal cancers[236]. JARID2, a PRC2 cofactor, also plays a role in mediating the cross-talk between different histone modifications such as H2AK119Ub1, H3K4me3 and H3K36me3 and its downregulation impairs the tumorigenicity of bladder cancer[237,238]. We observed that these genes described as oncogenic were less accessible when VRK1 was knocked-down, so VRK1 can be a likely candidate to inhibit their expression, promoting drug sensitivity and avoiding therapy resistance.

The ATAC-seq assay also reveals TFs binding motifs (the specific sequence of DNA that TFs recognize and bind) which are more accessible after VRK1 depletion or VRK-IN-1 treatment. Our analysis revealed that the most enriched TF binding motifs in VRK1 depletion compared with non-treated cells are activator AP-1 and NR4A1.

AP-1 is a group of TFs consisting of the Jun, Fos, Maf and ATF protein subfamilies that are activated by environmental stress, radiation, cytokines and growth factors[239]. Although AP-1 has been linked to tumor cell proliferation and survival, it has also been associated with the transcription of genes involved in differentiation and apoptosis[239,240]. In glioma, the main mechanism of apoptosis after different surgical treatments is controlled via the upregulation of AP-1[241]. In NSCLC, JNK1/AP-1 bind to the p53 up-regulated modulator of apoptosis (PUMA) promoter and stimulates PUMA expression, which exhibits pro-apoptotic function[242]. In ovarian cancer cells, ornithine decarboxylase inhibitors triggers the phosphorylation of JNK and activates AP-1 signaling, which finally induces apoptotic cell death[243]. Ventura *et al.* showed that short-term activation of JNK leads to survival, whereas the prolonged activation of JNK results in apoptosis[244]. Our results reveal that, following a VRK1 depletion sustained over time, there is increased enrichment of AP-1-

related motifs, perhaps because the cell is undergoing some apoptotic events.

In the case of the NR4A1 binding motif, it showed an increase after VRK1 depletion. Although, NR4A1 gene was less accessible and, thus, its expression was expected to be lower. Therefore, the expression of NR4A1 and its specific function after VRK1 depletion needs to be further explored.

However, all these results only show a global pattern of histone PTM and we cannot determine which chromatin regions are enriched in these acetylations and methylations. ChIP-Seq analysis would be necessary to answer this question and know which genes are affected specifically[245]. This information would allow to situate VRK1 as a chromatin remodeler in specific cellular processes and contexts. On the other hand, proteomics analysis by mass spectrometry can confirm the PTM level changes[246]. This approach would lead to the identification of more histone marks affected by VRK1 and serve as a catalog of which PTMs are present in the different biological contexts and, thereby, provide a detail-rich resource for exploring other histone modifications beyond the already studied. Conversely, these results cannot provide gene expression information - for this, a complementary RNA-seq analysis would be needed to shed light on the cellular transcriptome landscape[247].

Briefly, the role of VRK1 in cancer epigenetics is still unclear and requires further research, but it is known that VRK1 overexpression is related to poor prognosis in many tumor types such as breast, lung, head and neck squamous cell carcinomas, colon, liver, gliomas, multiple myeloma, esophageal carcinomas, and oral cancer[127,141-150]. This makes VRK1 a good candidate to target from an epigenetic therapeutic approach. In the meantime, combinatorial approaches have been increasingly investigated in clinical trials in order to further enhance the efficacy of cancer therapy[25,114]. In this work, we demonstrated that specific pharmacological inhibition of VRK1 showed similar effects to VRK1 depletion in cells. Moreover, VRK1 depletion or inhibition can mimic the effects of drugs targeting specific epigenetic enzymes that are deregulated in several cancers. The use of a kinase inhibitor might show synergy with existing chemotherapeutic drugs and allow to reduce their doses, improving patient outcome. Therefore, we propose targeting VRK1 in combination with another anti-epigenetic enzyme drug to disrupt histone PTM pattern and inhibit tumor growth more effectively than a single blockade strategy. Moreover, combined treatment could be a more tailored approach where epigenetic modulation is performed based on each patient's genetic background, using a personalized medicine approach that adapts to the epitranscriptome of each tumor, such as specific epigenetic enzymes overexpression. Finally, the present data not only provides a resource for investigating more specific inhibitors of VRK1, but they also open a door for new opportunities to target VRK1 as synthetic lethality.

Conclusions

6 Conclusions

1. VRK1 absence alters histone PTMs landscape. Specifically, there is a decrease in H3K4me3, H3K9ac, H3K27ac, H3K79me2 and H4K16ac levels, and an increase in H3K9me3 and H3K27me3 levels in VRK1 knock-down lung adenocarcinoma and osteosarcoma cells.

2. VRK1 depletion shows comparable results as some epigenetic enzyme inhibitors, mimicking:
   - Tazemetostat (KMTi) effect on H3K4me3 levels.
   - C646 (HATi) and JMJD2i and ORY-1001 (KDMi) impact on H3K9ac and H3K27ac.
   - MG149 (HATi) and EPZ004777 (KMTi) effect on H3K79me2 and H3K16ac.

3. VRK1 interacts with different epigenetic enzymes, including PCAF, HDAC1, SIRT1, SIRT2, SETDB1, LSD1, JMJD1A, and JMJD2A.

4. VRK-IN-1 treatment suppresses VRK1 activity in the same way as VRK1 depletion:
   - Preventing the specific phosphorylation of direct VRK1 targets such as H3 and P53.
   - Blocking cell migration.
   - Altering histone PTM pattern and repressing gene expression.
   - Impairing the phosphorylation of key DDR proteins and enhancing the accumulation of unrepaired DNA breaks in doxorubicin-induced DNA damage.

5. VRK1 depletion, but not VRK-IN-1 treatment, provokes widespread chromatin compaction:
   - Making some oncogenes less accessible, such as *MAP3K9*, *NR4A1* and *EGR1*, as well as some epigenetic enzymes genes, among which stand out *KAT2-6*, various *HDAC*s and *SIRT*s, *KMT2* and *KDM1-4-5*.
   - Triggering an increase of AP-1 and NR4A1 TFs binding motifs.

7 Conclusiones

1. La ausencia de VRK1 altera el patrón de PTMs de histonas. En concreto, se produce una disminución de los niveles de H3K4me3, H3K9ac, H3K27ac, H3K79me2 y H4K16ac, y un aumento de los niveles de H3K9me3 y H3K27me3 en células de adenocarcinoma de pulmón y osteosarcoma tras la depleción de VRK1.

2. La ausencia de VRK1 muestra resultados comparables a los inhibidores de enzimas epigenéticas, imitando el efecto de:
   - Tazemetostat (KMTi) sobre los niveles de H3K4me3.
   - C646 (HATi) y JMJD2i y ORY-1001 (KDMi) sobre H3K9ac y H3K27ac.
   - MG149 (HATi) y EPZ004777 (KMTi) sobre H3K79me2 y H3K16ac.

3. VRK1 interactúa con varias enzimas epigenéticas, incluyendo PCAF, HDAC1, SIRT1, SIRT2, SETDB1, LSD1, JMJD1A, y JMJD2A.

4. El tratamiento con VRK-IN-1 inhibe la actividad de VRK1 del mismo modo que la depleción de VRK1:
   - Impidiendo la fosforilación específica de sustratos directos de VRK1 como H3 y P53.
   - Bloqueando la migración celular.
   - Alterando el patrón de PTMs de histonas y reprimiendo la expresión génica.
   - Impidiendo la fosforilación de proteínas clave en la respuesta a daño génico inducido por doxorrubicina y aumentando la acumulación de roturas de ADN.

5. La depleción de VRK1, pero no el tratamiento con VRK-IN-1, provoca una compactación generalizada de la cromatina:
   - Haciendo menos accesibles algunos oncogenes, como *MAP3K9, NR4A1* y *EGR1*, así como genes que codifican enzimas epigenéticas, entre los que destacan *KAT2-6*, varias *HDAC*s y *SIRT*s, *KMT2* y *KDM1-4-5*.
   - Produciendo un aumento de los motivos de unión de los TFs AP-1 y NR4A1.

References

8 References

1. Audia, J. E. & Campbell, R. M. Histone Modifications and Cancer. *Cold Spring Harb. Lab. Press* 8:a019521 (2016).
2. Cutter, A. R. & Hayes, J. J. A brief review of nucleosome structure. *FEBS Lett.* **589**, 2914–2922 (2015).
3. Henikoff, S. & Smith, M. M. Histone Variants and Epigenetics. *Cold Spring Harb. Perspect. Biol.* **7**, a019364 (2015).
4. Quina, A. S., Buschbeck, M. & Di Croce, L. Chromatin structure and epigenetics. *Biochem. Pharmacol.* **72**, 1563–1569 (2006).
5. Goldberg, A. D., Allis, C. D. & Bernstein, E. Epigenetics: A Landscape Takes Shape. *Cell* **128**, 635–638 (2007).
6. Dawson, M. A. & Kouzarides, T. Cancer Epigenetics: From Mechanism to Therapy. *Cell* **150**, 12–27 (2012).
7. Nebbioso, A., Tambaro, F. P., Dell'Aversana, C. & Altucci, L. Cancer epigenetics: Moving forward. *PLOS Genet.* **14**, e1007362 (2018).
8. Cao, J. & Yan, Q. Cancer Epigenetics, Tumor Immunity, and Immunotherapy. *Trends Cancer* **6**, 580–592 (2020).
9. Bannister, A. J. & Kouzarides, T. Regulation of chromatin by histone modifications. *Cell Res.* **21**, 381–395 (2011).
10. Millán-Zambrano, G., Burton, A., Bannister, A. J. & Schneider, R. Histone post-translational modifications — cause and consequence of genome function. *Nat. Rev. Genet.* **23**, 563–580 (2022).
11. Kouzarides, T. Chromatin Modifications and Their Function. *Cell* **128**, 693–705 (2007).
12. Barnes, C. E., English, D. M. & Cowley, S. M. Acetylation & Co: an expanding repertoire of histone acylations regulates chromatin and transcription. *Essays Biochem.* **63**, 97–107 (2019).
13. Greer, E. L. & Shi, Y. Histone methylation: a dynamic mark in health, disease and inheritance. *Nat. Rev. Genet.* **13**, 343–357 (2012).
14. Sawan, C. & Herceg, Z. Chapter 3 - Histone Modifications and Cancer. in *Advances in Genetics* **70**, 57–85 (Elsevier Inc, 2010).
15. Kang, T.-H. *et al.* Mitotic Histone H3 Phosphorylation by Vaccinia-Related Kinase 1 in Mammalian Cells. *Mol. Cell. Biol.* **27**, 8533–8546 (2007).
16. Salzano, M., Sanz-García, M., Monsalve, D. M., Moura, D. S. & Lazo, P. A. VRK1 chromatin kinase phosphorylates H2AX and is required for foci formation induced by DNA damage. *Epigenetics* **10**, 373–383 (2015).
17. Lo, W.-S. *et al.* Phosphorylation of Serine 10 in Histone H3 Is Functionally Linked In Vitro and In Vivo to Gcn5-Mediated Acetylation at Lysine 14. *Mol. Cell* **5**, 917–926 (2000).

18. Rea, S. *et al.* Regulation of chromatin structure by site-specific histone H3 methyltransferases. *Nature* **406**, 593–599 (2000).

19. Hirota, T., Lipp, J. J., Toh, B.-H. & Peters, J.-M. Histone H3 serine 10 phosphorylation by Aurora B causes HP1 dissociation from heterochromatin. *Nature* **438**, 1176–1180 (2005).

20. Fischle, W. *et al.* Regulation of HP1–chromatin binding by histone H3 methylation and phosphorylation. *Nature* **438**, 1116–1122 (2005).

21. Plazas-Mayorca, M. D. *et al.* Quantitative proteomics reveals direct and indirect alterations in the histone code following methyltransferase knockdown. *Mol. Biosyst.* **6**, 1719–1729 (2010).

22. Nguyen, A. T. & Zhang, Y. The diverse functions of Dot1 and H3K79 methylation. *Genes Dev.* **25**, 1345–1358 (2011).

23. Valencia-Sánchez, M. I. *et al.* Regulation of the Dot1 histone H3K79 methyltransferase by histone H4K16 acetylation. *Science* **371**, eabc6663 (2021).

24. Li, J. *et al.* Involvement of Histone Methylation and Phosphorylation in Regulation of Transcription by Thyroid Hormone Receptor. **22**, 5688–5697 (2002).

25. Kaur, J., Daoud, A. & Eblen, S. T. Targeting Chromatin Remodeling for Cancer Therapy. *Curr. Mol. Pharmacol.* **12**, 215–229 (2019).

26. Camilo, V. & Jerónimo, C. Chapter 17 - Present and future perspectives for targeting histone modifications in therapy. in *Histone Modifications in Therapy* **20,** 415–457 (Academic Press, 2020).

27. Jin, Q. *et al.* Distinct roles of GCN5/PCAF-mediated H3K9ac and CBP/p300-mediated H3K18/27ac in nuclear receptor transactivation. *EMBO J.* **30**, 249–262 (2011).

28. Sterner, D. E. & Berger, S. L. Acetylation of Histones and Transcription-Related Factors. *Microbiol. Mol. Biol. Rev.* **64**, 435–459 (2000).

29. Kimura, A. & Horikoshi, M. Tip60 acetylates six lysines of a specific class in core histones in vitro. *Genes Cells* **3**, 789–800 (1998).

30. Wichmann, J. *et al.* Loss of TIP60 (KAT5) abolishes H2AZ lysine 7 acetylation and causes p53, INK4A, and ARF-independent cell cycle arrest. *Cell Death Dis.* **13**, 1–13 (2022).

31. Wang, P., Bao, H., Zhang, X.-P., Liu, F. & Wang, W. Regulation of Tip60-dependent p53 acetylation in cell fate decision. *FEBS Lett.* **593**, 13–22 (2019).

32. García-González, R., Morejón-García, P., Campillo-Marcos, I., Salzano, M. & Lazo, P. A. VRK1 Phosphorylates Tip60/KAT5 and Is Required for H4K16 Acetylation in Response to DNA Damage. *Cancers* **12**, 2986 (2020).

33. Li, Y. & Seto, E. HDACs and HDAC Inhibitors in Cancer Development and Therapy. *Cold Spring Harb. Perspect. Med.* **6**, a026831 (2016).

34. Bosch-Presegué, L. & Vaquero, A. Sirtuins in stress response: guardians of the genome. *Oncogene* **33**, 3764–3775 (2014).

35. Vaquero, A. *et al.* Human SirT1 Interacts with Histone H1 and Promotes Formation of Facultative Heterochromatin. *Mol. Cell* **16**, 93–105 (2004).

36. Vaquero, A. *et al.* SirT2 is a histone deacetylase with preference for histone H4 Lys 16 during mitosis. *Genes Dev.* **20**, 1256–1261 (2006).

37. Herz, H.-M., Garruss, A. & Shilatifard, A. SET for life: biochemical activities and biological functions of SET domain-containing proteins. *Trends Biochem. Sci.* **38**, 621–639 (2013).

38. Hyun, K., Jeon, J., Park, K. & Kim, J. Writing, erasing and reading histone lysine methylations. *Exp. Mol. Med.* **49**, e324 (2017).

39. Lehnertz, B. *et al.* Suv39h-mediated histone H3 lysine 9 methylation directs DNA methylation to major satellite repeats at pericentric heterochromatin. *Curr. Biol. CB* **13**, 1192–1200 (2003).

40. Shinkai, Y. & Tachibana, M. H3K9 methyltransferase G9a and the related molecule GLP. *Genes Dev.* **25**, 781–788 (2011).

41. Schultz, D. C., Ayyanathan, K., Negorev, D., Maul, G. G. & Rauscher, F. J. SETDB1: a novel KAP-1-associated histone H3, lysine 9-specific methyltransferase that contributes to HP1-mediated silencing of euchromatic genes by KRAB zinc-finger proteins. *Genes Dev.* **16**, 919–932 (2002).

42. Chang, C.-J. & Hung, M.-C. The role of EZH2 in tumour progression. *Br. J. Cancer* **106**, 243–247 (2012).

43. Shi, Y. *et al.* Histone Demethylation Mediated by the Nuclear Amine Oxidase Homolog LSD1. *Cell* **119**, 941–953 (2004).

44. Klose, R. J. & Zhang, Y. Regulation of histone methylation by demethylimination and demethylation. *Nat. Rev. Mol. Cell Biol.* **8**, 307–318 (2007).

45. Xiang, Y. *et al.* JARID1B is a histone H3 lysine 4 demethylase up-regulated in prostate cancer. *Proc. Natl. Acad. Sci. U. S. A.* **104**, 19226–19231 (2007).

46. Ruthenburg, A. J., Li, H., Patel, D. J. & David Allis, C. Multivalent engagement of chromatin modifications by linked binding modules. *Nat. Rev. Mol. Cell Biol.* **8**, 983–994 (2007).

47. Lee, K. K. & Workman, J. L. Histone acetyltransferase complexes: one size doesn't fit all. *Nat. Rev. Mol. Cell Biol.* **8**, 284–295 (2007).

48. Bian, C. *et al.* Sgf29 binds histone H3K4me2/3 and is required for SAGA complex recruitment and histone H3 acetylation. *EMBO J.* **30**, 2829–2842 (2011).

49. Laugesen, A., Højfeldt, J. W. & Helin, K. Molecular Mechanisms Directing PRC2 Recruitment and H3K27 Methylation. *Mol. Cell* **74**, 8–18 (2019).

50. Song, Y. *et al.* Mechanism of Crosstalk between the LSD1 Demethylase and HDAC1 Deacetylase in the CoREST Complex. *Cell Rep.* **30**, 2699-2711.e8 (2020).

51. Jones, P. A., Issa, J.-P. J. & Baylin, S. Targeting the cancer epigenome for therapy. *Nat. Rev. Genet.* **17**, 630–641 (2016).

52. Lu, C. *et al.* The MLL1-H3K4me3 Axis-Mediated PD-L1 Expression and Pancreatic Cancer Immune Evasion. *J. Natl. Cancer Inst.* **109**, djw283 (2017).

53. Zhao, Q.-Y. *et al.* Global histone modification profiling reveals the epigenomic dynamics during malignant transformation in a four-stage breast cancer model. *Clin. Epigenetics* **8**, 34 (2016).

54. Berger, L. *et al.* Expression of H3K4me3 and H3K9ac in breast cancer. *J. Cancer Res. Clin. Oncol.* **146**, 2017–2027 (2020).

55. Wei, Y. *et al.* Loss of trimethylation at lysine 27 of histone H3 is a predictor of poor outcome in breast, ovarian, and pancreatic cancers. *Mol. Carcinog.* **47**, 701–706 (2008).

56. Marsolier, J. *et al.* H3K27me3 conditions chemotolerance in triple-negative breast cancer. *Nat. Genet.* **54**, 459–468 (2022).

57. Lin, Y.-H. *et al.* Global reduction of the epigenetic H3K79 methylation mark and increased chromosomal instability in CALM-AF10-positive leukemias. *Blood* **114**, 651–658 (2009).

58. Shan, L., Hao, C., Jun, Z. & Qinghe, C. Histone methyltransferase Dot1L inhibits pancreatic cancer cell apoptosis by promoting NUPR1 expression. *J. Int. Med. Res.* **50**, 3000605221088431 (2022).

59. Weichert, W. *et al.* Association of patterns of class I histone deacetylase expression with patient prognosis in gastric cancer: a retrospective analysis. *Lancet Oncol.* **9**, 139–148 (2008).

60. Weichert, W. *et al.* Expression of Class I Histone Deacetylases Indicates Poor Prognosis in Endometrioid Subtypes of Ovarian and Endometrial Carcinomas. *Neoplasia N. Y. N* **10**, 1021–1027 (2008).

61. Mithraprabhu, S., Kalff, A., Chow, A., Khong, T. & Spencer, A. Dysregulated Class I histone deacetylases are indicators of poor prognosis in multiple myeloma. *Epigenetics* **9**, 1511–1520 (2014).

62. Alves-Fernandes, D. K. & Jasiulionis, M. G. The Role of SIRT1 on DNA Damage Response and Epigenetic Alterations in Cancer. *Int. J. Mol. Sci.* **20**, 3153 (2019).

63. Wang, R.-H. *et al.* Impaired DNA damage response, genome instability, and tumorigenesis in SIRT1 mutant mice. *Cancer Cell* **14**, 312–323 (2008).

64. Chen, G., Huang, P. & Hu, C. The role of SIRT2 in cancer: A novel therapeutic target. *Int. J. Cancer* **147**, 3297–3304 (2020).

65. Jia, Y.-L. *et al.* P300/CBP-associated factor (PCAF) inhibits the growth of hepatocellular carcinoma by promoting cell autophagy. *Cell Death Dis.* **7**, e2400 (2016).

66. Kim, J. J. *et al.* PCAF-Mediated Histone Acetylation Promotes Replication Fork Degradation by MRE11 and EXO1 in BRCA-Deficient Cells. *Mol. Cell* **80**, 327-344.e8 (2020).

67. Ikura, T. *et al.* Involvement of the TIP60 Histone Acetylase Complex in DNA Repair and Apoptosis. *Cell* **102**, 463–473 (2000).

68. Dreher, R. D. & Theisen, E. R. Lysine specific demethylase 1 is a molecular driver and therapeutic target in sarcoma. *Front. Oncol.* **12**, (2023).

69. Peters, A. H. *et al.* Loss of the Suv39h histone methyltransferases impairs mammalian heterochromatin and genome stability. *Cell* **107**, 323–337 (2001).

70. Wang, Z. *et al.* Inhibition of EZH2 Ameliorates Sepsis Acute Lung Injury (SALI) and Non-Small-Cell Lung Cancer (NSCLC) Proliferation through the PD-L1 Pathway. *Cells* **11**, 3958 (2022).

71. Yu, W. *et al.* EZH2: An Accomplice of Gastric Cancer. *Cancers* **15**, 425 (2023).

72. Zeng, J., Sun, L., Huang, J., Yang, X. & Hu, W. Enhancer of zeste homolog 2 is a negative prognostic biomarker and correlated with immune infiltrates in meningioma. *Front. Neurosci.* **16**, 1076530 (2022).

73. McCabe, M. T. *et al.* EZH2 inhibition as a therapeutic strategy for lymphoma with EZH2-activating mutations. *Nature* **492**, 108–112 (2012).

74. Shashikant, T. & Ettensohn, C. A. Chapter 8 - Genome-wide analysis of chromatin accessibility using ATAC-seq. in *Methods in Cell Biology* **151** 219–235 (Academic Press, 2019).

75. Grandi, F. C., Modi, H., Kampman, L. & Corces, M. R. Chromatin accessibility profiling by ATAC-seq. *Nat. Protoc.* **17**, 1518–1552 (2022).

76. Corces, M. R. *et al.* The chromatin accessibility landscape of primary human cancers. *Science* **362**, eaav1898 (2018).

77. Feng, S. & De Carvalho, D. D. Clinical advances in targeting epigenetics for cancer therapy. *FEBS J.* **289**, 1214–1239 (2022).

78. Santer, F. R. *et al.* Inhibition of the Acetyltransferases p300 and CBP Reveals a Targetable Function for p300 in the Survival and Invasion Pathways of Prostate Cancer Cell Lines. *Mol. Cancer Ther.* **10**, 1644–1655 (2011).

79. Ono, H. *et al.* C646 inhibits G2/M cell cycle-related proteins and potentiates anti-tumor effects in pancreatic cancer. *Sci. Rep.* **11**, 10078 (2021).

80. Wang, Y.-M. *et al.* Histone acetyltransferase p300/CBP inhibitor C646 blocks the survival and invasion pathways of gastric cancer cell lines. *Int. J. Oncol.* **51**, 1860–1868 (2017).

81. Muthukrishnan, S. D. *et al.* P300 promotes tumor recurrence by regulating radiation-induced conversion of glioma stem cells to vascular-like cells. *Nat. Commun.* **13**, 6202 (2022).

82. Moon, B. *et al.* Synergistic antitumor activity of sorafenib and MG149 in hepatocellular carcinoma cells. *BMB Rep.* **55**, 506–511 (2022).

83. Vansteenkiste, J. *et al.* Early phase II trial of oral vorinostat in relapsed or refractory breast, colorectal, or non-small cell lung cancer. *Invest. New Drugs* **26**, 483–488 (2008).

84. Wawruszak, A. *et al.* Vorinostat (SAHA) and Breast Cancer: An Overview. *Cancers* **13**, 4700 (2021).

85. Okubo, K., Isono, M., Miyai, K., Asano, T. & Sato, A. Fluvastatin potentiates anticancer activity of vorinostat in renal cancer cells. *Cancer Sci.* **111**, 112–126 (2020).

86. Juergens, R. A. *et al.* Combination epigenetic therapy has efficacy in patients with refractory advanced non-small cell lung cancer. *Cancer Discov.* **1**, 598–607 (2011).

87. Sidiropoulos, D. N. *et al.* Entinostat Decreases Immune Suppression to Promote Antitumor Responses in a HER2+ Breast Tumor Microenvironment. *Cancer Immunol. Res.* **10**, 656–669 (2022).

88. Pili, R. *et al.* Immunomodulation by entinostat in renal cell carcinoma patients receiving high dose interleukin 2: a multicenter, single-arm, phase 1/2 trial (NCI-CTEP#7870). *Clin. Cancer Res. Off. J. Am. Assoc. Cancer Res.* **23**, 7199–7208 (2017).

89. Shen, L. *et al.* Class I histone deacetylase inhibitor entinostat suppresses regulatory T cells and enhances immunotherapies in renal and prostate cancer models. *PloS One* **7**, e30815 (2012).

90. Gray, J. E. *et al.* A phase I, pharmacokinetic, and pharmacodynamic study of panobinostat, an HDAC inhibitor, combined with erlotinib in patients with advanced aerodigestive tract tumors. *Clin. Cancer Res. Off. J. Am. Assoc. Cancer Res.* **20**, 1644–1655 (2014).

91. Mithraprabhu, S. *et al.* Phase II trial of single-agent panobinostat consolidation improves responses after sub-optimal transplant outcomes in multiple myeloma. *Br. J. Haematol.* **193**, 160–170 (2021).

92. Wilson, A. J. *et al.* Panobinostat enhances olaparib efficacy by modifying expression of homologous recombination repair and immune transcripts in ovarian cancer. *Neoplasia N. Y. N* **24**, 63–75 (2022).

93. Ovejero-Sánchez, M. *et al.* Panobinostat Synergistically Enhances the Cytotoxicity of Microtubule Destabilizing Drugs in Ovarian Cancer Cells. *Int. J. Mol. Sci.* **23**, 13019 (2022).

94. Yousafzai, N. A. *et al.* SIRT1 deacetylated and stabilized XRCC1 to promote chemoresistance in lung cancer. *Cell Death Dis.* **10**, 363 (2019).

95. Ma, W., Zhao, X., Wang, K., Liu, J. & Huang, G. Dichloroacetic acid (DCA) synergizes with the SIRT2 inhibitor Sirtinol and AGK2 to enhance anti-tumor efficacy in non-small cell lung cancer. *Cancer Biol. Ther.* **19**, 835–846 (2018).

96. Zhao, Y. *et al.* Nuclear E-Cadherin Acetylation Promotes Colorectal Tumorigenesis via Enhancing β-Catenin Activity. *Mol. Cancer Res.* **17**, 655–665 (2019).

97. Campillo-Marcos, I., Monte-Serrano, E., Navarro-Carrasco, E., García-González, R. & Lazo, P. A. Lysine Methyltransferase Inhibitors Impair H4K20me2 and 53BP1 Foci in Response to DNA Damage in Sarcomas, a Synthetic Lethality Strategy. *Front. Cell Dev. Biol.* **9**, 715126 (2021).

98. Wang, H. *et al.* ROS/JNK/C-Jun Pathway is Involved in Chaetocin Induced Colorectal Cancer Cells Apoptosis and Macrophage Phagocytosis Enhancement. *Front. Pharmacol.* **12**, 729367 (2021).

99. Li, Z. *et al.* Chaetocin induces caspase-dependent apoptosis in ovarian cancer cells via the generation of reactive oxygen species. *Oncol. Lett.* **18**, 1915–1921 (2019).

100. Liao, X. *et al.* Identification of Chaetocin as a Potent non-ROS-mediated Anticancer Drug Candidate for Gastric Cancer. *J. Cancer* **10**, 3678–3690 (2019).

101. Ozyerli-Goknar, E. *et al.* The fungal metabolite chaetocin is a sensitizer for pro-apoptotic therapies in glioblastoma. *Cell Death Dis.* **10**, 894 (2019).

102. Hoy, S. M. Tazemetostat: First Approval. *Drugs* **80**, 513–521 (2020).

103. Izutsu, K. *et al.* Phase II study of tazemetostat for relapsed or refractory B-cell non-Hodgkin lymphoma with EZH2 mutation in Japan. *Cancer Sci.* **112**, 3627–3635 (2021).

104. Kazansky, Y. *et al.* Overcoming clinical resistance to EZH2 inhibition using rational epigenetic combination therapy. *BioRxiv Prepr. Serv. Biol.* 2023.02.06 (2023) doi:10.1101/2023.02.06.527192.

105. Daigle, S. R. *et al.* Selective Killing of Mixed Lineage Leukemia Cells by a Potent Small-Molecule DOT1L Inhibitor. *Cancer Cell* **20**, 53–65 (2011).

106. Salvati, A. *et al.* The Histone Methyltransferase DOT1L Is a Functional Component of Estrogen Receptor Alpha Signaling in Ovarian Cancer Cells. *Cancers* **11**, 1720 (2019).

107. Salvati, A. *et al.* Combinatorial targeting of a chromatin complex comprising Dot1L, menin and the tyrosine kinase BAZ1B reveals a new therapeutic vulnerability of endocrine therapy-resistant breast cancer. *Breast Cancer Res. BCR* **24**, 52 (2022).

108. Deng, Y. *et al.* Histone demethylase JMJD2D promotes the self-renewal of liver cancer stem-like cells by enhancing EpCAM and Sox9 expression. *J. Biol. Chem.* **296**, 100121 (2021).

109. Zhuo, M. *et al.* Inflammation-induced JMJD2D promotes colitis recovery and colon tumorigenesis by activating Hedgehog signaling. *Oncogene* **39**, 3336–3353 (2020).

110. Che, D. *et al.* KRT6A Promotes Lung Cancer Cell Growth and Invasion Through MYC-Regulated Pentose Phosphate Pathway. *Front. Cell Dev. Biol.* **9**, 694071 (2021).

111. Salamero, O. *et al.* First-in-Human Phase I Study of Iadademstat (ORY-1001): A First-in-Class Lysine-Specific Histone Demethylase 1A Inhibitor, in Relapsed or Refractory Acute Myeloid Leukemia. *J. Clin. Oncol. Off. J. Am. Soc. Clin. Oncol.* **38**, 4260–4273 (2020).

112. Leiendecker, L. *et al.* LSD1 inhibition induces differentiation and cell death in Merkel cell carcinoma. *EMBO Mol. Med.* **12**, e12525 (2020).

113. Cuyàs, E. *et al.* The LSD1 inhibitor iadademstat (ORY-1001) targets SOX2-driven breast cancer stem cells: a potential epigenetic therapy in luminal-B and HER2-positive breast cancer subtypes. *Aging* **12**, 4794–4814 (2020).

114. Lazo, P. A. Targeting Histone Epigenetic Modifications and DNA Damage Responses in Synthetic Lethality Strategies in Cancer? *Cancers* **14**, 4050 (2022).

115. Gkotzamanidou, M., Terpos, E., Dimopoulos, M. A. & Souliotis, V. L. The Combination of Panobinostat and Melphalan for the Treatment of Patients with Multiple Myeloma. *Int. J. Mol. Sci.* **23**, 15671 (2022).

116. Eleutherakis-Papaiakovou, E. *et al.* Efficacy of Panobinostat for the Treatment of Multiple Myeloma. *J. Oncol.* **2020**, 7131802 (2020).

117. Berdeja, J. G. *et al.* Panobinostat From Bench to Bedside: Rethinking the Treatment Paradigm for Multiple Myeloma. *Clin. Lymphoma Myeloma Leuk.* **21**, 752–765 (2021).

118. Zhang, H. *et al.* A subcellular map of the human kinome. *eLife* **10**, e64943 (2021).

119. Hanks, S. K. & Hunter, T. The eukaryotic protein kinase superfamily: kinase (catalytic) domain structure and classification1. *FASEB J.* **9**, 576–596 (1995).

120. Shin, J. *et al.* NMR Solution Structure of Human Vaccinia-related Kinase 1 (VRK1) Reveals the C-terminal Tail Essential for Its Structural Stability and Autocatalytic Activity*. *J. Biol. Chem.* **286**, 22131–22138 (2011).

121. Nichols, R. J. & Traktman, P. Characterization of Three Paralogous Members of the Mammalian Vaccinia Related Kinase Family*. *J. Biol. Chem.* **279**, 7934–7946 (2004).

122. Boyle, K. A. & Traktman, P. Members of a novel family of mammalian protein kinases complement the DNA-negative phenotype of a vaccinia virus ts mutant defective in the B1 kinase. *J. Virol.* **78**, 1992–2005 (2004).

123. Valbuena, A. *et al.* Identification of a dominant epitope in human vaccinia-related kinase 1 (VRK1) and detection of different intracellular subpopulations. *Arch. Biochem. Biophys.* **465**, 219–226 (2007).

124. Valbuena, A., López-Sánchez, I. & Lazo, P. A. Human VRK1 Is an Early Response Gene and Its Loss Causes a Block in Cell Cycle Progression. *PLoS ONE* **3**, e1642 (2008).

125. Nezu, J., Oku, A., Jones, M. H. & Shimane, M. Identification of Two Novel Human Putative Serine/Threonine Kinases, VRK1 and VRK2, with Structural Similarity to Vaccinia Virus B1R Kinase. *Genomics* **45**, 327–331 (1997).

126. Campillo-Marcos, I., García-González, R., Navarro-Carrasco, E. & Lazo, P. A. The human VRK1 chromatin kinase in cancer biology. *Cancer Lett.* **503**, 117–128 (2021).

127. Santos, C. R. *et al.* VRK1 Signaling Pathway in the Context of the Proliferation Phenotype in Head and Neck Squamous Cell Carcinoma. *Mol. Cancer Res.* **4**, 177–185 (2006).

128. Kang, T.-H., Park, D.-Y., Kim, W. & Kim, K.-T. VRK1 phosphorylates CREB and mediates CCND1 expression. *J. Cell Sci.* **121**, 3035–3041 (2008).

129. Moura, D. S. *et al.* Oncogenic Sox2 regulates and cooperates with VRK1 in cell cycle progression and differentiation. *Sci. Rep.* **6**, 28532 (2016).

130. Lopez-Borges, S. & Lazo, P. A. The human vaccinia-related kinase 1 (VRK1) phosphorylates threonine-18 within the mdm-2 binding site of the p53 tumour suppressor protein. *Oncogene* **19**, 3656–3664 (2000).

131. Barcia, R., López-Borges, S., Vega, F. M. & Lazo, P. A. Kinetic Properties of p53 Phosphorylation by the Human Vaccinia-Related Kinase 1. *Arch. Biochem. Biophys.* **399**, 1–5 (2002).

132. Sanz-García, M., Monsalve, D. M., Sevilla, A. & Lazo, P. A. Vaccinia-related Kinase 1 (VRK1) Is an Upstream Nucleosomal Kinase Required for the Assembly of 53BP1 Foci in Response to Ionizing Radiation-induced DNA Damage. *J. Biol. Chem.* **287**, 23757–23768 (2012).

133. Sanz-García, M., López-Sánchez, I. & Lazo, P. A. Proteomics Identification of Nuclear Ran GTPase as an Inhibitor of Human VRK1 and VRK2 (Vaccinia-related Kinase) Activities. *Mol. Cell. Proteomics MCP* **7**, 2199–2214 (2008).

134. Sapio, L. *et al.* Targeting CREB in Cancer Therapy: A Key Candidate or One of Many? An Update. *Cancers* **12**, 3166 (2020).

135. Molitor, T. P. & Traktman, P. Depletion of the protein kinase VRK1 disrupts nuclear envelope morphology and leads to BAF retention on mitotic chromosomes. *Mol. Biol. Cell* **25**, 891–903 (2014).

136. Moura, D. S., Campillo-Marcos, I., Vázquez-Cedeira, M. & Lazo, P. A. VRK1 and AURKB form a complex that cross inhibit their kinase activity and the phosphorylation of histone H3 in the progression of mitosis. *Cell. Mol. Life Sci.* **75**, 2591–2611 (2018).

137. Huang, R. & Zhou, P.-K. DNA damage repair: historical perspectives, mechanistic pathways and clinical translation for targeted cancer therapy. *Signal Transduct. Target. Ther*. **6**, 254 (2021).

138. Campillo-Marcos, I. & Lazo, P. A. Implication of the VRK1 chromatin kinase in the signaling responses to DNA damage: a therapeutic target? *Cell. Mol. Life Sci.* **75**, 2375–2388 (2018).

139. López-Sánchez, I. *et al.* VRK1 interacts with p53 forming a basal complex that is activated by UV-induced DNA damage. *FEBS Lett.* **588**, 692–700 (2014).

140. Monsalve, D. M. *et al.* VRK1 phosphorylates and protects NBS1 from ubiquitination and proteasomal degradation in response to DNA damage. *Biochim. Biophys. Acta BBA - Mol. Cell Res.* **1863**, 760–769 (2016).

141. Mon, A. M., MacKinnon, A. C. & Traktman, P. Overexpression of the VRK1 kinase, which is associated with breast cancer, induces a mesenchymal to epithelial transition in mammary epithelial cells. *PLOS ONE* **13**, e0203397 (2018).

142. Valbuena, A. *et al.* Alteration of the VRK1-p53 autoregulatory loop in human lung carcinomas. *Lung Cancer* **58**, 303–309 (2007).

143. Kim, I.-J. *et al.* Rewiring of human lung cell lineage and mitotic networks in lung adenocarcinomas. *Nat. Commun.* **4**, 1701 (2013).

144. Hennig, E. E., Mikula, M., Rubel, T., Dadlez, M. & Ostrowski, J. Comparative kinome analysis to identify putative colon tumor biomarkers. *J. Mol. Med. Berl. Ger.* **90**, 447–456 (2012).

145. Comparative Interactomes of VRK1 and VRK3 with Their Distinct Roles in the Cell Cycle of Liver Cancer. *Mol. Cells* (2017) doi:10.14348/molcells.2017.0108.

146. Ben, Z., Gong, L. & Qiu, Y. High expression of VRK1 is related to poor prognosis in glioma. *Pathol. Res. Pract.* **214**, 112–118 (2018).

147. So, J. *et al.* VRK1 as a synthetic lethal target in *VRK2* promoter–methylated cancers of the nervous system. *JCI Insight* **7**, (2022).

148. Liu, J. *et al.* Expression of vaccinia-related kinase 1 (VRK1) accelerates cell proliferation but overcomes cell adhesion mediated drug resistance (CAM-DR) in multiple myeloma. *Hematology* **21**, 603–612 (2016).

149. Li, J. *et al.* Expression of VRK1 and the downstream gene BANF1 in esophageal cancer. *Biomed. Pharmacother.* **89**, 1086–1091 (2017).

150. Fang, Z., Wang, F., Zhang, M., Huang, H. & Lin, Z. Identification of Co-Expression Modules and Genes Associated With Tumor Progression in Oral Squamous Cell Carcinoma. *Pathol. Oncol. Res.* **0**, (2022).

151. Navarro-Carrasco, E. & Lazo, P. A. VRK1 Depletion Facilitates the Synthetic Lethality of Temozolomide and Olaparib in Glioblastoma Cells. *Front. Cell Dev. Biol.* **9**, 683038 (2021).

152. Campillo-Marcos, I. & Lazo, P. A. Olaparib and ionizing radiation trigger a cooperative DNA-damage repair response that is impaired by depletion of the VRK1 chromatin kinase. *J. Exp. Clin. Cancer Res.* **38**, 203 (2019).

153. East, M. P. & Johnson, G. L. Adaptive chromatin remodeling and transcriptional changes of the functional kinome in tumor cells in response to targeted kinase inhibition. *J. Biol. Chem.* **298**, 101525 (2022).

154. Roskoski, R. Properties of FDA-approved small molecule protein kinase inhibitors: A 2023 update. *Pharmacol. Res.* **187**, 106552 (2023).

155. Ngow, Y. S., Rajan, S., Ye, H. & Yoon, H. S. Crystal structure of human vaccinia-related kinase 1 in complex with AMP-PNP, a non-hydrolyzable ATP analog. *Protein Sci. Publ. Protein Soc.* **28**, 524–532 (2019).

156. Carrión-Marchante, R. *et al.* DNA Aptamers against Vaccinia-Related Kinase (VRK) 1 Block Proliferation in MCF7 Breast Cancer Cells. *Pharmaceuticals* **14**, 473 (2021).

157. Serafim, R. A. M. *et al.* Development of Pyridine-Based Inhibitors for the Human Vaccinia-Related Kinases 1 and 2. 80.

158. Martín-Doncel, E., Rojas, A. M., Cantarero, L. & Lazo, P. A. VRK1 functional insufficiency due to alterations in protein stability or kinase activity of human VRK1 pathogenic variants implicated in neuromotor syndromes. *Sci. Rep.* **9**, 13381 (2019).

159. Morejon-Garcia, P. *et al.* Dysfunctional Homozygous VRK1-D263G Variant Impairs the Assembly of Cajal Bodies and DNA Damage Response in Hereditary Spastic Paraplegia. *Neurol. Genet.* **7**, e624 (2021).

160. Aghababazadeh, M. & Kerachian, M. A. Cell Fasting: Cellular Response and Application of Serum Starvation. *J. Nutr. Health* **2**, 147–150 (2014).

161. Shechter, D., Dormann, H. L., Allis, C. D. & Hake, S. B. Extraction, purification and analysis of histones. *Nat. Protoc.* **2**, 1445–1457 (2007).

162. Rashid, M. & Coombs, K. M. Serum-reduced media impacts on cell viability and protein expression in human lung epithelial cells. *J. Cell. Physiol.* **234**, 7718–7724 (2019).

163. Broussy, S., Laaroussi, H. & Vidal, M. Biochemical mechanism and biological effects of the inhibition of silent information regulator 1 (SIRT1) by EX-527 (SEN0014196 or selisistat). *J. Enzyme Inhib. Med. Chem.* **35**, 1124–1136 (2020).

164. Sacilotto, N. *et al.* Comprehensive in Vitro Characterization of the LSD1 Small Molecule Inhibitor Class in Oncology. *ACS Pharmacol. Transl. Sci.* **4**, 1818–1834 (2021).

165. Bowers, E. M. *et al.* Virtual Ligand Screening of the p300/CBP Histone Acetyltransferase: Identification of a Selective Small Molecule Inhibitor. *Chem. Biol.* **17**, 471–482 (2010).

166. Jiang, H. *et al.* Chaetocin: A review of its anticancer potentials and mechanisms. *Eur. J. Pharmacol.* **910**, 174459 (2021).

167. King, O. N. F. *et al.* Quantitative High-Throughput Screening Identifies 8-Hydroxyquinolines as Cell-Active Histone Demethylase Inhibitors. *PLOS ONE* **5**, e15535 (2010).

168. Yu, W. *et al.* Catalytic site remodelling of the DOT1L methyltransferase by selective inhibitors. *Nat. Commun.* **3**, 1288 (2012).

169. Li, G., Tian, Y. & Zhu, W.-G. The Roles of Histone Deacetylases and Their Inhibitors in Cancer Therapy. *Front. Cell Dev. Biol.* **8**, (2020).

170. Zhao, Z. *et al.* Role of histone methyltransferase SETDB1 in regulation of tumourigenesis and immune response. *Front. Pharmacol.* **13**, 1073713 (2022).

171. He, Y., Korboukh, I., Jin, J. & Juang. J. Targeting protein lysine methylation and demethylation in cancers. *Acta Biochim. Biophys. Sin.* **44**, 70–79 (2012).

172. Valbuena, A., Sanz-García, M., López-Sánchez, I., Vega, F. M. & Lazo, P. A. Roles of VRK1 as a new player in the control of biological processes required for cell division. *Cell. Signal.* **23**, 1267–1272 (2011).

173. Yan, F., Powell, D. R., Curtis, D. J. & Wong, N. C. From reads to insight: a hitchhiker's guide to ATAC-seq data analysis. *Genome Biol.* **21**, 22 (2020).

174. Hsu, H., Zhou, T. & Mountz, J. Nur77 Family of Nuclear Hormone Receptors. *Curr. Drug Target -Inflamm. Allergy* **3**, 413–423 (2004).

175. Kang, S.-A. *et al.* Regulation of Nur77 protein turnover through acetylation and deacetylation induced by p300 and HDAC1. *Biochem. Pharmacol.* **80**, 867–873 (2010).

176. Gui, T. & Burgering, B. M. T. FOXOs: masters of the equilibrium. *FEBS J.* **289**, 7918–7939 (2022).

177. Mitchell, S., Vargas, J. & Hoffmann, A. Signaling via the NFκB system. *Wiley Interdiscip. Rev. Syst. Biol. Med.* **8**, 227–241 (2016).

178. García-González, R., Monte-Serrano, E., Morejón-García, P., Navarro-Carrasco, E. & Lazo, P. A. The VRK1 chromatin kinase regulates the acetyltransferase activity of Tip60/KAT5 by sequential phosphorylations in response to DNA damage. *Biochim. Biophys. Acta BBA - Gene Regul. Mech.* **1865**, 194887 (2022).

179. Flavahan, W. A., Gaskell, E. & Bernstein, B. E. Epigenetic plasticity and the hallmarks of cancer. *Science* **357**, eaal2380 (2017).

180. Sevilla, A., Santos, C. R., Barcia, R., Vega, F. M. & Lazo, P. A. c-Jun phosphorylation by the human vaccinia-related kinase 1 (VRK1) and its cooperation with the N-terminal kinase of c-Jun (JNK). *Oncogene* **23**, 8950–8958 (2004).

181. Sevilla, A., Santos, C. R., Vega, F. M. & Lazo, P. A. Human vaccinia-related kinase 1 (VRK1) activates the ATF2 transcriptional activity by novel phosphorylation on Thr-73 and Ser-62 and cooperates with JNK. *J. Biol. Chem.* **279**, 27458–27465 (2004).

182. Monte-Serrano, E. *et al.* The pattern of histone H3 epigenetic posttranslational modifications is regulated by the VRK1 chromatin kinase. *Epigenetics Chromatin* **16**, 18 (2023).

183. Zhang, Y. *et al.* H3K27 acetylation activated-COL6A1 promotes osteosarcoma lung metastasis by repressing STAT1 and activating pulmonary cancer-associated fibroblasts. *Theranostics* **11**, 1473–1492 (2021).

184. Richards, A. L., Eckhardt, M. & Krogan, N. J. Mass spectrometry-based protein–protein interaction networks for the study of human diseases. *Mol. Syst. Biol.* **17**, e8792 (2021).

185. Monte-Serrano, E. & Lazo, P. A. VRK1 Kinase Activity Modulating Histone H4K16 Acetylation Inhibited by SIRT2 and VRK-IN-1. *Int. J. Mol. Sci.* **24**, 4912 (2023).

186. Li, Z. *et al.* SIRT2 inhibits non-small cell lung cancer cell growth through impairing Skp2-mediated p27 degradation. *Oncotarget* **7**, 18927–18939 (2016).

187. Fiskus, W. *et al.* SIRT2 Deacetylates and Inhibits the Peroxidase Activity of Peroxiredoxin-1 to Sensitize Breast Cancer Cells to Oxidant Stress-Inducing Agents. *Cancer Res.* **76**, 5467–5478 (2016).

188. He, X. *et al.* SIRT2 activity is required for the survival of C6 glioma cells. *Biochem. Biophys. Res. Commun.* **417**, 468–472 (2012).

189. Chabanon, R. M. *et al.* Targeting the DNA damage response in immuno-oncology: developments and opportunities. *Nat. Rev. Cancer* **21**, 701–717 (2021).

190. Luo, H. *et al.* Targeting the epigenetic processes to enhance antitumor immunity in small cell lung cancer. *Semin. Cancer Biol.* **86**, 960–970 (2022).

191. Zhou, V. W., Goren, A. & Bernstein, B. E. Charting histone modifications and the functional organization of mammalian genomes. *Nat. Rev. Genet.* **12**, 7–18 (2011).

192. Wang, H. *et al.* H3K4me3 regulates RNA polymerase II promoter-proximal pause-release. *Nature* **615**, 339–348 (2023).

193. Guenther, M. G., Levine, S. S., Boyer, L. A., Jaenisch, R. & Young, R. A. A Chromatin Landmark and Transcription Initiation at Most Promoters in Human Cells. *Cell* **130**, 77–88 (2007).

194. Wang, R. *et al.* An SETD1A/Wnt/β-catenin feedback loop promotes NSCLC development. *J. Exp. Clin. Cancer Res. CR* **40**, 318 (2021).

195. Zhao, D. *et al.* Histone Methyltransferase KMT2B Promotes Metastasis and Angiogenesis of Cervical Cancer by Upregulating EGF Expression. *Int. J. Biol. Sci.* **19**, 34–49 (2023).

196. Serra-Cardona, A., Duan, S., Yu, C. & Zhang, Z. H3K4me3 recognition by the COMPASS complex facilitates the restoration of this histone mark following DNA replication. *Sci. Adv.* **8**, eabm6246 (2022).

197. Lu, C. *et al.* WDR5-H3K4me3 epigenetic axis regulates OPN expression to compensate PD-L1 function to promote pancreatic cancer immune escape. *J. Immunother. Cancer* **9**, e002624 (2021).

198. Kotipalli, A., Banerjee, R., Kasibhatla, S. M. & Joshi, R. Analysis of H3K4me3-ChIP-Seq and RNA-Seq data to understand the putative role of miRNAs and their target genes in breast cancer cell lines. *Genomics Inform.* **19**, e17 (2021).

199. Xu, S., Wang, X., Yang, Y., Li, Y. & Wu, S. LSD1 silencing contributes to enhanced efficacy of anti-CD47/PD-L1 immunotherapy in cervical cancer. *Cell Death Dis.* **12**, 282 (2021).

200. Wong, S. H. K. *et al.* The H3K4-Methyl Epigenome Regulates Leukemia Stem Cell Oncogenic Potential. *Cancer Cell* **28**, 198–209 (2015).

201. Komura, K. *et al.* Resistance to docetaxel in prostate cancer is associated with androgen receptor activation and loss of KDM5D expression. *Proc. Natl. Acad. Sci. U. S. A.* **113**, 6259–6264 (2016).

202. Maeda, R. & Tachibana, M. HP1 maintains protein stability of H3K9 methyltransferases and demethylases. *EMBO Rep.* **23**, e53581 (2022).

203. Chen, Z. *et al.* H3K9 methylation enhances HP1-associated epigenetic silencing complex assembly and suppresses off-chromatin binding. *BioRxiv Prepr. Serv. Biol.* 2023.03.08 (2023).

204. Dunham, I. *et al.* An integrated encyclopedia of DNA elements in the human genome. *Nature* **489**, 57–74 (2012).

205. Gates, L. A. *et al.* Acetylation on histone H3 lysine 9 mediates a switch from transcription initiation to elongation. *J. Biol. Chem.* **292**, 14456–14472 (2017).

206. Lazaro-Camp, V. J., Salari, K., Meng, X. & Yang, S. SETDB1 in cancer: overexpression and its therapeutic implications. *Am. J. Cancer Res.* **11**, 1803–1827 (2021).

207. Yoo, J. *et al.* Advances in Histone Demethylase KDM3A as a Cancer Therapeutic Target. *Cancers* **12**, 1098 (2020).

208. Lee, D. H. *et al.* Advances in histone demethylase KDM4 as cancer therapeutic targets. *FASEB J.* **34**, 3461–3484 (2020).

209. Wapenaar, H. & Dekker, F. J. Histone acetyltransferases: challenges in targeting bi-substrate enzymes. *Clin. Epigenetics* **8**, (2016).

210. Patel, J. H. *et al.* The c-MYC oncoprotein is a substrate of the acetyltransferases hGCN5/PCAF and TIP60. *Mol. Cell. Biol.* **24**, 10826–10834 (2004).

211. Ramadoss, S., Guo, G. & Wang, C.-Y. Lysine demethylase KDM3A regulates breast cancer cell invasion and apoptosis by targeting histone and the non-histone protein p53. *Oncogene* **36**, 47–59 (2017).

212. Ding, X. *et al.* Epigenetic activation of AP1 promotes squamous cell carcinoma metastasis. *Sci. Signal.* **6**, ra28.1-13, S0-15 (2013).

213. Badie, A., Gaiddon, C. & Mellitzer, G. Histone Deacetylase Functions in Gastric Cancer: Therapeutic Target? *Cancers* **14**, 5472 (2022).

214. Liu, Z. *et al.* SETDB1 interactions with PELP1 contributes to breast cancer endocrine therapy resistance. *Breast Cancer Res. BCR* **24**, 26 (2022).

215. Zakharova, V. V. *et al.* SETDB1 fuels the lung cancer phenotype by modulating epigenome, 3D genome organization and chromatin mechanical properties. *Nucleic Acids Res.* **50**, 4389–4413 (2022).

216. Ueshima, S. & Fang, J. Histone H3K9 methyltransferase SETDB1 augments invadopodia formation to promote tumor metastasis. *Oncogene* **41**, 3370–3380 (2022).

217. Day, C. A., Hinchcliffe, E. H. & Robinson, J. P. H3K27me3 in Diffuse Midline Glioma and Epithelial Ovarian Cancer: Opposing Epigenetic Changes Leading to the Same Poor Outcomes. *Cells* **11**, 3376 (2022).

218. Raisner, R. *et al.* Enhancer Activity Requires CBP/P300 Bromodomain-Dependent Histone H3K27 Acetylation. *Cell Rep.* **24**, 1722–1729 (2018).

219. Song, Z. *et al.* The role of DOT1L in the proliferation and prognosis of gastric cancer. *Biosci. Rep.* **40**, BSR20193515 (2020).

220. Kurani, H. *et al.* DOT1L Is a Novel Cancer Stem Cell Target for Triple-Negative Breast Cancer. *Clin. Cancer Res. Off. J. Am. Assoc. Cancer Res.* **28**, 1948–1965 (2022).

221. Zhang, L.-Q. *et al.* Recognition of driver genes with potential prognostic implications in lung adenocarcinoma based on H3K79me2. *Comput. Struct. Biotechnol. J.* **20**, 5535–5546 (2022).

222. Tan, W. *et al.* Novel immune-related genes in the tumor microenvironment with prognostic value in breast cancer. *BMC Cancer* **21**, 126 (2021).

223. Zhang, Y., Chen, Z., Jiang, A. & Gao, G. KLRK1 as a prognostic biomarker for lung adenocarcinoma cancer. *Sci. Rep.* **12**, 1976 (2022).

224. Lj, L. *et al.* Differential Regulation of NK Cell Receptors in Acute Lymphoblastic Leukemia. *J. Immunol. Res.* **2022**, (2022).

225. Nguyen, K. *et al.* MAP3K Family Review and Correlations with Patient Survival Outcomes in Various Cancer Types. *Front. Biosci. Landmark Ed.* **27**, 167 (2022).

226. Fan, Y.-C. *et al.* Investigation of Anti-Tumor Effects of an MLK1 Inhibitor in Prostate and Pancreatic Cancers. *Biology* **10**, 742 (2021).

227. Ren, Q. *et al.* MicroRNA-361-5p induces hepatocellular carcinoma cell apoptosis and enhances drug sensitivity by targeting MAP3K9. *Exp. Ther. Med.* **21**, 574 (2021).

228. Fawdar, S. *et al.* Targeted genetic dependency screen facilitates identification of actionable mutations in FGFR4, MAP3K9, and PAK5 in lung cancer. *Proc. Natl. Acad. Sci. U. S. A.* **110**, 12426–12431 (2013).

229. Marusiak, A. A. *et al.* Mixed lineage kinases activate MEK independently of RAF to mediate resistance to RAF inhibitors. *Nat. Commun.* **5**, 3901 (2014).

230. Lee, S.-O. *et al.* Inactivation of the orphan nuclear receptor TR3/Nur77 inhibits pancreatic cancer cell and tumor growth. *Cancer Res.* **70**, 6824–6836 (2010).

231. Mohankumar, K., Shrestha, R. & Safe, S. Nuclear receptor 4A1 (NR4A1) antagonists target paraspeckle component 1 (PSPC1) in cancer cells. *Mol. Carcinog.* **61**, 73–84 (2022).

232. Wang, B. *et al.* The Role of the Transcription Factor EGR1 in Cancer. *Front. Oncol.* **11**, 642547 (2021).

233. Xiao, D., Chinnappan, D., Pestell, R., Albanese, C. & Weber, H. C. Bombesin Regulates Cyclin D1 Expression through the Early Growth Response Protein Egr-1 in Prostate Cancer Cells. *Cancer Res.* **65**, 9934–9942 (2005).

234. Hemming, M. L. *et al.* MOZ and Menin-MLL Complexes Are Complementary Regulators of Chromatin Association and Transcriptional Output in Gastrointestinal Stromal Tumor. *Cancer Discov.* **12**, 1804–1823 (2022).

235. Di Giorgio, E. *et al.* Different class IIa HDACs repressive complexes regulate specific epigenetic responses related to cell survival in leiomyosarcoma cells. *Nucleic Acids Res.* **48**, 646–664 (2020).

236. Wang, Z., Cai, H., Zhao, E. & Cui, H. The Diverse Roles of Histone Demethylase KDM4B in Normal and Cancer Development and Progression. *Front. Cell Dev. Biol.* **9**, 790129 (2021).

237. Kasinath, V. *et al.* JARID2 and AEBP2 regulate PRC2 in the presence of H2AK119ub1 and other histone modifications. *Science* **371**, eabc3393 (2021).

238. Zhu, X.-X. *et al.* Jarid2 is essential for the maintenance of tumor initiating cells in bladder cancer. *Oncotarget* **8**, 24483–24490 (2017).

239. Shaulian, E. & Karin, M. AP-1 as a regulator of cell life and death. *Nat. Cell Biol.* **4**, E131–E136 (2002).

240. Atsaves, V., Leventaki, V., Rassidakis, G. Z. & Claret, F. X. AP-1 Transcription Factors as Regulators of Immune Responses in Cancer. *Cancers* **11**, 1037 (2019).

241. Yu, S. *et al.* Irreversible Electroporation Mediates Glioma Apoptosis via Upregulation of AP-1 and Bim: Transcriptome Evidence. *Brain Sci.* **12**, 1465 (2022).

242. Chen, S. *et al.* Platycodin D induces apoptosis through JNK1/AP-1/PUMA pathway in non-small cell lung cancer cells: A new mechanism for an old compound. *Front. Pharmacol.* **13**, 1045375 (2022).

243. Hwang, W. Y. *et al.* Difluoromethylornithine Induces Apoptosis through Regulation of AP-1 Signaling via JNK Phosphorylation in Epithelial Ovarian Cancer. *Int. J. Mol. Sci.* **22**, 10255 (2021).

244. Ventura, J.-J. *et al.* Chemical Genetic Analysis of the Time Course of Signal Transduction by JNK. *Mol. Cell* **21**, 701–710 (2006).

245. Nakato, R. & Sakata, T. Methods for ChIP-seq analysis: A practical workflow and advanced applications. *Methods San Diego Calif* **187**, 44–53 (2021).

246. Noberini, R. *et al.* Extensive and systematic rewiring of histone post-translational modifications in cancer model systems. *Nucleic Acids Res.* **46**, 3817–3832 (2018).

247. Hong, M. *et al.* RNA sequencing: new technologies and applications in cancer research. *J. Hematol. Oncol.J Hematol Oncol* **13**, 166 (2020).

Appendices

9 Appendices

Supplementary Figure S1

A549 cell line

A549 NT | A549 siV-02 | A549 VRK-IN-1

U2OS cell line

U2OS NT | U2OS siV-02 | U2OS VRK-IN-1

Supplementary Figure S1. QR codes of wound healing assay videos of A549 and U2OS cell after VRK1 depletion or VRK-IN-1 treatment. Wound healing assay was performed for to study cell migration in A549 and U2OS cell line. Orange, purple and green QRs indicate NT, siV-02 and VRK-IN-1 conditions, respectively.

Supplementary Figure S2

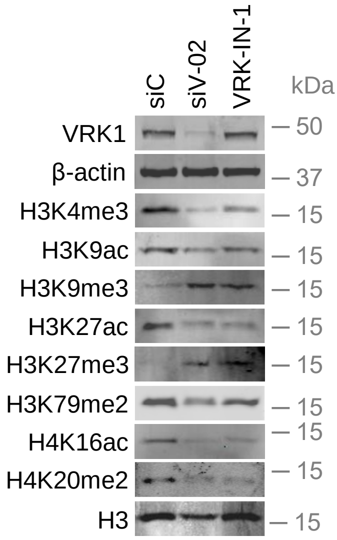

Supplementary Figure S2. VRK1 absence and VRK-IN-1 treatment alter histone PTM pattern. A549 cells were serum-deprived for 48 h. VRK1 was knocked down using a specific siRNA (siV-02) for 72 h or cells were incubated with 600 nM VRK-IN-1 for 24 h. WB shows the levels of different PTMs of histone acidic extracts. VRK1, β-actin and histone H3 were used as knock-down and loading control, respectively.

Supplementary Figure S3

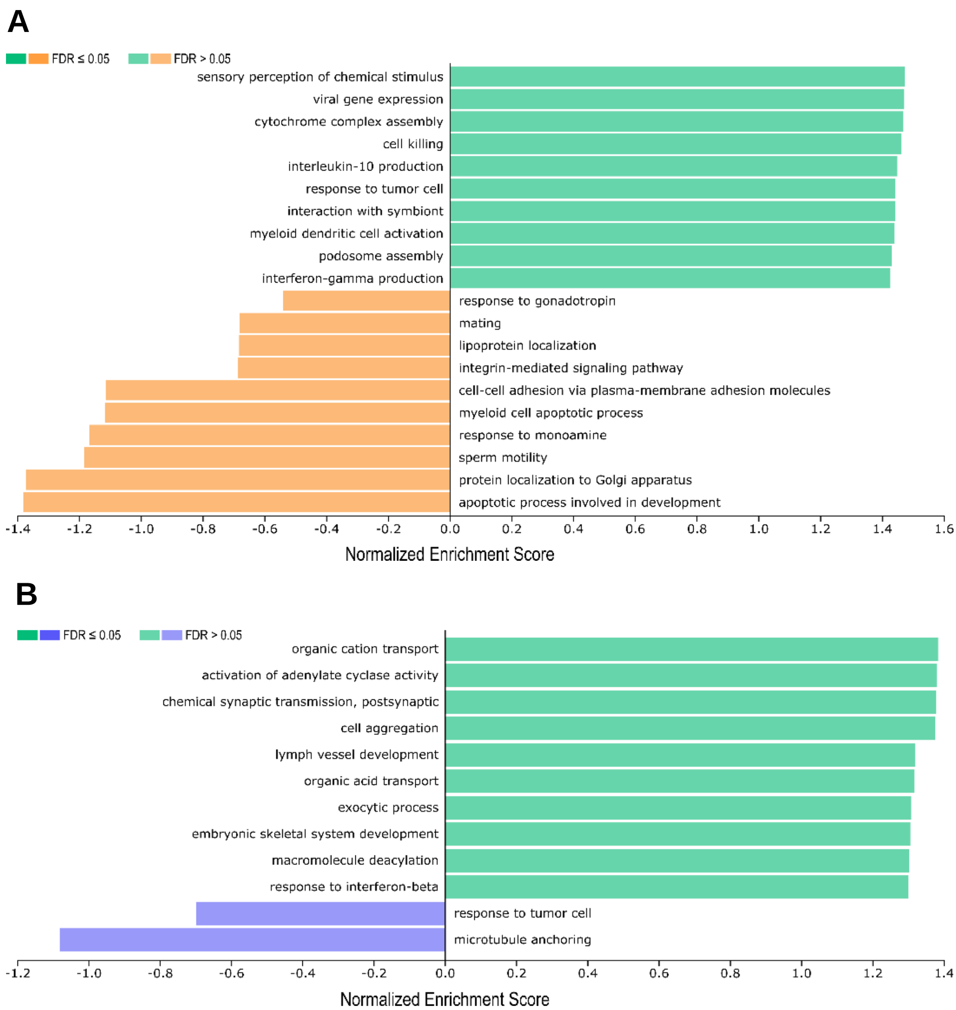

Supplementary Figure S3. Gene ontology analysis of genes associated with ATAC-seq peaks based on association by proximity. A. GO-BP analysis of NT vs VRK-IN-1. Green and orange are linked to enriched processes in VRK-IN-1 and NT condition, respectively. B. GO-BP analysis of VRK-IN-1 vs siV-02. Green and purple are associated with enriched processes in VRK-IN-1 and siV-02 condition, respectively.

Supplementary Figure S4

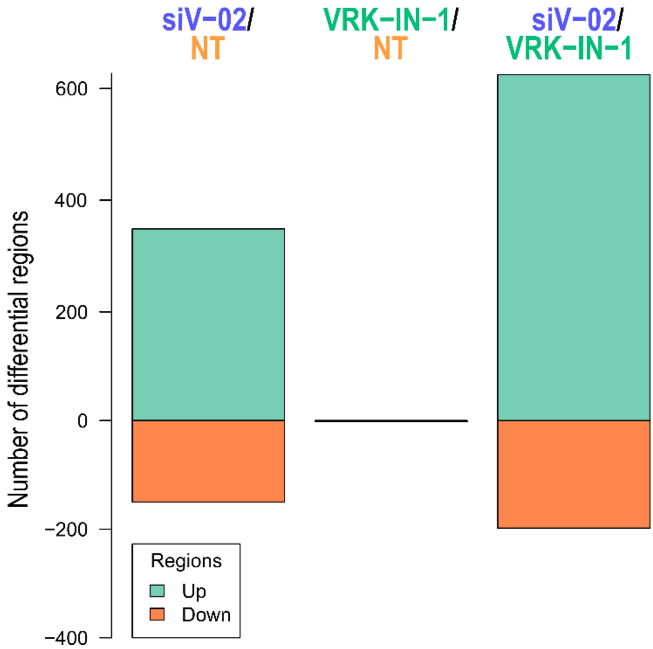

Supplementary Figure S4. Differential gene expression in A549 cells after VRK1 depletion or inhibition. Bar charts of differentially accessible regions identified by false discovery rate (FDR) < 0.1 and shrunken log2 fold change (shrunkenLFC) ≥ 0.3/ ≤ -0.3 between NT VS siV-02, NT VS VRK-IN-1 and siV-02 and VRK-IN-1 samples.

Supplementary Figure S5

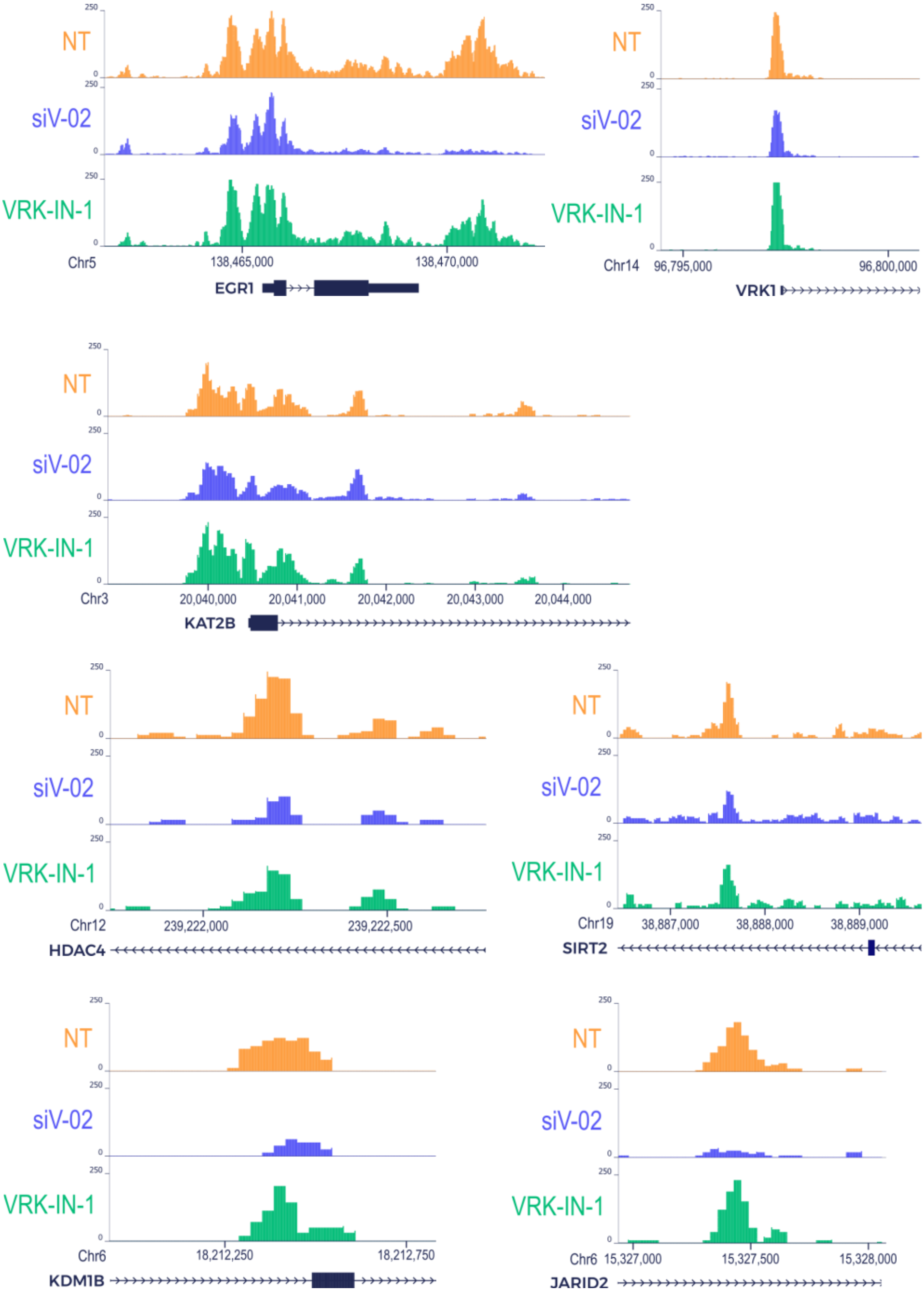

Supplementary Figure S5. ATAC-seq signal profile in A549 cells after VRK1 depletion or inhibition. Screen shot of ATAC signal of NT (orange), siV-02 (purple) and VRK1-IN-1-treated (green) cells in different chromosome regions. Human protein-coding genes taken from the NCBI RNA reference sequences collection (RefSeq) are shown.

Supplementary Figure S6

Upregulated TF binding site in siV-02 compared to NT

Rank	Motif	P-value	Best match/ Details	Motif File Link
1		1e-76	AP-1	
2		1e-18	NR4A1	
3		1e-13	TEAD3	
4		1e-13	FOXD3	

Downregulated TF binding site in siV-02 compared to NT

Rank	Motif	P-value	Best match/ Details	Motif File
1		1e-15	FOXO3	
2		1e-12	TEAD3	

Upregulated TF binding site in VRK-IN-1 compared to siV-02

Rank	Motif	P-value	Best match/ Details	Motif File
1		1e-17	Foxo3	
2		1e-13	NFkB-p65-Rel(RHD)	
3		1e-13	NF1(CTF)	
4		1e-12	TEAD3	

Downregulated TF binding site in VRK-IN-1 compared to siV-02

Rank	Motif	P-value	Best match/ Details	Motif File
1		1e-154	AP-1	
2		1e-18	Nur77(NR)	
3		1e-18	FOXM1	
4		1e-17	DUX4	

Supplementary Figure S6. **TF binding motifs enriched in A549 cells VRK1 depletion or inhibition.** HOMER motif analysis identifies the binding sequence of specific regulatory elements that are specifically up- or down-regulated after VRK1 depletion by siV-02 (compared with NT) or 600 nM VRK-IN-1 treatment (compared with siV-02).

Annexes

10 Annexes

Annex I. List of publications.

Published articles:

1. **Monte-Serrano E**, Lazo PA. The pattern of histone H3 epigenetic post-translational modifications is regulated by the VRK1 chromatin kinase. Epigenetics Chromatin 2023 May 13;16(1):18. doi: 10.1186/s13072-023-00494-7. PMID: 37179361.
2. **Monte-Serrano E**, Lazo PA. VRK1 activity modulating histone H4K16 acetylation inhibited by SIRT2 and VRK-IN-1. Int. J. Mol. Sci. 2023 Mar 24(5), 4912. doi: 10.3390/ijms24054912. PMID: 36902348. PMCID: PMC10003087.
3. García-Gonzalez R, **Monte-Serrano E**, Morejón-García P, Navarro-Carrasco E, Lazo PA. The VRK1 chromatin kinase regulates the acetyltransferase activity of TIP60/KAT5 by sequential phosphorylations in response to DNA damage. Biochim Biophys Acta Gene Regul Mech. 2022 Nov 1865(8):194887. doi: 10.1016/j.bbagrm.2022.194887. PMID: 36280132.
4. Campillo-Marcos I, **Monte-Serrano E**, Navarro-Carrasco E, García-González R, Lazo PA. Lysine Methyltransferase Inhibitors Impair H4K20me2 and 53BP1 Foci in Response to DNA Damage in Sarcomas, a Synthetic Lethality Strategy. Front Cell Dev Biol. 2021 Sep 3; 9: 715126. doi: 10.3389/fcell.2021.715126. PMID: 34540832; PMCID: PMC8446283.

Under revision articles:

1. Navarro-Carrasco E, **Monte-Serrano E**, Campos-Díaz A, Rolfs F, Goeij-de Haas R, Pham TV, Piersma SR, Jiménez CR, Lazo PA. VRK1 regulates sensitivity to oxidative stress by altering the nuclear phosphoproteome and histone epigenetic modifications. Cell. Mol. Life Sci.